

In-Depth Characterization of Human Retinoblastoma Subtype 2 and Preclinical Models

Daniela Ottaviani

▶ **To cite this version:**

Daniela Ottaviani. In-Depth Characterization of Human Retinoblastoma Subtype 2 and Preclinical Models. Cancer. Université Paris Saclay (COmUE), 2019. English. NNT : 2019SACLS001 . tel-03543361

HAL Id: tel-03543361
https://theses.hal.science/tel-03543361

Submitted on 26 Jan 2022

HAL is a multi-disciplinary open access archive for the deposit and dissemination of scientific research documents, whether they are published or not. The documents may come from teaching and research institutions in France or abroad, or from public or private research centers.

L'archive ouverte pluridisciplinaire **HAL**, est destinée au dépôt et à la diffusion de documents scientifiques de niveau recherche, publiés ou non, émanant des établissements d'enseignement et de recherche français ou étrangers, des laboratoires publics ou privés.

université PARIS-SACLAY

NNT : 2019SACLS001

Thèse de doctorat

UNIVERSITÉ PARIS SUD
Comprendre le monde, construire l'avenir

In-depth characterization of human retinoblastoma subtype 2 and preclinical models

Thèse de doctorat de l'Université Paris-Saclay
préparée à l'Université Paris-Sud

École doctorale n°582 Cancérologie : biologie - médecine – santé

Spécialité de doctorat: Aspects moléculaires et cellulaires de la biologie

Thèse présentée et soutenue à Paris, le 25 janvier 2019, par

Daniela OTTAVIANI

Composition du Jury :

Pr. Simon SAULE Professeur, Paris-Sud (INSERM U1021/CNRS UMR3347)	Président
Pr. Francesca ARIANI Professeure, Université de Sienne, Italie	Rapporteur
Dr. Isabelle JANOUEIX-LEROSEY Directrice de recherche, Institut Curie (INSERM U830)	Rapporteur
Dr. Ángel MONTERO CARCABOSO Directeur de recherche, Institut de Recherche Sant Joan de Déu, Espagne	Examinateur
Dr. Guillermo CHANTADA Directeur de recherche, Hôpital de Pédiatrie Garrahan, Argentine	Invité
Dr. François RADVANYI Directeur de recherche, Institut Curie (UMR144 CNRS)	Directeur de thèse

Résumé

Titre : Caractérisation approfondie du rétinoblastome humain de sous-type 2 et des modèles précliniques

Mots clés : rétinoblastome, sous-types moléculaires, *TFF1*, *MYC/MYCN*, OTX015/JQ1, modèles précliniques

Résumé : Le rétinoblastome, un cancer pédiatrique de la rétine en développement, est la tumeur intraoculaire la plus fréquente chez l'enfant et représente environ 4 % de tous les cancers infantiles. Bien qu'il s'agisse d'une maladie rare, l'hôpital Curie (centre de référence pour le rétinoblastome en France) accueille environ 50 à 60 nouveaux patients chaque année. Notre groupe a précédemment caractérisé deux sous-types de rétinoblastomes. Les tumeurs de type « cone-like » ou sous-type 1 sont plutôt différenciées et homogènes, présentent une surexpression des gènes liés aux cellules cônes (photorécepteurs) de la rétine, sont diagnostiquées cliniquement plus tôt et regroupent la majorité des formes héréditaires et bilatérales. Les tumeurs « mixed-type » ou sous-type 2, présentent une hétérogénéité intra-tumorale et une surexpression des gènes liés aux cellules des cônes et des cellules ganglionnaires de la rétine, sont enrichies en patients unilatéraux qui sont diagnostiqués cliniquement à des âges plus avancés. Le but général de ma thèse était d'approfondir la caractérisation moléculaire des rétinoblastomes de sous-type 2.
Nous avons caractérisé le paysage moléculaire et génomique du rétinoblastome dans une série de 102 tumeurs primaires, intégrant des échantillons de trois institutions : l'Institut Curie (France), l'Hôpital Garrahan (Argentine) et l'Hôpital Sant Joan de Déu (Espagne). Le développement d'une signature de méthylation par pyroséquençage pour la classification des échantillons nous a permis d'élargir nos échantillons classés, d'une première série de 72 à notre dernière série de 102 tumeurs. L'analyse du paysage mutationnel de notre série a révélé que les tumeurs du sous-type 2 avaient plus de mutations somatiques par échantillon que les tumeurs du sous-type 1. De plus les gènes *BCOR* et *ARID1A* étaient les deux seuls gènes mutés de manière récurrente, et identifiés uniquement dans le sous-type 2. La distribution des mutations sur le gène *RB1* jusqu'à présent a été analysée en fonction d'un seul groupe de rétinoblastomes. En divisant notre cohorte de tumeurs en sous-type 1 et en sous-type 2, la distribution des mutations le long de *RB1* était significativement différente. Par ailleurs, nous avons identifié une région de la protéine RB1 (dans le Domaine A) enrichie en mutations provenant des tumeurs du sous-type 2, avec très peu de mutations du sous-type 1. En plus des mutations somatiques, nous avons caractérisé deux événements récurrents de fusion chromosomique perturbant le gène *DACH1*. Les tumeurs de sous-type 2 sont caractérisées par une surexpression de *TFF1*, non exprimée dans la rétine normale. L'analyse par immunohistochimie de TFF1 dans des tumeurs localement invasives provenant de l'hôpital Garrahan a révélé la présence de cellules TFF1+ envahissant la région rétrolaminaire du nerf optique. Nous avons ensuite exploré un possible rôle oncogène de TFF1 dans le rétinoblastome lié à la survie cellulaire, à la migration cellulaire et à l'invasion cellulaire, qui n'a finalement pas été mis en évidence *in vitro*. Le sous-type moléculaire 2 regroupe les tumeurs *MYCN* amplifiées et les tumeurs avec une activation de la voie de signalisation MYC et des gènes cibles de *MYC*. L'utilisation de JQ1 et OTX015 (inhibiteurs des protéines BET bromodomaines) a fortement réduit la viabilité *in vitro* de lignées cellulaires de rétinoblastomes représentatives du sous-type 2, avec une régulation négative significative du gène et de la protéine MYC/MYCN. Nos résultats préliminaires suggèrent une nouvelle piste thérapeutique par l'inhibition des protéines BET dans le rétinoblastome. Les modèles précliniques largement utilisés dans la recherche sur le rétinoblastome n'ont pas été caractérisés ou classés au niveau moléculaire. Nous avons utilisé la même approche que pour la classification des tumeurs primaires et avons constaté que la plupart des modèles cellulaires et PDX étudiés étaient classés dans le sous-type moléculaire 2 et partageaient des caractéristiques moléculaires, génomiques et protéiques trouvés dans les tumeurs primaires de ce sous-type moléculaire. En conclusion, nous avons pu caractériser de façon plus approfondie le sous-type 2 des rétinoblastomes, qui semble présenter un phénotype plus agressif et qui est le sous-type représenté dans les modèles précliniques analysés.

Abstract

Title: In-depth characterization of human retinoblastoma subtype 2 and preclinical models

Keywords: retinoblastoma, molecular subtypes, TFF1, MYC/MYCN, OTX015/JQ1, preclinical models

Abstract: Retinoblastoma is a rare pediatric cancer of the developing retina that represents the most common intraocular tumor in children, and accounts for about 4% of all childhood cancers. Although being a rare disease, the Curie Hospital (the referral center for retinoblastoma in France) treats about 50-60 new patients each year. Our group has previously characterized two retinoblastoma subtypes. The cone-like or subtype 1 tumors rather differentiated and homogenous, presenting an overexpression of genes related to cone photoreceptor retinal cells, clinically diagnosed earlier and grouping the majority of hereditary and bilateral forms. The mixed-type or subtype 2 tumors, displaying an intra-tumoral heterogeneity and showing overexpression of genes related to cone and retinal ganglion cells, are enriched in unilateral patients clinically diagnosed at older ages. The general goal of my thesis was to extend the molecular characterization of these subtype 2 retinoblastomas.

We characterized the molecular and genomic landscape of retinoblastoma in a series of 102 primary tumors, integrating samples from three institutions: the Curie Institute (France), the Garrahan Hospital (Argentina) and the Sant Joan de Déu Hospital (Spain). The development of a pyrosequencing-based tool for sample classification allowed us to enlarge our classed samples, from an initial series of 72, to our final series of 102 tumors. Analysis of the mutational landscape in our series revealed that tumors from the subtype 2 had significantly more somatic mutations per sample than tumors from the subtype 1. Besides RB1 gene, BCOR and ARID1A where the only two recurrently mutated genes, and identified only in the subtype 2. Distribution of mutations alongside the RB1 gene has so far been analyzed in terms of a single group of retinoblastomas. When splitting our cohort in subtype 1 and subtype 2 tumors, the distribution of mutations was significantly different. Besides, we identified a region of the RB1 protein (in Domain A) enriched in mutations from tumors of the subtype 2, and devoid of mutations of the subtype 1. Besides somatic mutations, we characterized two recurrent chromosomal fusion events disrupting DACH1. Subtype 2 tumors are characterized by an overexpression of TFF1, not expressed in the normal retina. Immunohistochemical analysis of TFF1 in locally invasive tumors coming from the Garrahan Hospital revealed the presence of TFF1+ cells invading the retrolaminar region of the optic nerve. We then explored a possible oncogenic role of TFF1 in retinoblastoma related to cell survival, cell migration and cell invasion, which was not fully uncovered. Molecular subtype 2 regroups the MYCN amplified tumors and tumors with MYC signaling pathway activation and upregulation of hallmark MYC target genes. The use of JQ1 and OTX015 (BET bromodomains inhibitors) strongly reduced the viability in vitro of retinoblastoma cell lines representatives of the subtype 2, together with a significant MYC/MYCN gene and protein downregulation. We provided preliminary results to explore a new therapeutic avenue of BET protein inhibition in retinoblastoma. Preclinical models widely used in retinoblastoma research has not been characterized or classified at the molecular level. We have used the same approach as for primary human tumor's classification, and found that most cellular and PDX models studied classed in the molecular subtype 2 and shared many of the molecular, genomic and protein characteristics found in primary tumors of this molecular subtype. Taken together, we have performed a deeper characterization of subtype 2 retinoblastomas, which seems to represent a more aggressive phenotype, and is the represented subtype in the preclinical models analyzed.

ACKNOWLEDGEMENTS

First, I would like to thank François Radvanyi for all these years of continuous learning. Thank you for allowing me being part of your team for these four years, where I could participate in different projects and exciting discussions, from which I always learned something new. Thank you for challenge me (a new project, now? really?), allowing me to work freely and trust my work. Encore merci pour les réunions de dernière minute (de l'improvisation, on apprend aussi), et pour les chocolats et les bonbons Sugus !

I would like to thank Guillermo Chantada, for encouraging me into the research field and for trust in my work. Thanks for the many discussions we had throughout this period. The Retino Team is always happy to receive you in Curie and learn from you. Thank you for sending me to Paris! Where I was supposed to stay for one year and it has been four since that. Es un orgullo poder trabajar con vos, gracias por tu generosidad.

I would like to thank the members of my thesis committee, the reviewers Pr.Francesca Ariani and Dr.Isabelle Janoueix-Lerosey, the jury president Pr.Simon Saule, as well as the examiner Dr.Ángel Montero Carcaboso, to review and evaluate my work. Thank you for the travelling to Paris for the defense.

I thank my mid-term thesis committee Ana Maria Lennon, Christophe Ginestier and Christian Auclair for the exciting discussions, propositions and new ideas that helped me a lot to accomplish my work.

Je remercie la Fondation Nelia et Amadeo Barletta et Esteban Cvitkovic, et la Societé Française de lutte contre les cancers et les léucemies de l'enfant et de l'adolescent (SFCE) d'avoir contribué au financement de ma thèse. Et Retinostop d'avoir financé notre projet de modèles précliniques.

Je suis très reconnaissante aux cliniciens de l'Hôpital Curie pour leur participation active à nos projets et pour toutes les discussions passionnantes que nous avons eues, notamment Isabelle Aerts, François Doz and Paul Frenaux. Merci Paul pour ton temps et les après-midis de lecture de lames. Claude Houdayer et Catherine Dehainault. L'investissement de tous les membres du CRB (merci Élodie), du LIP (Ahmed, Élodie), des plateformes de pathologie expérimentale (merci Renaud), de génomique (Audrey, Élodie, Cécile, Benoit et David) et d'imagerie (Ludovic et Vincent).

I would like to thank the many people with whom I had the opportunity to collaborate during my thesis, including Alice Pinheiro, Danijela Vignjevic, Pablo Sáez, Pablo Vargas, Jorge Barbazan, Mathieu Maurin. Thanks for your time and generosity.

Un grand MERCI à l'équipe Rétino! Meriem, tu as été le début de ce grand projet. Céline, avec qui j'ai beaucoup travaillé et appris d'elle. Elodie pour être toujours disponible à nous aider. Merci Jing

de m’avoir beaucoup aidé à déchiffrer les données transcriptomiques ! À Narjesse pour avoir fait un grand travail en collectant tous les modèles PDX et avoir beaucoup aidé dans le projet de modèles précliniques. À Nanor, qui depuis son arrivée, nous a beaucoup aidé dans chacun des projets en cours.

Je garderai toujours de très bons souvenirs de tous les membres passés et présents de l’équipe Oncologie Moléculaire. Merci Isabelle, Florent et Hélène pour votre aide et commentaires généreux sur mes projets. Jennifer, MingJun (MingJuan merci de ton aide et ta compagnie les nombreux week-ends au labo), Laure, Jacqueline, Yanish, Linda. Vir et Aura The latin OM! Fatima pour ses sourires du matin, et Michèle toujours là quand il faut, toujours disponible à nous aider.

Merci Cocó d'avoir écouté et partagé mes peines et mes joies pendant ces quatre années !

A mis amigos de acá y de allá, a los de siempre, que aún a la distancia me acompañan. Gracias por bancarme a mí y a mis tantos “no puedo, estoy escribiendo” de este año. Ya casi termino!

A mamá, papá y Franco, mi familia adorada.

Gracias a mi amor, por acompañarme incondicionalmente a todos lados.

IN-DEPTH CHARACTERIZATION OF HUMAN RETINOBLASTOMA SUBTYPE 2 AND PRECLINICAL MODELS

List of abbreviations

HSJD	Sant Joan de Déu Hospital
CRB	biological resources center, Curie Institute
LIP	preclinical investigation laboratory, Curie Institute
CL-	cell line
PDX	patient derived xenograft
RB1	retinoblastoma susceptibility 1 gene
RB1	retinoblastoma susceptibility 1 protein
CNA	copy number alterations
CNV	copy number variations
BAC	bacterial artificial chromosome
SNP	single nucleotide polymorphism
WES	whole exome sequencing
CGH	comparative genomic hybridization
C1	retinoblastoma subtype 1, “cone-like” subtype
C2	retinoblastoma subtype 2, “mixed-type” subtype
9-CpG	methylome based signature for pyrosequencing analysis
SNV	single nucleotide variants
Indels	inframe/frameshift short deletions or insertions
LINC	long intervening noncoding RNA
TCGA	the cancer genome atlas
FBS	fetal bovine serum
IMDM	Iscove's Modified Dulbecco's cell culture Medium
RPMI	Roswell Park Memorial Institute cell culture medium
siRNA	short interfering RNA
siC	control siRNA
BET	bromodomain and Extra-Terminal motif proteins
BETi	BET bromodomain inhibitors
OTX015	BETi
JQ1	active JQ1; BETi
(+)-JQ1	active JQ1; BETi
(-)-JQ1	inactive JQ1
HES	hematoxylin erythrosine saffron staining
IHQ	immunohistochemistry
AFA	alcohol-formaldehyde-acetic acid
FFPE	formalin-fixed paraffin-embedded
ChIP-seq	Chromatin Immunoprecipitation Sequencing
STR	short tandem repeat
GO	gene ontology

Index

IN-DEPTH CHARACTERIZATION OF HUMAN RETINOBLASTOMA SUBTYPE 2 AND PRECLINICAL MODELS 1

List of abbreviations 2

INTRODUCTION 5

THE EYE AND THE NEURAL RETINA 5

Anatomy and physiology of the neural retina 6

Macula and fovea 7

Photoreceptors 8

Retina development 9

RETINOBLASTOMA 12

Epidemiology and global incidence 12

Clinical presentation 12

Genetic origins of retinoblastoma 13

Histopathology of retinoblastoma and degree of differentiation 17

Clinical management 18

General treatment of intraocular retinoblastoma 22

Treatment improvements in retinoblastoma 23

BIBLIOGRAPHY 24

OBJECTIVES 28

CONTEXT 28

RATIONALE 28

TIMELINE 29

CHAPTERS 30

Chapter 1 - MUTATIONAL LANDSCAPE AND MOLECULAR CLASSIFICATION OF RETINOBLASTOMA 30

Chapter 2 - *TFF1* GENE IN RETINOBLASTOMA 30

Chapter 3 - *MYC*, *MYCN* AND BROMODOMAIN INHIBITORS IN RETINOBLASTOMA 31

Chapter 4 - MOLECULAR CLASSIFICATION OF RETINOBLASTOMA PRECLINICAL MODELS 31

CHAPTER 1 33

CHAPTER 2 96

CHAPTER 3 132

CHAPTER 4 172

FINAL CONCLUSIONS AND PERSPECTIVES 232

Figures

FIGURE 1. ANATOMY OF THE EYE 5
FIGURE 2. LAYERS OF THE RETINA 6
FIGURE 3. THE MACULA AND FOVEA REGIONS OF THE HUMAN RETINA 8
FIGURE 4. CONE AND ROD PHOTORECEPTORS 9
FIGURE 5. CHRONOLOGICAL ORDER AND TRANSCRIPTIONAL REGULATION OF RETINAL CELL BIRTH 10
FIGURE 6. THE COMPETENCE MODEL OF RETINAL CELL-FATE DETERMINATION 11
FIGURE 7. CHRONOLOGICAL BIRTH ORDER OF RETINAL CELLS IN HUMAN INDUCED PLURIPOTENT STEM 11
FIGURE 8. UNIFOCAL AND MULTIFOCAL RETINOBLASTOMA 12
FIGURE 9. RETINOBLASTOMA MOST COMMON PRESENTING SIGNS 13
FIGURE 10. TWO GENETIC HITS TO RETINOBLASTOMA 14
FIGURE 11. MECHANISMS OF RB1 INACTIVATION IN HUMAN CANCER 15
FIGURE 12. ROLE OF RB1 AS A TRANSCRIPTIONAL CO-FACTOR AND AS AN ADAPTOR PROTEIN 16
FIGURE 13. ONCOGENIC EVENTS IN RETINOBLASTOMA 17
FIGURE 14. RETINOBLASTOMA DIFFERENTIATION 18
FIGURE 15. RETINOBLASTOMA DIAGNOSIS 19
FIGURE 16. PROGRESSION OF RETINOBLASTOMA 22

Tables

TABLE 1. CLASSIFICATION SYSTEMS FOR INTRAOCULAR RETINOBLASTOMA 20
TABLE 2. INTERNATIONAL RETINOBLASTOMA STAGING SYSTEM (IRSS) 21

INTRODUCTION

THE EYE AND THE NEURAL RETINA

The eye is an optical device that transmits and focuses light onto the neural retina. The eye is made up of three coats: the outermost layer is composed by the sclera, the middle layer by the choroid, and the innermost layer is the retina (**Figure 1**). The sclera is the tough outer coat (white part) of the eye that maintains the structural integrity of the eye and provides support for all the other eye tissues. The choroid is the layer between the retina and sclera, it is full of blood vessels and is responsible for supplying nutrients to the retina. It contains melanin pigment that absorbs any excess light in the eye. The vitreous humor is the jelly-like substance that fills the vitreous cavity between the lens and the retina, it is transparent and thus allows light to be focused onto the retina. The retina is the light-sensitive innermost lining of the eyeball, it comprises the retinal pigment epithelial layer and neurosensory retina. The optic nerve is composed of over one million nerve fibers. It transmits bio-electrical information from the neurosensory retina to the brain (Mescher, 2018).

The retina, a specialized ~0.2mm-thick region of the central nervous system, is the first station of the visual system. In addition to acting as a light receiver, the retina carries out considerable image processing through circuits that involve five main classes of neurons: photoreceptors, bipolar cells, amacrine cells, horizontal cells, and ganglion cells (**Figure 2B**). Neuronal processes collectively amplify, extract, and compress signals to preserve relevant information before it gets transmitted to the midbrain and the thalamus through the optical nerves, formed by the axons of the ganglion cells (Baccus, 2007). Müller cells, the major type of glial cells in the retina, are responsible for the homeostatic and metabolic support of retinal neurons (Reichenbach and Bringmann, 2013).

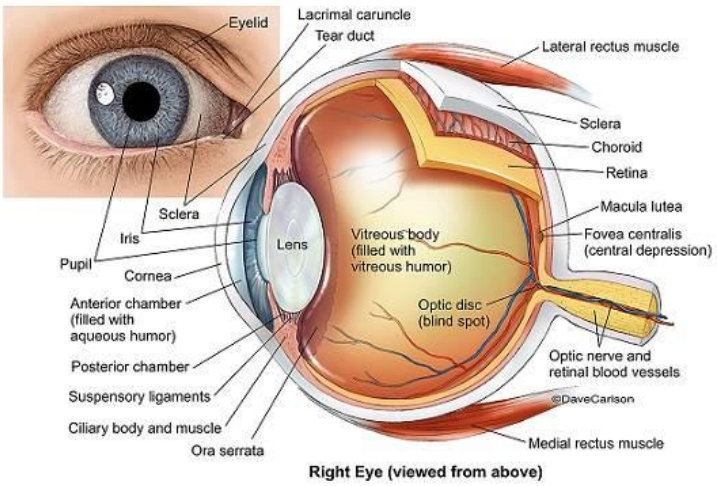


Figure 1. Anatomy of the eye
(Image from http://www.vision-and-eye-health.com/eye-anatomy.html).

Anatomy and physiology of the neural retina

The adult retina is a laminated structure that is bordered apically by the retinal pigment epithelium (RPE), a single cuboidal layer of epithelial cells, and basally by the vitreous, the fluid-filled cavity that separates the retina from the lens. The nuclei and processes of the retinal cells are segregated into alternate, anatomically distinctive layers (**Figure 2A**). Photoreceptors lie in the outer part of the retina, the region farthest from incoming light. Light passes through transparent inner retinal layers before it can be captured by the photoreceptors. Though such an organization may seem counterintuitive, it allows the RPE cells that lie juxtaposed to the apical side of the photoreceptors to absorb scattered light or light unabsorbed by the photoreceptors (Wallace, 2011).

Visual perception begins when the captured photon isomerizes the chromophore conjugated with the visual pigment in the photoreceptor cell. The photo excited visual pigment then initiates a signal transduction cascade that amplifies the signal and leads to the closure of cation channels on the plasma membranes. As a result, the cells become hyperpolarized. The change in membrane potential is sensed by the synapses, which react by releasing fewer neurotransmitters (Yau and Hardie, 2009). This information is relayed to the bipolar cells, and subsequently, the ganglion cells via a forward pathway. This information is also modified by their lateral interactions with the interneurons amacrine and horizontal cells (Sung and Chuang, 2010).

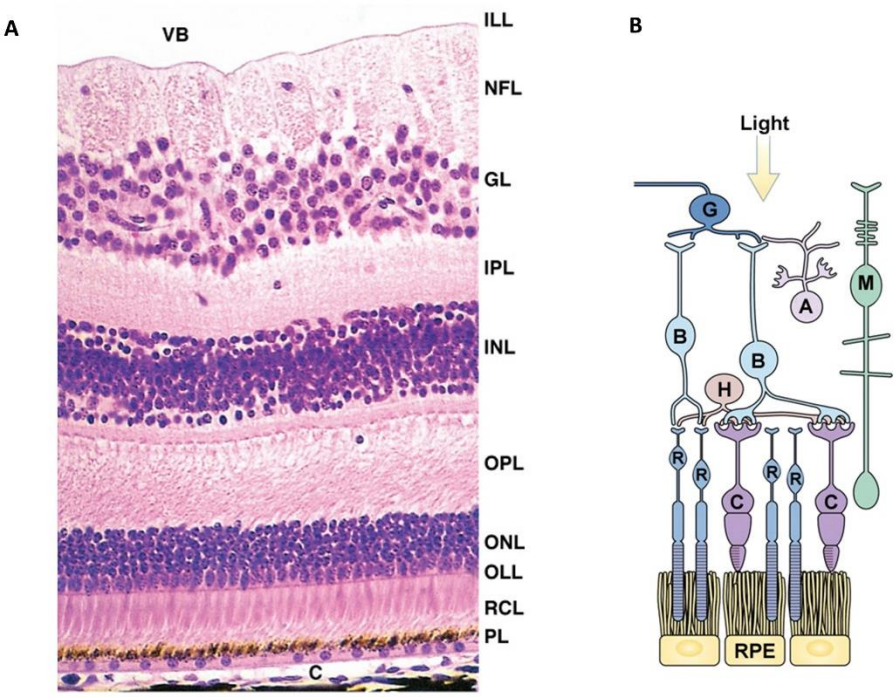


Figure 2. Layers of the retina

A) H&E-stained transverse section of human retina. Between the vitreous body (VB) and the choroid (C), the retina can usually be seen to have ten distinct layers. Following the path of the light, these are: the inner limiting layer (ILL); the nerve fiber layer (NFL), containing the axons of the ganglion cells that converge at the optic disc and form the optic nerve; the ganglion cell layer (GL), containing cell bodies of the ganglion cells; the inner plexiform layer (IPL), containing fibers and synapses of the ganglion cells and the bipolar neurons of the next layer; the inner nuclear layer

(INL), which contain nuclei of the bipolar cells, amacrine cells, horizontal cells, and Müller glial cells; the outer plexiform layer (OPL), contains the processes and synaptic terminals of photoreceptors, horizontal cells, and bipolar cells; the outer nuclear layer (ONL), with the cell bodies and nuclei of the photosensitive rod and cone cells; the outer limiting layer (OLL), which is a fine line formed by the junctional complexes holding the rod and cone cells to the intervening Müller glia cells; the rod and cone cell layer (RCL), which contains the outer segments of these cells where the photoreceptors are located; and the pigmented layer (PL) which is not sensory, but has several supportive functions important for maintenance of the neural retina. Image from (Mescher, 2018). B) Diagram of the organization of retinal cells in the laminated layers of the healthy human retina. (R) rods; (C) cones; (B) bipolar cells; (H) horizontal cell; (A) amacrine cell; (G) ganglion cell; (M) Müller glia cell. Image adapted from (Sung and Chuang, 2010).

Macula and fovea

The macula and foveal regions are specializations of the mammalian retina only present in humans and primates. The posterior pole of the retina that is just temporal to the optic nerve head and lies between the major vascular arcades is the macula (**Figure 3A**). The macula covers an area of about 5mm in diameter and histologically is defined as containing two or more layers of ganglion cells, whereas in the peripheral retina only a single layer of ganglion cells is present (Gregory-Evans et al., 2013). Within the macula there is a ~700µm-diameter foci near the central retina called the fovea (**Figure 3A**), and is identified as a depression in the macular region with sloping sides, where the inner retinal layers are absent. The fovea has the highest visual acuity in comparison with other parts of the retina due to several structural and compositional modifications of this region. The cell bodies of the proximal retinal neurons have been shifted to the side, enabling light paths to enter photoreceptors with minimal distortion. In addition, the fovea is characterized by a high density of cone photoreceptors, with a rod-free central region known as the foveola that is avascular and is comprised of elongated cone outer segments and Müller cell processes. The cone system has a higher resolution: each fovea cone is connected to only one bipolar and one ganglion cell. In other areas of the retina, each bipolar cell and ganglion cell serves multiple photoreceptors (Bringmann et al., 2018).

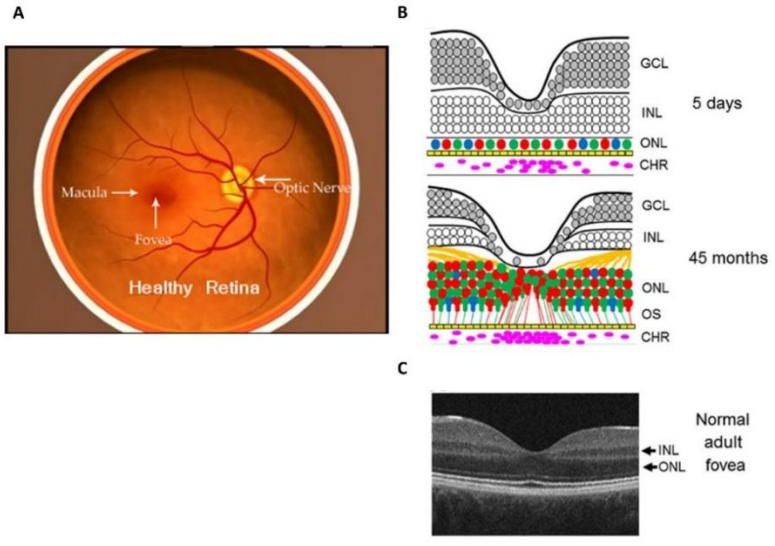


Figure 3. The macula and fovea regions of the human retina
A) Image of a healthy retina showing the macula and fovea regions. Optic nerve head is also shown. B) Development of the foveal specialization. At around the time of birth (upper panel) the foveal pit has formed but there is only a single row of cone nuclei in the ONL. At about 45 months of age (lower panel), many cones have migrated into the ONL and the inner and outer segments of the photoreceptors have formed. Directly underneath the foveal pit, the outer segments are much longer and the choroidal vasculature has thickened. Blue cones are notably absent from the center of the fovea. GCL, ganglion cell layer. CHR, choroid (pink ovals). B) Optical coherence tomography imaging of a normal adult human fovea. INL, inner nuclear layer; ONL, outer nuclear layer. Image adapted from (Gregory-Evans et al., 2013).

Photoreceptors

The human retina has a unique spatial organization of rods and cone photoreceptors (Curcio et al., 1990). Cones and rods are the two types of photoreceptors (**Figure 4**). Cones mediate vision in bright light, including color vision. Cones are named after their conically shaped light-sensing outer segments (OS). The OS is a modified cilium, a light-sensing organelle in which phototransduction occurs. The cone OS is commonly considered as a structure containing an orderly stack of membranous laminella that are continuous to the plasma membrane and form a highly convoluted surface membrane. Humans are trichromatic, with three cone pigments (opsins) with maximal absorption for different wavelengths of light, packed into the OS disc membranes of different types of cone cells. Each of these photopigments has a different sensitivity to light of different wavelengths, and for this reason are referred to as “blue,” “green,” and “red,” or, more appropriately, short-wavelength (S), medium-wavelength (M), and long-wavelength (L) cones, terms that more or less describe their spectral sensitivities (Neitz and Neitz, 2011). Rods mediate vision in dim light. Unlike other retinal cells, there is only one kind of rod photoreceptor (and one rod pigment: rhodopsin), and it is the predominant cell type in the retina. Humans have ~130 million photoreceptors, ~5 million bipolar cells, and ~1 million ganglion cells. Rods outnumber cones by ~20-fold, and are distributed throughout the retina with the exception of the fovea region.

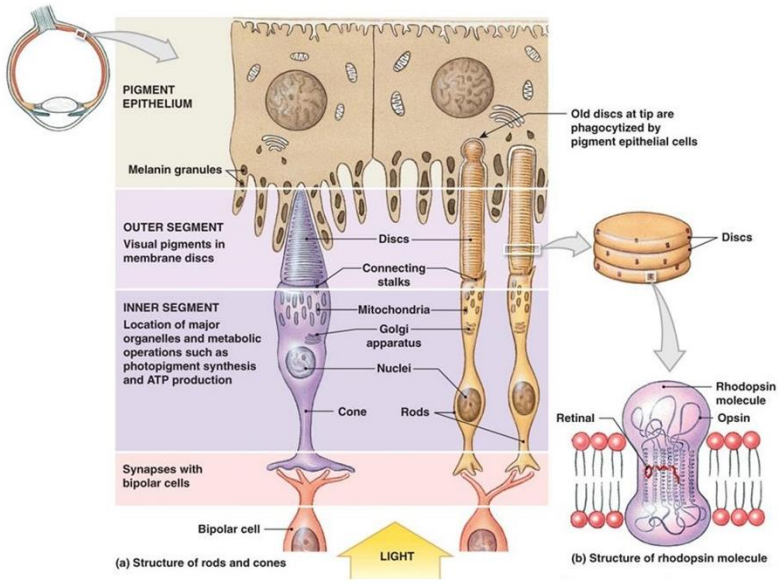


Figure 4. Cone and rod photoreceptors
A) Structure or cones and rods. The pigment epithelium absorbs photons that are not absorbed by visual pigments. It also phagocytizes old discs shed from the tip of the outer segment. The outer segment of a photoreceptor contains flattened membranous plates or discs that contain the visual pigments. The inner segment contain photoreceptor's major organelles and is responsible for all cell functions other than photoreception. It also releases neurotransmitters. B) Structure of rhodopsin molecule. Rods contain the visual pigment rhodopsin, which is embedded in a stack of membranous disks in the rod's outer segment. Rhodopsin consist of the light-absorbing molecule retinal bonded to opsin, a protein that has seven alpha helices that span the disk membrane. Image adapted from 2015 Person Education, Inc.

Retina development

The developmental sequence of retinal neurogenesis

The adult retina comprises six types of neurons (rod and cone photoreceptors, bipolar, amacrine, horizontal, and ganglion cells) and one type of glial cell (the Müller glia). These different cell types are generated from a pool of multipotent retinal progenitor cells. It has been proposed that mammalian retinal cell type specification is conserved and occurs through a series of overlapping temporal windows (Ohsawa and Kageyama, 2008; Rapaport et al., 2004; Young, 1984). Initially, the retinal neuroepithelium consists entirely of proliferating progenitor cells, and the onset of neurogenesis is marked by the appearance of the first postmitotic neurons, the ganglion cells, in the center of the retina at approximately embryonic day 11 (E11) in mouse (Young, 1985). In fact, in all vertebrate species studied, ganglion cells are the first neurons to differentiate and the remaining retinal neurons and glia are generated in a temporal, but overlapping, sequence that is fairly well conserved across vertebrate species (**Figure 5**) (Livesey et al., 2001). This implies that the timing mechanism controlling cell birth order is intrinsically maintained within retinal progenitor cells lineages, and has led to the widely accepted model that multipotent retinal progenitor cells go through a series of "competence states" where they progressively lose the ability to generate specific cell types or gain the competence to produce other cell types (**Figure 6**) (Livesey et al., 2001). Ganglion cell development is followed closely by the development of cones, horizontal cells, and

roughly half of the amacrine cells during embryogenesis. The remaining amacrine cells, bipolar cells, and Müller glia develop in a second postnatal wave. Rod photoreceptors are the exception, as they are generated throughout the period of retinal development (Young, 1985). However, it is important to emphasize that there is considerable overlap in the production of retinal cell types at any given time (Bassett and Wallace, 2012).

Retinal neurogenesis is also spatially regulated, as differentiation is initiated in the central retina and progresses toward the periphery, such that the central retina (close to where the ganglion cell axons exit the retina through the optic nerve head) is more developmentally advanced than the periphery. The proliferation phase of retinal development ends at approximately postnatal day 7 (P7) in the mouse and is followed by a period of synapse formation and remodeling, cell death, and morphological maturation of photoreceptors that continues until P21 (Wallace, 2011).

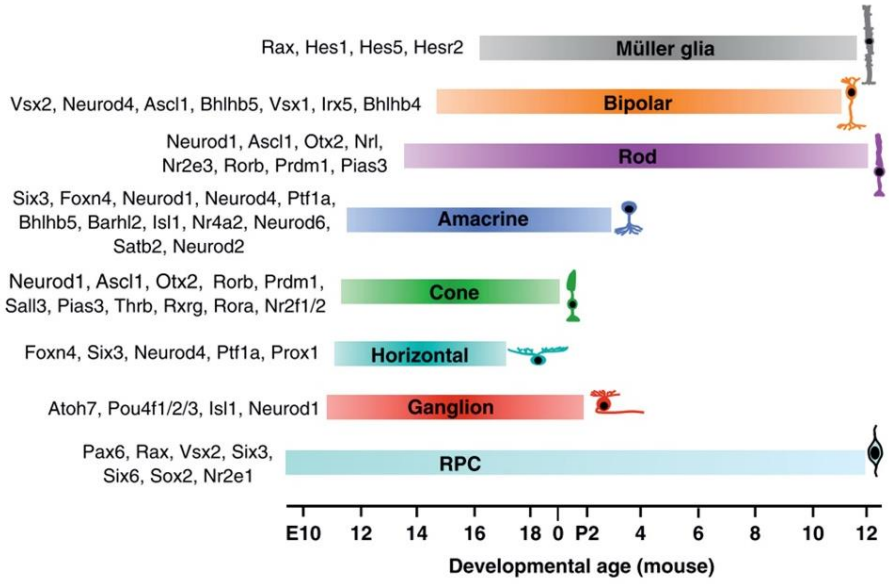


Figure 5. Chronological order and transcriptional regulation of retinal cell birth
Chronological order and transcriptional regulation of retinal cell birth. Retinal formation takes several weeks in the mouse embryo and several months in the human embryo. During this time, retinal progenitor cells (RPC) are dividing and generating postmitotic cells that commit to different neural and glial cell fates and differentiate to form necessary synaptic connections for proper visual signal processing. Embryonic and postnatal times based on mouse development. Image adapted from (Bassett and Wallace, 2012).

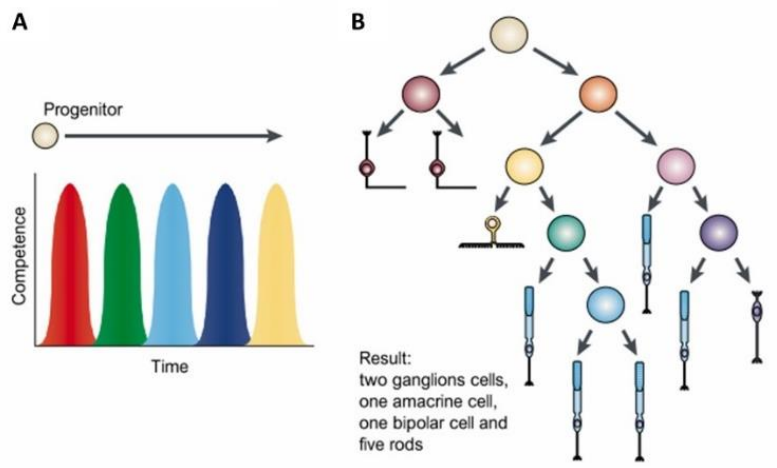


Figure 6. The competence model of retinal cell-fate determination
A) A progenitor passes through waves of competence, indicated by different colors, during which it is competent to generate only a subset of types of postmitotic cells. A key feature of this model is that cells both acquire and lose the ability to make various cell types. This is in contrast to a model of progressive restriction, in which cells can make all cell types early in development, but then gradually lose the ability to make the early cells. B) The predicted lineage tree built up by cell divisions of multipotent progenitors over time. With each division, a progenitor generates two progeny, which might be either mitotic or postmitotic. The first division shown generates two progenitors, whereas all of the other divisions generate either a progenitor and a postmitotic cell or two postmitotic cells. Different colours of progenitor cells denote different competence states. More than one type of progenitor is predicted to produce a particular cell fate, here a rod photoreceptor (blue). In vivo lineage analysis using retroviral labelling has shown that such multi-cell type clones are typical in the vertebrate retina (Turner et al., 1990). Image adapted from (Livesey et al., 2001).

The chronological birth order of retinal cells is recapitulated by human induced pluripotent stem (hiPS)

More recently, the production of retinal cells from hiPS cultured in pro-neural medium, has demonstrated to generate both retinal pigmented epithelial cells and self-forming neural retina-like structures containing retinal progenitor cells that can be differentiated into all retinal cell types, including retinal ganglion cells and precursors of photoreceptors (Reichman and Goureau, 2014) in a similar chronological order (**Figure 7**) as described for the mouse retina.

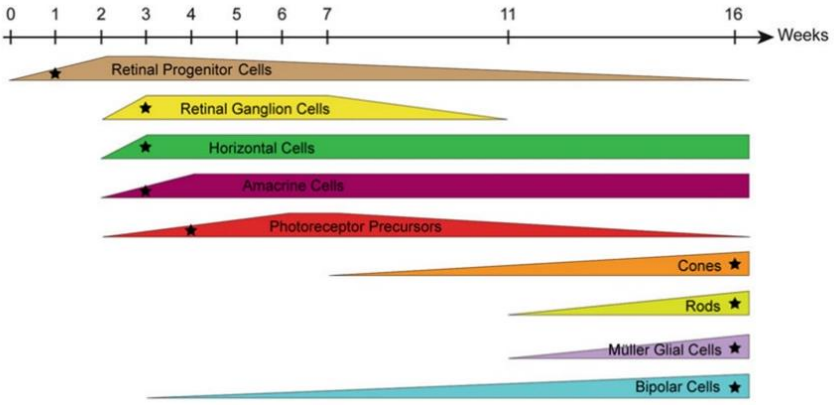


Figure 7. Chronological birth order of retinal cells in human induced pluripotent stem
Colored blocks represent evolution of each specific retinal cell type and black stars indicate the time when each specific retinal cell was undoubtedly detected. Image adapted from (Reichman and Goureau, 2014)

RETINOBLASTOMA

Epidemiology and global incidence

Retinoblastoma is a rare pediatric cancer of the developing retina that represents the most common intraocular tumor in children, and accounts for about 4% of all childhood cancers (Abramson, 2005). The global retinoblastoma incidence is 1 in 16.000–18.000 live births per year, predicting approximately 8.000 new cases each year (Dimaras et al., 2015).

Clinical presentation

Retinoblastoma is generally diagnosed at birth or during early childhood, with a median age of diagnosis of 18 months (Abramson et al., 2002). The diagnosis of retinoblastoma in children 6 years or older is extremely rare. Disease can be either unilateral or bilateral, affecting one or both eyes, respectively. Retinoblastoma can also develop as a single tumor within the eye (unifocal retinoblastoma) or as multiple tumor foci (multifocal retinoblastoma) (**Figure 8**). Unilateral retinoblastomas count for 60% of cases and have a median age at diagnosis of two years, while 40% of cases are bilateral with a median age at diagnosis of one year. All bilateral cases are heritable, while only ~15% of unilateral cases (multifocal) can be passed on to future generations (Aerts et al., 2006; Dimaras et al., 2015).

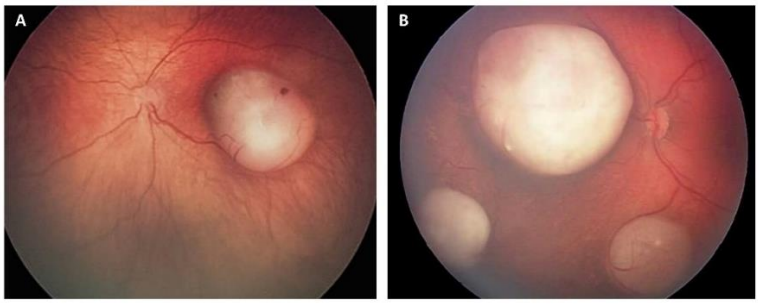


Figure 8. Unifocal and multifocal retinoblastoma
A) Unifocal foveal tumor confined to the retina (image from (Fabian et al., 2018)). B) Multifocal retinoblastoma with three tumor foci (image from https://www.willseye.org/disease_condition/retinoblastoma/)

First signs and symptoms

Age at retinoblastoma diagnosis is a result of both the molecular basis (heritable retinoblastoma presents at a younger age than does non-heritable disease) and the medico-social response to its symptoms and signs. The most common sign is leukocoria (white pupil, **Figure 9A**) and is first apparent when the tumor is still contained within the eye. The second most common sign is strabismus (misaligned eyes, **Figure 9B**), that results from a loss of central vision in one or both eyes causing the ocular misalignment. Advanced disease stage might present with iris rubeosis (neovascularization of the iris), hypopyon (inflammatory cells in the anterior chamber of the eye),

hyphema (blood in the anterior chamber of the eye), buphthalmia (enlargement of the eyeball), orbital cellulitis (inflammation of the soft tissues of the eye), and exophthalmia or proptosis (bulging of the eye anteriorly out of the orbit) (Abramson et al., 2003; Aerts et al., 2006).

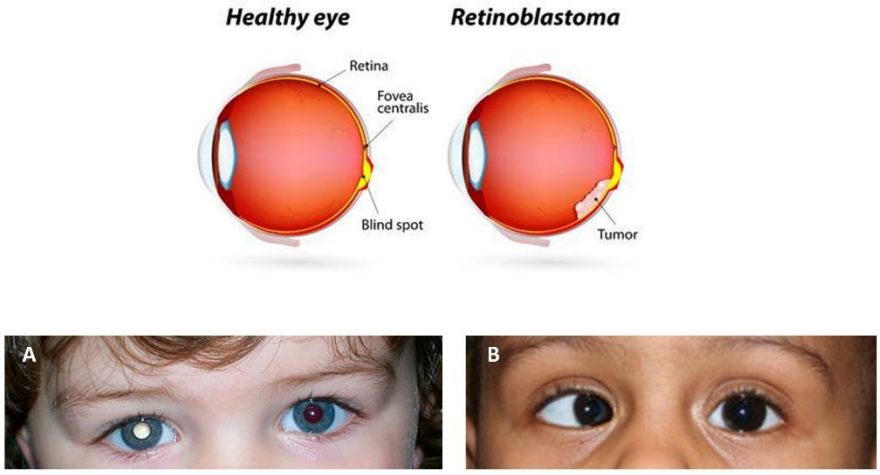


Figure 9. Retinoblastoma most common presenting signs
A) Leukocoria: the normal red reflex is given by light influencing in the vascularized choroid that lies the healthy retina. Because retinoblastoma has a white appearance, a white reflex replaces the red one. B) Strabismus results from a loss of central vision in one or both eyes causing the ocular misalignment.

Genetic origins of retinoblastoma

Knudson's analysis on the laterality and the age at diagnosis of retinoblastoma provided the today known "two-hit" model for tumor-suppressor gene inactivation. In 1971, Knudson developed the hypothesis that retinoblastoma is a cancer caused by two mutational events (**Figure 10**) (Knudson, 1971). He postulated that one of those mutations might be inherited as a result of a previous germinal mutation, and that these patients developed tumors earlier than those who develop the nonhereditary form of the disease. He also analyzed the number of tumors per individual and noted that in the majority of cases those who inherited a mutation developed more than one tumor. On the other hand, the probability that an individual not inheriting a mutation would develop more than one tumor was vanishingly small, so that nonhereditary cases were invariably unifocal. Cytogenetic analysis linking the deletion of chromosomal band 13q14 and predisposition to retinoblastoma (Cavenee et al., 1983), and the posterior molecular cloning of the retinoblastoma susceptibility 1 gene *(RB1)* (Friend et al., 1986; Lee et al., 1987) have verified the essential features of the hypothesis formulated by Knudson: the first Knudson's event was the inactivation of an *RB1* allele and the second event was the inactivation of the second *RB1* allele. *RB1* became the first tumor-suppressor gene to be characterized.

One of the important and unexpected consequences of the identification of the *RB1* gene was the discovery that this pathway is mutated in virtually every human cancer (Hanahan and Weinberg,

2000). Thus, by studying a rare pediatric cancer, Knudson and others identified one of the most important tumor suppressor pathways in human cancer.

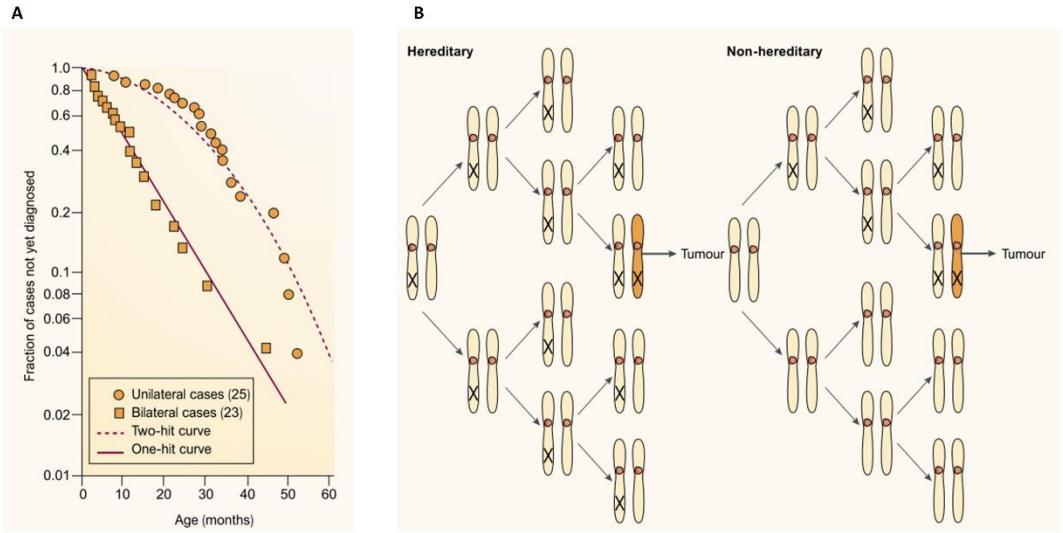


Figure 10. Two genetic hits to retinoblastoma
A) One-hit and two-hit curves for retinoblastoma. These semilog plots of the fraction of 23 bilateral (heritable) cases and 25 unilateral (most expected to be non-heritable) cases that were still not diagnosed at plotted ages (analyzed retrospectively) show that the bilateral cases match the expected shape of a one-hit curve, whereas the unilateral cases match the shape of a two-hit curve. As the bilateral cases inherit one genetic hit, both heritable and spontaneous retinoblastoma are due to two hits. B) Two-hit tumor formation in both hereditary and nonhereditary retinoblastoma. A "one- hit" clone is a precursor to the tumor in nonhereditary retinoblastomas, whereas all cells of the body are "one-hit" clones in hereditary retinoblastoma. Image adapted from (Knudson, 2001).

The RB1 tumor suppressor role

The *RB1*-encoded protein (RB1) is well known as a negative cell cycle regulator, the first cellular function described for RB1 (Goodrich et al., 1991; Weinberg, 1995) and the most thoroughly studied. The textbook model for RB1 function is appealingly simple. RB1 is a chromatin-associated protein that limits the transcription of cell cycle genes, primarily via regulation of the E2F transcription factors. In addition to binding to E2F, RB1 interacts with chromatin regulators. These contacts allow RB1 to recruit and stabilize complexes that repress transcription. By suppressing transcription of E2F targets, RB1 restricts the expression of genes that are needed for cell proliferation. RB1 is broadly expressed, but its activity is controlled by cyclin-dependent kinases (CDKs). Active RB1 is found in quiescent cells, during G1 phase of the cell cycle, and during check-point-mediated cell cycle arrest. Hyperphosphorylation of RB1 at the G1/S transition relieves RB1's inhibition of E2F and allows cell cycle progression. RB1 is functionally compromised in many tumors either as a result of mutations in *RB1* or mutations that increase the phosphorylation of RB1 or through the expression of viral oncoproteins that target RB1 protein (**Figure 11**) (Goodrich, 2006).

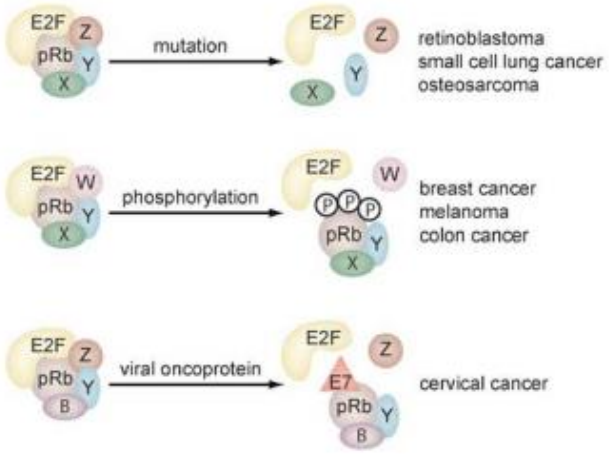


Figure 11. Mechanisms of RB1 inactivation in human cancer

RB1 tumor suppressor function was originally thought to be largely due to its capacity to arrest cells in G1 by inhibiting the activity of E2F transcription factors, but research over the past decades has given an increasingly complex picture of RB1 action (**Figure 12**). In addition to the repression of E2F-regulated genes, RB1 has been implicated in many other cellular processes relevant to cancer including cell differentiation (Korenjak and Brehm, 2005; McClellan et al., 2007; Nguyen and McCance, 2005), cell survival (Chau and Wang, 2003; Delston and Harbour, 2006; Hallstrom and Nevins, 2009), senescence (Ben-Porath and Weinberg, 2005; Liu et al., 2004), and genome stability (Knudsen et al., 2006). Moreover, recent studies have also demonstrated that control of the stability of the p27 cell cycle inhibitor (encoded by CDKN1B) by RB1, through the interaction of RB1 with the anaphase-promoting complex/cyclosome (APC/C), is an important part of the capacity of RB1 to arrest cells in G1 (**Figure 12D**). Therefore, E2Fs are not the sole mediators of the capacity of RB1 to control the G1/S cell cycle transition (Binné et al., 2007; Ji et al., 2004). RB1 is now viewed as a transcriptional co-factor that can bind to and either antagonize or potentiate the function of numerous transcription factors (**Figure 12E**) (Macaluso et al., 2006; Morris and Dyson, 2001). Furthermore, RB1 is also an adaptor protein that recruits chromatin remodeling enzymes to control the expression of specific target genes and to modify chromatin structure at a chromosome-wide level (Brehm and Kouzarides, 1999; Gonzalo and Blasco, 2005).

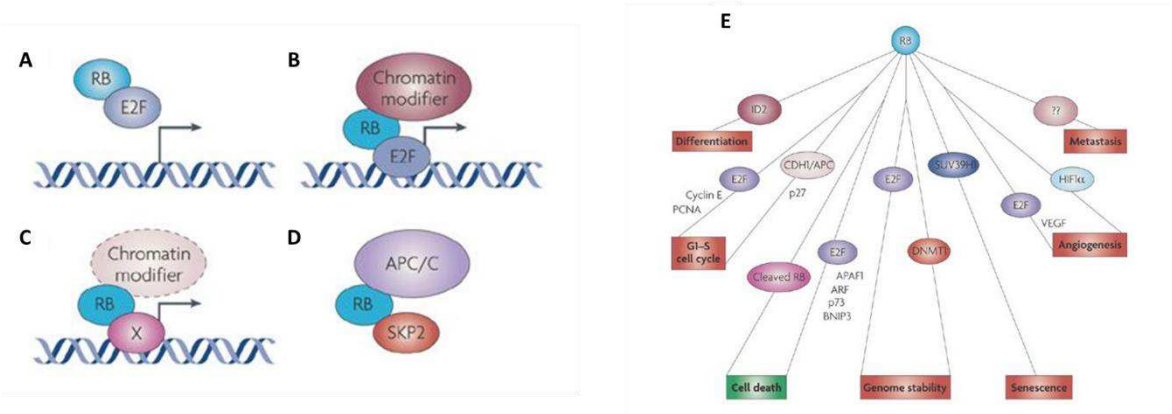


Figure 12. Role of RB1 as a transcriptional co-factor and as an adaptor protein
A) Classically, RB1 binds to E2F transcription factors and recruits them away from their target genes. B) Alternatively, RB1 is recruited to the promoter of target genes by E2F and inhibits their transactivation activity and further recruits chromatin remodeling complexes including HDAC (histone deactylase), DNMT1 (DNA methyltransferase 1), HP1A (heterochromatin protein 1A) and SUV39H1 (Histone-lysine N-methyltransferase) to repress transcription. C) RB1 is a transcriptional co-factor for non-E2F transcription factors or other co-factors, such as the HIF1α (hypoxia-induced factor 1α), MYOD (Myoblast determination protein 1) and SP1 transcription factors. D) RB1 serves as a non-chromatin-associated protein adaptor: illustrated is one example of RB1 acting to recruit APC/C (anaphase promoting complex/cyclosome) and SKP2 (S-phase kinase-associated protein 2) to the same complex, promoting SKP2 degradation. E) RB1 binding partners and transcriptional targets that might mediate its tumor suppressor ability. APAF1, apoptotic peptidase activating factor 1; BNIP3, BCL2-interacting protein 3; CDH1, cadherin 1; DNMT1, DNA methylatransferase 1; HIF1α, hypoxia-induced factor 1α; PCNA, proliferating cell nuclear antigen; VEGF, vascular endothelial growth factor. Image adapted from (Burkhart and Sage, 2008).

Oncogenic events in retinoblastoma tumorigenesis beyond RB1 inactivation

Biallelic *RB1* inactivation is necessary to initiate most retinoblastomas, but it is not sufficient, as the benign retinal lesion *retinoma* similarly involves loss of both *RB1* alleles (**Figure 13**) (Dimaras et al., 2008). Further genetic or epigenetic changes are probably needed for malignant transformation (Thériault et al., 2014). Epigenetic alterations might drive retinoblastoma formation by inducing histone H3 Lys4 (H3K4) trimethylation and H3K9 and H3K14 acetylation marks and expression of the spleen tyrosine kinase (SYK) oncogene (Zhang et al., 2012). Comparative genomic hybridization studies have identified DNA copy number gains encompassing the candidate retinoblastoma oncogenes mitotic kinesin family member 14 (KIF14) and the p53 regulator MDM4 (1q32), transcription factors E2F3 and DEK (6p22), and the oncogenic microRNA clusters miR‑106-25 (7q22.1) and miR-17-92 (13q31), as well as losses encompassing the cadherin 11 (CDH11; 16q21) and the RB1 family member retinoblastoma-like 2 (RBL2; 16q12.2) tumor-suppressor genes (Thériault et al., 2014). Whole-genome/exome sequencing has identified inactivating mutations in the transcriptional co-repressor BCL-6 co-repressor (BCOR) (Kooi et al., 2016; Zhang et al., 2012). Interestingly, some tumors had no detected alterations, consistent with acquisition of such changes during tumor progression.

Although both *RB1* alleles are mutated in nearly all retinoblastomas, Rushlow and colleagues have reported a small subset of unilateral tumors (~1,5%) without *RB1* mutation ($RB1^{+/+}$) and with high-level amplification of the oncogene *MYCN* (Rushlow et al., 2013). These $RB1^{+/+}$ $MYCN^{A}$ tumors are

always unilateral, are diagnosed in much younger children than unilateral *RB1*$^{-/-}$ tumors and have a distinct morphology, reflecting a unique subtype.

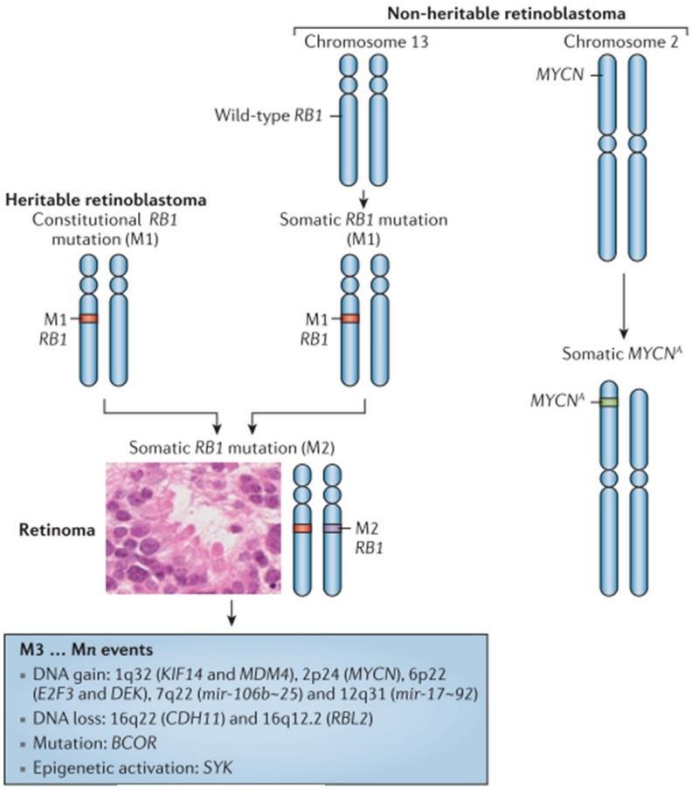


Figure 13. Oncogenic events in retinoblastoma
Patients with heritable retinoblastoma have a constitutive inactivating mutation ("hit 1" M1) in the *RB1* tumor-suppressor retinoblastoma gene in all cells of their body. A second somatic mutation ("hit 2" M2) in a susceptible retinal cell can lead to benign retinoma. Further genetic and/or epigenetic events (M3 … Mn) are likely required to transform the retinoma into retinoblastoma. Non-heritable *RB1*$^{-/-}$ retinoblastomas progress similarly, except that both M1 and M2 occur in one susceptible retinal cell. *RB1*$^{+/+}$ *MYCN*^{A} retinoblastoma is a rare, non-heritable subtype driven by amplification of *MYCN* oncogene with normal *RB1*. BCOR, BCL-6 co-repressor; CDH11, cadherin 11; KIF14, kinesin family member 14; RBL2, retinoblastoma-like 2; SYK, spleen tyrosine kinase. Image adapted from (Dimaras et al., 2015).

Histopathology of retinoblastoma and degree of differentiation

Macroscopically, retinoblastoma is soft and friable, and it tends to outgrow its blood supply, with resulting necrosis and calcification. Necrotic cells appear pink on hematoxylin and eosin (H&E) staining and calcification has a hint of violet or purple. Because of its friability, is common to find dissemination within the vitreous and retina, in the form of white small nodules (seeds) (Amram et al., 2017). Microscopically, retinoblastoma cells are medium sized (twice the size of lymphocytes), have high nuclear-cytoplasmic ratio, marked apoptotic and mitotic activity, and stain blue with H&E stain. Tumor appearance depends on its degree of differentiation. Undifferentiated retinoblastoma (**Figure 14A**) is composed of small, round, densely packed cells with hyperchromatic nuclei and scant cytoplasm. Several degrees of photosensory differentiation have been described and are

characterized by distinctive arrangements of tumor cells: the Homer-Wright rosettes (**Figure 14B**) most often seen in other neuroblastic tumors such as neuroblastoma and medulloblastoma; the Flexner-Wintersteiner rosettes (**Figure 14C**) specific for retinoblastoma and seen in 70% of the tumors; and the fleurettes structures (**Figure 14D**) more characteristic of well-differentiated tumors (Mendoza et al., 2015). $RB1^{+/+}$ $MYCN^{A}$ retinoblastomas are reported to have a distinct morphology, rather undifferentiated, with rounded nuclei and prominent nucleoli related to the high levels of *MYCN* (Rushlow et al., 2013).

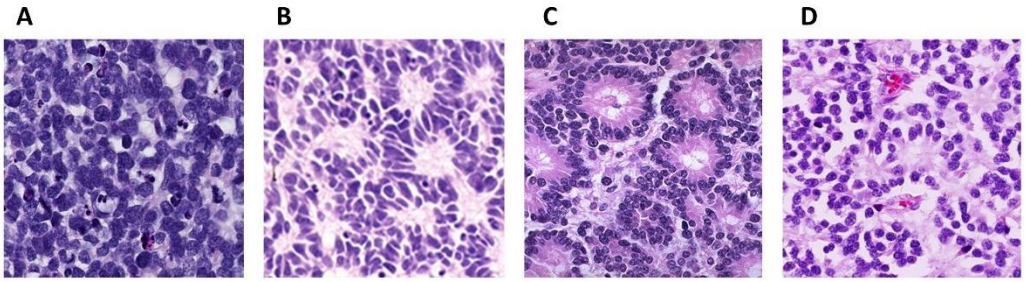


Figure 14. Retinoblastoma differentiation
A) Undifferentiated retinoblastoma. B) A ring of cells with an eosinophilic fibrillary center is called a Homer-Wright rosette. C) A ring of cells surrounding an empty lumen is known as a Flexner-Wintersteiner rosette. D) Fleurettes are retinoblastoma cells that have undergone greater photoreceptor differentiation and group together as a bouquet. Fleurettes lack mitosis or necrosis. A tumor composed of fleurettes is deemed benign and called retinoma or retinocytoma.

A critical role of pathology in the management of retinoblastoma is the identification of pathologic features that predispose to extraocular relapse. These include invasion into the choroid, the sclera, and/or the optic nerve (Chantada et al., 2007; Sastre et al., 2009). Although there is no clear consensus among ocular oncologists, these features are used to decide whether a child will require adjuvant chemotherapy after enucleation to prevent relapse with extraocular disease (Chantada et al., 2004).

Clinical management

Clinical diagnosis

Diagnosis of retinoblastoma does not rely on histopathological examination because biopsy incurs risk of metastasis (Karcioglu, 2002). Detailed retinal examination under general anesthesia is required to distinguish the differential diagnoses (Coats disease, persistent fetal vasculature and vitreous hemorrhage), and to classify the severity of the intraocular disease. Accurate fundus drawing is essential to map tumor burden and location. Where resources allow, the wide-angle, hand-held fundus camera is used to view and record the whole retina (**Figure 15A**). High frequency (50 MHz) ultrasound biomicroscopy (Moulin et al., 2012) and Optical coherence tomography (OCT) (**Figure 15B**) (Rootman et al., 2013) are useful for discovering invisible tumors in children with

familial disease. MRI is used to assess invasion of the optic nerve (**Figure 15C**) (de Jong et al., 2014a) and the presence of trilateral retinoblastoma (pinealoblastoma and primitive neuroectodermal intracranial tumors associated with *RB1* germline mutations) (de Jong et al., 2014a, 2014b). Computed tomography scans are avoided because radiation can induce second primary cancers in people carrying *RB1* germline mutations (MacCarthy et al., 2013).

Poor outcome correlates with late diagnosis, difficulty accessing retinoblastoma-specific health care and socio-economic issues that lead to poor compliance, including family refusal to remove the affected eye (enucleation) and abandonment of therapy (Chantada et al., 2011; Gichigo et al., 2015; Kumar et al., 2013). Without timely diagnosis and appropriate treatment, metastatic disease is likely to develop (Chantada et al., 2007).

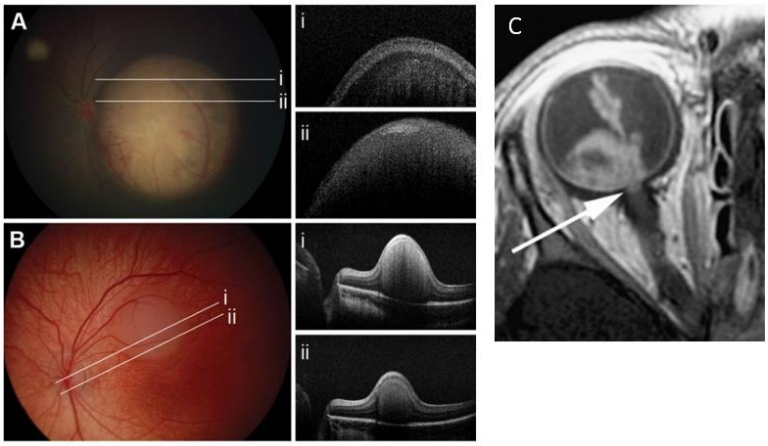


Figure 15. Retinoblastoma diagnosis
A) RetCam eye fundus image (left) of a medium-sized macular retinoblastoma tumor in left eye of a 3-week-old patient with inherited retinoblastoma. Hand-held spectral domain optical coherence tomography (HHSD) (right) images at two positions: i) demonstrates relative preservation of the superficial retinal architecture in the peripheral tumor; ii) the retinoblastoma lesion involves the full thickness of the retina with a patch of calcification and shadowing. B) RetCam photograph (left) of another medium-sized retinoblastoma tumor. HHSD OCT images (right) at positions i and ii, demonstrating a large isodense intraretinal lesion confined to the inner retinal layers, with relative preservation of the overlying inner retina. Image adapted from (Rootman et al., 2013). C) Magnetic resonance imaging (MRI) scan showing abnormal enhancement of the distal optic nerve in continuity with tumor, as a sign of postlaminar optic nerve invasion. Image adapted from (De Graaf et al., 2012).

Intraocular retinoblastoma classification and staging

Classification is necessary to determine appropriate management and predict disease outcome. For intraocular retinoblastoma, the first classification system was introduced by Reese and Ellsworth (R-E) in the 1960s to predict the chances of saving the eye following external beam radiotherapy (Reese and Ellsworth, 1963). In the 1980s, radiotherapy was discovered to induce a high risk of secondary malignancy in children with constitutional *RB1* mutations and its use was progressively abandoned. When intravenous chemotherapy for intraocular retinoblastoma was introduced in the 1990s, the R-E classification system was no longer appropriate and a new classification scheme, the International Intraocular Retinoblastoma Classification (IIRC) was developed (Murphree, 2005). The IIRC scheme

groups tumors from A-E, depending on their size, location, and additional features including the presence of retinoblastoma "seeds" (small colonies of cancerous cells in the vitreous) and/or retinal detachment, with Group E being the most severe. Shields and colleagues developed a modified scheme, the Intraocular Classification of Retinoblastoma (ICRB), which differed from the IIRC mainly in the definitions of the advanced groups, D and E and was found to successfully predict the outcome of intravenous chemotherapy (Shields et al., 2006). Both the IIRC and ICRB classification systems are now used as the main classification schemes for intraocular retinoblastoma (**Table 1**) (Scelfo et al., 2017).

Table 1. Classification systems for intraocular retinoblastoma

	International Intraocular Retinoblastoma Classification (IIRC)	**Intraocular Classification of Retinoblastoma (ICRB)**
Group A (very low risk)	All tumors are 3mm or smaller, confined to the retina and at least 3mm from the foveola and 1.5 mm from the optic nerve. No vitreous or subretinal seeding is allowed	Retinoblastoma ≤ 3 mm (in basal dimension or thickness)
Group B (low risk)	Eyes with no vitreous or subretinal seeding and discrete retinal tumour of any size or location. Retinal tumors may be of any size or location not in group A. Small cuff of subretinal fluid extending ≤5 mm from the base of the tumour is allowed	Retinoblastoma > 3 mm (in basal dimension or thickness) or • Macular location (≤3 mm to foveola) • Juxtapapillary location (≤1.5 mm to disc) • Additional subretinal fluid (≤3 mm from margin)
Group C (moderate risk)	Eyes with focal vitreous or subretinal seeding and discrete retinal tumours of any size and location. Any seeding must be local, fine, and limited so as to be theoretically treatable with a radioactive plaque. Up to one quadrant of subretinal fluid may be present	Retinoblastoma with: • Subretinal seeds ≤ 3 mm from tumour • Vitreous seeds ≤ 3 mm from tumour • Both subretinal and vitreous seeds ≤ 3 mm from tumour
Group D (high risk)	Eyes with diffuse vitreous or subretinal seeding and/or massive, non-discrete endophytic or exophytic disease Eyes with more extensive seeding than Group C Massive and/or diffuse intraocular disseminated disease including exophytic disease and >1 quadrant of retinal detachment. May consist of 'greasy' vitreous seeding or avascular masses. Subretinal seeding may be plaque-like	Retinoblastoma with: • Subretinal seeds > 3 mm from tumour • Vitreous seeds > 3 mm from tumour • Both subretinal and vitreous seeds > 3 mm from retinoblastoma
Group E (very high risk)	Eyes that have been destroyed anatomically or functionally with one or more of the following: Irreversible neovascular glaucoma, massive intraocular haemorrhage, aseptic orbital cellulitis, tumour anterior to anterior vitreous face, tumour touching the lens, diffuse infiltrating retinoblastoma and phthisis or pre-phthisis	• Extensive retinoblastoma occupying >50% globe or with • Neovascular glaucoma • Opaque media from haemorrhage in anterior chamber, vitreous or subretinal space • Invasion of postlaminar optic nerve, • choroid (>2 mm), sclera, orbit, anterior chamber

Extraocular retinoblastoma

If retinoblastoma is left untreated, it will extend beyond the eye. Unfortunately, this is the type most commonly seen in low- and middle-income countries, mainly due to a delay in diagnosis (Chantada et al., 2011). The tumor can invade the choroid and sclera, and penetrate the globe wall and be visible in and around the eye. It can also reach the central nervous system via the optic nerve, or it can

spread to other parts of the body via the blood stream and metastasize (**Figure 16**). When retinoblastoma has metastasized outside the eye it is seldom curable, even with intensive treatments (Leal-Leal et al., 2006). In 2006, Chantada and colleagues developed the International Retinoblastoma Staging System (IRSS) (Chantada et al., 2006), that sub-classifies the disease from stage 0 to IV (**Table 2**). Stage 0 is intraocular disease, usually having a good outcome with treatment, and stage IV is retinoblastoma with metastases, which has a poor prognosis.

Table 2. International Retinoblastoma Staging System (IRSS)

Stage	Clinical Description
0	Patient treated conservatively
I	Eye enucleated, completely resected histologically
II	Eye enucleated, microscopic residual tumor
III	Regional extension
a.	Overt orbital disease
b.	Pre-auricular or cervical lymph node extension
IV	Metastatic disease
a.	Heamatogenous metastasis (without central nervous system involvement) 1 Single lesion 2 Multiple lesions
b.	Central nervous system extension (with or without any other site of regional or metastatic disease) 1 Prechiasmatic lesion 2 Central nervous system mass 3 Leptomeningeal and cerebrospinal fluid disease

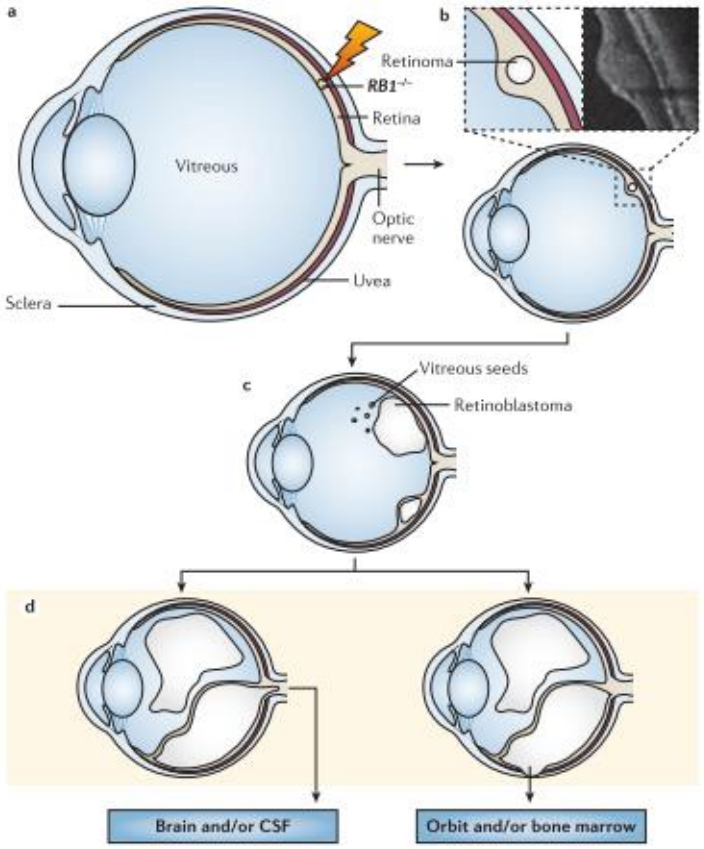


Figure 16. Progression of retinoblastoma
A) Anatomical features of a healthy eye. Functional inactivation of the retinoblastoma gene (RB1) in a developing retinal cell. B) Genomic instability leads to the formation of a benign retinoma; only 5% of patients have retinoma without retinoblastoma. Inset shows a small retinoma that is not visible except by optical coherence tomography. C) Intraretinal retinoblastoma arises as additional genomic changes promote uncontrolled cell proliferation; the tumour grows and seeds become independent, floating under the retina and into the vitreous. D) Retinoblastoma can invade adjacent tissues, such as the optic nerve, uvea or sclera, which constitutes a high-risk pathological feature. Eventually, retinoblastoma can extend extraocularly into the orbit and metastasize, especially to the bone marrow, or into the brain (direct or via the cerebrospinal fluid (CSF). Image adapted from (Dimaras et al., 2015).

General treatment of intraocular retinoblastoma

When the disease is diagnosed in its early intraocular stages, as is usually the case in developed countries, the probability of disease-free survival has been greater than 80-90% for decades (Lumbroso-Le Rouic et al., 2015; MacCarthy et al., 2009; Moll et al., 1997). These encouraging survival figures are not only the result of the use of sophisticated treatments since enucleation of the affected eye, a simple surgical procedure, is usually curative in cases of intraocular retinoblastoma. In developed countries, sophisticated conservative treatments are applied in order to preserve eyes with useful vision without affecting survival (Lumbroso-LeRouic et al., 2008; Shields et al., 2005).

In order of approximate frequency of global use in developed countries, primary treatments for intraocular disease include enucleation, IVC (intravitreal chemotherapy) with focal therapy (laser therapy or cryotherapy), intra- arterial chemotherapy (IAC) with focal therapy, and focal therapy alone (when tumors are small at diagnosis). External beam radiotherapy is no longer recommended

for first-line therapy for primary intraocular retinoblastoma, as radiation, especially in the first year of life, imposes a high risk of developing secondary cancers when the patient carries a germline *RB1* mutation (Eng et al., 1993; MacCarthy et al., 2013).

Treatment improvements in retinoblastoma

Improvements in protocol-driven clinical trials and supportive care for children and adolescents with cancer have reduced mortality rates by more than 50% over the past three decades. Overall, the 5-year survival rate for pediatric cancer patients has increased to approximately 80% (Pui et al., 2011). This success has been mainly built on the use of cytotoxic chemotherapy and radiotherapies that are often associated with major side effects and can ultimately reduce the children's quality of life (Hudson et al., 2012). Although cure rates for childhood cancers are impressive relative to those for adult malignancies, cancer remains the leading cause of death by disease among children over 1 year of age in developed countries (Siegel et al., 2013). It is generally believed that new, less toxic curative treatments of childhood cancers should target the genetic alterations that drive these diseases. Elucidating the genetic abnormalities that underlie childhood cancers is therefore an essential step toward understanding the pathobiology of these diseases and using the information gained to develop more effective and less toxic treatments.

A combination of preclinical models and direct clinical trials for many of the more common types of cancer in adults is the most efficient means to improve treatment. However, childhood cancer, retinoblastoma in particular, poses unique challenges for exploring new treatment options in clinical trials. For example, there are only approximately 300 new cases of pediatric retinoblastoma diagnosed each year in the United States, and approximately 60% of those patients have unilateral retinoblastoma and will undergo enucleation without additional chemotherapy or focal therapy. Therefore, only 100 to 200 patients each year would benefit from clinical trials for novel treatments. This small number of cases limits the number and size of clinical trials designed to identify the best treatment protocols (Zhang et al., 2004). Retinoblastoma presents an even greater challenge than other childhood cancers because the prognosis for patients with metastatic disease is dismal (fewer than 10% survive) (Leal-Leal et al., 2006). Early detection combined with enucleation can save approximately 95% of children with retinoblastoma. However, blindness because of bilateral enucleation is a debilitating side effect of such life-saving treatment. New treatment protocols directed toward saving vision in these children must weigh the benefit of saving vision with the potential increased risk of metastatic cancer.

BIBLIOGRAPHY

Abramson, D.H. (2005). Retinoblastoma in the 20th century: Past success and future challenges. The Weisenfeld Lecture. Investig. Ophthalmol. Vis. Sci. *46*, 2684–2691.

Abramson, D.H., Du, T.T., and Beaverson, K.L. (2002). (Neonatal) retinoblastoma in the first month of life. Arch. Ophthalmol. (Chicago, Ill. 1960) *120*, 738–742.

Abramson, D.H., Beaverson, K., Sangani, P., Vora, R.A., Lee, T.C., Hochberg, H.M., Kirszrot, J., and Ranjithan, M. (2003). Screening for retinoblastoma: presenting signs as prognosticators of patient and ocular survival. Pediatrics *112*, 1248–1255.

Aerts, R.I., Lumbroso-Le Rouic, L., Gauthier-Villars, M., Brisse, H., Doz, F., and Desjardins, L. (2006). Retinoblastoma. Orphanet J. Rare Dis. *1*, 1–11.

Amram, A.L., Rico, G., Kim, J.W., Chintagumpala, M., Herzog, C.E., Gombos, D.S., and Chévez-Barrios, P. (2017). Vitreous Seeds in Retinoblastoma: Clinicopathologic Classification and Correlation. Ophthalmology *124*, 1540–1547.

Baccus, S.A. (2007). Timing and Computation in Inner Retinal Circuitry. Annu. Rev. Physiol. *69*, 271–290.

Bassett, E. a, and Wallace, V. a (2012). Cell fate determination in the vertebrate retina. Trends Neurosci. *35*, 565–573.

Ben-Porath, I., and Weinberg, R.A. (2005). The signals and pathways activating cellular senescence. Int. J. Biochem. Cell Biol. *37*, 961–976.

Binné, U.K., Classon, M.K., Dick, F.A., Wei, W., Rape, M., Kaelin, W.G., Näär, A.M., and Dyson, N.J. (2007). Retinoblastoma protein and anaphase-promoting complex physically interact and functionally cooperate during cell-cycle exit. Nat. Cell Biol. *9*, 225–232.

Brehm, A., and Kouzarides, T. (1999). Retinoblastoma protein meets chromatin. Trends Biochem. Sci. *24*, 142–145.

Bringmann, A., Syrbe, S., Görner, K., Kacza, J., Francke, M., Wiedemann, P., and Reichenbach, A. (2018). The primate fovea: Structure, function and development. Prog. Retin. Eye Res. *66*, 49–84.

Burkhart, D.L., and Sage, J. (2008). Cellular mechanisms of tumour suppression by the retinoblastoma gene. Nat. Rev. Cancer *8*, 671–682.

Cavenee, W.K., Dryja, T.P., Phillips, R.A., Benedict, W.F., Godbout, R., Gallie, B.L., Murphree, A.L., Strong, L.C., and White, R.L. (1983). Expression of recessive alleles by chromosomal mechanisms in retinoblastoma. Nature *305*, 779–784.

Chantada, G., Doz, F., Antoneli, C.B.G., Grundy, R., Clare Stannard, F.F., Dunkel, I.J., Grabowski, E., Leal-Leal, C., Rodríguez-Galindo, C., Schvartzman, E., et al. (2006). A proposal for an international retinoblastoma staging system. Pediatr. Blood Cancer *47*, 801–805.

Chantada, G., Qaddoumi, I., Canturk, S., Khetan, V., Ma, Z., Kimani, K., Yeniad, B., Sultan, I., Sitorus, R., Tacyldiz, N., et al. (2011). Strategies to Manage Retinoblastoma in Developing Countries. Pediatr. Blood Cancer *56*, 341–348.

Chantada, G.L., Dunkel, I.J., de Dávila, M.T.G., and Abramson, D.H. (2004). Retinoblastoma patients with high risk ocular pathological features: who needs adjuvant therapy? Br. J. Ophthalmol. *88*, 1069–1073.

Chantada, G.L., Dunkel, I.J., Antoneli, C.B.G., de Dávila, M.T.G., Arias, V., Beaverson, K., Fandiño, A.C., Chojniak, M., and Abramson, D.H. (2007). Risk factors for extraocular relapse following enucleation after failure of chemoreduction in retinoblastoma. Pediatr. Blood Cancer *49*, 256–260.

Chau, B.N., and Wang, J.Y.J. (2003). Coordinated regulation of life and death by RB. Nat. Rev. Cancer *3*, 130–138.

Curcio, C.A., Sloan, K.R., Kalina, R.E., and Hendrickson, A.E. (1990). Human photoreceptor topography. J. Comp. Neurol. *292*, 497–523.

Delston, R.B., and Harbour, J.W. (2006). Rb at the interface between cell cycle and apoptotic decisions. Curr. Mol. Med. *6*, 713–718.

Dimaras, H., Khetan, V., Halliday, W., Orlic, M., Prigoda, N.L., Piovesan, B., Marrano, P., Corson, T.W., Eagle, R.C., Squire, J.A., et al. (2008). Loss of RB1 induces non-proliferative retinoma: increasing genomic instability correlates with progression to retinoblastoma. Hum. Mol. Genet. *17*, 1363–1372.

Dimaras, H., Corson, T.W., Cobrinik, D., White, A., Zhao, J., Munier, F.L., Abramson, D.H., Shields, C.L., Chantada, G.L., Njuguna, F., et al. (2015). Retinoblastoma. Nat. Rev. Dis. Prim. *1*.

Eng, C., Li, F.P., Abramson, D.H., Ellsworth, R.M., Wong, F.L., Goldman, M.B., Seddon, J., Tarbell, N., and Boice, J.D. (1993). Mortality from second tumors among long-term survivors of retinoblastoma. J. Natl. Cancer Inst. *85*, 1121–1128.

Fabian, I.D., Reddy, A., and Sagoo, M.S. (2018). Classification and staging of retinoblastoma. COMMUNITY EYE Heal. J. *31*, 11–13.

Friend, S.H., Bernards, R., Rogelj, S., Weinberg, R.A., Rapaport, J.M., Albert, D.M., and Dryja, T.P. (1986). A human DNA segment with properties of the gene that predisposes to retinoblastoma and osteosarcoma. Nature *323*, 643–646.

Gichigo, E.N., Kariuki–Wanyoike, M.M., Kimani, K., and Nentwich, M.M. (2015). Retinoblastom in Kenia. Der Ophthalmol. *112*, 255–260.

Gonzalo, S., and Blasco, M.A. (2005). Role of Rb family in the epigenetic definition of chromatin. Cell Cycle *4*, 752–755.

Goodrich, D.W. (2006). The retinoblastoma tumor-suppressor gene, the exception that proves the rule. Oncogene *25*, 5233–5243.

Goodrich, D.W., Wang, N.P., Qian, Y.W., Lee, E.Y., and Lee, W.H. (1991). The retinoblastoma gene product regulates progression through the G1 phase of the cell cycle. Cell *67*, 293–302.

De Graaf, P., Göricke, S., Rodjan, F., Galluzzi, P., Maeder, P., Castelijns, J.A., Brisse, H.J., Galluzzi, P., Brisse, H.J., De Graaf, P., et al. (2012). Guidelines for imaging retinoblastoma: imaging principles and MRI standardization. Pediatr Radiol *42*, 2–14.

Gregory-Evans, C.Y., Wallace, V.A., and Gregory-Evans, K. (2013). Gene networks: Dissecting pathways in retinal development and disease. Prog. Retin. Eye Res. *33*, 40–66.

Hallstrom, T.C., and Nevins, J.R. (2009). Balancing the decision of cell proliferation and cell fate. Cell Cycle *8*, 532–535.

Hanahan, D., and Weinberg, R.A. (2000). The Hallmarks of Cancer.

Hudson, M.M., Neglia, J.P., Woods, W.G., Sandlund, J.T., Pui, C.-H., Kun, L.E., Robison, L.L., and Green, D.M. (2012). Lessons from the past: Opportunities to improve childhood cancer survivor care through outcomes investigations of historical therapeutic approaches for pediatric hematological malignancies. Pediatr. Blood Cancer *58*, 334–343.

Ji, P., Jiang, H., Rekhtman, K., Bloom, J., Ichetovkin, M., Pagano, M., and Zhu, L. (2004). An Rb-Skp2-p27 pathway mediates acute cell cycle inhibition by Rb and is retained in a partial-penetrance Rb mutant. Mol. Cell *16*, 47–58.

de Jong, M.C., de Graaf, P., Noij, D.P., Göricke, S., Maeder, P., Galluzzi, P., Brisse, H.J., Moll, A.C., Castelijns, J.A., and European Retinoblastoma Imaging Collaboration (ERIC) (2014a). Diagnostic Performance of Magnetic Resonance Imaging and Computed Tomography for Advanced Retinoblastoma. Ophthalmology *121*, 1109–1118.

de Jong, M.C., Kors, W.A., de Graaf, P., Castelijns, J.A., Kivelä, T., and Moll, A.C. (2014b). Trilateral retinoblastoma: a systematic review and meta-analysis. Lancet Oncol. *15*, 1157–1167.

Karcioglu, Z.A. (2002). Fine needle aspiration biopsy (FNAB) for retinoblastoma. Retina *22*, 707–710.

Knudsen, E.S., Sexton, C.R., and Mayhew, C.N. (2006). Role of the retinoblastoma tumor suppressor in the maintenance of genome integrity. Curr. Mol. Med. *6*, 749–757.

Knudson, A.G. (1971). Mutation and Cancer: Statistical Study of Retinoblastoma.

Knudson, A.G. (2001). Two genetic hits (more or less) to cancer. Nature *1*.

Kooi, I.E., Mol, B.M., Massink, M.P.G., Ameziane, N., Meijers-Heijboer, H., Dommering, C.J., Van Mil, S.E., De Vries, Y., Van Der Hout, A.H., Kaspers, G.J.L., et al. (2016). Somatic genomic alterations in retinoblastoma beyond RB1 are rare and limited to copy number changes. Sci. Rep. *6*, 1–11.

Korenjak, M., and Brehm, A. (2005). E2F–Rb complexes regulating transcription of genes important for differentiation and development. Curr. Opin. Genet. Dev. *15*, 520–527.

Kumar, A., Moulik, N.R., Mishra, R.K., and Kumar, D. (2013). Causes, outcome and prevention of abandonment in retinoblastoma in India. Pediatr. Blood Cancer *60*, 771–775.

Leal-Leal, C.A., Rivera-Luna, R., Flores-Rojo, M., Juárez-Echenique, J.C., Ordaz, J.C., and Amador-Zarco, J. (2006). Survival in extra-orbital metastatic retinoblastoma:treatment results. Clin. Transl. Oncol. *8*, 39–44.

Lee, W.H., Bookstein, R., Hong, F., Young, L.J., Shew, J.Y., and Lee, E.Y. (1987). Human retinoblastoma susceptibility gene: cloning, identification, and sequence. Science *235*, 1394–1399.

Liu, H., Dibling, B., Spike, B., Dirlam, A., and Macleod, K. (2004). New roles for the RB tumor suppressor protein. Curr. Opin. Genet. Dev. *14*, 55–64.

Livesey, F.J., Cepko, C.L., and Medical, H.H. (2001). VERTEBRATE NEURAL CELL-FATE DETERMINATION : LESSONS FROM THE RETINA. *2*.

Lumbroso-Le Rouic, L., Savignoni, A., Levy-Gabriel, C., Aerts, I., Cassoux, N., Salviat, F., Gauthier-Villars, M., Freneaux, P., Brisse, H., Dendale, R., et al. (2015). Treatment of retinoblastoma: The Institut Curie experience on a series of 730 patients (1995 to 2009). J. Fr. Ophtalmol. *38*, 535–541.

Lumbroso-LeRouic, L., Aerts, I., Lévy-Gabriel, C., Dendale, R., Sastre, X., Esteve, M., Asselain, B., Bours, D., Doz, F., and Desjardins, L. (2008). Conservative Treatments of Intraocular Retinoblastoma. Ophthalmology *115*, 1405–1410.e2.

Macaluso, M., Montanari, M., and Giordano, A. (2006). Rb family proteins as modulators of gene expression and new aspects regarding the interaction with chromatin remodeling enzymes. Oncogene *25*, 5263–5267.

MacCarthy, A., Birch, J.M., Draper, G.J., Hungerford, J.L., Kingston, J.E., Kroll, M.E., Stiller, C.A., Vincent, T.J., and Murphy, M.F.G. (2009). Retinoblastoma: treatment and survival in Great Britain 1963 to 2002. Br. J. Ophthalmol. *93*, 38–39.

MacCarthy, A., Bayne, A.M., Brownbill, P.A., Bunch, K.J., Diggens, N.L., Draper, G.J., Hawkins, M.M., Jenkinson, H.C., Kingston, J.E., Stiller, C.A., et al. (2013). Second and subsequent tumours among 1927 retinoblastoma patients diagnosed in Britain 1951–2004. Br. J. Cancer *108*, 2455–2463.

McClellan, K.A., Ruzhynsky, V.A., Douda, D.N., Vanderluit, J.L., Ferguson, K.L., Chen, D., Bremner, R., Park, D.S., Leone, G., and Slack, R.S. (2007). Unique Requirement for Rb/E2F3 in Neuronal Migration: Evidence for Cell Cycle-Independent Functions. Mol. Cell. Biol. *27*, 4825–4843.

Mendoza, P.R., Specht, C.S., Hubbard, G.B., Wells, J.R., Lynn, M.J., Zhang, Q., Kong, J., and Grossniklaus, H.E. (2015). Histopathologic grading of anaplasia in retinoblastoma. Am. J. Ophthalmol. *159*, 764–776.

Mescher, A. (2018). Chapter 23. The Eye and Ear: Special Sense Organs. Junqueira's Basic Histology: Text and Atlas (The McGraw-Hill Companies).

Moll, A.C., Kuik, D.J., Bouter, L.M., Den Otter, W., Bezemer, P.D., Koten, J.W., Imhof, S.M., Kuyt, B.P., and Tan, K.E. (1997). Incidence and survival of retinoblastoma in The Netherlands: a register based study 1862-1995. Br. J. Ophthalmol. *81*, 559–562.

Morris, E.J., and Dyson, N.J. (2001). Retinoblastoma protein partners. Adv. Cancer Res. *82*, 1–54.

Moulin, A.P., Gaillard, M.-C., Balmer, A., and Munier, F.L. (2012). Ultrasound biomicroscopy evaluation of anterior extension in retinoblastoma: a clinicopathological study. Br. J. Ophthalmol. *96*, 337–340.

Murphree, A.L. (2005). Intraocular Retinoblastoma: the Case for a New Group Classification. Ophthalmol. Clin. North Am. *18*, 41–53.

Neitz, J., and Neitz, M. (2011). The genetics of normal and defective color vision. Vision Res. *51*, 633–651.

Nguyen, D.X., and McCance, D.J. (2005). Role of the retinoblastoma tumor suppressor protein in cellular differentiation. J. Cell. Biochem. *94*, 870–879.

Ohsawa, R., and Kageyama, R. (2008). Regulation of retinal cell fate specification by multiple transcription factors. Brain Res. *1192*, 90–98.

Pui, C.-H., Gajjar, A.J., Kane, J.R., Qaddoumi, I.A., and Pappo, A.S. (2011). Challenging issues in pediatric oncology. Nat. Rev. Clin. Oncol. *8*, 540–549.

Rapaport, D.H., Wong, L.L., Wood, E.D., Yasumura, D., and LaVail, M.M. (2004). Timing and topography of cell genesis in the rat retina. J. Comp. Neurol. *474*, 304–324.

Reese, A.B., and Ellsworth, R.M. (1963). The evaluation and current concept of retinoblastoma therapy. Trans Am Acad Ophthalmol Otolaryngol *67*, 164–172.

Reichenbach, A., and Bringmann, A. (2013). New functions of Müller cells. Glia *61*, 651–678.

Reichman, S., and Goureau, O. (2014). Production of Retinal Cells from Confluent Human iPS Cells. Methods Mol. Biol. 257–284.

Rootman, D.B., Gonzalez, E., Mallipatna, A., VandenHoven, C., Hampton, L., Dimaras, H., Chan, H.S.L., Gallie, B.L., and Heon, E. (2013). Hand-held high-resolution spectral domain optical coherence tomography in retinoblastoma: clinical and morphologic considerations. Br. J. Ophthalmol. *97*, 59–65.

Rushlow, D.E., Mol, B.M., Kennett, J.Y., Yee, S., Pajovic, S., Thériault, B.L., Prigoda-Lee, N.L., Spencer, C., Dimaras, H., Corson, T.W., et al. (2013). Characterisation of retinoblastomas without RB1 mutations: genomic, gene expression, and clinical studies. Lancet Oncol. *14*, 327.

Sastre, X., Chantada, G.L., Doz, F., Wilson, M.W., De Davila, M.T.G., Carlos Rodríguez-Galindo, ;, Chintagumpala, M., and Chévez-Barrios, P. (2009). Proceedings of the Consensus Meetings From the International Retinoblastoma Staging Working Group on the Pathology Guidelines for the Examination of Enucleated Eyes and Evaluation of Prognostic Risk Factors in Retinoblastoma.

Scelfo, C., Francis, J.H., Khetan, V., Jenkins, T., Marr, B., Abramson, D.H., Shields, C.L., Pe'er, J., Munier, F., Berry, J., et al. (2017). An international survey of classification and treatment choices for group D retinoblastoma. Int. J. Ophthalmol. *10*, 961–967.

Shields, C.L., Mashayekhi, A., Au, A.K., Czyz, C., Leahey, A., Meadows, A.T., and Shields, J.A. (2006). The International Classification of Retinoblastoma Predicts Chemoreduction Success. Ophthalmology *113*, 2276–2280.

Shields, J.A., Shields, C.L., and Meadows, A.T. (2005). Chemoreduction in the Management of Retinoblastoma. Am. J. Ophthalmol. *140*, 505–506.

Siegel, R., Naishadham, D., and Jemal, A. (2013). Cancer statistics, 2013. CA. Cancer J. Clin. *63*, 11–30.

Sung, C.H., and Chuang, J.Z. (2010). The cell biology of vision. J. Cell Biol. *190*, 953–963.

Thériault, B.L., Dimaras, H., Gallie, B.L., and Corson, T.W. (2014). The genomic landscape of retinoblastoma: a review. Clin. Experiment. Ophthalmol. *42*, 33–52.

Turner, D.L., Snyder, E.Y., and Cepko, C.L. (1990). Lineage-independent determination of cell type in the embryonic mouse retina. Neuron *4*, 833–845.

Wallace, V. a (2011). Concise review: making a retina--from the building blocks to clinical applications. Stem Cells *29*, 412–417.

Weinberg, R.A. (1995). The retinoblastoma protein and cell cycle control. Cell *81*, 323–330.

Yau, K.-W., and Hardie, R.C. (2009). Phototransduction Motifs and Variations. Cell *139*, 246–264.

Young, R.W. (1984). Cell death during differentiation of the retina in the mouse. J. Comp. Neurol. *229*, 362–373.

Young, R.W. (1985). Cell differentiation in the retina of the mouse. Anat. Rec. *212*, 199–205.

Zhang, J., Schweers, B., and Dyer, M.A. (2004). The first knockout mouse model of retinoblastoma. Cell Cycle *3*, 952–959.

Zhang, J., Benavente, C.A., McEvoy, J., Flores-Otero, J., Ding, L., Chen, X., Ulyanov, A., Wu, G., Wilson, M., Wang, J., et al. (2012). A novel retinoblastoma therapy from genomic and epigenetic analyses. Nature *481*, 329–334.

OBJECTIVES

CONTEXT

The Curie Hospital is the referral center for retinoblastoma in France. Although being a rare disease, the Institute receives between 50-60 patients each year. The search for new treatments and the improvement of the existing ones to best preserve children's eye and vision is a main issue for the Institute. In 2006 was lauched the first PIC[1] innovative cross-disciplinary research program involving medical doctors, biologists, chemists and physicists, the starting point of retinoblastoma research in my host team.

The Molecular Oncology group led by Dr. François Radvanyi aims to the identification of genetic and epigenetic events involved in tumor progression using bioinformatics based on large-scale data, validating interesting candidate genes through *in vitro* and *in vivo* experiments. The team historically worked on bladder cancer and more recently started focusing on retinoblastoma (2006). The first doctoral thesis based on was finished in 2015, and those first results were the basis for the different projects I worked during my PhD.

RATIONALE

The molecular and cellular characteristics of a given tumor reflect its cell of origin and may therefore provide new clues for its treatment. Retinoblastoma has often been described as a homogenous disease and the cell- of- origin has been extensively debated, being the most accepted one the retinal cone photoreceptor cell. The controversy extends to the existence of different molecular groups of retinoblastomas. Molecular stratification in cancer is extremely important to gain depth knowledge of the biological characteristics of a given tumor, the identification of new therapeutic targets and the development of more successfully and specific targeted therapies. Preclinical cancer models (cell lines, patient-derived tumor xenografts, transgenic mice) help to understand tumor progression and are used as tools to test and validate therapeutic targets predicted by the molecular study of these models and primary tumors.

A collaborative retinoblastoma research initiative at the Curie Institute has built a comprehensive molecular portrait of retinoblastomas by integrating gene expression data, epigenomic data, genomic alteration data as well gene mutation and clinical data. This study focused on an initial set of tumoral samples coming from the Curie Hospital, from patients having received no treatment prior to tumor removal. The data collected led to the discovery that two subgroups displaying different clinical and molecular features exist for this cancer. However, which of these groups' features were

[1] Incentive and Cooperative Program

important for tumor progression and invasiveness was unclear. Two main obstacles have hindered the investigation of these questions. The first was the relative small number of tumors studied at that moment and the second, that those cases were localized forms of retinoblastoma or rarely locally invasive. The overall lack of invasive cases of retinoblastomas at the Curie Institute was the main motivation to establish a collaborative project with the pediatric Garrahan Hospital, the referral center for retinoblastoma in Argentina (approximately 40 cases diagnosed annually) where advanced cases of this disease (invasive or metastatic retinoblastoma) are more frequent.

TIMELINE

I started my doctoral research in the context of a collaborative project initiated in 2013 between the Curie Institute and the Garrahan Hospital, where we selected, collected and processed samples to be included in the project initiated by the Curie Institute. Samples and clinical data collected was possible thanks to the close collaboration with ophthalmologists, clinicians, pathologists and biologists of the Garrahan Hospital that kindly help to recover all the required material. My work at the hospital was under the supervision of Dr. Guillermo Chantada.

When I arrived at the Curie Institute, I joined the already started project of retinoblastoma characterization where two retinoblastomas subtypes had been characterized. The “cone-like” group (subtype 1, C1) rather differentiated and homogenous, presenting an overexpression of genes related to cone photoreceptor retinal cells, clinically diagnosed earlier and grouping the majority of hereditary forms. The second subtype, diagnosed at older ages, was better characterized since then and we called it the “mixed-type” (subtype 2, C2) because of the existence of two differentiation forms within the same tumor, displaying intra-tumoral heterogeneity and showing overexpression of genes related to cone and retinal ganglion cells. Then, the general goal of my thesis was to extend the molecular characterization of the “mixed-type” subtype tumors and to depict the main molecular and clinical features of different retinoblastoma preclinical models available, in the context of retinoblastoma as a heterogeneous disease.

CHAPTERS

Chapter 1 - MUTATIONAL LANDSCAPE AND MOLECULAR CLASSIFICATION OF RETINOBLASTOMA

A first series of whole-exome sequencing had been performed. Then, in order to expand the mutational landscape of retinoblastoma and to find new candidate genes implicated in the tumorigenesis of this cancer, we launched a second series that included primary tumors from France, Argentina and Spain[2]. My first objective was the experimental validation of mutations detected by the bioinformatics analysis of the exome data. This enormous task was performed together with Céline Desbrousses, former biologist engineer in the group. Meriem Sefta (former PhD student; first doctoral thesis of retinoblastoma in the team) was in charge of the bioinformatics analysis. Jing Liu (PhD student, bioinformatics) joined the team in 2017 and continued with the bioinformatics analysis of omics data. Beyond validation tests, we aimed to analyze the list of mutated genes and figure out possible signaling pathway involved in each tumor subtype, and to correlate mutations detected with the clinical presentation of patients, particularly interested in patients with advanced tumors. In addition, we planned to characterize the mutations found in the retinoblastoma susceptibility gene (*RB1*) and to analyze their distribution along the gene and the protein, in the context of the existence of two different tumor subtypes. To further explore the mutational landscape, we then looked for gene fusions analyzing the RNA sequencing from a series of samples. One recurrent fusion event was found in two tumor samples and my goal here was to validate and characterize the implicated gene involved in the fusion and its partner.

Molecular attribution of retinoblastomas to one subtype was based on transcriptomic, methylomic and copy number data, not always available for all samples. Therefore, in order to assign a subtype to uncharacterized samples in a faster and cheaper way, a methylation signature was developed by Aurélien de Reyniès, co-author of this project (senior bioinformatician of the CIT team, LNCC[3]). My objectives here were the validation of this developed signature and its application to classify uncharacterized samples. This laborious and time-consuming task was also made together with Céline Desbrousses. Results are part of a paper intended to be submitted at the end of 2018.

Chapter 2 - *TFF1* GENE IN RETINOBLASTOMA

Preliminary molecular analyses at the Curie Institute indicated that the *TFF1* gene could play an important role in retinoblastoma. Transcriptomic studies have shown that it was overexpressed in approximately half of retinoblastoma tumors, while it is not expressed in the healthy retina. This was

[2] Collaboration with the Sant Joan de Déu Hospital from Spain established in 2015. Dr. Ángel Montero Carcaboso shared several primary tumor samples that were included in the running projects in France, as well as cell and animals models to its molecular characterization.

[3] Carte d'Identité des tumeurs (CIT) Ligue Nationale Contre le Cancer (LNCC)

confirmed through immunohistochemical markings of healthy retinas and retinoblastomas. Several studies have already implicated *TFF1* in cancer cell migration and invasion, controversially stated as a tumor suppressor or an oncogene. We then though to explore the role of *TFF1* in retinoblastoma.

At the beginning of this part of my project, tumor subtypes have been recently described and the nature of this difference was unknown. We first hypothesized that *TFF1* could induce an undifferentiated phenotype in the transformed cells given that: i) subtype 2 tumors were generally more undifferentiated than subtype 1 tumors, and ii) subtype 2 tumors displayed an intra-tumoral heterogeneity (immunohistochemical staining) characterized by a mutual exclusive pattern of TFF1 and ARR3 protein staining (ARR3 cone cell marker, upregulated in the cone-like subtype). At that moment, cell lines available in our lab had not been yet characterized at the transcriptomic level, and so we performed an extended bibliographical research in order to select specific markers of each retinal cell type and evaluate their expression after *TFF1* knock down. Then, we decided to explore the possible role of *TFF1* regarding cell viability, cell migration and cell invasion. We first entailed an immunohistochemical study of TFF1 in retinoblastoma samples coming from the Garrahan Hospital in order to visualize its expression pattern in locally invasive tumors. The presence of positive stained cells invading the optic nerve encouraged us to continue exploring its possible role in cell invasion. Cell imaging was performed to explore cell motility in cell lines expressing *TFF1*, as well as several *in vitro* experiment to assess cell migration and invasion.

Chapter 3 - *MYC*, *MYCN* AND BROMODOMAIN INHIBITORS IN RETINOBLASTOMA

Through the study of copy number variation data in our series of tumors, we found amplifications of *MYCN* gene in approximately 10% of cases, and all of them were classed in the mixed-subtype. The analysis of the transcriptome revealed several gene pathways differentially expressed between the two retinoblastomas subtypes. We noticed that *MYC* target genes were upregulated in the mixed-subtype and that the *MYC* pathway was the most significantly upregulated in this group. In addition, this subtype also presented overexpression of cell cycle genes. These upregulated pathways and the knowledge that *MYCN* amplification are also exclusive of the mixed-subtype, led us to hypothesized that retinoblastoma cell lines representative of the subtype 2 might be sensitive to the treatment with BET bromodomain inhibitors, commonly used to trigger repression of *MYC* oncogene in different human cancers.

Chapter 4 - MOLECULAR CLASSIFICATION OF RETINOBLASTOMA PRECLINICAL MODELS

Models widely used in retinoblastoma research are not characterized or classified at the molecular level. The importance of having this kind of information is simply and crucially important as the

choice of the best model to work with. In this last part of my doctoral research, we aim to characterize at the transcriptomic and the protein level, various patient-derived xenografts developed in the Preclinical Investigation Laboratory (LIP) of the Curie Institute, and cellular retinoblastoma models obtained both commercially and thanks to the many collaborations established since the beginning of this project. Using the same transcriptomic-based approach for primary tumor's classification, we aimed to attribute preclinical models to a molecular subtype. In order to confirm (or refute) our hypothesis that the heterogeneity found in mixed retinoblastomas is an intrinsic property of the tumor, immunohistochemical analysis in cell lines and patient-derived xenograft together with (when available) its original tumor were performed. Beyond molecular classification, transcriptomic analysis will allow us to gain insights in the molecular background of the models studied. This part of the project was financed by RETINOSTOP[4]. Results will be available to the scientific community, greatly improving research in the retinoblastoma field.

[4] RÉTINOSTOP is a French association supporting retinoblastoma scientific research, created in 1994 by parents of affected children

CHAPTER 1

MUTATIONAL LANDSCAPE AND MOLECULAR CLASSIFICATION OF RETINOBLASTOMA

Index

MUTATIONAL LANDSCAPE AND MOLECULAR CLASSIFICATION OF RETINOBLASTOMA 33

INTRODUCTION 37

PAN-CANCER ANALYSIS IN PEDIATRIC CANCER 37

RB1 INACTIVATION IN RETINOBLASTOMA 38

SOMATIC ALTERATIONS IN RETINOBLASTOMA BEYOND *RB1* 39

THE RETINOBLASTOMA CELL OF ORIGIN 39

CURRENT MOLECULAR CLASSIFICATION STATUS OF RETINOBLASTOMA 41

MATERIALS AND METHODS 43

PATIENTS 43

TUMOR SAMPLE PROCESSING AND NUCLEIC ACIDS EXTRACTIONS 43

Curie Institute samples 43

Garrahan Hospital and Sant Joan de Déu Hospital samples 43

NORMAL TISSUE (BLOOD) DNA EXTRACTION 44

GENE EXPRESSION DATA ARRAYS 44

COPY NUMBER ANALYSIS 44

Gistic analysis 45

APPROACHES USED FOR MOLECULAR CLASSIFICATION OF PRIMARY HUMAN RETINOBLASTOMAS 45

Consensus clustering 45

Cluster-of-clusters and Centroid classification 46

DNA METHYLATION ARRAYS 46

DNA methylation analysis 47

Array-based methylation signature 47

Outline of the pyrosequencing assay procedure 48

Pyrosequencing reaction efficiencies 48

WHOLE-EXOME SEQUENCING 49

Analysis pipeline and mutation annotation 49

TARGETED NEXT GENERATION SEQUENCING 50

EXPERIMENTAL VALIDATION OF MUTATIONS DETECTED BY WHOLE EXOME SEQUENCING AND TARGETED SEQUENCING 50

FUSION GENE SCREENING BY ANALYZING RNA SEQUENCING DATA 51

Experimental validation of fusion events identified 51

BIOINFORMATICS 52

RESULTS 53

MOLECULAR CLASSIFICATION OF PRIMARY HUMAN RETINOBLASTOMAS 53

Development of a DNA methylation-based signature using a small panel of nine CpGs for retinoblastomas classification 54
Validation of the methylation signature by pyrosequencing 55
Classification of retinoblastoma samples based on the pyrosequencing signature 55
Final classification of the 102 retinoblastoma cohort 57
SOMATIC MUTATIONAL LANDSCAPE IN RETINOBLASTOMA 57
Whole-exome sequencing 57
Targeted sequencing of recurrently mutated genes 58
Sequencing results 58
RB1 MUTATIONS IN THE 102-RETINOBLASTOMA COHORT 59
RB1 mutations characterization 59
Germline and somatic mutation's distribution across retinoblastomas subtypes 60
A NOVEL RECURRENT FUSION EVENT DISRUPTING *DACH1* IN RETINOBLASTOMA 63
DISCUSSION AND CONCLUSIONS 67
MOLECULAR CLASSIFICATION OF HUMAN RETINOBLASTOMA 67
SOMATIC MUTATIONAL LANDSCAPE IN RETINOBLASTOMA 68
RB1 GERMLINE AND SOMATIC MUTATIONS 69
CHROMOSOMAL FUSION EVENTS DISRUPTING *DACH1* 70
BIBLIOGRAPHY 92

Figures

FIGURE 1. SOMATIC MUTATIONS IN A PEDIATRIC PAN-CANCER COHORT 38
FIGURE 2. SPECTRUM OF RB1 MUTATIONS 39
FIGURE 3. THE CELL OF ORIGIN OF RETINOBLASTOMA 41
FIGURE 4. RETINOBLASTOMA MOLECULAR SUBTYPES 42
FIGURE 5. MUTATIONAL ANALYSIS PIPELINE APPLIED FOR MUTATION'S DETECTION AND EXPERIMENTAL VALIDATION 50
FIGURE 6. VENN DIAGRAM SHOWING TECHNOLOGIES USED IN THE MOLECULAR CHRACTERISATION OF THE SERIES OF 102 PATIENTS INCLUDED IN THIS STUDY 53
FIGURE 7. MOLECULAR CLASSIFICATION OF PRIMARY RETINOBLASTOMAS BASED ON TRANSCRIPTOMIC, METHYLOMIC AND COPY NUMBER ALTERATION DATA 54
FIGURE 8. DEVELOPMENT OF A METHYLATION-BASED SIGNATURE AND SELECTION OF CANDIDATE CPGS 55
FIGURE 9. VALIDATION SET FOR THE 9-CPG METHYLATION SIGNATURE 56
FIGURE 10. RETINOBLASTOMA CLASSIFICATION ASSED BY PYROSEQUENCING USING THE 9-CPG METHYLATION SIGNATURE 56
FIGURE 11. MUTATIONAL LANDSCAPE IN THE 102-RETINOBLASTOMA TUMORS COHORT 59
FIGURE 12. RB1 MUTATIONAL SPECTRUM IN SUBTYPE 1 AND SUBTYPE 2 RETINOBLASTOMAS 62
FIGURE 13. C1-LIKE COHORT OF PATIENTS CARRYING RB1 GERMLINE POINT MUTATIONS 63
FIGURE 14. STRUCTURE OF THE DACH1-LINC FUSIONS IDENTIFIED IN SAMPLE RB50 64
FIGURE 15. STRUCTURE OF THE DACH1-LINC FUSION IDENTIFIED IN SAMPLE RB39 65
FIGURE 16. DACH1 PROTEIN 66
FIGURE 17. FINAL CLASSIFICATION AND MAIN CLINICAL DIFFERENCES BETWEEN RETINOBLASTOMA SUBTYPES 68

Tables

TABLE 1. PANEL OF THE NINE CPGS SIGNIFICANTLY DIFFERENTIALLY METHYLATED SELECTED TO USE FOR SAMPLE CLASSIFICATION 72
TABLE 2. PRIMERS USED FOR PCR AMPLIFICATION AND (PYRO) SEQUENCING 72
TABLE 3. CLINICAL DATA OF THE 102 PRIMARY RETINOBLASTOMA'S COHORT 73
TABLE 4. TECHNOLOGIES USED FOR THE MOLECULAR CHARACTERIZATION OF 102 PRIMARY RETINOBLASTOMAS 78
TABLE 5. FINAL CLASSIFICATION OF 102 RETINOBLASTOMAS 81
TABLE 6. ARID1A AND BCOR MUTATIONS IDENTIFIED BY WHOLE-EXOME SEQUENCING 84
TABLE 7. LIST OF RB1 MUTATIONS IDENTIFIED BY TARGETED SEQUENCING 85
TABLE 8. RB1 MUTATIONS IDENTIFIED IN BY WES AND TARGETED SEQUENCING, ALONG WITH DATA FROM THE GENETIC SERVICE OF THE CURIE HOSPITAL AND THE SANT JOAN DE DÉU HOSPITAL 86
TABLE 9. FUSION EVENTS IDENTIFIED IN 34 RETINOBLASTOMAS 89

INTRODUCTION

PAN-CANCER ANALYSIS IN PEDIATRIC CANCER

Pediatric cancers represent 1% of all cancers1[1] and comprise cancer cases diagnosed in children younger than 14 years, and adolescents and young adults aged 15–19 years (Siegel et al., 2017). Pediatric cure rates for childhood cancers have increased to about 80% in recent decades, but still cancer represent the leading cause of death by disease in developed countries among children over one year of age (Pui et al., 2011; Siegel et al., 2017). Furthermore, many children who survive cancer suffer from long-term sequelae of surgery, cytotoxic chemotherapy, and radiotherapy, including mental disabilities, organ toxicities, and secondary cancers (Townsend et al., 2016). A crucial step in developing more specific and less damaging therapies is the unravelling of the complete genetic repertoire of pediatric malignancies, which differ from adult malignancies in terms of their histopathological entities and molecular subtypes (Downing et al., 2012). The introduction of next-generation sequencing in cancer research has substantially improved our knowledge of the genomic landscapes of diverse pediatric cancers. More recently, a pan-cancer analysis started to be performed, to complement the larger government-funded genomic efforts focused on adult cancers[2]. Gröbner et al. have performed an analysis of 24 different pediatric cancers, where retinoblastoma represents one of the childhood cancers with the lowest detected mutation rates (**Figure 1**) (Gröbner et al., 2018). This pan-cancer analysis are especially important for rare diseases such as retinoblastoma, in order to detect significant mutated genes in larger cohorts that may not be apparent in smaller cohorts, as mentioned before.

[1] American Cancer Society (2016). Key statistics for childhood cancers. https://www.cancer.org/cancer/cancerinchildren/detailedguide/cancer-in-children-key-statistics

[2] US National Human Genome Research Institute (NHGRI)/National Cancer Institute (NCI) Cancer Genome Atlas (TCGA), and the International Cancer Genome Consortium (ICGC)

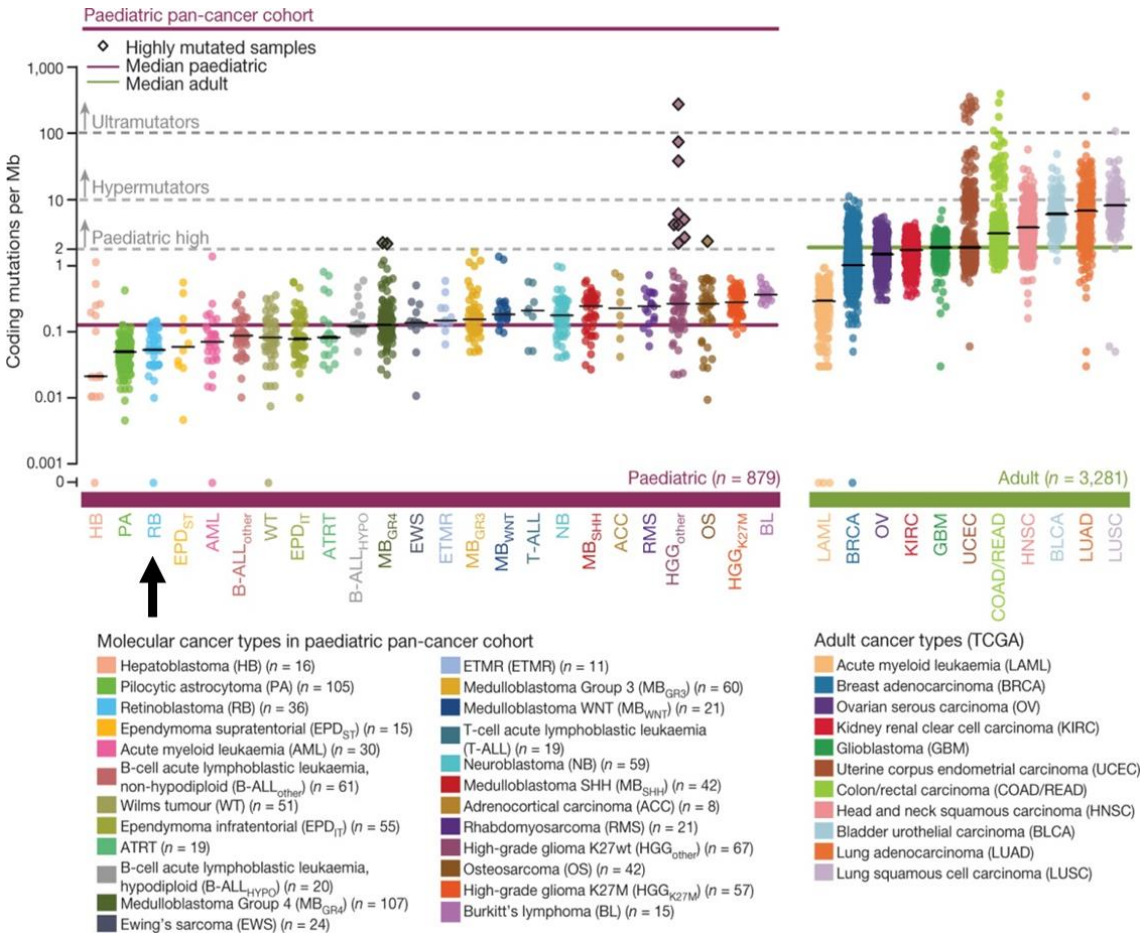


Figure 1. Somatic mutations in a pediatric pan-cancer cohort
Somatic coding mutation frequencies in 24 pediatric (n=879 primary tumors), and 11 adult (n=3281) cancer types (TCGA). Retinoblastoma is indicated with a black arrow. Median mutation loads are shown as solidlines (black, cancer types; purple, all paediatric; green, all adult). Image adapted from Gröbner et al., 2018.

RB1 INACTIVATION IN RETINOBLASTOMA

RB1 is a large (190 kb) gene located in chromosome 13q14.2, with 27 coding exons for a 4.7 kb mRNA that translates into a protein (RB1) of 928 amino acids (Friend et al., 1986; Lee et al., 1987). Many genetic and genomic modifications haven been found to impair RB1 function, including point mutations, promoter methylation, small deletions or insertions (indels) and large deletions encompassing the entire chromosome arm (Houdayer et al., 2004; Lohmann, 1999; Valverde et al., 2005). Recently, chromothrypsis of chromosome 13 disrupting the *RB1* locus has been described as an alternative mechanism for *RB1* inactivation (McEvoy et al., 2014).

Germline and somatic *RB1* mutations has been largely described in the past decades. Mutations are thought to occurred alongside the *RB1* gene, scattered in all coding exons (except for exons 26 and 27), where few hot spots have been described (**Figure 2**) (Valverde et al., 2005).

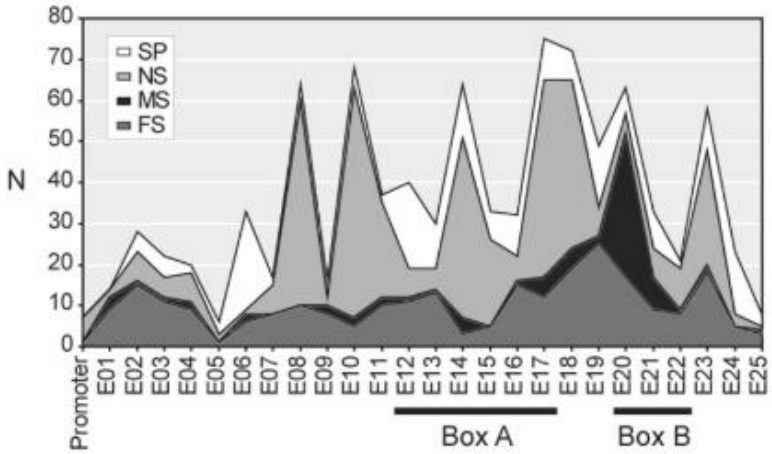


Figure 2. Spectrum of RB1 mutations
Mutations are identified alongside the coding exons of the *RB1* gene, including the promoter region, and excluding exons 26 and 27. Mutations accumulates in discrete spots of high recurrence in exon exons 8, 10, 11, 14, 15, 17, 18 and 23. These mutations correspond to C>T transitions find in CGA-arginine codons. SP (splicing), NS (nonsense), MS (missense), FS (frameshift) mutations. A black bar indicates conserved protein A and B domains. Image adapted from (Valverde et al., 2005).

SOMATIC ALTERATIONS IN RETINOBLASTOMA BEYOND *RB1*

Biallelic inactivation of the *RB1* gene is considered the initiating genetic lesion in nearly all retinoblastomas. Since its discovery, researchers have focused on identifying secondary genetic lesions that cooperate with *RB1* inactivation and contribute to tumorigenesis (Corson and Gallie, 2007). In the past 18 years, next-generation sequencing approaches have made it possible to achieve nucleotide resolution for the retinoblastoma genome. The first retinoblastoma whole-genome sequencing study was carried out in 2012 (Zhang et al., 2012) using 4 primary retinoblastomas and their matched germline DNA. Despite the small size of the discovery cohort, this study led to the identification of recurrent mutations in *BCOR*[3] gene (6/46, 13%). Until that moment, this was the only other gene besides *RB1* that was recurrently mutated in retinoblastoma. In 2016, a larger whole-exome sequencing study was published (Kooi et al., 2016) in which 71 matched tumoral and germline DNA were analyzed. In this study, the recurrent mutated genes besides *RB1* were restricted to *BCOR* (5/71, 7%) and *CREBBP*[4] (2/71, 3%).

THE RETINOBLASTOMA CELL OF ORIGIN

Given that therapeutic agents are developed to target particular molecular pathways in cancer cells, identifying molecular subtypes, and the cell of origin of the disease, becomes increasingly important. For example, if the cell of origin of a pediatric cancer was a progenitor cell, a different strategy should

[3] *BCOR* is a *BCL6* corepressor that regulates gene expression by epigenetic mechanisms (Fan et al., 2009; Gearhart et al., 2006)
[4] *CREBBP* has intrinsic histone acetyltransferase activity (HAT) and is involved in the transcriptional coactivation of many different transcription factors (Gao et al., 2017)

be employed to target particular pathways in that progenitor cell than if it was a highly specialized differentiated cell from the same tissue. This is particularly true for tumors of the central nervous system, because neurons are incredibly diverse and use a variety of signal transduction pathways that may be co-opted during tumorigenesis.

The human retina is composed of six neuronal cell types, rod, cone, horizontal, amacrine, bipolar and ganglion cells, and one glial cell type (Müller glia), all of which are derived from a common retinal progenitor cell. Several studies of both human retinoblastoma and mouse retinoblastoma models have sought to define the retinal cell-of-origin of retinoblastoma and to understand why these cells are susceptible to oncogenic transformation following *RB1* mutation. The first attempt to formulate a link between tumor cell features and a specific retinal cell type as the cell of origin was in 1897 with the description of retinoblastoma rosettes[5]. In subsequent decades, this hypothesis was extended to include morphological analysis using transmission electron microscopy (Dickson et al., 1976; Ts'O et al., 1970), immunohistochemistry (arrestin and rhodopsin, for cone and rod photoreceptors) (Donoso et al., 1985; Mirshahi et al., 1986; Vrabec et al., 1989), and immunofluorescence (CRX and opsins, for photoreceptors) (Glubrecht et al., 2009; Xu et al., 2009). Since then, this question have offered puzzling results, suggesting that retinoblastoma may arise from a progenitor cell (Beemer et al., 1984; Donovan et al., 2006; Glubrecht et al., 2009; Kyritsis et al., 1984b, 1984a; McEvoy et al., 2011; Zhong et al., 2007), a glial cell (Schrøder, 1987), an interneuron such as an amacrine cell (Ajioka et al., 2007; Johnson et al., 2007; Kyritsis et al., 1986; Tsokos et al., 1986), or a cone-photoreceptor cell (Xu et al., 2009). Nevertheless, several works showed evidence that human retinoblastomas appear to develop from postmitotic cone photoreceptor precursors (**Figure 3**) (Bremner and Sage, 2014; Singh et al., 2018; Xu et al., 2009, 2014).

[5] Wintersteiner H. Das Neuroepithelioma Retinae. Franz Deutioke; Vienna: 1897

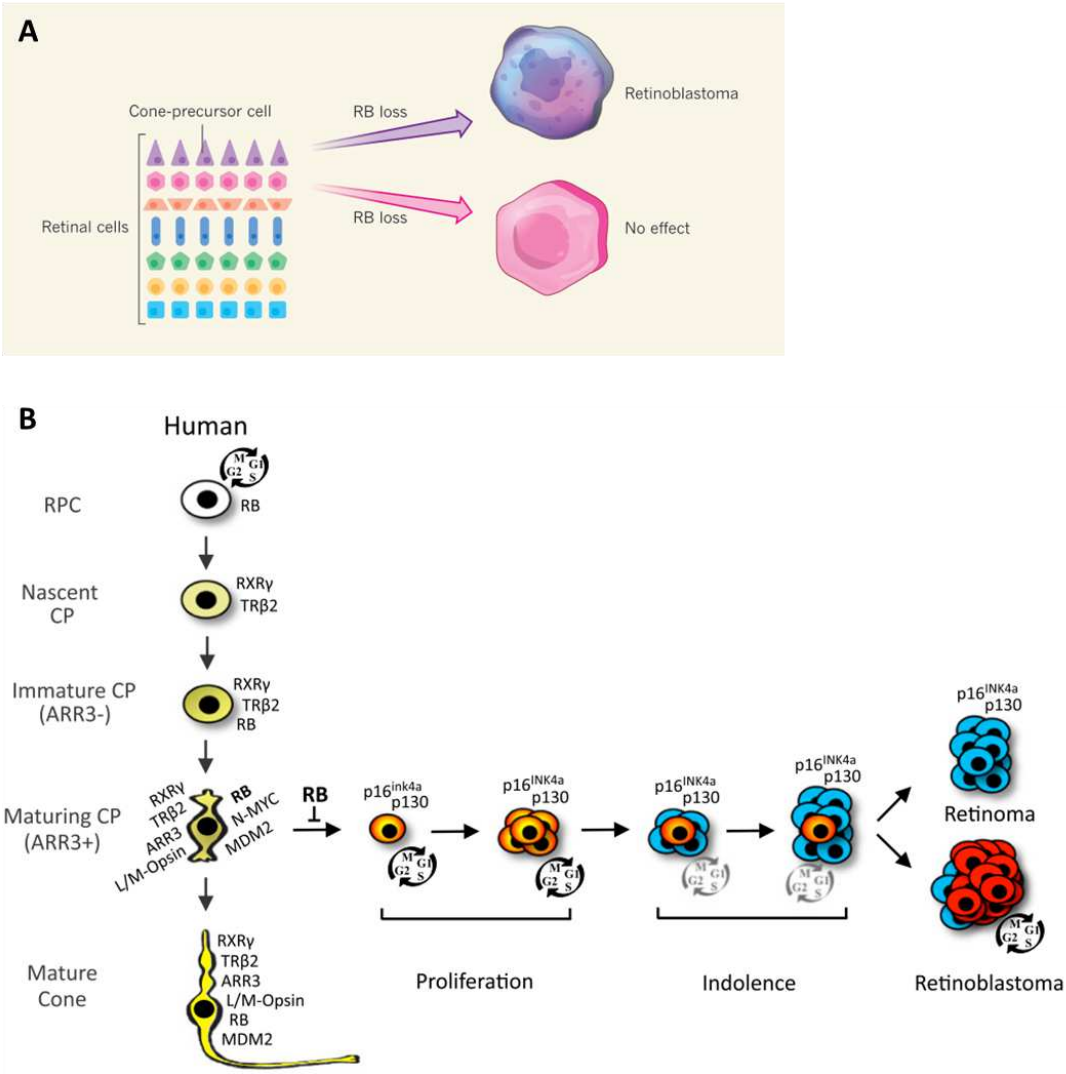


Figure 3. The cell of origin of retinoblastoma

A) Human retinal progenitor cells give rise to seven distinct cell types. Retinoblastoma develops specifically from differentiating cone precursors, owing to the molecular circuitry in these cells, which includes high expression of N-Myc, SKP2 and MDM2 proteins. This expression pattern permits the cells to proliferate and undergo a cancerous transformation when the tumour-suppressor protein RB is lost. In other retinal cell types, loss of RB either has no detectable effect or induces cell death. B) Response to RB1 loss in human cone precursors. The cartoon depicts the generation of cone precursors (CP) from retinal progenitor cells (RPC) and the distinct human CP protein expression and responses to RB1 loss at different developmental stages. Nascent CP are RXRγ+,TRβ2+ and have minimal RB1 expression in humans. RB1 increases during CP maturation but to far higher levels and in association with N-MYC and MDM2 expression in humans. This study showed that in human retina, RB1 loss causes maturing (ARR3+) CP cell-cycle entry and proliferation (orange) followed by cell-cycle withdrawal (blue) and an indolent phase that may give rise to permanently quiescent retinomas or to retinoblastoma tumors (red). Images adapted from (Bremner and Sage, 2014; Singh et al., 2018).

CURRENT MOLECULAR CLASSIFICATION STATUS OF RETINOBLASTOMA

Retinoblastoma is no longer consider a homogeneous disease nevertheless, no consensus for its molecular stratification exist until today. Three main groups have approached this issue based on gene expression analysis, leading to different outcomes (**Figure 4**). In 2011, McEvoy et al. pointed to the existence of a single retinoblastoma subtype. They proposed that human retinoblastomas had molecular, cellular and neurochemical features of multiple cell classes, principally

amacrine/horizontal interneurons, retinal progenitors and photoreceptor cells, which could only be explained by a co-expression of these multiple cell type-specific developmental programs in individual retinoblastoma cells. This notion implied a progenitor/neuronal hybrid cell as the cell of origin (McEvoy et al., 2011). In 2013, Kapatai et al. proposed the existence of two different subtypes of retinoblastomas: one group expressing genes associated with a range of different retinal cell types, suggesting derivation from a retinal progenitor cell, and the other group retaining characteristics of cone photoreceptor cells, suggesting development from a cone lineage cell (Kapatai et al., 2013). In 2015, Kooi et al. proposed that retinoblastomas should not be categorized in distinct molecular subtypes, but rather be described according to their stage of progression (Kooi et al., 2015). They proposed that retinoblastomas were highly diverse as a consequence of tumor progression driven by cumulative genetic alterations, and reflected by a gradual loss of differentiation and photoreceptor expression signature.

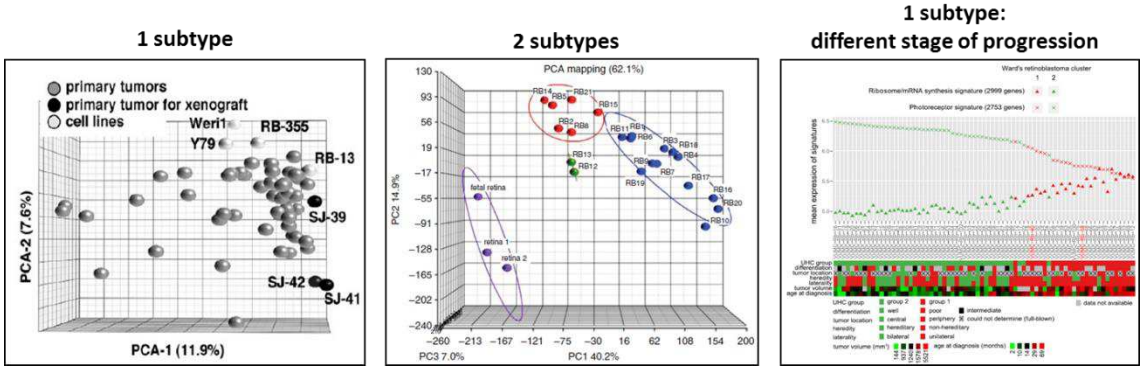


Figure 4. Retinoblastoma molecular subtypes

McEvoy et al. 2011 (left): One subtype of retinoblastoma showing molecular, cellular, and neurochemical features of multiple cell classes, principally amacrine/horizontal interneurons, retinal progenitor cells, and photoreceptors. Kapatai. et al. 2013 (middle): Two different subtypes of retinoblastomas, one expressing genes associated with a range of different retinal cell types, and the other retaining many characteristics of cone photoreceptor cells. Kooi et al. 2015 (right): one subtype of retinoblastoma explained by tumor progression, reflected by a gradual loss of differentiation and photoreceptor expression signature.

More recently, a comprehensive molecular and clinical characterization of retinoblastoma has been performed by our group in which two different subtypes has been identified, based on gene expression data, copy number alteration data and methylomic data (unpublished, in preparation). The first group is characterized by upregulation of genes related to cone photoreceptor cells, with few genomic copy number changes, and displays a phenotypic intratumoral homogeneity (**box 1**, **chapter 4**). The second group is characterized by upregulation of retinal ganglion cell-associated genes, displaying more genomic copy number alterations, and presents with phenotypic intratumoral heterogeneity (**box 1, chapter 4**). *MYCN* amplified tumors are classed within this second subtype. This molecular classification was based on an initial set of 72 primary tumors, and we have recently enlarge the series to 102 retinoblastomas. In this chapter, we outline the molecular based classification and described the main clinical and genetic differences of these tumor subtypes.

MATERIALS AND METHODS

PATIENTS

A total of 102 tumors from 50 male and 52 female patients were included in this study. These patients came from three different hospitals: the Curie Hospital in Paris, France (78 patients), the Garrahan Hospital in Buenos Aires, Argentina (19 patients), and the Sant Joan de Déu Hospital in Barcelona, Spain (5 patients). Median age at diagnosis was 19.9 months (minimum: 27 days, maximum: 9.65 years). Six patients had received treatment prior to enucleation.

All experiments were performed retrospectively and in accordance with the French Bioethics Law 2004-800, the French National Institute of Cancer (INCa) Ethics Charter, the Ethical Committee of the Sant Joan de Déu Hospital, the institutional review board of Garrahan Hospital and the Declaration of Helsinki.

TUMOR SAMPLE PROCESSING AND NUCLEIC ACIDS EXTRACTIONS

Curie Institute samples

Immediately following enucleation, a needle was inserted through the anterior chamber of the eye to extract a tumor sample by aspiration. The tumor specimen was placed in RPMI medium on ice, cells were re-suspended, counted and separated into two or three tubes (for DNA, RNA and protein preparation). The tubes were then centrifuged to remove all media and snap frozen for later extraction. The remainder of the ocular globe was paraffin embedded. For tumor DNA extraction, samples were first incubated in a lysis buffer with recombinant proteinase K (Roche). They were next incubated with RNAse A (Roche). DNA was then extracted using a standard phenol-chloroform protocol. Tumor RNA was extracted using Qiazol (Qiagen, Courtaboeuf, France) according to the manufacturer instructions and purified using miRNeasy Mini kit (Qiagen). DNA and RNA concentration was determined with a NanoVue Plus spectrophotometer (Dutscher) and/or Qubit Fluorometer quantitation assay (Thermo Fisher Scientific). DNA integrity and purity was assessed by 1% agarose gel electrophoresis. The RNA quality was assessed by capillary electrophoresis (Bio-analyzer; Agilent, Inc., Santa Clara, CA, USA) based on the RNA 6000 Pico LabChip kit (Agilent) that assigns per sample quantification and integrity.

Garrahan Hospital and Sant Joan de Déu Hospital samples

Immediately following enucleation, a needle was inserted through the anterior chamber of the eye to extract a tumor sample by aspiration. The tumor specimen was placed either in guanidine thiocyanate or snap frozen for later extraction. For tumoral samples preserved in guanidine

thiocyanate, alkaline phenol/chloroform/isoamyl alcohol (24:1:25) extraction was used for tumor DNA extraction. For the snap frozen tumoral samples, commercial affinity columns (QIAamp DNA Mini Kit, Qiagen) or a standard phenol-chloroform protocol were used for tumor DNA extraction. Integrity and purity of DNA samples were assessed by 1% agarose gel electrophoresis. DNA concentration was determined with a NanoDrop 2000 spectrophotometer (Fisher Scientific) and/or QubIt Fluorometric quantitation assay (Thermo Fisher Scientific).

NORMAL TISSUE (BLOOD) DNA EXTRACTION

The DNA was extracted from Curie Hospital normal tissue samples using a perchlorate/chloroform protocol or by FujiFilm QuickGene technology (Kurabo Biomedical, Osaka, Japan). For Garrahan Hospital samples, normal DNA was extracted with a phenol/chloroform/isoamyl alcohol (24:1:25) protocol or with commercial affinity columns (QIAamp DNA Mini Kit, Qiagen). For Sant Joan de Déu Hospital samples, a standard isopropanol precipitation protocol was used. The concentration, integrity and purity of each DNA sample was assessed by agarose gel electrophoresis, and by using a NanoDrop 2000 spectrophotometer (Fisher Scientific), as well as a QubIt Fluorometric quantitation assay (Thermo Fisher Scientific).

GENE EXPRESSION DATA ARRAYS

RNA of 59 samples were hybridized to Affymetrix Human Genome U133 plus 2.0 Array Plates (Santa Clara, CA) according to Affymetrix standard protocols. Raw CEL files were RMA43 normalized using R statistical software. Batch effects were corrected with the help of the bioconductor package SVA. The arrays were mapped to genes with a Brainarray Custom CDF (EntrezG version 20.0) (Dai et al., 2005).

COPY NUMBER ANALYSIS

Copy-number alterations (CNAs) were analyzed in 102 tumors using WES data (N=71), SNP arrays (Illumina HumanCNV370 quad N=52; Affymetrix Cytoscan N=18) and BAC arrays (3511 markers N=5; 5310 markers N=20). BAC arrays were analyzed using GLAD algorithm (Hupé et al., 2004) to smooth log-ratio profiles into homogeneous segments and assign a discrete status to each segment (homozygous deletion, deletion, normal, gain, amplification). SNP arrays were analyzed using the Genome Alteration Print method (Popova et al., 2009) which takes into account both the log ratio and B allele frequency signals to determine normal cell contamination, tumor ploidy and the absolute copy-number of each segment. The median absolute copy-number was considered to be the zero level of each sample. Segments with an absolute copy-number > zero + 0.5 or < zero - 0.5 were considered to have gains and deletions, respectively. Segments with an absolute copy-number ≥ 5 or ≤ 0.5 were considered to have high-level amplifications and homozygous deletions, respectively. To

identify CNAs using WES data, we calculated the log ratio of the coverage in each tumor and its matched normal sample for each bait of the exome capture kit with a coverage ≥30X in the normal sample. Log-ratio profiles were then smoothed using the circular binary segmentation algorithm as implemented in the Bioconductor package DNAcopy (Venkatraman and Olshen, 2007) (default parameters except min.width=4, undo.splits=« sdundo », undo.SD=1.5). The most frequent smoothed value was considered to be the zero level of each sample. Segments with a smoothed log ratio > zero + 0.15 or < zero − 0.15 were considered to have gains and deletions, respectively. High-level amplification and homozygous deletion thresholds were defined as the mean +/- 5 s.d. of log ratios in regions of normal copy-number. Visual inspection of the profiles allowed to validate recurrent focal amplifications and homozygous deletions.

Gistic analysis

The copy number alteration data for the 72 retinoblastomas studied by consensus clustering were first analyzed using GISTIC2.0 (Mermel et al., 2011). Twelve significant recurrent copy number alteration regions were thus identified. The average copy number for each sample across these regions was then used for consensus clustering of the copy number alteration data.

APPROACHES USED FOR MOLECULAR CLASSIFICATION OF PRIMARY HUMAN RETINOBLASTOMAS

Consensus clustering

Consensus clustering, also called aggregation of clustering (or partitions), refers to the situation in which a number of different (input) clusterings have been obtained for a particular dataset and it is desired to find a single (consensus) clustering which is a better fit than the existing clusterings. Consensus clustering is thus the problem of reconciling clustering information about the same data set coming from different sources or from different runs of the same algorithm (Filkov and Skiena, 2003).

Consensus clustering was performed on the transcriptomic (N=59), methylomic (N=66) and gistic-processed copy number alteration data (N=72) of 72 retinoblastoma samples. mRNA expression was assessed through Affymetrix U133plus2.0 arrays, genome methylation through Illumina Infinium HumanMethylation450 BeadChip arrays, and somatic copy number alterations through SNP arrays or CGH-BAC arrays. For the transcriptomic data, hierarchical clustering analysis of the 59 retinoblastoma samples was derived from a series of 24 hierarchical cluster analyses, obtained from 8 data subsets and 3 different linkage methods (average, complete and Ward), using 1-Pearson correlation as a distance metric. Subsets of data corresponded to unsupervised selections of probe sets based on two criteria: minimal robust coefficient of variation (rCV) and maximal Pvalue of a variance test. Between 96 and 5193 probe sets were selected (rCV thresholds spanning the 99.5th

to the 60th percentiles and a Pvalue lower than 0.01 for the test of variance). The intrinsic stability of initial dendrograms was assessed at a global level by comparing them with cluster results derived from perturbation/resampling tests (200 iterations for each). Perturbation of data sets was performed by the addition of random Gaussian noise (μ = zero, σ = 1.5 × median variance calculated from the data set). The symmetric difference distance was used as a stability measure. This distance is designed to compare two partitions and gives the proportion of retention of the pairs of samples that are in the same group (score is between zero and 1: a score of one corresponds to equal partitions). Each dendrogram was cut to yield a partition of k groups (k=2-8) and then compared partitions at each level of k. Consensus clustering of the methylomic data (n=66 retinoblastomas) was performed in a similar manner, this time with between 2086 and 87937 CpG selected (rCV thresholds spanning the 99.5th to the 60th percentiles and a Pvalue lower than 0.01 for the test of variance). Consensus clustering of the gistic-processed copy number alteration data (n=72 retinoblastomas) was also performed in a similar manner, this time 3 or 4 significant copy number regions selected (rCV thresholds spanning the 80th to the 50th percentiles and a Pvalue lower than 0.01 for the test of variance).

Cluster-of-clusters and Centroid classification

To identify cluster-of-clusters across all three genomic platforms (transcriptome, methylome, copy number) in an unsupervised manner, a sample co-classification matrix was built. Matrix values ranged from 0 to 1, with 0 corresponding to a pair of samples that never co-classify in any genomic dataset, and 1 corresponding to a pair of samples that always co-classify. This matrix was then subjected to hierarchical clustering using complete linkage. Three cluster-of-clusters were thus identified (N=27, N=37 and N=8). The two larger cluster-of-clusters corresponded to two core molecular retinoblastomas subtypes. The smallest cluster-of-clusters corresponded to ambiguous samples whose cluster assignments were not consistent across all three genomic platforms. To classify these remaining unclassified samples, a two centroid-based transcriptomic and methylomic predictors was next built. The two larger core cluster-of-clusters were used to train these classifiers. For the transcriptomic data, the 483 genes most significantly differentially expressed between the two clusters were used. Similarly, for the methylomic data the 6000 CpG most significantly differentially methylated between the two clusters were used. This second centroid-based step classified 6 of the 8 samples without initial cluster-of-cluster attributions (four were assigned to cluster 1 and two to cluster 2).

DNA METHYLATION ARRAYS

Sixty-six DNA samples were hybridized on Infinium HumanMethylation450 BeadChip arrays (Illumina, San Diego, CA). Four microliters of bisulfite-converted DNA were used for hybridization,

following the Illumina Infinium HD Methylation protocol (Bibikova et al., 2011). Data was normalized using the R statistical software, with the help of the Minfi package (Aryee et al., 2014).

DNA methylation analysis

DNA methylation is an epigenetic modification of the genome, whereby a methyl group is covalently linked at position 5 of the cytosine pyrimidine ring (5-MeC), typically occurring in a 5'-CpG-3'dinucleotide context. These CpG sites are often concentrated in distinct areas of the genome and are called "CpG islands" (Gardiner-Garden & Frommer, 1994). The gold-standard method to determine and quantify the methylation state of a genomic region at single-nucleotide resolution is by analysis of DNA sequence after bisulfite conversion (pyrosequencing) where deamination of cytosine residues to uracil occurs and 5-MeC remains nonreactive (Clark, Harrison, Paul, & Frommer, 1994).

Array-based methylation signature

From the analysis of the methylome data array (N=66), we selected the most differentially methylated CpG island between the two retinoblastomas subtypes. First, the top 50 hypermethylated CpGs in C2 compared to C1 subtype were selected by p values of Wilcoxon test of beta values. Within these 50 CpGs, those whose absolute differences of methylation beta value was larger than 0.38 were selected. Then the top 30 of hypomethylated CpGs in C2 compared to C1 were selected by Wilcoxin test of beta values. Within these 30 CpGs, we selected the CpGs whose absolute differences of methylation beta value was larger than 0.4:

#CpG	Wilcoxon test (p values)	GM.1	GM.2	FC.1vs2
#cg12750745	8.859330e-14	0.1285418	0.5541586	-0.4256168
#cg08091439	1.157760e-13	0.2400174	0.6874420	-0.4474246
#cg23877497	1.505587e-13	0.2331429	0.6819304	-0.4487875
#cg11324957	1.944947e-13	0.3973842	0.8604477	-0.4630635
#cg19787076	1.944947e-13	0.2322002	0.7062312	-0.4740310
#cg09470010	4.070743e-13	0.1612397	0.5420055	-0.3807658
#cg18693822	1.963587e-12	0.3243872	0.7083503	-0.3839631
#cg20641531	2.218993e-16	0.6682888	0.1552796	0.5130092
#cg03670369	1.664245e-15	0.8413417	0.2757081	0.5656335
#cg10007051	2.496367e-15	0.5610808	0.1567623	0.4043185
#cg07857792	3.716813e-15	0.7318207	0.2670876	0.4647331
#cg17341366	3.716813e-15	0.6596688	0.1988143	0.4608545
#cg21214455	5.381058e-15	0.6511162	0.1647284	0.4863878
#cg10316527	5.381058e-15	0.5646209	0.1613257	0.4032952

This method led to the selection of an initial set of fourteen CpGs and finally selected nine of them based on the possibility to generate an amplifiable product that could be then analyzed by pyrosequencing. The list of the nine single CpG used in the pyrosequencing signature is provided in **Table 1** (page 72).

Outline of the pyrosequencing assay procedure

Bisulfite treatment of genomic DNA (500ng) from samples included in the validation set as well as for samples to be classified was performed using the EZ DNA Methylation kit (Zymo Research) following manufacturer's instructions. Unmethylated (0%) and methylated (100%) controls were also included. Bisulfite-treated DNA was quantified with a NanoDrop 2000 spectrophotometer (Fisher Scientific).

Primer design for each target was performed using the PyroMark Assay Design2.0 software where a trio of primers was generated: forward and reverse used for PCR amplification (one of them carried a biotin label at its 5'-terminus) and the third for the pyrosequencing reaction (**Table 2**, page 72). Amplicons including the CpG of interested ranged from 130pb to 240pb.

The target region was amplified by PCR using the PyroMark PCR kit (Qiagen) in a final volume of 25µL, containing 400nM of each primer complementary to the bisulfite-treated DNA sequence, 1X Coral Load Concentrate, in 1X PyroMark PCR Master Mix and 20ng of bisulfite-treated DNA. The initial denaturation (95°C, 15min), was followed by 45 cycles of 30sec at 94°C, 30 sec at 56°C and 30sec at 72°C, and a final extension step at 72°C for 10min. After PCR amplification, all uracil and thymine residues are amplified as thymine and only 5-MeC residues are amplified as cytosine. Correct size of amplicons was checked by electrophoresis in a 2% agarose gel.

We used the pyrosequencing technology to assess the degree of methylation at each CpG position on the target sequence. Twenty microliters of the biotinylated PCR product was immobilized on streptavidin-coated beads. Then captured with the vacuum tool on the PyroMark Q24 Vacuum Prep Workstation (Qiagen), and thoroughly washed and denaturized. The single-stranded template DNA was then released into a pyrosequencing reaction plate containing the pyrosequencing primer (75nM) complementary to the single-stranded template. After primer annealing, the reaction plate was placed into the PyroMark Q24 instrument where the pyrosequencing reaction was performed by the sequential addition of single nucleotides in a predefined order. For each series of sample analyzed, 0% methylated DNA and 100% methylated DNA controls were used.

Pyrograms obtained were analyzed using the PyroMark Q24 software (Qiagen). Methylation percentage was calculated at each CpG of interest, determined from the ratio of thymines and cytosines sequenced.

Pyrosequencing reaction efficiencies

In order to assess quantification accuracy and linearity at the interrogated CpG positions, primer efficiency was evaluated by correlating the observed methylation values (pyrosequencing) to the expected methylation values (known DNA methylation curve), obtaining high correlation in the methylation values with the primers designed.

WHOLE-EXOME SEQUENCING

Exome sequencing was performed in 71 retinoblastomas and matched normal (blood) samples. For 32 tumor/normal sample pairs, sequence capture and exome sequencing were performed by the Curie sequencing platform. Nextera exome enrichment kit (Illumina) was used for DNA library preparation. The eluted fraction was amplified by PCR and sequenced on an Illumina HiSeq 2500 sequencer as paired-end 100x100bp or 150x150bp reads. The remaining 39 tumor/normal sample pairs, sequence capture and exome sequencing were performed by IntegraGen SA (Evry, France). The detailed protocol is described in (Gnirke et al., 2009). Briefly, agilent in-solution enrichment (SureSelect Human All Exon Kit v4+UTR) was used for DNA library preparation. The eluted fraction was amplified by PCR and sequenced on an Illumina HiSeq 2000 sequencer as paired-end 75-bp reads.

Analysis pipeline and mutation annotation

Sample reads were aligned using Burrows–Wheeler Aligner (BWA) (Li and Durbin, 2009). Targeted regions were sequenced to an average depth of 82×, with 99% of the regions covered by ≥ 1×, 97.0% covered by ≥ 4× , and 87% covered by ≥ 20×. For detection of somatic single nucleotide variants (SNVs) and base insertions or deletions (indels), we used two separate variant calling pipelines whose results were then merged. The first pipeline used MuTect (Cibulskis et al., 2013) for SNV calling and the GATK SomaticIndelDetector for indel calling (Van der Auwera et al., 2013; DePristo et al., 2011; McKenna et al., 2010). The second pipeline, used VarScan somatic and VarScan somatic filter for both SNV and indel calling (http://varscan.sourceforge.net) (Koboldt et al., 2012). After the variants called by both pipelines were merged, they were annotated using Annovar (Yang and Wang, 2015). Custom filters and manual curation using the Integrative Genomics Viewer (IGV) (Thorvaldsdottir et al., 2013) were then used to maximize the number of true positive calls and minimize the number of false positives. These bioinformatics analysis were developped in parallel to the Sanger sequencing validation of the mutations detected (**Figure 5**).

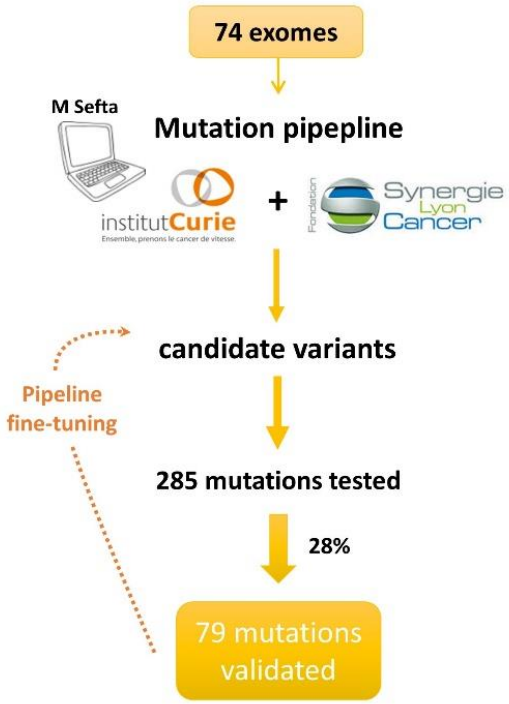


Figure 5. Mutational analysis pipeline applied for mutation's detection and experimental validation
In 2015, 74 exomes were analyzed by whole-exome sequencing (Then, three samples were excluded from the final analysis; results showed in this chapter correspond to 71 exomes). The bioinformatics analysis and custom filters applied for somatic mutation's detection were developped by Meriem Sefta, in collaboration with the Foundation Synergy Lyon Cancer. From the list of putative mutations (candidate variants), a total of 285 putative mutations were Sanger-sequenced (mutations tested). From these, 79 mutations (28%) were experimentally validated. This experimental validation was also useful for the calibration of the filters applied.

TARGETED NEXT GENERATION SEQUENCING

Targeted sequencing of the exonic regions of *RB1*, *BCOR* and *ARID1A* genes was performed by IntegraGen SA (Evry, France) on 23 samples. The Fluidigm Access Array microfluidic system was used. PCR products were barcoded, pooled and subjected to Illumina sequencing on a MiSeq instrument as paired-end 150-bp reads.

EXPERIMENTAL VALIDATION OF MUTATIONS DETECTED BY WHOLE EXOME SEQUENCING AND TARGETED SEQUENCING

Nonsynonymous variants identified by the previously described approaches were verified in 44 tumor/normal sample pairs (WES), 12 tumoral and 11 tumor/normal sample pairs (targeted sequencing) by Sanger dye-terminator sequencing. Primer design for each target was performed using Primer3 plus software (Untergasser et al., 2007).

PCR amplifications were carried out in a Mastercycler pro PCR System instrument (Eppendorf) using the HotStarTaq plus DNA Polymerase kit (Qiagen) in a final volume of 20µL containing 300nM of each primer, 0,2mM of a dNTPs mix, 0,05 U/µL of HotStarTaq plus DNA Polymerase (Qiagen) in buffer 1X Master Mix and 20ng of genomic DNA as template. Thermal cycling included one initial denaturation

at 95°C (15min), followed by 35 cycles at 94°C (1min), 56°C (30sec) and 72°C (1min), and a final extension step at 72°C (10 min). Amplicons' correct size was verified by electrophoresis in a 2% agarose gel, and then purified using Illustra ExoProStar purification kit (GE Healthcare).

Sanger sequencing PCR was performed in a final volume of 10µL containing 500nM of the forward and reverse primers (in separate reactions), using 0,25X BigDye Terminator V3.1 (for DNA fragments >500pb) or 0,25X BigDye® Terminator V1.1 (for DNA fragments <500pb) (Thermo Fisher) in 0,75X sequencing buffer and 2µL of PCR. Thermal cycle was performed in a Mastercycler pro PCR System instrument (Eppendorf) as follows: an initial step at 96°C for 1 minute, followed by 25 cycles at 96°C (20sec), 50°C (15sec) and 60°C (4sec). Ten microliters of H2O were added to the final product. Fragments were analyzed at the Genomic Platform of the Curie Institute, in a 3730xl DNA Analyzer (Applied Biosystems, Life Technologies). Sequence analysis was carried out using Sequencher® version 5.4.1 sequence analysis software (Gene Codes Corporation, Ann Arbor, MI USA). The somatic nature of mutations was confirmed by sequencing tumors and their paired normal tissue.

FUSION GENE SCREENING BY ANALYZING RNA SEQUENCING DATA

Quality of reads was assessed for each sample using FastQC (http://www.bioinformatics.babraham.ac.uk/projects/fastqc/). A subset of 500.000 reads from each Fastq file was aligned to the reference human genome hg19/GRCh37 with tophat2 to determine insert sizes with Picard. Full Fastq files were aligned to the reference human genome hg19/GRCh37 with tophat2 (Kim et al., 2013). We removed reads mapping to multiple locations. Fusions initially detected by TopHat2 were filtered using the TopHatFusion-post algorithm. To identify recurrent fusions, we used the most reliable fusions, i.e. fusions that were validated by BLAST and with at least 10 pairs of read spanning and validating the fusion event. Further filtering was done by removing fusions readily detected in control samples and considering only fusions involving genes separated by at least 200kb and three genes according to Gencode transcriptome annotation (version hg19v19). We compared the 5' and 3' partners of the fusion transcripts identified in our RNA-seq data sets to the TCGA Fusion Gene Database (Yoshihara et al., 2015).

Experimental validation of fusion events identified

One microgram of total RNA was reverse-transcribed with the High-Capacity cDNA Reverse Transcription kit (Applied Biosystems) in a final volume of 20µL containing dNTP Mix 1X (4mM), RT Random Primers 1X, RNase Inhibitor (1U/µl), MultiScribe RT (2.5U/µl) in a RT Buffer 1X. Reaction was run in a Mastercycler pro PCR System (Eppendorf) as follows: 25°C (10sec), 37°C (120min), 85°C (5sec). Size of the amplicons was checked by electrophoresis in a 2% agarose gel. Then purified, Sanger sequenced and analyzed as described above.

BIOINFORMATICS

Bioinformatic analysis was performed by Meriem Sefta (Curie Institute, former PhD fellow in bioinformatics: WES, RNA sequencing, RNA expression arrays), Jing Liu (Curie institute, PhD fellow in bioinformatics: DNA methylation arrays, RNA expression arrays) and Aurelién de Reynès (PhD, senior bioinformatics in La ligue contre le Cancer: CNV, DNA methylation arrays, Methylation signature, RNA expression arrays).

RESULTS

We have performed an extensive and integrative analysis to characterize the molecular and genomic landscape of retinoblastoma using whole exome sequencing (WES) (N=71), RNA sequencing (N=34), genomic copy number variation (CNV) (N=95), DNA methylation arrays (N=66) and RNA expression arrays (N=59) on a series of 102 primary tumors (**Figure 6**). We integrated samples coming from three institutions: the Curie Institute (France), the Garrahan Hospital (Argentina) and Sant Joan de Déu Hospital (Spain). Clinical data from all patients included in this study and technologies used for their characterization can be find detailed in **Table 3** (page 73) and **Table 4** (page 78), respectively. Results obtained from the analysis of data coming from all these technologies will be exploited throughout the different chapters of this thesis.

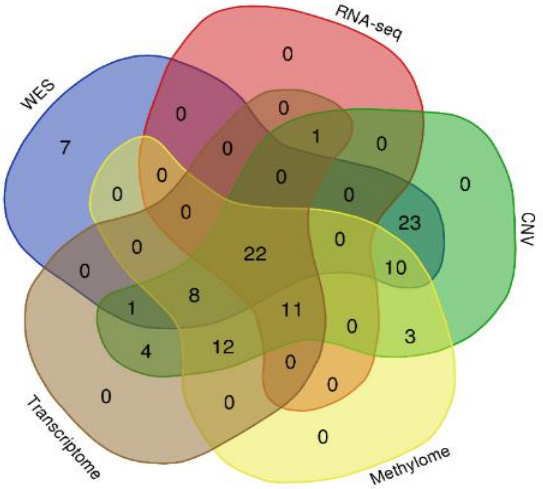


Figure 6. Venn diagram showing technologies used in the molecular chracterisation of the series of 102 patients included in this study
WES: Whole-Exome sequencing N=71; RNA-seq: RNA sequencing N=34; CNV: genomic Copy Number Variation Data N=95; Methylome: DNA methylation arrays N=66; Transcriptome: RNA expression arrays N=59.

MOLECULAR CLASSIFICATION OF PRIMARY HUMAN RETINOBLASTOMAS

We had previously analyzed mRNA expression, DNA methylation and CNV data of 72 primary tumors trying to address the question of the existence of molecular subtypes in retinoblastoma. All three datasets were available for 74% (N=53/72) of tumor samples and at least two out of the three datasets were available for all samples (**Table 4**, page 78). Using *consensus clustering*, two transcriptome-based tumor clusters, two methylome based-tumor clusters and five CNV-based tumor clusters were first identified (**Figure 7**, top). A *cluster of clusters approach* using unsupervised clustering attributed 89% (N=64/72) of tumor samples into two molecular subtypes, while eight samples were left unclassed (**Figure 7**, middle). A *nearest centroid classification* using two centroid-

based transcriptomic and methylomic predictors, attributed to the same subtypes 98% (N=63/64) of samples classified by the former approach, and six of the eight unclassed samples could be attributed to a subtype. In total, 96% of samples (N=69/72) were classified in a molecular subtype: 31 tumors were attributed to the subtype 1 (C1, also called the "cone-like" subtype) and 38 to subtype 2 (C2, also called the "mixed-type" subtype) **(Figure 7**, bottom).

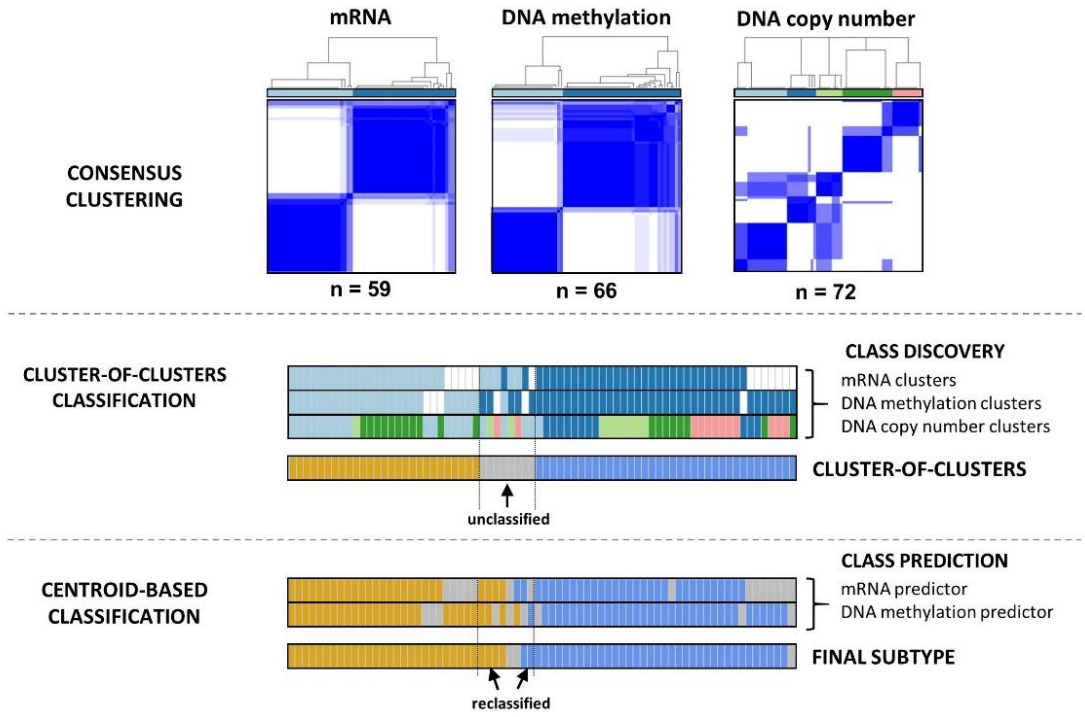


Figure 7. Molecular classification of primary retinoblastomas based on transcriptomic, methylomic and copy number alteration data

Consensus clustering analysis separated primary tumors in at least two retinoblastomas subtypes (top). Cluster-of-clusters classification allowed classification of 89% of samples in two molecular subgroups (middle). Centroid classification based on 483 genes attributed a subtype to six of the eight samples that had remained unclassed with the previous method. Only one sample classed as C2 with the cluster-of-clusters could not be attributed to any subtype. In total, 31 tumors were attributed to subtype 1, 38 to subtype 2, and 3 samples were left unclassed.

Development of a DNA methylation-based signature using a small panel of nine CpGs for retinoblastomas classification

In an effort to enlarge the previous characterized series of retinoblastomas based on the analysis of high-throughput data (transcriptome, methylome and genomic copy number alteration), we designed a DNA methylation-based tool that allows the classification of new samples in a faster and low-cost way.

We used a methylation array to screen differentially methylated CpGs in a discovery cohort of 63 patients and selected an initial set of fourteen CpGs. Subsequently, we narrowed the selection to nine candidate CpGs, based on the possibility of generating an amplifiable product that could be then

analyzed by pyrosequencing, and built a signature (**Figure 8, Table 1**-page 72). Three of this CpGs were hypermethylated in the C2 subtype (cg1, cg2 and cg3), and six of them were hypermethylated in the C1 subtype (cg6, cg8, cg10, cg13, cg14), allowing good discrimination of both groups.

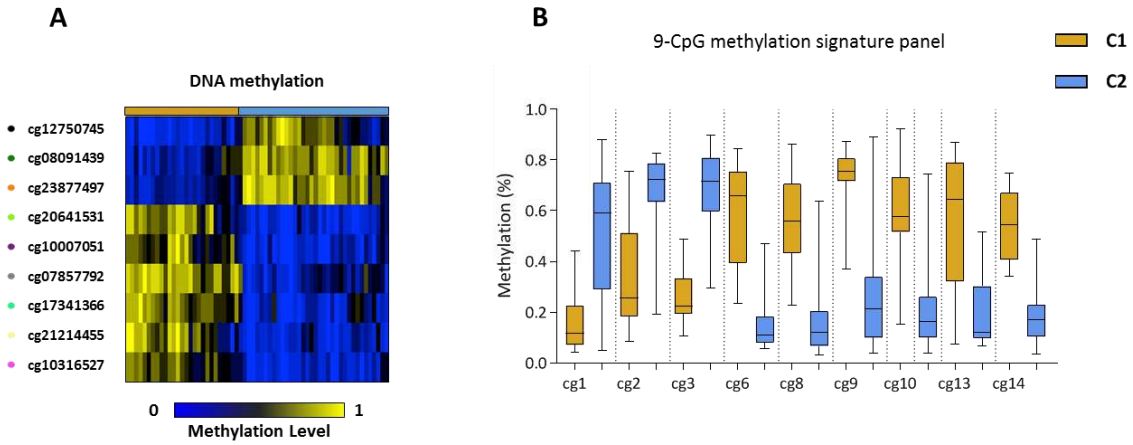


Figure 8. Development of a methylation-based signature and selection of candidate CpGs
A) Heatmap showing methylation values for the 9-CpGs selected. Heatmap was constructed using methylomic data from retinoblastoma samples already assigned to a subtype (N=63). B) The 9 CpGs are significantly differentially methylated between the tumors subtype (Wilcoxon test p<0.0001, see **Table 1**).

Validation of the methylation signature by pyrosequencing

Next, we validated this 9-CpG methylation signature in an internal validation cohort of 15 tumor samples that had been already classed by the centroid-based method (C1 N=8, C2 N=7). All samples from the validation set were correctly classed into the already given subtype. Methylation values assessed by pyrosequencing showed high correlation to that of the array's methylation values (Pearson's correlation, pvalue (two-tailed) : cg1 r=0,9928, p<0,0001; cg2 r=0,9847, p<0,0001; cg3 r=0,9797, p<0,0001; cg6 r=0,9854, p<0,0001; cg8 r=0,9804, p<0,0001; cg9 r=0,9922, p<0,0001; cg10 r=0,9854, p<0,0001; cg13 r=0,9914, p<0,0001; cg14 r=0,9803, p<0,0001) (**Figure 9**).

Classification of retinoblastoma samples based on the pyrosequencing signature

Finally, we used our 9-CpG signature to assess a tumor subtype to the thirty left unclassed samples from our series of 102 retinoblastomas. Ninety percent of these samples (N=27/30) could be attributed to a tumor subtype: seven samples were classed in the subtype 1, twenty in the subtype 2, and three were left unclassed (**Figure 10**). The development of this 9-CpG signature is especially useful for samples with no available or degraded RNA (as was the case of many samples coming from Garrahan Hospital) that cannot be analyzed by transcriptomic arrays.

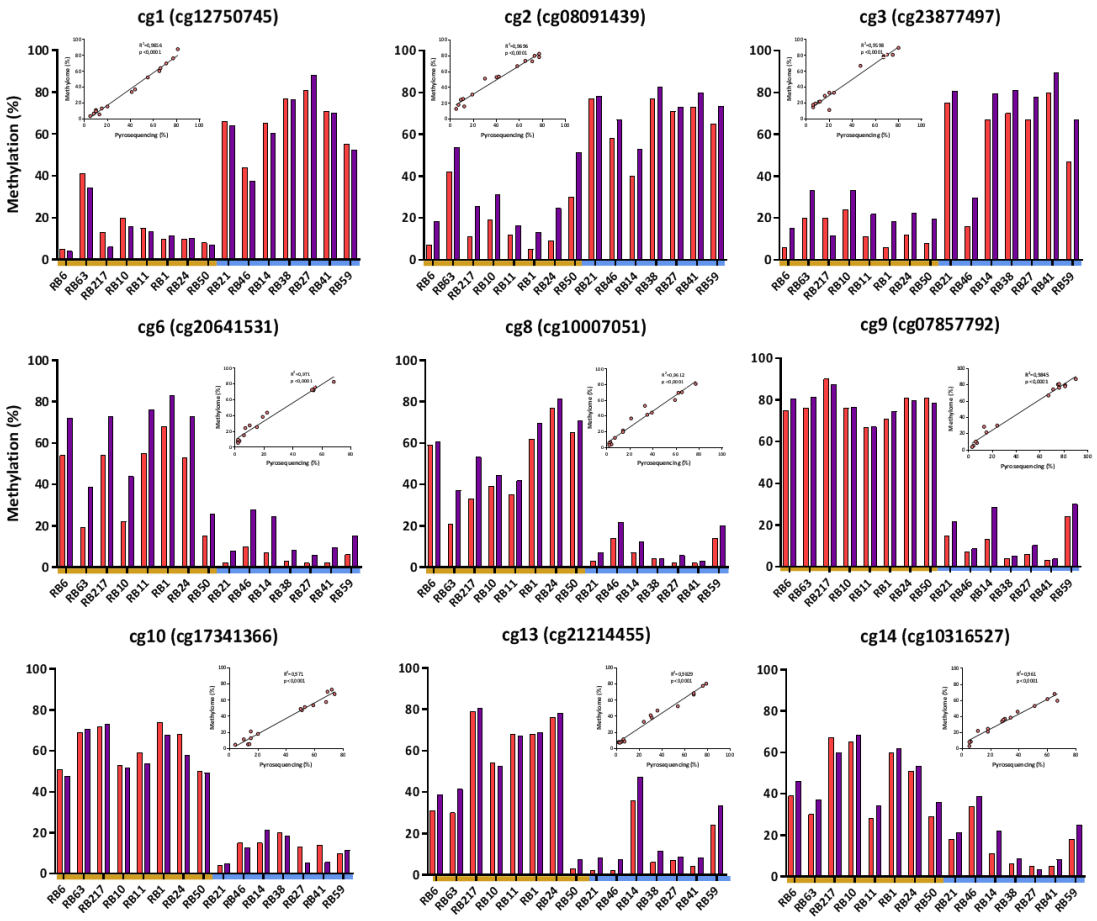


Figure 9. Validation set for the 9-CpG methylation signature

Eight C1 tumors and seven C2 tumors were used as the validation set for the 9-CpG methylation signature. Methylation values assessed by pyrosequencing (red bars) and obtained by the methylome array (violet bars) were significantly correlated. A gold bar and a blue bar below samples indicates tumor's subtype 1 and subtype 2, respectively.

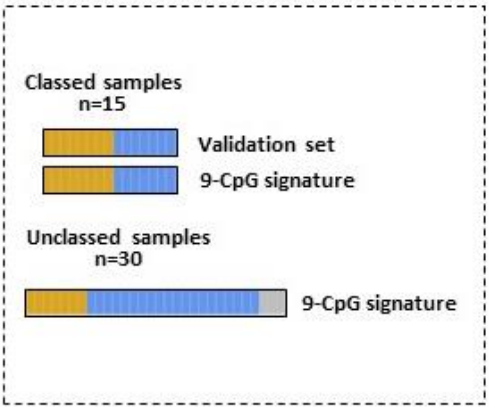


Figure 10. Retinoblastoma classification assed by pyrosequencing using the 9-CpG methylation signature

The validation set of 15 classed samples (N=8, subtype 1, in gold; N=7 subtype 2, in blue) were attributed to the same subtype (top). Thirty unclassed samples were finally classed in subtype 1 (N=7/30) and subtype 2 (N=20/30), whereas three samples could not be attributed to any subtype (NA=3/30).

Final classification of the 102 retinoblastoma cohort

Using a combination of both methods, the centroid-based and the 9-CpG methylation signature assessed by pyrosequencing, 94% of primary tumors could be attributed to a molecular subtype. In total, 38 tumors were attributed to C1 subtype, 58 tumors to C2 subtype, and 6 samples could not be attributed to any of these groups (**Table 5**, page 81). The main clinical differences of these subtypes is discussed later in this chapter.

SOMATIC MUTATIONAL LANDSCAPE IN RETINOBLASTOMA

Whole-exome sequencing

We sought to define the mutational landscape of our cohort of 102 primary tumors and identify new candidate genes involved in retinoblastoma tumorigenesis. To achieve that, we performed whole-exome capture followed by paired-end massively parallel sequencing on genomic DNA from 71 tumors and matched normal samples (**Table 4**, page 78).

We identified 235 somatic mutations in 182 genes. Eighty percent (N=188/235) corresponded to nonsynonymous single nucleotide variants (SNV) or inframe/frameshift short deletions or insertions (indels), while 20% (N=48/235) were synonymous SNV (**Figure 11A**). SNV represented 90% (N=212/235) of all mutations found and the mutation spectrum was characterized by predominance of C>T transitions (32%, N=67/212) (**Figure 11B**). Except for one highly mutated sample from a patient who had received multimodal therapies prior to enucleation (HSJD-RBT3: 35 somatic mutations, including one *RB1* mutation), tumors harbored a median of two exonic mutations, corresponding to a median somatic mutation rate in coding sequences of 0.05 mutations per megabase (Mb). Distribution of nonsynonymous coding mutations between tumor subtypes was significantly different ($p=2,22x10^{-6}$) (**Figure 11D**). The median of somatic mutations per sample was one mutation for C1 tumors (range: 0-5 mutations per sample) and four mutations for C2 tumors (range: 1-7 mutations per sample). Number of mutations per sample was not correlated with the age at diagnosis of the patient (C1: r 0,01642, p=0,5415; C2 r 0,02072, p=0,3692, Pearson's correlation test).

In order to validate mutations identified by WES, we performed Sanger sequencing on 84 tumoral and normal samples from 42 patients. Sequencing constitutional DNA (normal samples) allowed us to define the somatic mutational status. We sequenced 40% of somatic mutations found by WES (N=93/235). Overall, we experimentally validated 86 nonsynonymous mutations identified by exome sequencing, leading to a validation rate of 92% (N=86/93).

Non recurrent somatic mutations

Non-recurrent coding mutations were found across 179 genes. Gene ontology functional enrichment analysis, including biological processes, molecular functions, pathways and diseases, did not result in any significantly overrepresented ontology, probably due to the relatively low number of genes used in the analysis.

Recurrent somatic mutations

Only three genes were found mutated recurrently (at least two mutations found in at least two different patients) across the exome-sequenced series: *RB1*, *BCOR* and *ARID1A*. Thirty-nine *RB1* mutations were identified in 34 patients. Nine *BCOR* mutations were found in 9 patients and two *ARID1A* mutations in 2 patients (**Table 6**, page 84).

Targeted sequencing of recurrently mutated genes

We then we seek to extend the series of sequenced samples by performing targeted sequencing for the three recurrent mutated genes (*RB1*, *BCOR and ARID1A*). Targeted sequencing was performed in 37 patients (**Table 4**, page 78) of which 14 have been already sequenced by WES. One additional somatic *RB1* mutation was found in one patient (RB617) not previously detected by WES, probably due to lack of coverage of the region. In the group of the 23 first time-sequenced patients (12 tumoral samples and 11 matched normal and tumoral samples), ten additional *RB1* somatic mutations were identified in 8 patients (**Table 7**, page 85). All mutations detected by this technology were validated by Sanger sequencing. No additional mutations of *BCOR* and *ARID1A* were identified.

Sequencing results

Overall, mutational analysis was performed in 92% of patients included in the cohort (N=94/102 patients: N=71, WES; N=23, targeted sequencing). The somatic mutation rate for *RB1* gene was 51% (N=48 mutations in 43 patients), *BCOR* 9.6% (N=9 mutations) and *ARID1A* 2% (N=2 mutations) (**Figure 11E**). *BCOR* and *ARD1A* mutations were found exclusively in the retinoblastoma subtype 2. These mutations in our cohort were previously discussed (http://www.theses.fr/2015SACLS074). We will further focus on *RB1* mutations.

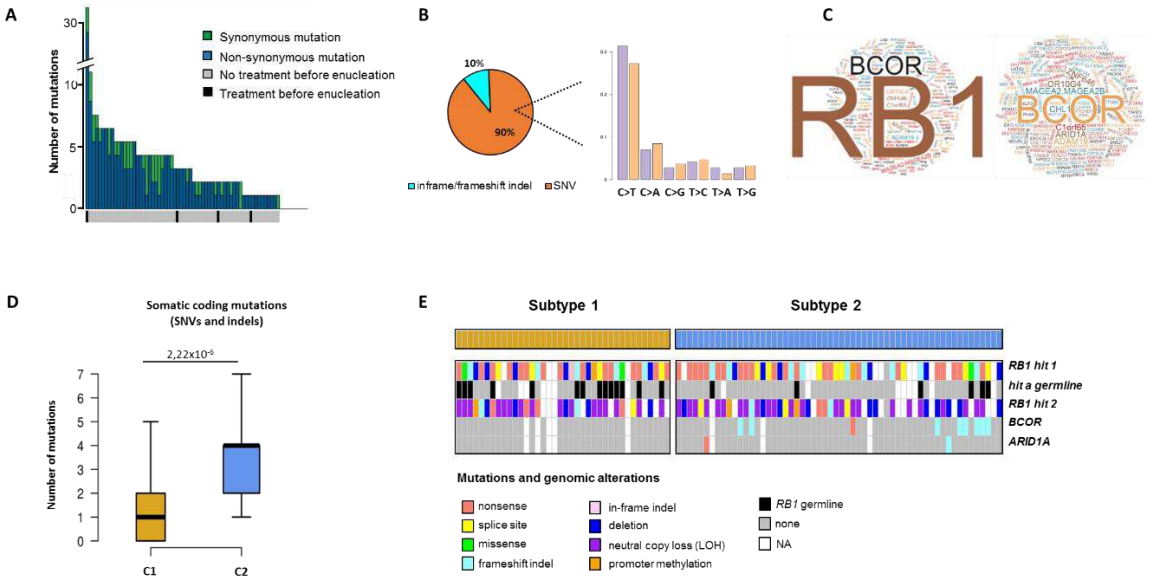


Figure 11. Mutational landscape in the 102-retinoblastoma tumors cohort
A) Synonymous (20%, in green)) and non-synonymous (80%, in blue) somatic mutations identified by whole-exome sequencing of 71 primary tumors. In black are indicated the samples that received treatment prior enucleation. Sample displaying 35 somatic mutations (HSJD-RBT3) received chemotherapy and radiotherapy before being enucleated. B) Single nucleotide variants (SNV) represented 90% of all somatic mutations identified, while inframe or frameshift indels (insertions or deletions) counted for 10% of mutations. SNV mutation spectrum was characterized by a predominance of C>T transitions. The relative proportions of the six different possible base-pair substitutions are shown. C) A word cloud generator was used for depicting the representation of somatic mutated genes including (left) and excluding (right) RB1 mutations. The size of words is in relation to the number of mutations found for each gene. D) The distribution of nonsynonymous somatic coding mutations identified by WES is significantly different between tumor subtypes (Wilcoxon test: $p=2,22x10^{-6}$), being higher in tumors of the subtype 2. D) Distribution of recurrent mutations between tumor subtypes assessed by WES and target sequencing. BCOR and ARID1A mutations are found in subtype 2 tumors. For RB1 mutations, we integrated date provided by the Genetic Service of the Curie Institute in order to determine the germline status (in black) of RB1 mutations, when was not available from our analysis.

RB1 MUTATIONS IN THE 102-RETINOBLASTOMA COHORT

We next moved to analyze the distribution of *RB1* mutations in our cohort. The Genetic Service of the Curie Institute provided the mutational status for those patients who had not been sequenced by either WES or targeted sequencing. The total list of *RB1* mutations is provided in **Table 8** (page 86).

RB1 mutations characterization

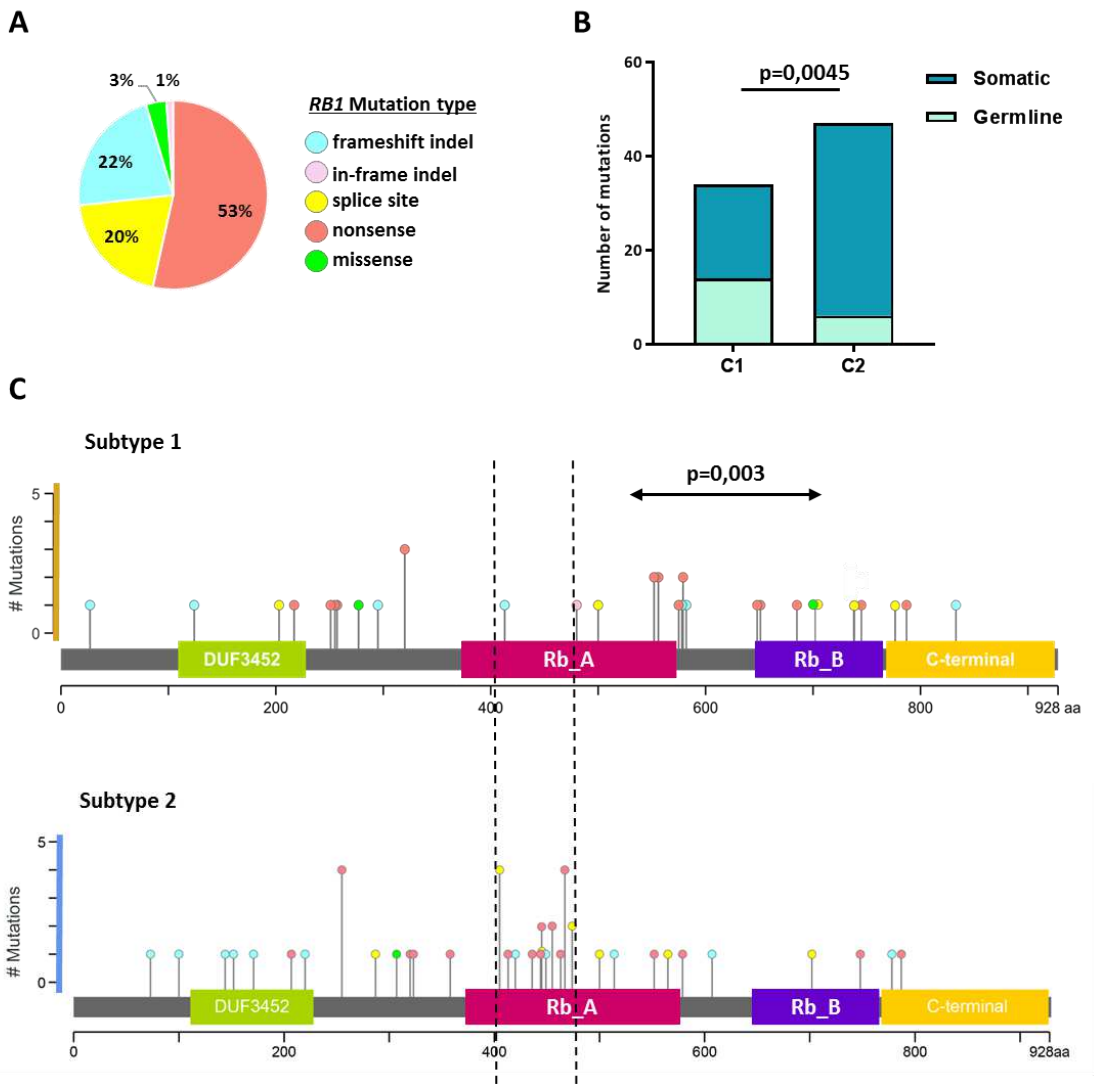
Eighty-six *RB1* point mutations (SNV or indels) were identified across the *RB1* gene, except for exons 21, 26 and 27. Regarding mutation type, most of them corresponded to nonsense mutations (53%, N=46/86) (**Figure 12**). Exon 8 was the most recurrent mutated (N=10; 1 splice site and 9 nonsense mutations), followed by exon 17 (N=8; 1 frameshift indel, 2 splice site and 5 nonsense mutations) and exons 14 (N=7; 1 splice site, 1 frameshift indel and 5 nonsense mutations) and 18 (N=7; 2 frameshift indels and 5 nonsense mutations). The most recurrent mutation in our cohort was a splice site mutation located in intron 12 (N=5; c. 1215+1G>A), followed by R255X in exon 8 (N=4), R320X in

exon 10 (N=4), R467X in exon 15 (N=4) and R579X in exon 18 (N=4). The rest of *RB1* alterations found across patients were somatic exon and gene deletions, and hypermethylation of the *RB1* promotor.

Germline and somatic mutation's distribution across retinoblastomas subtypes

RB1 point mutations were identified in most patients (N=72/102) regardless of tumor subtype, and corresponded to 21 germline mutations and 65 somatic mutations. The distribution of germline and somatic mutations in tumor subtypes was significantly different (p= 0.0045, Fisher's Exact test). Patients from the subtype 1 carried most of the germline mutations, representing 41% (N=14/34) of total *RB1* mutations identified in this group. Patients from the subtype 2 carried only 13% (N=6/47) germline mutations (**Figure 12B**). The unclassed group of six patients carried four somatic and one *RB1* germline mutation. Ten patients were left uncharacterized (N=3, subtype 1; N=6, subtype 2; N=1 NA) given that no study was performed or no sample was available. No *RB1* mutations were identified in one patient (RB222) of our cohort (subtype 2), and corresponded to a sample carrying a *MYCN* amplification (see **chapter 3**).

We then analyzed the distribution of somatic and germline point mutations across the RB1 protein (RB1) which turned out to be significantly different between both subtypes (p=0.003, Kolmogorov–Smirnov test). Moreover, we noted a gap in the RB1-Domain A (corresponding to gene exons 12 to 15), where there were virtually no mutations in tumors from the subtype 1 (**Figure 12C**). Besides, mutations in *RB1* exons 14 and 15 were exclusively found in subtype 2 tumors (**Figure 12D**). The absence of mutations in exons 14 and 15 in tumors of the subtype 1 implied two possibilities: 1) a possible splicing event occurring only in this type of tumors, thus no mutations are detected because exons are not present, or 2) there is less representation of tumors of the subtype 1 because patients with these mutations are not enucleated. To test our hypothesis, we selected four samples of each subtype (based on RNA availability) and simply performed a RT-PCR of *RB1* exons 13 to 16. The presence of a single band and its subsequent Sanger-sequencing confirmed the presence of the mentioned exons in both subtypes (**Figure 12E**).


A
3%
1%
22%
53%
20%
RB1 Mutation type
frameshift indel
in-frame indel
splice site
nonsense
missense
B
p=0,0045
Somatic
Germline
Number of mutations
60
40
20
0
C1
C2
C
Subtype 1
p=0,003
# Mutations
5
0
DUF3452
Rb_A
Rb_B
C-terminal
0
200
400
600
800
928 aa
Subtype 2
Mutations
5
0
DUF3452
Rb_A
Rb_B
C-terminal
0
200
400
600
800
928aa

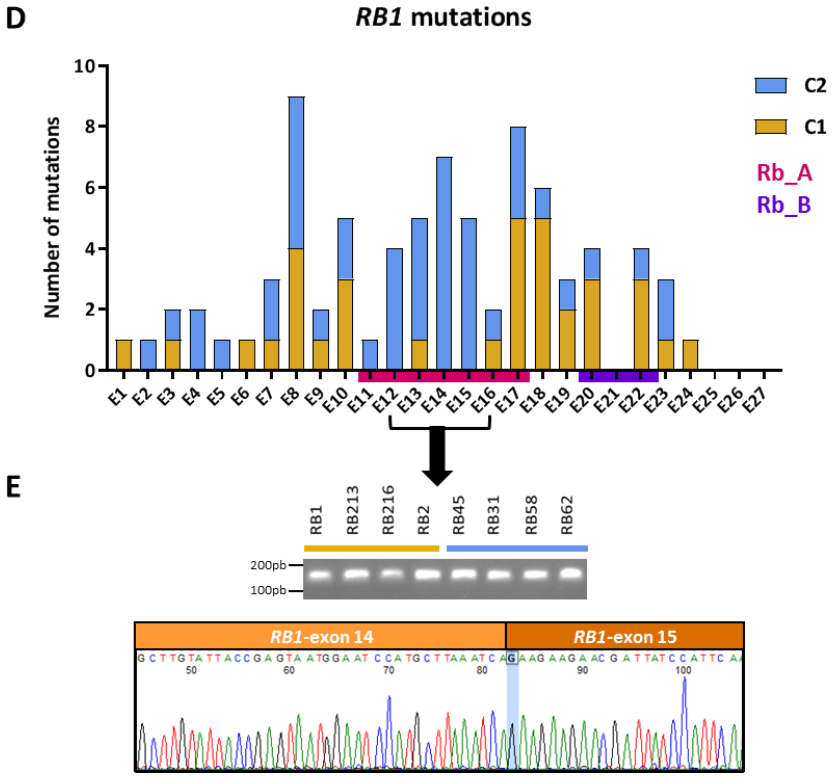


Figure 12. RB1 mutational spectrum in subtype 1 and subtype 2 retinoblastomas
A) *RB1* point mutation types and proportions across retinoblastomas. B) Distribution of germline and somatic *RB1* mutations is significantly different between tumor subtypes (Fisher's Exact test, p-value : 0.0045). C) Lollipop graph showing germline and somatic mutations in tumor subtypes. Mutations' distribution alongside the RB1 protein is significantly different between subtypes (p=0.003; Kolmogorov–Smirnov test). Dotted lines delimits the region in RB1 A domain where almost no mutations were detected in subtype 1. Subtype 1: 34 mutations, 27 patients. Subtype 2: 47 mutations, 40 patients. Graphs were generated with the cBioPortal visualization tools (http://www.cbioportal.org/). DUF3452: Domain of unknown function (DUF3452); Rb_A; Retinoblastoma-associated protein A domain; RB_B; Retinoblastoma-associated protein B domain; C-terminal: Retinoblastoma-associated protein C-terminal domain. D) Mutations' distribution across the *RB1* gene. Mutations occurring in exons 14 and 15, coding for A domain, were detected only in tumors of the subtype 2. E) RT-PCR of exons 13 to 16 and subsequent sequencing revealed the presence of these exons both tumor subtypes.

To further test our hypothesis, we analyzed a bigger C1-like cohort. We used an independent database of patients carrying germline point mutations (N=142) from the Genetic Service of the Curie Hospital[6]. We took this criterion as most of our C1 tumors carries a constitutional mutation. In this database, we found mutations in both exons 14 and 15. We next tried to analyze this series by subdividing the cohort by having received or not an enucleation. Interestingly, we found an enrichment of *RB1* mutations in exon 14 of non-enucleated patients, and a significantly difference in the distribution of exons 14 and 15' mutations between the enucleated vs the non-enucleated group of patients (p=0.0048, Fisher's Exact test) (**Figure 13**). As our analysis was based in tumoral DNA, this finding led us to suppose that the absence of mutations in exon 14 in our C1 series was because

[6] Patients included in this cohort were hereditary cases, harboring *RB1* germline mutations, and had received radiotherapy. Mutations were detected in the blood of patients (constitutional DNA).

patients with C1 tumors with mutations in exon 14 have not been enucleated. A larger series should be analyzed to confirm this finding and to answer this open question.

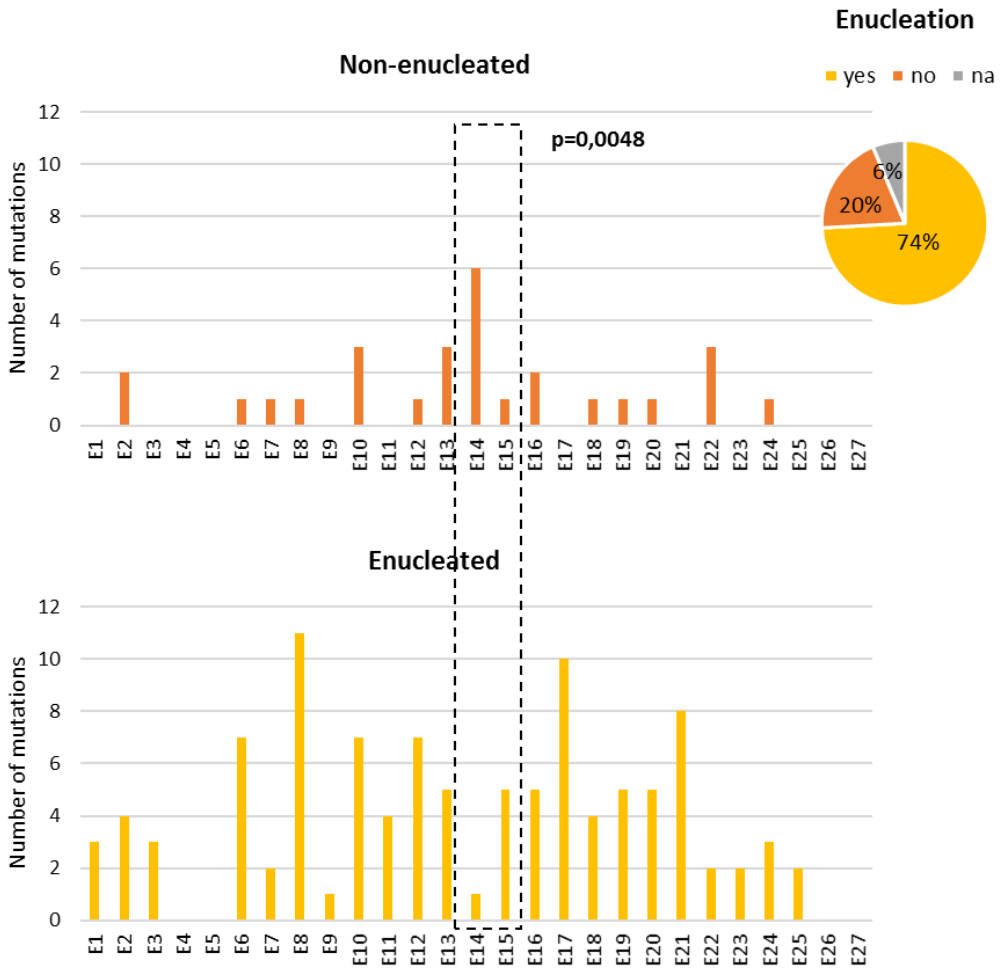


Figure 13. C1-like cohort of patients carrying RB1 germline point mutations
Mutations were found in both exons 14 and 15 but the distribution between enucleated and non-enucleated patients was significantly different (p=0.0048, Test Exact de Fisher). Non-enucleated patients were enriched in mutations occurring in the exon 14 of the *RB1* gene.

A NOVEL RECURRENT FUSION EVENT DISRUPTING *DACH1* IN RETINOBLASTOMA

For further investigation of the oncogenic events existing in retinoblastoma, we analyzed the RNA-sequencing of 34 tumor samples of our series, screening for fusion genes. We identified 33 fusion transcripts in eleven samples (**Table 9**, page 89). In 10 fusion transcripts, one of the two partners involved a non-coding RNA. Five out of the 33 fusions identified were interchromosomal, while the remaining 28 were intrachromosomal. Two tumor samples carried multiple intrachromosomal fusion transcripts (RB59, subtype2: ten on chromosome 1; RB50, subtype 1: nine on chromosome 13). Only one recurrent intrachromosomal fusion event was found in two tumor samples: RB50 (subtype 1) and RB39 (subtype 2). This fusion involved *DACH1* gene (located on chromosome 13) as a recurrent 5' partner of three long non-protein coding RNA (LINC).

In RB50, the fusion event was associated with a homozygous intragenic deletion of *DACH1* (data not shown). In this sample, *DACH1*-exon 1 (ENSE00003729171) was fused with two different long non-protein coding RNA: LINC01074-exon 2 (ENSE00001682921) and LINC01075-exon 2 (ENSE00001726291) (**Figure 14**). Both fusions were heterozygous, as confirmed by PCR amplification and Sanger-sequencing of *DACH1* exon1/exon2 junctions (**Figure 14B**). The predicted coding sequence of the fusion transcripts expected the appearance of a STOP codon, 54 and 9 amino acids after the fusion site, respectively (data not shown), probably disrupting normal function of the DACH1 protein.

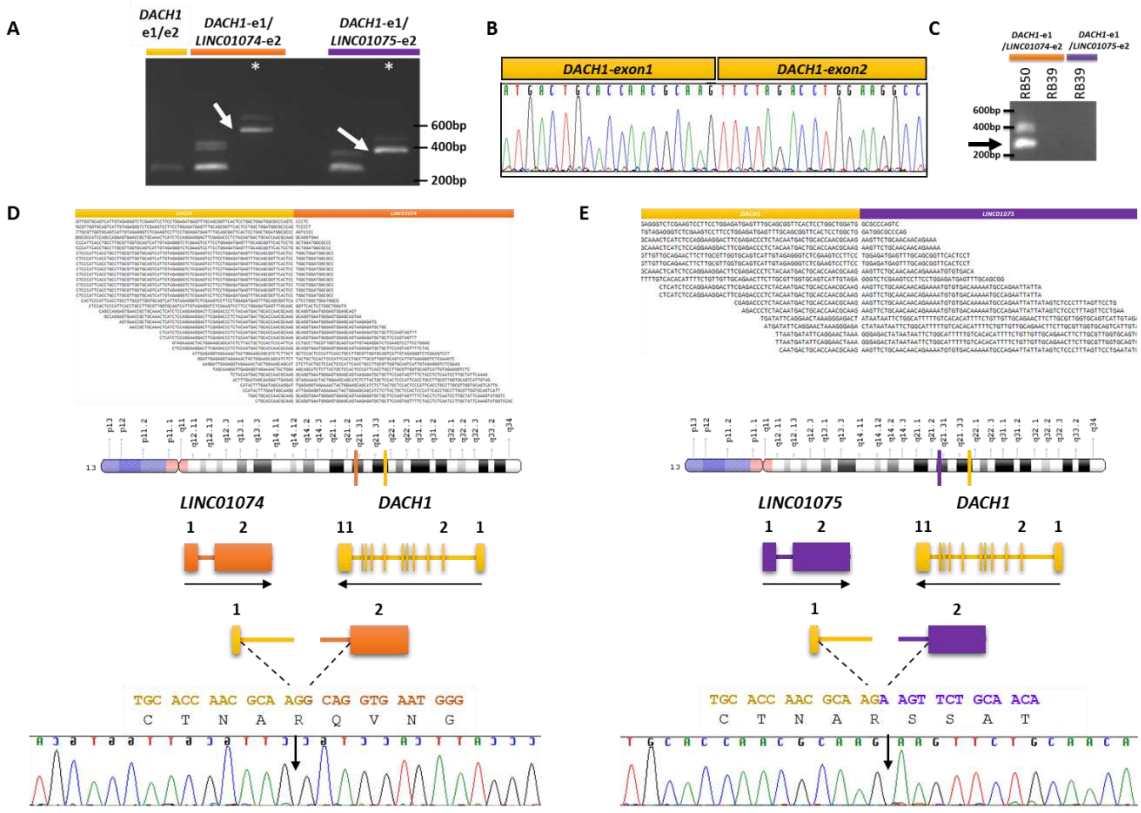


Figure 14. Structure of the DACH1-LINC fusions identified in sample RB50

A) RT-PCR amplification using specific primers to the DACH1-LINC01074 (orange) and the DACH1-LINC01075 (violet) fusions. White arrows indicate the amplified fusion transcript. RT-PCR amplification of DACH1 exons1/exon2 junction (yellow) revealed the heterozygous state of the fusions events detected. B) Sanger sequencing of wild type DACH1 exon1/exon2 junction. C) Specificity validation using primers to these fusions in another sample (RB39) with DACH1 fusions. Alignment to an *in silico* reconstruction of the (D) DACH1-LINC01074 and (E) DACH1-LINC01075 fusions, with reads spanning the junction site of the two genes (white vertical line). Yellow bar on top indicates exon 1 of *DACH1* gene, orange bar indicates the exon 2 of the LINC01074 and violet bar indicates exon 2 of the LINC01075. Chromosomal location of *DACH1,* and LINC01074/LINC01075 on 13q21.33 and 13q21.31, respectively. Genes are 9544kbp (LINC01074) and 9642kbp (LINC01075) apart (middle). Sanger sequencing confirmed both fusions in this tumor sample (bottom). Transcript: DACH1-202 (ENST00000613252.4, Chr13: 71,437,966-71,867,192 reverse strand. Gene LINC01074 (ENSG00000227611, Chr13: 62,321,305-62,322,398 forward strand). Gene LINC01075 (ENSG00000230142, Chr13: 62,212,577-62,249,947 forward strand).

In RB59 sample, two fusions involving *DACH1*-exon 1 (ENSE00003729171) with LINC00437-exon 1 (ENSE00001613832) and LINC00437-exon 2 (ENSE00001723883) were found (**Figure 15**). Both events were heterozygous, as confirmed by PCR amplification and Sanger-sequencing of *DACH1* exon1/exon2 junctions (**Figure 15B**). The predicted coding sequence of the fusion transcripts expected a shift in the coding sequence of the DACH1 protein (LINC00437-exon 1) and the appearance of a STOP codon 13 amino acids after the fusion point (LINC00437-exon 2) (data not shown), probably resulting in a defective protein.

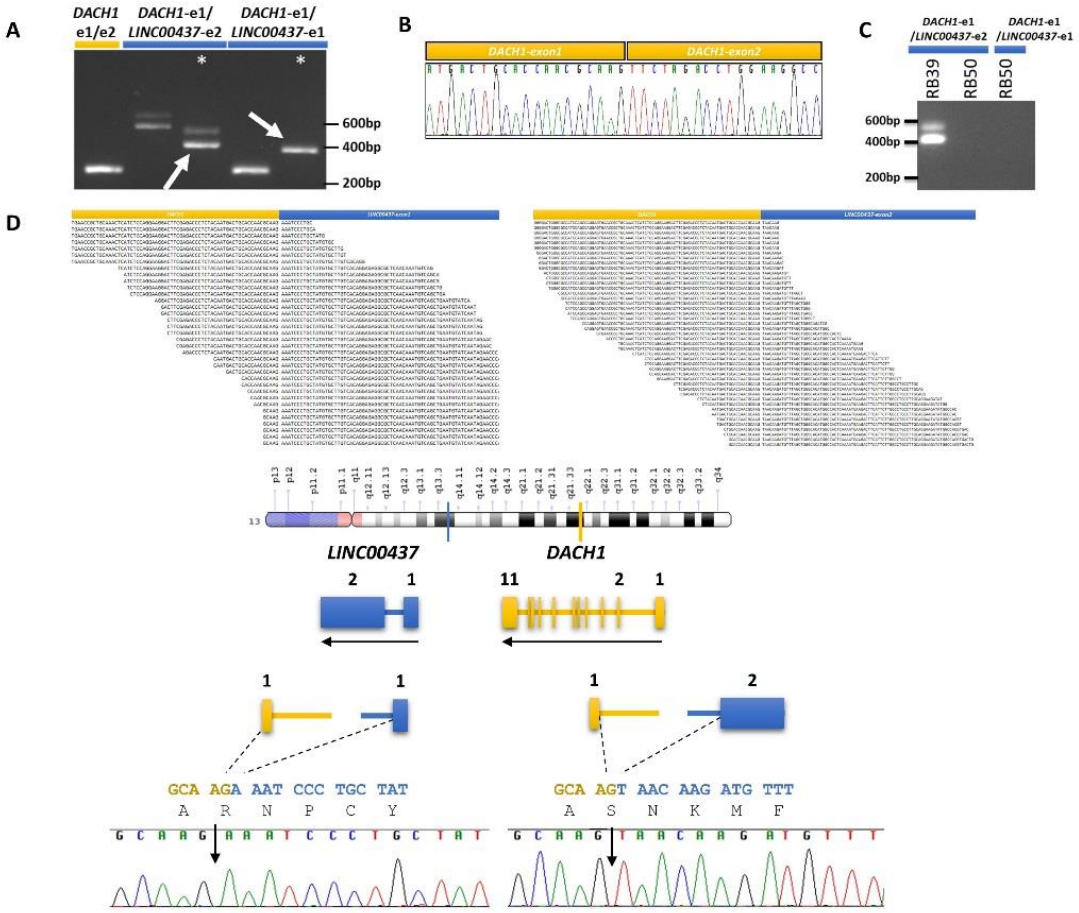


Figure 15. Structure of the DACH1-LINC fusion identified in sample RB39
A) RT-PCR amplification using specific primers to the fusion DACH1-LINC00437 exons 1 and 2, confirms the presence of the fusion event in sample RB39. White arrows indicates the amplified fusion transcript. In yellow is indicated the RT-PCR amplified product of wild type *DACH1* exons1/exon2 junction, revealing the heterozygous state of the fusions events detected. B) Sanger sequencing of the amplified wild type product DACH1 exon 1/exon 2. C) Specificity validation using RT-PCR specific primers to these fusions in another sample (RB50) with *DACH1* fusions. D) Alignment to an *in silico* reconstruction of the DACH1-LINC00437 exons 1 (left) and 2 (right) fusions, with reads spanning the junction site of the two genes (white vertical line) (top). Chromosomal location of *DACH1* and LINC00437 on 13q21.33 and 13q13.3, respectively. Genes are located 33321kbp apart (middle). Sanger sequencing confirmed the fusion events in the tumor sample (bottom). Transcript: DACH1-202 (ENST00000613252.4, Chr13: 71,437,966-71,867,192 reverse strand). Gene: LINC00437 (ENSG00000236354, Chr13: 38,533,343-38,545,299 reverse strand).

DACH1 encodes a chromatin-associated protein that is critically involved in retina development. Together with *EYA1* and *SIX6* integrates the retinal determination gene network (Pignoni et al., 1997). *DACH1* in combination with *SIX6* regulates proliferation of retinal and pituitary precursor cells by repressing cyclin-dependent kinase inhibitors (Li et al., 2002). *DACH1*-exon 2 codes for the conserved DACHbox-N domain, through which directly binds to specific chromatin DNA sequences, regulating gene transcription (Kim et al., 2002) (**Figure 16**). Besides, *DACH1* expression is lost in several human cancer and has been reported to act as a tumor suppressor gene (Liu et al., 2016; Mardon G, 1994; Watanabe et al., 2011; Wu et al., 2006, 2009).

Our results here described, involved recurrent fusion events between *DACH1*-exon 1 and a LINC gene fragment. These events replace the 3'-end coding region of *DACH1*, including exon 2 that codes for the DNA binding domain, potentially giving rise to a non-functional protein or to a protein with an aberrant function. Functional experimental analyses remain to be performed in order to determine a possible tumor suppressor role or a dominant negative effect of *DACH1* in retinoblastoma.

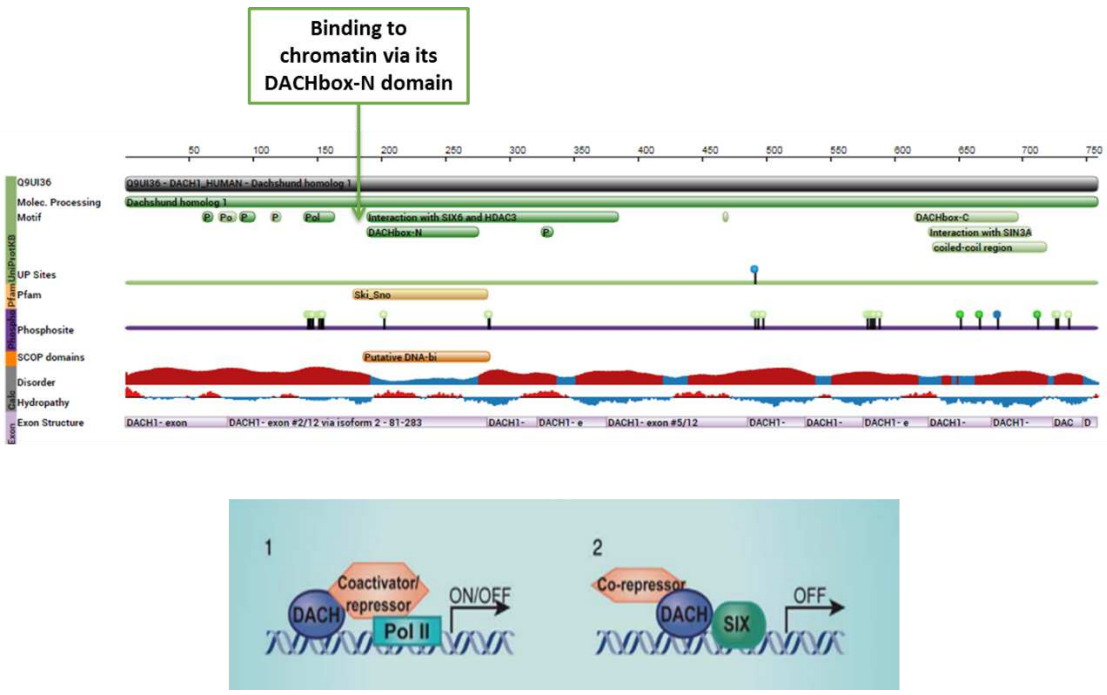


Figure 16. DACH1 protein
DACH1-exon 1 codes for the conserved DACHbox-N domain (top), through which binds to specific chromatin DNA sequences (bottom) regulating gene transcription. Image adapted from the PDB protein data bank and from Liu et al. 2016.

DISCUSSION AND CONCLUSIONS

MOLECULAR CLASSIFICATION OF HUMAN RETINOBLASTOMA

One of the main motivations for stratifying a cohort of patients of a given disease is to identify specific genes and signaling pathways involved in a given subtype, to a better understanding of the biology of the tumor itself and for the developing of new targeted treatments.

Retinoblastoma is no longer consider a homogeneous disease nevertheless, no consensus for its molecular stratification exist until today. Previous work of my group (unpublished, in preparation) have demonstrated the existence of two molecular subtypes of retinoblastoma, based on omics techniques. In an effort to enlarge the previous characterized series, we designed a 9-CpG methylation-based signature tool to classify thirty additional samples by assessing methylation by pyrosequencing. The use of this 9CpG-signature in combination with the omics-based classification, led us to the classification 102 retinoblastomas into two molecular subtypes with distinct molecular and clinical characteristics. From a clinical point of view, subtype 1 and subtype 2 tumors are significantly different regarding tumor laterality ($p=1,51x10^{-3}$, Chi^2 test), age at diagnosis ($p=2,13x10^{-9}$, Kruskal-wallis rank test), heritability of the disease (*RB1* germline mutations) ($p=7,68x10^{-4}$, Fisher's exact test), tumor growth pattern ($7,33x10^{-4}$, Chi^2 test), and presence of tumoral necrosis (p=0,0203, Chi^2 test). Other clinical parameters such as tumor diameter (p=0,2094, Kruskal-wallis rank test), optic nerve invasion (p=0,7467, Fisher's exact test), and choroidal and scleral invasion (p=0,6468, Fisher's exact test) are not significantly different between tumor subtypes (**Figure 17**). Molecular subtype 1 is enriched in bilateral patients being diagnosed at earlier ages (<18 months). This group of tumors is enriched in patients harboring *RB1* germline mutations, and mostly displays an exophytic tumoral growth patter (tumor growing into the subretinal space). In the other hand, the molecular subtype 2 is enriched in unilateral patients diagnosed at older ages (>18 months) with few cases presenting *RB1* germline mutations, and mostly displays endophytic tumoral growth pattern (tumor growing forward into the vitreous). Importantly, no significant differences within each molecular subtype exists regarding the median age at diagnosis, for patients with bilateral or unilateral tumors, nor by comparing heritable versus non-heritable retinoblastomas (data not shown).

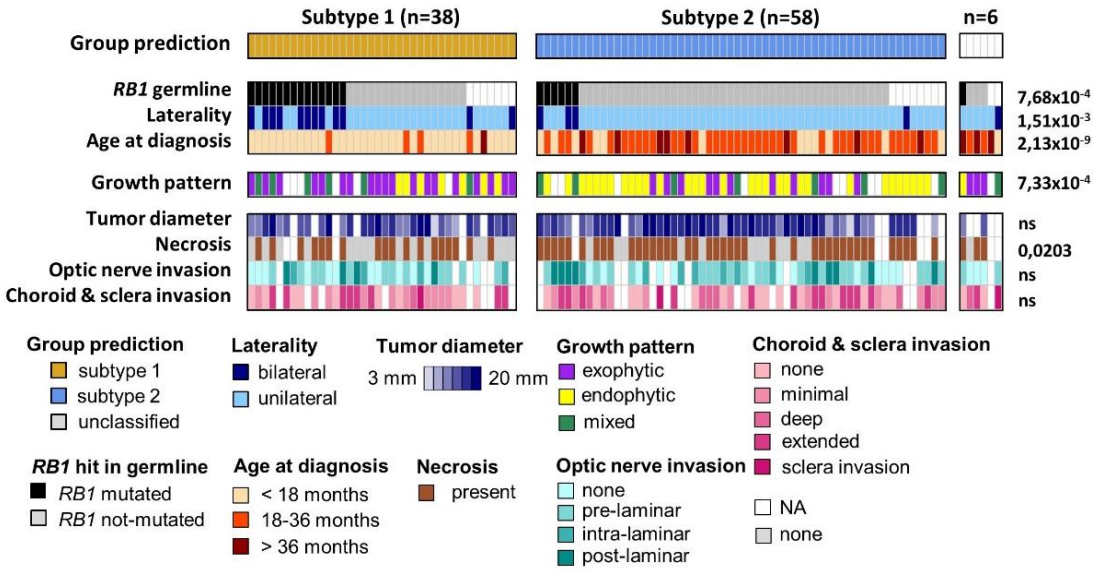


Figure 17. Final classification and main clinical differences between retinoblastoma subtypes
Significant differences between tumors subtypes exists regarding heritable constitutional *RB1* mutations, tumor laterality, age at diagnosis, tumor growth pattern, and presence of tumoral necrosis. Subtype 1 median age at diagnosis is 11 months, while for subtype 2 is 23.9 months. No differences within each molecular subtype exists regarding the median age at diagnosis, for patients with bilateral or unilateral tumors, nor by comparing heritable versus non-heritable retinoblastomas.

SOMATIC MUTATIONAL LANDSCAPE IN RETINOBLASTOMA

We explored the mutational landscape of our cohort seeking to discover new genes involved in retinoblastoma tumorigenesis, by whole exome sequencing of 71 tumoral and normal matched pairs, and by next-generation targeted sequencing of all exons coding for *BCOR* and *ARID1A* genes, the only two recurrently mutated genes in our series besides *RB1*.

Somatic mutations identified by WES were found in most tumors (89%, N=63/71), and corresponded to coding SNV (90%) and indels (10%), and were found in similar frequencies as that reported for a pan-cancer analysis of pediatric cancers (93% SNV and 7% indels) (Gröbner et al., 2018). Most SNV mutations were C>T substitutions, as found in most adult and childhood solid tumors (Gröbner et al., 2018; Ma et al., 2018). The prevalence of somatic mutations in our cohort (0.05 mutations per Mb) is in line with the low somatic mutation rates described for retinoblastoma and other pediatric cancers (between 0.02–0.49 mutations per Mb) (Gröbner et al., 2018) (**Figure 1**). These frequencies are more than 10 times lower to the reported mutations frequencies in adult cancers (0.28 and 8.15 mutations per Mb) (Kandoth et al., 2013).

Somatic non-recurrent mutations were found across 179 genes. No significant affected pathways were found to be involved in enrichment analysis. Allelic frequencies ranged from 13% to 100%, suggesting that these mutational events occurred at different moments during tumorigenesis.

Considering the two retinoblastoma subtypes, tumors from the subtype 2 had significantly more somatic mutations per sample than tumors from the subtype 1 (median of 1 vs 4 mutations). Besides, *ARID1A* and *BCOR* mutations were identified only in subtype 2. No differences in number of mutations were found across more advanced cases coming from the Garrahan Hospital and the series from Curie. Interestingly, the number of mutations per tumor was not correlated with the age at diagnosis of the patient, as could be expected for mutations occurring over time during tumorigenesis. Instead, these differences could reflect different susceptibilities of a (putative) distinct cell of origin in each subtype, needing less or more oncogenic events to oncogenic transformation.

BCOR and *ARID1A* were the only recurrently mutated genes found in our cohort, besides *RB1*. *BCOR* mutations haven been already identified in retinoblastoma at similar frequencies (10-13%) (Kooi et al., 2016; Zhang et al., 2012), while somatic *ARID1A* mutations has not been previously described. Kooi et al. (Kooi et al., 2016) identified somatic mutations on *CREBBP* in two out of the 72 tumors analyzed (3%), in similar frequencies that our *ARID1A* mutations (N=2/102, 2%). These findings highlights two important aspects. First, the three genes mentioned above are involved in chromatin remodeling, playing roles in transcriptional repression and activation (Gao et al., 2017; Gearhart et al., 2006; Kadoch and Crabtree, 2015), emphasizing the potential importance of epigenetics in retinoblastoma progression. Second, the importance of carrying out pan-cancer analysis or large-scale studies across bigger series, which can help to discover new recurrent genes in pediatric cancers such as retinoblastoma, with low somatic mutation rates.

RB1 GERMLINE AND SOMATIC MUTATIONS

RB1 point mutations or gene alterations (exon and gene deletions, and promotor hypermethylation) were identified in 90% of samples analyzed (N=92/102). One unilateral patient (RB222) with no detectable *RB1* mutation carried a *MYCN* amplification, and clinically presented extended choroidal and postlaminar optic nerve invasion, consistent with the aggressive histological features of $RB1^{+/+}$ $MYCN^{A}$ tumors (Rushlow et al., 2013). However, this patient had been diagnosed at 13.3 months, notably older that described in the literature (4.5months) for these group of patients (Rushlow et al., 2013).

The majority of *RB1* mutations are reported to be scattered throughout the gene, although several recurrent mutations and mutation hotspots exist and correspond to C to T transitions in CGA-arginine codons, in exons 8, 10, 11, 14, 15, 17, 18 and 23 (Harbour, 1998; Price et al., 2014; Valverde et al., 2005). Recurrent mutations found in our cohort correspond to these hotspots reported. In the majority of tumors, the second hit was a loss of the non-mutated gene (loss of heterozygosity, LOH)

(81%, N=42/52), in line with previous reports (Mol et al., 2014; Ottaviani et al., 2013; Price et al., 2014; Richter et al., 2003; Zhu et al., 1992).

Distribution of mutations alongside the *RB1* gene has so far been analyzed in terms of a single group of retinoblastomas, or separated according to laterality of the tumor, state of the mutation (germline, somatic) or if it was familial or not. In our cohort, we found a mixture of these characteristics in each molecular subtype, although tendencies and correlations do exist. For example, our subtype 1 is enriched in bilateral cases with germinal mutations but there are also unilateral and non-family cases that are classed together. When we separated our cohort in subtype 1 and subtype 2 tumors, the distribution of mutations was significantly different (p=0.003, **Figure 12**) and in addition, a region (Domain A) of the RB1 protein where there were virtually no mutations in the C1 group became apparent. We then analyzed *RB1* mutations in a larger germline mutated cohort and noticed a significant enrichment of *RB1* mutations in exon 14 of non-enucleated patients. We hypothesized that these findings could be explain by a relatively benignity of these mutations in the retinal cone-cell context of subtype 1 tumors, and the no need for surgery as the tumor responds well to treatment. In our cohort, as we analyzed DNA from tumor material, necessarily all patients had an enucleation, and that could be the explanation of why we did not find mutations in exon 14 in our C1 cohort of tumors. A larger series will be required to test this hypothesis and to analyze the *RB1* mutation distribution alongside the RB1 protein.

CHROMOSOMAL FUSION EVENTS DISRUPTING *DACH1*

Pediatric cancers differ from adult tumors, especially by their very low mutational rate. Therefore, their etiology could be explained in part by other oncogenic mechanisms such as chromosomal rearrangements, supporting the possible implication of fusion genes in the development of pediatric cancers (Dupain et al., 2017). Fusion genes result from chromosomal rearrangements leading to the juxtaposition of two previously separate genes localized on the same (intra-chromosomal) or two different (inter-chromosomal) chromosomes, and consequently, an abnormal activation or inactivation of one or both genes is observed.

Disrupting events targeting *DACH1* suggested a tumor suppressor role for this gene in retinoblastoma. *DACH1* encodes a transcription factor involved in retina development, first identified in Drosophila, and is reported to act as a tumor suppressor gene in various types of human cancer (Liu et al., 2016; Mardon G, 1994; Wu et al., 2006). Together with *EYA1* and *SIX6* integrates the retinal determination gene network. Mutations occurring in members of this gene network has been reported in retinoblastoma by other group (one somatic mutation in *EYA1* in a series of 71 tumor samples (Kooi et al., 2016) and by us: in our cohort one somatic mutation in *SIX6* (HSJD-RBT7) was detected. Once again, these findings emphasize the powerfulness that is acquired when analyzing

bigger sample cohorts as a whole. Besides, *DACH1* transcriptional activation function seems also to involve association of *CREBBP* (Wu et al., 2007), a gene found to be mutated in Kooi's cohort.

DACH1 has been reported to be involved in a fusion protein with PAX5 (t(9;13)(p12;q21) PAX5/DACH1) in B-cell acute lymphoblastic leukemia (Nebral et al., 2009). In this case, the predicted fusion protein contained the DNA binding paired domain of PAX5 (N-term) and the DACHbox-C of *DACH1* (C-term). The two recurrent fusion events identified in our study involved the N-ter of DACH1 protein, corresponding to *DACH1*-exon 1, and resulted in the replacement of its 3'-end coding region with a fragment of a LINC gene. *DACH1*-exon 2 (coding for the highly conserved DNA-binding domain) is replaced by the LINC sequence, potentially giving rise to a DACH1 protein with an aberrant function. Fusion genes affecting tumor suppressor genes, generally leads to inactivation, leading to cell transformation. Inactivation of the tumor suppressor gene can occur through different mechanisms: the fusion can either act as the second hit or lead to a dominant effect on the wild-type protein or even provoke haploinsufficiency of the disrupted protein (Ågerstam et al., 2007; Coyaud et al., 2010; Storlazzi et al., 2005). Functional experimental analyses remain to be performed in order to determine the functional meaning of this fusion event detected in retinoblastoma.

Table 1. Panel of the nine CpGs significantly differentially methylated selected to use for sample classification

CpG ID	CpG position	Wilcoxon test (p values)	C1	C2	FC C1vsC2	Chrom. position	Strand	Gene	Ref.Seq	CpG to gene
cg1	cg12750745	8,86E-14	0,129	0,554	-0,426	1p34.1	R			
cg2	cg08091439	1,16E-13	0,24	0,687	-0,447	1p13.3	R	AHCYL1	NM_006621	Body
cg3	cg23877497	1,51E-13	0,233	0,682	-0,449	6q25.3	F	TULP4	NM_020245	Body
cg6	cg20641531	2,22E-16	0,668	0,155	0,513	7p21.3	F	ICA1	NM_022307	TSS1500
cg8	cg10007051	2,50E-15	0,561	0,157	0,404	7q21.13	R			
cg9	cg07857792	3,72E-15	0,732	0,267	0,465	19p13.11	R	KCNN1	NM_002248	TSS1500
cg10	cg17341366	3,72E-15	0,66	0,199	0,461	2p25.1	F			
cg13	cg21214455	5,38E-15	0,651	0,165	0,486	15q23	F	SENP8	NM_145204	5UTR
cg14	cg10316527	5,38E-15	0,565	0,161	0,403	15p25.2	F			

FC: fold change; Ref Seq: sequence of reference; Chrom. Position: chromosome position; CpG to gene: position of the CpG analyzed respect to the gene

Table 2. Primers used for PCR amplification and (pyro) sequencing

Target ID	Forward (5'-3')	Reverse (5'-3')	Sequencing (5'-3')
cg1 (cg12750745)	AGTAGGTATGGGGGAAAATT	[B]-CCAATTACTCCAAAAATAACTTCTAATCC	GGGTTGTTAGTTTTTAGTTATG
cg2 (cg08091439)	AGGGTTAAATTATTTTTTGGTAGAGT	[B]-CACAACTAAAATCCAATTCCACAATC	GATTTAGTAGTTTGGGG
cg3 (cg23877497)	ATATTTGGTAAAAGTTAAGAGATGT	[B]-CATTAACCCAAACAACTTTTCATCAA	AAAAATGAGTTTGGAATAGTATA
cg6 (cg20641531)	ATGTGGAAATGAAATTTTAATGTAGTATGA	[B]-ACATAAAACTAACACTCCATCCATATT	AGTATGATTTTATTTTTAGTTATG
cg8 (cg10007051)	[B]-AGGGGTAGTTAAAATTTAGTAAGAAAA	CCCTTAACACTCAACATTTAAAAATAATAT	AAAAATTATTTCCCATCCTT
cg9 (cg07857792)	GTTTTTGAGGATTATTTTTTTTAGGGGTAT	[B]-ACCACCCTTTACCCAACTA	GGATTATTTTTTTTAGGGGTATA
cg10 (cg17341366)	TGTTGGGTGTTGATGTGATTG	[B]-AACAACCTCCCATCTTTCTAT	GTGGATATTATTTAGTAAGAGAG
cg13 (cg21214455)	GGTTAAGGTAGGAGAATGGTATGAA	[B]-TCCCATTTCCCAAACCAATTATTC	GGAGTTTGTAGTGAGT
cg14 (cg10316527)	[B]-TGTGTTTTTTTTTTGGGGGAGAA	ACCCCAATAAAATTACAAAAATCCAC	AATTACAAAAATCCACAAAATT
RB1-e13/16	GGGTTGTGTCGAAATTGGAT	TGTGGCCATTACAACCTCAA	both
DACH1-e1/LINC00437-e1	CAAAGTGGCTTCCTTCACG	TTGAATGTGATGTTTGAACTTGTG	both
DACH1-e1/LINC00437-e2	ACGGTCTACACCAAGCTGAA	ACTATGGCCTTTCCCCTCAT	both
DACH1-e1/LINC01074-e2	CAAAGTGGCTTCCTTCACG	AATGGCGGTGCTACTCAAAC	both
DACH1-e1/LINC01075-e2	TGCAAAATGGTGGATCTGAG	GGGAGACTATAATAATTCTGGCATTT	both
DACH1-e1/e2	CTGCACCAACGCAAGTTCTA	TGGTGGAATTATCCCAGGAG	both

[B]- : biotin

Table 3. Clinical data of the 102 primary retinoblastoma's cohort

ID sample	Center	Sex	Age at diagnosis (months)	Laterality	Germline *RB1* mutation	Familial	Treatment prior enucleation	Growth	Tumor diameter (mm)	Necrosis	Optic nerve invasion	Choroid and sclera invasion	Anterior segment invasion	R-E staging (right,left)
RB1	Curie	male	11,7	bilateral	yes	yes	no	exophytic	11	no	no	no	none	3,5
RB2	Curie	male	7,6	unilateral	yes	no	no	mixed	12	yes	no	choroid_minimal	none	5
RB3	Curie	female	37,2	unilateral	no	no	no	endophytic	13	yes	intralaminar	choroid_extended	NA	5
RB4	Curie	female	1,7	bilateral	yes	no	no	exophytic	15	no	no	no	NA	3,5
RB6	Curie	male	15,1	unilateral	no	no	no	exophytic	15	no	prelaminar	choroid_extended	none	5
RB7	Curie	male	28,3	unilateral	no	no	no	endophytic	11	no	no	choroid_deep	none	5
RB9	Curie	female	7,6	unilateral	no	no	no	NA	NA	no	postlaminar	choroid_extended	none	5
RB10	Curie	male	9,4	unilateral	no	no	no	mixed	15	no	intralaminar	choroid_minimal	yes	5
RB11	Curie	male	6,2	bilateral	Mosaicism	no	no	mixed	19	yes	prelaminar	choroid_extended	none	3,5
RB13	Curie	female	17,0	unilateral	no	no	no	endophytic	17	yes	prelaminar	no	none	5
RB14	Curie	male	16,3	unilateral	no	no	no	endophytic	15	yes	no	choroid_deep	none	5
RB15	Curie	male	25,8	unilateral	no	no	no	endophytic	17	yes	prelaminar	choroid_minimal	none	5
RB21	Curie	male	45,5	unilateral	no	no	no	NA	20	no	NA	NA	NA	5
RB22	Curie	female	14,8	bilateral	yes	no	yes[a]	mixed	15	yes	NA	NA	NA	2,5
RB23	Curie	male	18,1	bilateral	NA	no	no	mixed	17	yes	NA	NA	NA	1,5
RB24	Curie	female	10,8	unilateral	no	no	no	exophytic	17	no	no	choroid_extended	NA	5
RB25	Curie	female	5,0	unilateral	no	no	no	exophytic	18	yes	no	no	none	5
RB27	Curie	female	27,5	unilateral	no	no	no	endophytic	NA	no	NA	NA	NA	NA
RB28	Curie	female	12,3	unilateral	no	no	no	exophytic	13	yes	prelaminar	NA	none	5
RB30	Curie	female	9,5	unilateral	NA	no	no	exophytic	13	no	no	no	none	5

RB31	Curie	female	21,2	unilateral	NA	no	no	endophytic	17	yes	no	no	none	5
RB32	Curie	female	26,7	unilateral	no	no	no	endophytic	13	yes	prelaminar	no	none	5
RB33	Curie	male	43,0	unilateral	NA	no	no	endophytic	NA	no	NA	NA	NA	5
RB34	Curie	female	14,6	bilateral	yes	yes	no	exophytic	12	no	NA	NA	NA	3,5
RB35	Curie	male	5,4	unilateral	no	no	no	exophytic	15	yes	prelaminar	choroid_minimal	none	5
RB37	Curie	male	29,3	unilateral	no	no	no	endophytic	12	yes	no	no	none	5
RB38	Curie	female	21,2	unilateral	no	no	no	endophytic	18	yes	intralaminar	choroid_minimal	none	5
RB39	Curie	female	21,1	unilateral	no	no	no	exophytic	20	yes	NA	NA	NA	5
RB40	Curie	female	8,4	unilateral	NA	no	no	exophytic	17	yes	NA	NA	NA	5
RB41	Curie	male	38,9	unilateral	no	no	no	endophytic	15	yes	no	choroid_extended_and_sclera	none	5
RB42	Curie	female	55,0	unilateral	no	no	no	exophytic	20	yes	NA	NA	NA	5
RB43	Curie	male	21,5	unilateral	no	no	no	mixed	16	yes	no	choroid_extended	none	5
RB44	Curie	female	14,2	unilateral	NA	no	no	endophytic	14	no	prelaminar	choroid_extended	none	5
RB45	Curie	male	21,6	unilateral	no	no	no	exophytic	15	no	intralaminar	NA	NA	5
RB46	Curie	female	38,6	unilateral	no	no	no	endophytic	20	yes	NA	NA	NA	5
RB47	Curie	male	6,5	unilateral	NA	no	no	exophytic	17	no	intralaminar	choroid_extended	none	5
RB48	Curie	female	19,1	unilateral	no	no	no	endophytic	15	yes	intralaminar	no	NA	5
RB49	Curie	male	11,2	unilateral	no	no	no	endophytic	10	no	no	no	none	5
RB50	Curie	female	20,3	unilateral	no	no	no	endophytic	10	yes	prelaminar	choroid_minimal	none	5
RB51	Curie	female	17,8	unilateral	no	no	no	endophytic	19	no	prelaminar	choroid_deep	none	5
RB52	Curie	female	13,5	unilateral	no	no	no	exophytic	15	no	no	choroid_deep	none	5
RB54	Curie	male	21,8	unilateral	no	no	no	exophytic	17	yes	prelaminar	choroid_deep	none	5
RB55	Curie	female	34,6	unilateral	yes	no	no	endophytic	13	yes	prelaminar	no	none	5

RB56	Curie	male	19,8	unilateral	no	no	no	exophytic	15	yes	prelaminar	choroid_deep	none	5
RB57	Curie	male	30,9	unilateral	NA	no	no	endophytic	17	yes	no	choroid_deep	none	5
RB58	Curie	female	28,3	unilateral	no	no	no	endophytic	8	yes	intralaminar	no	none	5
RB59	Curie	male	33,9	unilateral	no	no	no	exophytic	18	yes	prelaminar	choroid_minimal	NA	5
RB60	Curie	male	33,0	unilateral	no	no	no	exophytic	NA	no	no	choroid_deep	none	5
RB61	Curie	female	73,8	unilateral	NA	no	no	NA	NA	NA	NA	NA	NA	NA
RB62	Curie	female	24,7	unilateral	no	no	no	mixed	15	yes	intralaminar	NA	none	5
RB63	Curie	female	12,5	unilateral	yes	yes	no	NA	14	NA	postlaminar	choroid_extended	none	NA
RB64	Curie	male	23,9	unilateral	no	no	no	NA	17	yes	prelaminar	no	none	5
RB109	Curie	female	15,9	unilateral	Mosaicism	no	no	NA	NA	NA	intralaminar	no	none	5
RB111	Curie	female	33,0	unilateral	no	NA	no	endophytic	18	no	no	choroid_extended	none	5
RB200	Curie	male	31,2	unilateral	no	no	no	endophytic	15	no	prelaminar	no	none	5
RB202	Curie	female	23,9	unilateral	no	no	no	endophytic	15	no	prelaminar	no	none	5
RB203	Curie	male	29,7	unilateral	no	no	no	endophytic	19	yes	intralaminar	choroid_extended_and_sclera	none	5
RB204	Curie	female	55,1	unilateral	no	no	no	exophytic	NA	yes	no	choroid_extended	none	5
RB205	Curie	female	33,4	unilateral	no	no	no	exophytic	15	yes	intralaminar	NA	NA	5
RB206	Curie	female	13,0	unilateral	no	no	no	exophytic	20	no	no	choroid_minimal	none	5
RB208	Curie	female	31,7	unilateral	no	no	no	exophytic	13	yes	no	no	none	5
RB209	Curie	female	19,1	unilateral	no	no	no	endophytic	12	no	no	no	none	5
RB211	Curie	male	40,8	unilateral	no	no	no	endophytic	18	no	NA	NA	NA	5
RB212	Curie	male	29,1	unilateral	no	no	no	exophytic	15	yes	no	choroid_extended	none	5
RB213	Curie	female	13,1	bilateral	yes	no	no	NA	13	yes	prelaminar	no	none	4,5
RB215	Curie	female	15,5	unilateral	no	no	no	endophytic	19	no	prelaminar	no	none	5

RB216	Curie	male	10,3	bilateral	yes	no	no	mixed	14	no	no	NA	NA	1,5
RB217	Curie	female	10,1	bilateral	yes	no	no	exophytic	NA	yes	prelaminar	choroid_minimal	NA	3,5
RB218	Curie	male	2,1	bilateral	yes	no	no	exophytic	13	yes	prelaminar	NA	none	5,1
RB219	Curie	male	27,9	unilateral	yes	no	no	mixed	20	yes	no	choroid_minimal	none	5
RB220	Curie	female	17,5	unilateral	no	no	no	endophytic	15	no	intralaminar	choroid_minimal	none	5
RB221	Curie	male	15,0	bilateral	NA	no	yes[b]	exophytic	14	no	NA	NA	NA	5,5
RB222	Curie	male	13,3	unilateral	no	no	no	mixed	20	yes	postlaminar	choroid_extended	none	5
RB223	Curie	male	22,9	unilateral	no	no	no	exophytic	17	yes	prelaminar	choroid_extended	none	5
RB224	Curie	male	20,6	bilateral	NA	no	no	endophytic	16	yes	NA	NA	NA	5,5
RB225	Curie	male	19,4	unilateral	NA	no	no	endophytic	15	yes	NA	NA	NA	5
RB300	Curie	female	41,3	unilateral	NA	no	no	endophytic	NA	NA	prelaminar	choroid_minimal	none	5
RB304	Curie	female	23,9	unilateral	NA	no	no	endophytic	NA	NA	prelaminar	choroid_extended	NA	5
RB590	Garrahan	female	16,7	unilateral	yes	no	no	NA	15	yes	postlaminar	choroid_minimal	none	5
RB593	Garrahan	male	11,2	unilateral	no	yes	no	exophytic	8	yes	postlaminar	choroid_minimal	none	5
RB598	Garrahan	male	33,5	unilateral	no	no	no	NA	9	yes	postlaminar	choroid_minimal	none	5
RB603	Garrahan	male	4,3	unilateral	no	no	no	exophytic	6	yes	postlaminar	choroid_minimal	none	5
RB617	Garrahan	male	23,7	unilateral	NA	no	no	NA	13	yes	postlaminar	no	none	5
RB625	Garrahan	male	0,9	bilateral	yes	yes	no	NA	NA	NA	no	no	yes	5, NA
RB630	Garrahan	female	115,9	unilateral	yes	no	no	endophytic	10	yes	prelaminar	no	none	5
RB632	Garrahan	male	27,1	unilateral	no	no	no	NA	10	yes	prelaminar	choroid_extended	yes	5
RB634	Garrahan	male	14,6	unilateral	no	no	no	endophytic	13	yes	prelaminar	choroid_minimal	none	5
RB635	Garrahan	female	27,6	unilateral	NA	no	no	endophytic	4	yes	prelaminar	choroid_extended	none	5
RB647	Garrahan	male	85,4	unilateral	no	no	no	exophytic	15	yes	no	choroid_extended	none	5
RB659	Garrahan	female	20,0	unilateral	no	no	no	mixed	12	yes	prelaminar	no	none	5

RB663	Garrahan	male	1,8	unilateral	NA	NA	no	NA	12	yes	prelaminar	choroid_minimal	NA	5
RB671	Garrahan	male	14,4	unilateral	no	NA	no	exophytic	7	yes	NA	no	NA	5
RB704	Garrahan	female	28,8	unilateral	no	no	no	NA	12	yes	postlaminar	choroid_extended	none	5
RB707	Garrahan	female	22,8	unilateral	yes	no	no	NA	13	yes	postlaminar	choroid_extended	none	5
RB714	Garrahan	male	4,6	bilateral	yes	no	no	exophytic	12	yes	postlaminar	choroid_extended	none	NA, 5
RB715	Garrahan	female	25,1	unilateral	no	no	no	NA	NA	NA	no	choroid_minimal	yes	5
RB716	Garrahan	male	31,4	bilateral	yes	no	no	endophytic	10	yes	postlaminar	choroid_extended	none	NA, 5
HSJD-RBT2	Sant Joan Déu	male	7,0	bilateral	NA	no	yes[c]	mixed	NA	NA	postlaminar	choroid_minimal	none	5,NA
HSJD-RBT3	Sant Joan Déu	male	1,3	bilateral	NA	no	yes[d]	mixed	NA	NA	prelaminar	choroid_extended_and_sclera	none	4,NA
HSJD-RBT7	Sant Joan Déu	female	5,7	unilateral	no	no	no	mixed	NA	NA	prelaminar	choroid_minimal	none	5
HSJD-RBT8	Sant Joan Déu	female	16,0	unilateral	no	no	yes[c]	endophytic	NA	NA	no	no	none	5
HSJD-RBT9	Sant Joan Déu	female	8,2	unilateral	no	no	yes[e]	endophytic	NA	NA	prelaminar	no	none	5

R-E: Reese-Ellsworth staging (right,left)

Table 4. Technologies used for the molecular characterization of 102 primary retinoblastomas

ID sample	Whole Exome Sequencing	Target sequencing	Transcriptome (array)	RNA seq	Methylome (array)	Pyroseq	Copy number variation (array)
RB1	normal and tumoral	no	AffyU133plus2.0	yes	Illumina450K	yes	Curie3K_BAC
RB2	normal and tumoral	no	AffyU133plus2.0	no	Illumina450K	no	Illumina370K_SNP
RB3	normal and tumoral	no	no	no	Illumina450K	no	Illumina370K_SNP
RB4	normal and tumoral	no	AffyU133plus2.0	yes	Illumina450K	no	Illumina370K_SNP
RB6	no	tumoral	AffyU133plus2.0	yes	Illumina450K	yes	Illumina370K_SNP
RB7	normal and tumoral	no	AffyU133plus2.0	yes	Illumina450K	no	Illumina370K_SNP
RB9	no	tumoral	AffyU133plus2.0	yes	Illumina450K	no	Curie3K_BAC
RB10	normal and tumoral	no	AffyU133plus2.0	yes	Illumina450K	yes	Illumina370K_SNP
RB11	normal and tumoral	no	AffyU133plus2.0	yes	Illumina450K	yes	Curie3K_BAC
RB13	normal and tumoral	no	no	no	no	yes	Curie3K_BAC
RB14	normal and tumoral	no	AffyU133plus2.0	yes	Illumina450K	yes	Illumina370K_SNP
RB15	normal and tumoral	no	AffyU133plus2.0	no	Illumina450K	no	Curie3K_BAC
RB21	normal and tumoral	tumoral	AffyU133plus2.0	yes	Illumina450K	yes	Illumina370K_SNP
RB22	no	no	AffyU133plus2.0	no	no	yes	Curie3K_BAC
RB23	no	tumoral	AffyU133plus2.0	yes	Illumina450K	no	Illumina370K_SNP
RB24	no	tumoral	AffyU133plus2.0	yes	Illumina450K	yes	Illumina370K_SNP
RB25	normal and tumoral	no	AffyU133plus2.0	yes	Illumina450K	no	Curie3K_BAC
RB27	no	tumoral	AffyU133plus2.0	no	Illumina450K	yes	Illumina370K_SNP
RB28	normal and tumoral	no	AffyU133plus2.0	yes	Illumina450K	no	Illumina370K_SNP
RB30	no	tumoral	no	no	Illumina450K	no	Illumina370K_SNP
RB31	no	normal and tumoral	AffyU133plus2.0	yes	Illumina450K	no	Illumina370K_SNP
RB32	normal and tumoral	no	AffyU133plus2.0	no	no	no	Illumina370K_SNP
RB33	no	no	AffyU133plus2.0	no	no	no	Curie3K_BAC
RB34	normal and tumoral	no	AffyU133plus2.0	yes	Illumina450K	no	Illumina370K_SNP
RB35	no	no	AffyU133plus2.0	yes	no	yes	Illumina370K_SNP
RB37	no	normal and tumoral	AffyU133plus2.0	no	Illumina450K	no	Curie3K_BAC
RB38	normal and tumoral	tumoral	AffyU133plus2.0	yes	Illumina450K	yes	Illumina370K_SNP
RB39	normal and tumoral	no	AffyU133plus2.0	yes	Illumina450K	no	Curie3K_BAC
RB40	no	tumoral	AffyU133plus2.0	no	Illumina450K	no	Curie3K_BAC
RB41	normal and tumoral	tumoral	AffyU133plus2.0	yes	Illumina450K	yes	Illumina370K_SNP
RB42	normal and tumoral	no	AffyU133plus2.0	yes	Illumina450K	no	Illumina370K_SNP
RB43	no	no	AffyU133plus2.0	yes	Illumina450K	no	Illumina370K_SNP
RB44	no	no	AffyU133plus2.0	no	no	yes	Curie3K_BAC
RB45	normal and tumoral	no	AffyU133plus2.0	no	Illumina450K	no	Illumina370K_SNP

RB46	normal and tumoral	no	AffyU133plus2.0	yes	Illumina450K	yes	Illumina370K_SNP
RB47	no	no	AffyU133plus2.0	no	no	no	Curie3K_BAC
RB48	no	normal and tumoral	AffyU133plus2.0	yes	Illumina450K	no	Curie3K_BAC
RB49	normal and tumoral	no	AffyU133plus2.0	yes	Illumina450K	no	Curie3K_BAC
RB50	normal and tumoral	no	AffyU133plus2.0	yes	Illumina450K	yes	Illumina370K_SNP
RB51	normal and tumoral	no	AffyU133plus2.0	yes	Illumina450K	no	Illumina370K_SNP
RB52	normal and tumoral	no	AffyU133plus2.0	yes	Illumina450K	no	Illumina370K_SNP
RB54	no	normal and tumoral	AffyU133plus2.0	yes	Illumina450K	no	Curie3K_BAC
RB55	normal and tumoral	tumoral	no	no	no	yes	Curie3K_BAC
RB56	normal and tumoral	no	AffyU133plus2.0	yes	Illumina450K	no	Illumina370K_SNP
RB57	normal and tumoral	no	AffyU133plus2.0	yes	Illumina450K	no	Illumina370K_SNP
RB58	no	normal and tumoral	AffyU133plus2.0	no	Illumina450K	no	Curie3K_BAC
RB59	no	normal and tumoral	AffyU133plus2.0	yes	Illumina450K	yes	Illumina370K_SNP
RB60	normal and tumoral	no	AffyU133plus2.0	no	Illumina450K	no	Illumina370K_SNP
RB61	no	tumoral	AffyU133plus2.0	no	Illumina450K	no	Curie3K_BAC
RB62	normal and tumoral	no	AffyU133plus2.0	yes	Illumina450K	no	Illumina370K_SNP
RB63	no	tumoral	AffyU133plus2.0	yes	Illumina450K	yes	Illumina370K_SNP
RB64	no	normal and tumoral	no	no	Illumina450K	no	Affymetrix_CytoScan
RB109	normal and tumoral	no	no	no	Illumina450K	no	Illumina370K_SNP
RB111	normal and tumoral	no	no	no	Illumina450K	no	Curie3K_BAC
RB200	normal and tumoral	no	no	no	Illumina450K	no	Illumina370K_SNP
RB202	normal and tumoral	no	no	no	no	yes	Illumina370K_SNP
RB203	normal and tumoral	no	no	no	Illumina450K	no	Illumina370K_SNP
RB204	normal and tumoral	no	no	no	no	yes	Illumina370K_SNP
RB205	normal and tumoral	tumoral	no	no	no	yes	Illumina370K_SNP
RB206	normal and tumoral	no	no	no	Illumina450K	no	Illumina370K_SNP
RB208	normal and tumoral	no	no	no	Illumina450K	no	Illumina370K_SNP
RB209	normal and tumoral	normal and tumoral	no	no	Illumina450K	no	Illumina370K_SNP
RB211	no	normal and tumoral	AffyU133plus2.0	no	Illumina450K	no	Illumina370K_SNP
RB212	no	no	AffyU133plus2.0	no	Illumina450K	no	Curie5K_BAC
RB213	normal and tumoral	no	AffyU133plus2.0	no	Illumina450K	no	Curie5K_BAC
RB215	normal and tumoral	no	no	no	no	yes	Illumina370K_SNP
RB216	no	normal and tumoral	AffyU133plus2.0	no	Illumina450K	no	Curie5K_BAC
RB217	normal and tumoral	normal and tumoral	AffyU133plus2.0	no	Illumina450K	yes	Curie5K_BAC
RB218	normal and tumoral	no	no	no	Illumina450K	no	Illumina370K_SNP

RB219	normal and tumoral	no	AffyU133plus2.0	no	Illumina450K	no	Illumina370K_SNP
RB220	no	normal and tumoral	AffyU133plus2.0	no	Illumina450K	no	Illumina370K_SNP
RB221	no	no	AffyU133plus2.0	no	Illumina450K	no	Curie5K_BAC
RB222	normal and tumoral	no	AffyU133plus2.0	no	Illumina450K	no	Illumina370K_SNP
RB223	no	normal and tumoral	AffyU133plus2.0	no	Illumina450K	no	Illumina370K_SNP
RB224	no	tumoral	AffyU133plus2.0	yes	Illumina450K	no	Illumina370K_SNP
RB225	no	tumoral	AffyU133plus2.0	no	Illumina450K	no	Illumina370K_SNP
RB300	no	tumoral	no	no	Illumina450K	no	Illumina370K_SNP
RB304	normal and tumoral	no	no	no	Illumina450K	no	Illumina370K_SNP
RB590	normal and tumoral	no	no	no	no	yes	Affymetrix_CytoScan
RB593	normal and tumoral	no	no	no	no	yes	Affymetrix_CytoScan
RB598	normal and tumoral	no	no	no	no	yes	Affymetrix_CytoScan
RB603	normal and tumoral	no	no	no	no	yes	Affymetrix_CytoScan
RB617	normal and tumoral	tumoral	no	no	no	yes	Affymetrix_CytoScan
RB625	normal and tumoral	no	no	no	no	yes	Affymetrix_CytoScan
RB630	normal and tumoral	no	no	no	no	yes	no
RB632	normal and tumoral	no	no	no	no	yes	Affymetrix_CytoScan
RB634	normal and tumoral	no	no	no	no	yes	Affymetrix_CytoScan
RB635	normal and tumoral	tumoral	no	no	no	yes	Affymetrix_CytoScan
RB647	normal and tumoral	no	no	no	no	yes	no
RB659	normal and tumoral	tumoral	no	no	no	yes	Affymetrix_CytoScan
RB663	normal and tumoral	no	no	no	no	yes	Affymetrix_CytoScan
RB671	normal and tumoral	no	no	no	no	yes	Affymetrix_CytoScan
RB704	normal and tumoral	tumoral	no	no	no	yes	Affymetrix_CytoScan
RB707	normal and tumoral	no	no	no	no	yes	Affymetrix_CytoScan
RB714	normal and tumoral	no	no	no	no	yes	Affymetrix_CytoScan
RB715	normal and tumoral	tumoral	no	no	no	yes	Affymetrix_CytoScan
RB716	normal and tumoral	tumoral	no	no	no	yes	Affymetrix_CytoScan
HSJD-RBT2	normal and tumoral	no	no	no	no	yes	no
HSJD-RBT3	normal and tumoral	no	no	no	no	yes	no
HSJD-RBT7	normal and tumoral	normal and tumoral	no	no	no	yes	no
HSJD-RBT8	normal and tumoral	no	no	no	no	yes	no
HSJD-RBT9	normal and tumoral	no	no	no	no	yes	no

RNA seq: RNA sequencing; Pyroseq: pyrosequencing

Table 5. Final classification of 102 retinoblastomas

Sample ID	Transcriptome cluster	Methylome cluster	CNV cluster	Cluster of clusters	Centroid-based reclassification	Pyroseq. signature	Final subtype
RB1	1	1	1	1	no change	C1 validation set	**C1**
RB2	1	1	1	1	no change	NA	**C1**
RB3	no	2	2	2	no change	NA	**C2**
RB4	1	1	1	1	no change	NA	**C1**
RB6	1	1	1	1	no change	C1 validation set	**C1**
RB7	2	2	3	2	no change	NA	**C2**
RB9	1	1	1	1	no change	NA	**C1**
RB10	1	1	1	1	no change	C1 validation set	**C1**
RB11	1	1	1	1	no change	C1 validation set	**C1**
RB13	no	no	no	no	no	C2	**C2**
RB14	2	2	3	2	no change	C2 validation set	**C2**
RB15	2	2	2	2	no change	NA	**C2**
RB21	2	2	2	2	no change	C2 validation set	**C2**
RB22	2	no	1	3	2	NA	**C2**
RB23	1	2	3	3	1	no	**C1**
RB24	1	1	4	1	no change	C1 validation set	**C1**
RB25	1	1	4	1	no change	NA	**C1**
RB27	2	2	5	2	no change	C2 validation set	**C2**
RB28	1	1	4	1	no change	no	**C1**
RB30	no	1	4	1	no change	no	**C1**
RB31	2	2	2	2	no change	no	**C2**
RB32	2	no	2	2	no change	no	**C2**
RB33	1	no	5	3	1	no	**C1**
RB34	1	1	3	1	no change	no	**C1**
RB35	1	no	1	1	no change	NA	**C1**
RB37	2	2	4	2	no change	no	**C2**
RB38	2	2	2	2	no change	C2 validation set	**C2**
RB39	2	2	2	2	no change	no	**C2**
RB40	1	1	4	1	no change	no	**C1**
RB41	2	2	3	2	no change	C2 validation set	**C2**
RB42	2	2	2	2	no change	no	**C2**
RB43	2	2	5	2	no change	no	**C2**
RB44	1	no	1	1	no change	C1	**C1**
RB45	2	2	5	2	no change	no	**C2**
RB46	2	2	3	2	no change	C2 validation set	**C2**
RB47	1	no	4	1	no change	no	**C1**

RB48	2	2	5	2	no change	no	**C2**
RB49	1	1	4	1	no change	no	**C1**
RB50	1	2	1	3	1	C1 validation set	**C1**
RB51	2	2	4	2	no change	no	**C2**
RB52	2	1	1	3	1	no	**C1**
RB54	2	2	5	2	no change	no	**C2**
RB55	no	no	no	no	no	C2	**C2**
RB56	2	2	5	2	no change	no	**C2**
RB57	2	2	4	2	no change	no	**C2**
RB58	2	2	4	2	no change	no	**C2**
RB59	2	2	5	2	no change	C2 validation set	**C2**
RB60	1	2	5	3	no change	no	**NA**
RB61	1	2	3	3	no change	no	**NA**
RB62	2	2	2	2	no change	no	**C2**
RB63	1	1	4	1	no change	C1 validation set	**C1**
RB64	no	2	5	2	no change	no	**C2**
RB109	no	1	1	1	no change	no	**C1**
RB111	no	2	5	2	no change	no	**C2**
RB200	no	2	2	2	no change	no	**C2**
RB202	no	no	no	no	no	C2	**C2**
RB203	no	1	1	1	no change	no	**C1**
RB204	no	no	no	no	no	NA	**NA**
RB205	no	no	no	no	no	C2	**C2**
RB206	no	1	1	1	no change	no	**C1**
RB208	no	2	4	2	3	no	**NA**
RB209	no	2	1	3	2	no	**C2**
RB211	2	2	3	2	no change	no	**C2**
RB212	2	2	4	2	no change	no	**C2**
RB213	1	1	1	1	no change	no	**C1**
RB215	no	no	no	no	no	C2	**C2**
RB216	1	1	4	1	no change	no	**C1**
RB217	1	1	4	1	no change	C1 validation set	**C1**
RB218	no	1	1	1	no change	no	**C1**
RB219	1	1	4	1	no change	no	**C1**
RB220	2	2	3	2	no change	no	**C2**
RB221	1	1	1	1	no change	no	**C1**
RB222	2	2	1	2	no change	no	**C2**
RB223	2	2	2	2	no change	no	**C2**
RB224	2	2	3	2	no change	no	**C2**
RB225	2	2	4	2	no change	no	**C2**
RB300	no	2	4	2	no change	no	**C2**
RB304	no	2	5	2	no change	no	**C2**

RB590	no	no	no	no	no	C2	**C2**
RB593	no	no	no	no	no	C2	**C2**
RB598	no	no	no	no	no	C2	**C2**
RB603	no	no	no	no	no	C1	**C1**
RB617	no	no	no	no	no	C2	**C2**
RB625	no	no	no	no	no	C1	**C1**
RB630	no	no	no	no	no	NA	**NA**
RB632	no	no	no	no	no	C2	**C2**
RB634	no	no	no	no	no	C1	**C1**
RB635	no	no	no	no	no	C2	**C2**
RB647	no	no	no	no	no	C2	**C2**
RB659	no	no	no	no	no	C2	**C2**
RB663	no	no	no	no	no	C1	**C1**
RB671	no	no	no	no	no	C1	**C1**
RB704	no	no	no	no	no	C2	**C2**
RB707	no	no	no	no	no	C2	**C2**
RB714	no	no	no	no	no	C1	**C1**
RB715	no	no	no	no	no	C2	**C2**
RB716	no	no	no	no	no	C2	**C2**
HSJD-RBT2	no	no	no	no	no	C2	**C2**
HSJD-RBT3	no	no	no	no	no	NA	**NA**
HSJD-RBT7	no	no	no	no	no	C2	**C2**
HSJD-RBT8	no	no	no	no	no	C2	**C2**
HSJD-RBT9	no	no	no	no	no	C1	**C1**

Pyroseq. Signature: pyrosequencing signature

Table 6. ARID1A and BCOR mutations identified by Whole-Exome sequencing

Sample ID	Gene Symbol	Chrom	Ref	Var	Mutation type	Exon	cDNA	PROT	Allelic freq (%)	Sanger seq	Validated
RB21	ARID1A	chr1	G	T	nonsense	20	c.G6232T	p.E2078X	40	yes	yes
RB635	ARID1A	chr1	-	T	frameshift indel	18	:c.4391dupT	p.V1464fs	46,74	yes	yes
RB38	BCOR	chrX	-	CCCAG	frameshift indel	4	c.2162_2163ins	p.G721fs	36,88	yes	yes
RB41	BCOR	chrX	G	-	frameshift indel	7	c.3512delC	p.S1171fs	93,33	yes	yes
RB205	BCOR	chrX	G	A	nonsense	10	c.C4384T	p.R1462X	38,29	yes	yes
RB617	BCOR	chrX	C	-	frameshift indel	9	c.4234delG	p.E1412fs	90,74	yes	yes
RB659	BCOR	chrX	-	GTCAGTG	frameshift indel	8	c.3983_3984ins	p.T1328fs	26,92	yes	yes
RB704	BCOR	chrX	CG	-	frameshift indel	7	c.3512_3513del	p.S1171fs	84,52	yes	yes
RB715	BCOR	chrX	-	TG	frameshift indel	4	c.449_450ins	p.K150fs	39,64	yes	yes
RB716	BCOR	chrX	TGAGACT	-	frameshift indel	6	c.3357_3363del	p.K1119fs	62,5	yes	yes
HSJD-RBT2	BCOR	chrX	-	GACA	frameshift indel	9	c.4073_4074ins	p.S1358fs	66,67	yes	yes

BCOR transcript reference: NM_001123384; *ARID1A* transcript reference: NM_006015; Chrom: chromosome; Ref: nucleotide of reference; Var: nucleotide change; Allelic freq: frequency of the mutation; Sanger seq: Sanger sequencing

Table 7. List of RB1 mutations identified by targeted sequencing

Sample	Gene Symbol	Chrom	Ref	Var	Mutation type	Allelic freq (%)	Type	WES	Target seq	Sanger seq	Status
RB9	RB1	chr13	A	-	frameshift indel	44,52	indel	no	yes	yes	somatic
RB23	RB1	chr13	G	A	splicing	93,83	snv	no	yes	yes	NA
RB27	RB1	chr13	C	T	nonsense	98,95	snv	no	yes	yes	somatic
RB30	RB1	chr13	C	T	nonsense	98,95	snv	no	yes	yes	NA
RB31	RB1	chr13	C	T	nonsense	98,76	snv	no	yes	yes	NA
RB40	RB1	chr13	C	T	nonsense	95,84	snv	no	yes	yes	NA
RB54	RB1	chr13	AGGATAT	-	frameshift indel	99,2	indel	no	yes	yes	somatic
RB59	RB1	chr13	C	T	nonsense	48,49	snv	no	yes	yes	somatic
RB59	RB1	chr13	G	A	splicing	54,34	snv	no	yes	yes	somatic
RB63	RB1	chr13	C	-	frameshift indel	47,51	indel	no	yes	yes	somatic
RB64	RB1	chr13	C	T	nonsense	53,47	snv	no	yes	yes	somatic
RB64	RB1	chr13	-	TA	frameshift indel	49,26	indel	no	yes	yes	somatic
RB211	RB1	chr13	G	-	frameshift indel	81,62	indel	no	yes	yes	somatic
RB216	RB1	chr13	C	T	nonsense	62,82	snv	no	yes	yes	germline
RB223	RB1	chr13	GG	-	frameshift indel	56,53	indel	no	yes	yes	somatic
RB224	RB1	chr13	C	T	nonsense	34,34	snv	no	yes	yes	NA
RB225	RB1	chr13	G	A	splicing	99,25	snv	no	yes	yes	NA
RB21	RB1	chr13	C	T	nonsense	99,84	snv	yes	yes	yes	germline
RB617	RB1	chr13	C	T	nonsense	99,62	snv	yes	yes	yes	somatic
RB55	RB1	chr13	C	T	nonsense	53,04	snv	yes	yes	yes	germline
RB217	RB1	chr13	C	T	nonsense	26,04	snv	yes	yes	yes	germline
RB716	RB1	chr13	C	T	nonsense	100	snv	yes	yes	no	germline

Chrom: chromosome; Ref: nucleotide of reference; Var: nucleotide change; Allelic freq: frequency of the mutation; WES: Whole Exome Sequencing; Target seq: targeted sequencing; Sanger seq: Sanger sequencing

Table 8. RB1 mutations identified in by WES and targeted sequencing, along with data from the Genetic Service of the Curie Hospital and the Sant Joan de Déu Hospital

ID sample	Group	*RB1* germinal	Somatic RB1 Hit1				Somatic RB1 Hit2			
			type	exon	cDNA	PROT	type	exon	cDNA	PROT
RB1	C1	yes	nonsense	10	c.958C>T	R320X	LOH			
RB2	C1	yes	missense	20	c.2104C>A	Q702K	LOH			
RB3	C2	no	nonsense	14	c.1388C>A	S463X	LOH			
RB4	C1	yes	frameshift indel	9	c.885delT	N295fs	LOH			
RB6	C1	no	exon del	7-17			prom meth			
RB7	C2	no	NA				1 allele del			
RB9	C1	no	nonsense	17	c.1654C>T	R552X	frameshift indel	3	c.372delA	I124fs
RB10	C1	no	hom del				hom del			
RB11	C1	mosaic	nonsense	17	c.1654C>T	R552X	nonsense	10	c.958C>T	R320X
RB13	C2	no	nonsense	11	c.1072C>T	R358X	LOH			
RB14	C2	no	nonsense	14	c.1333C>T	R445X	LOH			
RB15	C2	no	nonsense	7	c.619C>T	Q207X	splice site	12	c.1215+1G>A	N405
RB21	C2	no	nonsense	14	c.1363C>T	R455X	LOH			
RB22	C2	yes	frameshift indel	7	c.660delAT	L220fs	NA			
RB23	C1	NA	splice site	17	c.1499-1G>A	R500	LOH			
RB24	C1	no	NA				LOH			
RB25	C1	no	nonsense	17	c.1666C>T	R556X	LOH			
RB27	C2	no	nonsense	8	c.763C>T	R255X	LOH			
RB28	C1	no	hom del				hom del			
RB30	C1	NA	nonsense	18	c.1735C>T	R579X	LOH			
RB31	C2	NA	nonsense	13	c.1330C>T	Q444X	LOH			
RB32	C2	no	frameshift indel	2	c.218-24del	R73fs	prom meth			
RB33	C1	NA	nonsense	18	c.1735C>T	R579X	nonsense	19	c.1943C>A	S648X
RB34	C1	yes	frameshift indel	22	c.2326-1delG	R775fs	LOH			
RB35	C1	no	frameshift indel	18	c.1723delC	P582fs	nonsense	7	c.649C>T	Q217X
RB37	C2	no	exon del	3-27			NA			
RB38	C2	no	nonsense	8	c.763C>T	R255X	LOH			
RB39	C2	no	nonsense	8	c.763C>T	R255X	LOH			
RB40	C1	NA	nonsense	20	c.2053C>T	Q685X	NA			
RB41	C2	no	nonsense	10	c.958C>T	R320X	frameshift indel	23	c.2333delC	T778fs
RB42	C2	no	splice site	12	c.1215+1G>A	N405	LOH			
RB43	C2	no	exon del	7-12			exon del	18-27		
RB44	C1	NA	NA				NA			
RB45	C2	no	splice site	17	c.1695+3A>T	S565	LOH			
			neutral	12	c.1140C>T	N380N				
RB46	C2	no	nonsense	15	c.1399C>T	R467X	LOH			
RB47	C1	NA	NA				NA			

RB48	C2	no	hom del				hom del			
RB49	C1	no	nonsense	23	c.2359C>T	R787X	LOH			
RB50	C1	no	hom del				Hom del			
RB51	C2	no	nonsense	18	c.1735C>T	R579X	splice Site	14	c.1333-1G>C	R445
RB52	C1	no	inframe indel	16	c.1439-41delACA	N480	LOH			
RB54	C2	no	frameshift indel	13	c.1259-65del	K420fs	LOH			
RB55	C2	yes	nonsense	15	c.1399C>T	R467X	prom meth			
RB56	C2	no	frameshift indel	19	c.1820-21del	L607fs	LOH			
			neutral	26	c.2670T>C	H890H				
RB57	C2	NA	NA				1 allele del			
RB58	C2	no	NA				NA			
RB59	C2	no	splice site	12	c.1215+1G>A	N405	nonsense	14	c.1363C>T	R455X
RB60	NA	no	splice site	25	c.2663+1G>A	S888	1 allele del			
RB61	NA	NA	NA				NA			
RB62	C2	no	nonsense	13	c.1237G>T	E413X	nonsense	22	c.2242T>G	E748X
RB63	C1	yes	frameshift indel	1	c.45-79dup	P27fs	frameshift indel	18	c.1734delC	D578fs
RB64	C2	no	nonsense	15	c.1399C>T	R467X	frameshift indel	5	c.513insTA	L171fs
RB109	C1	mosaic	nonsense	22	c.2233A>T	K745X	NA			
RB111	C2	no	splice site	20	c.2106+2T>G	Q702	LOH			
RB200	C2	no	splice site	12	c.1215+1G>T	N405	LOH			
RB202	C2	no	frameshift indel	3	c.302-303insA	G100fs	splice site	15	c.1421+12-32del	K474
RB203	C1	no	hom del				hom del			
RB204	NA	no	splice site	12	c.1215+1G>T	N405	LOH			
RB205	C2	no	prom meth				LOH			
RB206	C1	no	prom meth				LOH			
RB208	NA	no	nonsense	11	c.1072C>T	R358X	splice site	3	c.265-2A>C	G89
RB209	C2	no	nonsense	23	c.2359C>T	R787X	LOH			
RB211	C2	no	frameshift indel	4	c.456delG	L152fs	NA			
RB212	C2	no	1 allele del				1 allele del			
RB213	C1	yes	splice site	6	c.607+1G>A	G203	LOH			
RB215	C2	no	NA				1 allele del			
			neutral	13	c.1332G>A	Q444Q				
RB216	C1	yes	nonsense	8	c.763C>T	R255X	LOH			
RB217	C1	yes	nonsense	17	c.1666C>T	R556X	NA			
RB218	C1	yes	frameshift indel	24	c.2498insT	V833fs	LOH			
RB219	C1	yes	missense	8	c.830T>C	L277P	nonsense	8	c.769C>T	Q257X
RB220	C2	no	NA				NA			
RB221	C1	NA	NA				NA			
RB222	C2	no	no mutation				no mutation			

RB223	C2	no	frameshift indel	14	c.1345-46delGG	G449fs	LOH			
RB224	C2	NA	nonsense	8	c.763C>T	R255X	NA			
RB225	C2	NA	splice site	16	c.1498+1G>A	R500	NA			
RB300	C2	NA	NA				LOH			
RB304	C2	NA	NA				NA			
RB590	C2	yes	frameshift indel	17	c.1542delC	F514fs	LOH			
RB593	C2	no	hom del				hom del			
RB598	C2	NA	NA				NA			
RB603	C1	no	nonsense	10	c.958C>T	R320X	splice site	22	c.2212-1G>C	T738
RB617	C2	no	nonsense	15	c.1399C>T	R467X	1 allele del			
RB625	C1	yes	nonsense	19	c.1953T>G	Y651X	LOH			
RB630	NA	yes	nonsense	18	c.1735C>T	R579X	NA			
RB632	C2	no	nonsense	10	c.967G>T	E323X	LOH			
RB634	C1	no	frameshift indel	13	c.1238delA	E413fs	NA			
RB635	C2	no	NA				1 allele del			
RB647	C2	no	nonsense	14	c.1333C>T	R445X	NA			
RB659	C2	no	nonsense	17	c.1654C>T	R552X	1 allele del			
RB663	C1	no	1 allele del				1 allele del			
RB671	C1	no	nonsense	8	c.751C>T	R251X	NA			
RB704	C2	no	splice site	8	c.861+3A>C	E287	LOH			
RB707	C2	yes	missense	9	c.920C>T	T307I	NA			
RB714	C1	yes	splice site	20	c.2106+1G>A	Q702	LOH			
RB715	C2	no	frameshift indel	4	c.431 32insA	V144fs	LOH			
RB716	C2	yes	nonsense	13	c.1306C>T	Q436X	LOH			
HSJD-RBT2	C2	yes	NA				NA			
HSJD-RBT3	NA	NA	nonsense	8	c.751C>T	R251X	NA			
HSJD-RBT7	C2	no	NA				NA			
HSJD-RBT8	C2	no	hom del				NA			
HSJD-RBT9	C1	no	nonsense	18	c.1723C>T	Q575X	NA			

exon del: exon deletion; hom del: homozygote deletion; prom meth: gene promotor methylation; 1 allele del: deletion of one allele; LOH: Copy-neutral loss of heterozygosity

Table 9. Fusion events identified in 34 retinoblastomas

Fusion	Gene X	Gene Y	Sample ID	Fusion location	Strand	inFrame	Karyotype	Type X	Type Y	Distance partners (kb)	X in TCGA	X TCGA partner	Y in TCGA	Y TCGA partner
ADAR_FLAD1	ADAR	FLAD1	RB59	chr1:154570878-chr1:154960581	-/+	TRUE	t(1;1)(q21.3;q21.3)	full_exon_CDS	full_exon_CDS	390	no		yes	RP11-540D14.8, EFNA4
ADIPOR1_LINC00303	ADIPOR1	LINC00303	RB59	chr1:202927313-chr1:204002995	-/-	FALSE	t(1;1)(q32.1;q32.1)	full_exon_UTR	full_exon_UTR	1076	yes	CYB5R1, RGS8	no	
AP2A1_ATP13A3	AP2A1	ATP13A3	RB46	chr19:50270457-chr3:194182965	+/-	FALSE	t(19;3)(q13.33;q29)	full_exon_CDS	partial_exon_UTR	inter	no		no	
ATP8A2_RNF219-AS1	ATP8A2	RNF219-AS1	RB50	chr13:26349097-chr13:78848388	+/+	FALSE	t(13;13)(q12.13;q22.3)	full_exon_CDS	partial_exon_UTR	52499	no		no	
BCL9_ENSG00000271845	BCL9	ENSG00000271845	RB14	chr1:147054041-chr1:150227537	+/-	FALSE	t(1;1)(q21.2;q21.2)	intron_retention	partial_exon_UTR	3173	yes	SMCP, IVL	no	
BCL9_HORMAD1	BCL9	HORMAD1	RB14	chr1:147013444-chr1:150679285	+/-	TRUE	t(1;1)(q21.2;q21.3)	full_exon_UTR	full_exon_CDS	3666	yes	SMCP, IVL	yes	XPO1, GOLPH3L
C1orf194_UQCR10	C1orf194	UQCR10	RB59	chr1:109650634-chr22:30163373	-/+	FALSE	t(1;22)(p13.3;q12.2)	partial_exon_CDS	partial_exon_UTR	inter	no		no	
CCNF_FBXO31	CCNF	FBXO31	RB24	chr16:2489827-chr16:87398100	+/-	FALSE	t(16;16)(p13.3;q24.2)	full_exon_CDS	intron_retention	84908	no		no	
CTNNA2_LRRTM4	CTNNA2	LRRTM4	RB56	chr2:79740333-chr2:76976042	+/-	FALSE	t(2;2)(p12;p12)	full_exon_UTR	full_exon_CDS	2764	no		no	
DACH1_LINC01074	DACH1	LINC01074	RB50	chr13:72440054-chr13:62896059	-/+	TRUE	t(13;13)(q21.33;q21.31)	full_exon_CDS	partial_exon_UTR	9544	yes	PAX5 IVL	no	
DACH1_LINC00437	DACH1	LINC00437	RB39	chr13:72440054-chr13:39119419	-/-	TRUE	t(13;13)(q21.33;q13.3)	full_exon_CDS	intron_retention	33321	yes	PAX5	no	
DACH1_LINC01075	DACH1	LINC01075	RB50	chr13:72440054-chr13:62798231	-/+	FALSE	t(13;13)(q21.33;q21.31)	full_exon_CDS	partial_exon_UTR	9642	yes	PAX5	no	

DOCK9_PCDH9	DOCK9	PCDH9	RB50	chr13:99532801-chr13:66879160	-/-	FALSE	t(13;13)(q32.3;q21.32)	full_exon_CDS	full_exon_CDS	32654	no		yes	KIAA1033, RNF121
KLF12_LINC00348	KLF12	LINC00348	RB43	chr13:74708109-chr13:71741502	-/+	FALSE	t(13;13)(q22.1;q21.33)	full_exon_UTR	partial_exon_UTR	2967	no		no	
FAM124A_GTF2F2	FAM124A	GTF2F2	RB50	chr13:51805515-chr13:45781559	+/+	TRUE	t(13;13)(q14.3;q14.12)	full_exon_CDS	full_exon_CDS	6024	no		no	
FOXO1_EXOSC8	FOXO1	EXOSC8	RB50	chr13:41239720-chr13:37576625	-/+	TRUE	t(13;13)(q14.11;q13.3)	full_exon_CDS	full_exon_CDS	3663	no		no	
GABPB2_DCST1	GABPB2	DCST1	RB59	chr1:151043410-chr1:155018369	+/+	FALSE	t(1;1)(q21.3;q22)	full_exon_UTR	full_exon_CDS	3975	no		no	
INTS6_NBEA	INTS6	NBEA	RB50	chr13:52004430-chr13:35864526	-/+	FALSE	t(13;13)(q14.3;q13.3)	full_exon_UTR	full_exon_CDS	16140	no		yes	PEX1, GTF2F2
LHFPL2_FAM172A	LHFPL2	FAM172A	RB57	chr5:77805607-chr5:92956835	-/-	TRUE	t(5;5)(q14.1;q15)	full_exon_CDS	full_exon_CDS	15151	no		yes	CAST, CDC73
NUF2_FAM49A	NUF2	FAM49A	RB14	chr1:163298697-chr2:16747035	+/-	TRUE	t(1;2)(q23.3;p24.2)	full_exon_CDS	full_exon_CDS	inter	no		no	
PAN3_CAB39L	PAN3	CAB39L	RB50	chr13:28752072-chr13:49933968	+/-	TRUE	t(13;13)(q12.2;q14.2)	full_exon_CDS	full_exon_CDS	21182	no		no	
PCGF6_ARL3	PCGF6	ARL3	RB59	chr10:105104781-chr10:104459246	-/-	FALSE	t(10;10)(q24.33;q24.32)	full_exon_CDS	full_exon_CDS	646	no		no	
PI4KB_LOC730102	PI4KB	LOC730102	RB59	chr1:151280050-chr1:178006936	-/-	FALSE	t(1;1)(q21.3;q25.2)	full_exon_CDS	full_exon_UTR	26727	no		no	
POLR1D_PAN3	POLR1D	PAN3	RB50	chr13:28196146-chr13:28771322	+/+	FALSE	t(13;13)(q12.2;q12.2)	full_exon_CDS	full_exon_CDS	575	no		no	
PTPRR_LOC100507534	PTPRR	LOC100507534	RB31	chr12:71286459-chr16:47883859	-/-	FALSE	t(12;16)(q15;q12.1)	full_exon_CDS	full_exon_UTR	inter	yes	CHPT1, VWC2	no	
RAI1_MED9	RAI1	MED9	RB25	chr17:17627473-chr17:17394593	+/+	FALSE	t(17;17)(p11.2;p11.2)	full_exon_UTR	full_exon_CDS	233	yes	IGF2BP1, PEMT, IFT20	no	

RFWD2_PIGR	RFWD2	PIGR	RB59	chr1:176015317-chr1:207111096	-/-	FALSE	t(1;1)(q25.2;q32.1)	full_exon_CDS	full_exon_CDS	31096	yes	XPR1, SRGAP2, KIF14	no
RPRD2_ASH1L-AS1	RPRD2	ASH1L-AS1	RB59	chr1:150378172-chr1:155531944	+/+	FALSE	t(1;1)(q21.3;q22)	intron_retention	partial_exon_UTR	5154	yes	VPS45, SHC1, S100A2 BOLA1	no
SLC30A5_TSC22D1	SLC30A5	TSC22D1	RB57	chr5:68404263-chr13:45010231	+/-	FALSE	t(5;13)(q13.2;q14.11)	full_exon_CDS	full_exon_CDS	inter	no		no
TAOK1_NSRP1	TAOK1	NSRP1	RB31	chr17:27718042-chr17:28499560	+/+	TRUE	t(17;17)(q11.2;q11.2)	full_exon_UTR	full_exon_CDS	782	yes	1-	no
VAX2_ZNF638	VAX2	ZNF638	RB56	chr2:71148415-chr2:71607352	+/+	TRUE	t(2;2)(p13.3;p13.2)	full_exon_CDS	full_exon_CDS	459	no		no
VPS72_LOC100132111	VPS72	LOC100132111	RB59	chr1:151156793-chr1:151811502	-/+	TRUE	t(1;1)(q21.3;q21.3)	full_exon_CDS	partial_exon_UTR	655	yes	ROBO2, RORC	no
YY1AP1_IPO9	YY1AP1	IPO9	RB59	chr1:155649200-chr1:201837776	-/+	FALSE	t(1;1)(q22;q32.1)	full_exon_CDS	full_exon_CDS	46189	no		no

Gene X/Gene Y: genes involved in the fusion; Strand: DNA strand sense; Type X/Type Y: region involved in the fusion; X/Y in TCGA: gene involved in the fusion reported in TCGA; X/Y TCGA partner: the gene partner involved in the fusion reported in TCGA

BIBLIOGRAPHY

Ågerstam, H., Lilljebjörn, H., Lassen, C., Swedin, A., Richter, J., Vandenberghe, P., Johansson, B., and Fioretos, T. (2007). Fusion gene-mediated truncation ofRUNX1 as a potential mechanism underlying disease progression in the 8p11 myeloproliferative syndrome. Genes, Chromosom. Cancer *46*, 635–643.

Ajioka, I., Martins, R.A.P., Bayazitov, I.T., Donovan, S., Johnson, D.A., Frase, S., Cicero, S.A., Boyd, K., Zakharenko, S.S., and Dyer, M.A. (2007). Differentiated Horizontal Interneurons Clonally Expand to Form Metastatic Retinoblastoma in Mice. Cell *131*, 378–390.

Aryee, M.J., Jaffe, A.E., Corrada-Bravo, H., Ladd-Acosta, C., Feinberg, A.P., Hansen, K.D., and Irizarry, R.A. (2014). Minfi: a flexible and comprehensive Bioconductor package for the analysis of Infinium DNA methylation microarrays. Bioinformatics *30*, 1363–1369.

Van der Auwera, G.A., Carneiro, M.O., Hartl, C., Poplin, R., del Angel, G., Levy-Moonshine, A., Jordan, T., Shakir, K., Roazen, D., Thibault, J., et al. (2013). From FastQ Data to High-Confidence Variant Calls: The Genome Analysis Toolkit Best Practices Pipeline. In Current Protocols in Bioinformatics, (Hoboken, NJ, USA: John Wiley & Sons, Inc.), p. 11.10.1-11.10.33.

Beemer, F.A., Van Veelen, C.W., and Staal, G.E. (1984). How did retinoblastoma arise? Nature *310*, 731.

Bibikova, M., Barnes, B., Tsan, C., Ho, V., Klotzle, B., Le, J.M., Delano, D., Zhang, L., Schroth, G.P., Gunderson, K.L., et al. (2011). High density DNA methylation array with single CpG site resolution. Genomics *98*, 288–295.

Bremner, R., and Sage, J. (2014). The origin of human retinoblastoma. Nature *514*, 312–313.

Cibulskis, K., Lawrence, M.S., Carter, S.L., Sivachenko, A., Jaffe, D., Sougnez, C., Gabriel, S., Meyerson, M., Lander, E.S., and Getz, G. (2013). Sensitive detection of somatic point mutations in impure and heterogeneous cancer samples. Nat. Biotechnol. *31*, 213–219.

Corson, T.W., and Gallie, B.L. (2007). One Hit , Two Hits , Three Hits , More ? Genomic Changes in the Development of Retinoblastoma. Genes. Chromosomes Cancer *46*, 617–634.

Coyaud, E., Struski, S., Prade, N., Familiades, J., Eichner, R., Quelen, C., Bousquet, M., Mugneret, F., Talmant, P., Pages, M.-P., et al. (2010). Wide diversity of PAX5 alterations in B-ALL: a Groupe Francophone de Cytogenetique Hematologique study. Blood *115*, 3089–3097.

Dai, M., Wang, P., Boyd, A.D., Kostov, G., Athey, B., Jones, E.G., Bunney, W.E., Myers, R.M., Speed, T.P., Akil, H., et al. (2005). Evolving gene/transcript definitions significantly alter the interpretation of GeneChip data. Nucleic Acids Res. *33*, e175.

DePristo, M.A., Banks, E., Poplin, R., Garimella, K. V, Maguire, J.R., Hartl, C., Philippakis, A.A., del Angel, G., Rivas, M.A., Hanna, M., et al. (2011). A framework for variation discovery and genotyping using next-generation DNA sequencing data. Nat. Genet. *43*, 491–498.

Dickson, D.H., Ramsey, M.S., and Tonus, J.G. (1976). Synapse formation in retinoblastoma tumours. Br. J. Ophthalmol. *60*, 371–375.

Donoso, L.A., Folberg, R., and Arbizo, V. (1985). Retinal S antigen and retinoblastoma. A monoclonal antibody histopathologic study. Arch. Ophthalmol. (Chicago, Ill. 1960) *103*, 855–857.

Donovan, S.L., Schweers, B., Martins, R., Johnson, D., and Dyer, M.A. (2006). Compensation by tumor suppressor genes during retinal development in mice and humans. BMC Biol. *4*, 14.

Downing, J.R., Wilson, R.K., Zhang, J., Mardis, E.R., Pui, C.-H., Ding, L., Ley, T.J., and Evans, W.E. (2012). The Pediatric Cancer Genome Project.

Dupain, C., Harttrampf, A.C., Urbinati, G., Geoerger, B., and Massaad-Massade, L. (2017). Relevance of Fusion Genes in Pediatric Cancers: Toward Precision Medicine.

Fan, Z., Yamaza, T., Lee, J.S., Yu, J., Wang, S., Fan, G., Shi, S., Wang, C.-Y., Cell, N., and Author, B. (2009). BCOR regulates mesenchymal stem cell function by epigenetic mechanisms. Nat Cell Biol *11*, 1002–1009.

Filkov, V., and Skiena, S. (2003). Integrating microarray data by consensus clustering. In Proceedings. 15th IEEE International Conference on Tools with Artificial Intelligence, (IEEE Comput. Soc), pp. 418–426.

Friend, S.H., Bernards, R., Rogelj, S., Weinberg, R.A., Rapaport, J.M., Albert, D.M., and Dryja, T.P. (1986). A human DNA segment with properties of the gene that predisposes to retinoblastoma and osteosarcoma. Nature *323*, 643–646.

Gao, C., Zhang, R.-D., Liu, S.-G., Zhao, X.-X., Cui, L., Yue, Z.-X., Li, W.-J., Chen, Z.-P., Li, Z.-G., Rao, Q., et al. (2017). Low *CREBBP* expression is associated with adverse long-term outcomes in paediatric acute lymphoblastic leukaemia. Eur. J. Haematol. *99*, 150–159.

Gearhart, M.D., Corcoran, C.M., Wamstad, J.A., and Bardwell, V.J. (2006). Polycomb Group and SCF Ubiquitin Ligases Are Found in a Novel BCOR Complex That Is Recruited to BCL6 Targets. Mol. Cell. Biol. *26*, 6880–6889.

Glubrecht, D.D., Kim, J.H., Russell, L., Bamforth, J.S., and Godbout, R. (2009). Differential CRX and OTX2 expression in human retina and retinoblastoma. J. Neurochem. *111*, 250–263.

Gnirke, A., Melnikov, A., Maguire, J., Rogov, P., LeProust, E.M., Brockman, W., Fennell, T., Giannoukos, G., Fisher, S., Russ, C., et al. (2009). Solution hybrid selection with ultra-long oligonucleotides for massively parallel targeted sequencing. Nat. Biotechnol. *27*, 182–189.

Gröbner, S.N., Worst, B.C., Weischenfeldt, J., Buchhalter, I., Kleinheinz, K., Rudneva, V.A., Johann, P.D., Balasubramanian, G.P., Segura-Wang, M., Brabetz, S., et al. (2018). The landscape of genomic alterations across childhood cancers. Nature *555*, 321–327.

Harbour, J.W. (1998). Overview of RB Gene Mutations in Patients with Retinoblastoma Implications for Clinical Genetic Screening.

Houdayer, C., Gauthier-Villars, M., Laugé, A., Pagès-Berhouet, S., Dehainault, C., Caux-Moncoutier, V., Karczynski, P., Tosi, M., Doz, F., Desjardins, L., et al. (2004). Comprehensive screening for constitutional *RB1* mutations by DHPLC and QMPSF. Hum. Mutat. *23*, 193–202.

Hupé, P., Stransky, N., Thiery, J.-P., Radvanyi, F., and Barillot, E. (2004). Analysis of array CGH data: from signal ratio to gain and loss of DNA regions. Bioinformatics *20*, 3413–3422.

Johnson, D.A., Zhang, J., Frase, S., Wilson, M., Rodriguez-Galindo, C., and Dyer, M.A. (2007). Neuronal Differentiation and Synaptogenesis in Retinoblastoma. Cancer Res. *67*, 2701–2711.

Kadoch, C., and Crabtree, G.R. (2015). Mammalian SWI/SNF chromatin remodeling complexes and cancer: Mechanistic insights gained from human genomics. Sci. Adv. *1*, 1–17.

Kandoth, C., Mclellan, M.D., Vandin, F., Ye, K., Niu, B., Lu, C., Xie, M., Zhang, Q., Mcmichael, J.F., Wyczalkowski, M.A., et al. (2013). Mutational landscape and significance across 12 major cancer types. Nature *502*, 333–339.

Kapatai, G., Brundler, M., Jenkinson, H., Kearns, P., Parulekar, M., Peet, a C., and McConville, C.M. (2013). Gene expression profiling identifies different sub-types of retinoblastoma. Br. J. Cancer *109*, 512–525.

Kim, D., Pertea, G., Trapnell, C., Pimentel, H., Kelley, R., and Salzberg, S.L. (2013). TopHat2: accurate alignment of transcriptomes in the presence of insertions, deletions and gene fusions. Genome Biol. *14*, R36.

Kim, S.-S., Zhang, R.-G., Braunstein, S.E., Joachimiak, A., Cvekl, A., and Hegde, R.S. (2002). Structure of the Retinal Determination Protein Dachshund Reveals a DNA Binding Motif.

Koboldt, D.C., Zhang, Q., Larson, D.E., Shen, D., McLellan, M.D., Lin, L., Miller, C.A., Mardis, E.R., Ding, L., and Wilson, R.K. (2012). VarScan 2: somatic mutation and copy number alteration discovery in cancer by exome sequencing. Genome Res. *22*, 568–576.

Kooi, I.E., Mol, B.M., Moll, A.C., van der Valk, P., de Jong, M.C., de Graaf, P., et al. (2015). Loss of photoreceptorness and gain of genomic alterations in retinoblastoma reveal tumor progression. EBioMedicine *2*, 660–670.

Kooi, I.E., Mol, B.M., Massink, M.P.G., Ameziane, N., Meijers-Heijboer, H., Dommering, C.J., et al. (2016). Somatic genomic alterations in retinoblastoma beyond RB1 are rare and limited to copy number changes. Sci. Rep. *6*, 1–11.

Kyritsis, A., Tsokos, M., and Chader, G. (1984b). Attachment culture of human retinoblastoma cells: long-term culture conditions and effects of dibutyryl cyclic AMP. Exp. Eye Res. *38*, 411–421.

Kyritsis, A., Joseph, G., and Chader, G.J. (1984a). Effects of Butyrate , Retinol , and Retinoic Acid on Human Y-79 Retinoblastoma Cells Growing in Monolayer Cultures 1. *73*, 649–654.

Kyritsis, A.P., Tsokos, M., Triche, T.J., and Chader, G.J. (1986). Retinoblastoma: a primitive tumor with multipotential characteristics. Invest. Ophthalmol. Vis. Sci. *27*, 1760–1764.

Lee, W.H., Bookstein, R., Hong, F., Young, L.J., Shew, J.Y., and Lee, E.Y. (1987). Human retinoblastoma susceptibility gene: cloning, identification, and sequence. Science *235*, 1394–1399.

Li, H., and Durbin, R. (2009). Fast and accurate short read alignment with Burrows-Wheeler transform. Bioinformatics *25*, 1754–1760.

Li, X., Perissi, V., Liu, F., Rose, D.W., and Rosenfeld, M.G. (2002). Tissue-specific regulation of retinal and pituitary precursor cell proliferation. Science (80-.). *297*, 1180–1183.

Liu, Y., Han, N., Zhou, S., Zhou, R., Yuan, X., Xu, H., Zhang, C., Yin, T., and Wu, K. (2016). The DACH/EYA/SIX gene network and its role in tumor initiation and progression. Int. J. Cancer *138*, 1067–1075.

Lohmann, D.R. (1999). RB1 gene mutations in retinoblastoma. Hum. Mutat. *14*, 283–288.

Ma, X., Liu, Y., Liu, Y., Alexandrov, L.B., Edmonson, M.N., Gawad, C., Zhou, X., Li, Y., Rusch, M.C., et al. (2018). Pan-cancer genome and transcriptome analyses of 1,699 paediatric leukaemias and solid tumours. Nature *555*, 371–376.

Mardon G, S.N. and R.G. (1994). dachshund encodes a nuclear protein required for normal eye and leg development in Drosophila. Development *120*, 3473–3486.

McEvoy, J., Flores-Otero, J., Zhang, J., Nemeth, K., Brennan, R., Bradley, C., Krafcik, F., Rodriguez-Galindo, C., Wilson, M., Xiong, S., et al. (2011). Coexpression of normally incompatible developmental pathways in retinoblastoma genesis. Cancer Cell *20*, 260–275.

McEvoy, J., Nagahawatte, P., Finkelstein, D., Richards-Yutz, J., Valentine, M., Ma, J., Mullighan, C., Song, G., Chen, X., Wilson, M., et al. (2014). RB1 gene inactivation by chromothripsis in human retinoblastoma. Oncotarget *5*.

McKenna, A., Hanna, M., Banks, E., Sivachenko, A., Cibulskis, K., Kernytsky, A., Garimella, K., Altshuler, D., Gabriel, S., Daly, M., et al. (2010). The Genome Analysis Toolkit: a MapReduce framework for analyzing next-generation DNA sequencing data. Genome Res. *20*, 1297–1303.

Mermel, C.H., Schumacher, S.E., Hill, B., Meyerson, M.L., Beroukhim, R., and Getz, G. (2011). GISTIC2.0 facilitates sensitive and confident localization of the targets of focal somatic copy-number alteration in human cancers. Genome Biol. *12*, R41.

Mirshahi, M., Boucheix, C., Dhermy, P., Haye, C., and Faure, J.P. (1986). Expression of the photoreceptor-specific S-antigen in human retinoblastoma. Cancer *57*, 1497–1500.

Mol, B.M., Massink, M.P.G., van der Hout, A.H., Dommering, C.J., Zaman, J.M.A., et al. (2014). High resolution SNP array profiling identifies variability in retinoblastoma genome stability. Genes. Chromosomes Cancer *53*, 1–14.

Nebral, K., Denk, D., Attarbaschi, A., König, M., Mann, G., Haas, O.A., and Strehl, S. (2009). Incidence and diversity of PAX5 fusion genes in childhood acute lymphoblastic leukemia. Leukemia *23*, 134–143.

Ottaviani, D., Parma, D., Giliberto, F., Ferrer, M., Fandino, A., Davila, M.T., Chantada, G., and Szijan, I. (2013). Spectrum of RB1 mutations in argentine patients: 20-years experience in the molecular diagnosis of retinoblastoma. Ophthalmic Genet. *34*, 189–198.

Pignoni, F., Hu, B., Zavitz, K.H., Xiao, J., Garrity, P.A., and Zipursky, S.L. (1997). The eye-specification proteins So and Eya form a complex and regulate multiple steps in Drosophila eye development. Cell *91*, 881–891.

Popova, T., Manié, E., Stoppa-Lyonnet, D., Rigaill, G., Barillot, E., and Stern, M.H. (2009). Genome Alteration Print (GAP): a tool to visualize and mine complex cancer genomic profiles obtained by SNP arrays. Genome Biol. *10*, R128.

Price, E.A., Price, K., Kolkiewicz, K., Hack, S., Reddy, M.A., Hungerford, J.L., Kingston, J.E., and Onadim, Z. (2014). Spectrum of RB1 mutations identified in 403 retinoblastoma patients. J. Med. Genet. *51*, 208–214.

Pui, C.-H., Gajjar, A.J., Kane, J.R., Qaddoumi, I.A., and Pappo, A.S. (2011). Challenging issues in pediatric oncology. Nat. Rev. Clin. Oncol. *8*, 540–549.

Richter, S., Vandezande, K., Chen, N., Zhang, K., Sutherland, J., Anderson, J., Han, L., Panton, R., Branco, P., and Gallie, B. (2003). Sensitive and Efficient Detection of RB1 Gene Mutations Enhances Care for Families with Retinoblastoma.

Rushlow, D.E., Mol, B.M., Kennett, J.Y., Yee, S., Pajovic, S., Thériault, B.L., Prigoda-Lee, N.L., Spencer, C., Dimaras, H., Corson, T.W., et al. (2013). Characterisation of retinoblastomas without RB1 mutations: Genomic, gene expression, and clinical studies. Lancet Oncol. *14*, 327–334.

Schrøder, H.D. (1987). Immunohistochemical demonstration of glial markers in retinoblastomas. Virchows Arch. A. Pathol. Anat. Histopathol. *411*, 67–72.

Siegel, R.L., Miller, K.D., and Jemal, A. (2017). Cancer Statistics, 2017. CA. Cancer J. Clin. *67*, 7–30.

Singh, H.P., Wang, S., Stachelek, K., Lee, S., Reid, M.W., Thornton, M.E., Craft, C.M., Grubbs, B.H., and Cobrinik, D. (2018). Developmental stage-specific proliferation and retinoblastoma genesis in RB-deficient human but not mouse cone precursors. Proc. Natl. Acad. Sci. *115*, 9391–9400.

Storlazzi, C.T., Von Steyern, F.V., Domanski, H.A., Mandahl, N., and Mertens, F. (2005). Biallelic somatic inactivation of theNF1 gene through chromosomal translocations in a sporadic neurofibroma. Int. J. Cancer *117*, 1055–1057.

Thorvaldsdottir, H., Robinson, J.T., and Mesirov, J.P. (2013). Integrative Genomics Viewer (IGV): high-performance genomics data visualization and exploration. Brief. Bioinform. *14*, 178–192.

Townsend, E.C., Murakami, M.A., Christodoulou, A., Christie, A.L., Köster, J., et al. (2016). The Public Repository of Xenografts (ProXe) enables discovery and randomized phase II-like trials in mice. Cancer Cell *29*, 574.

Ts'O, M.O.M., Fine, B.S., and Zimmerman, L.E. (1970). The Nature of Retinoblastoma. Ii. Photoreceptor Differentiation: An Electron Microscopic Study. Am. J. Ophthalmol. *69*, 350–359.

Tsokos, M., Kyritsis, A.P., Chader, G.J., and Triche, T.J. (1986). Differentiation of human retinoblastoma in vitro into cell types with characteristics observed in embryonal or mature retina. Am. J. Pathol. *123*, 542–552.

Untergasser, A., Nijveen, H., Rao, X., Bisseling, T., Geurts, R., and Leunissen, J.A.M. (2007). Primer3Plus, an enhanced web interface to Primer3. Nucleic Acids Res. *35*, W71–W74.

Valverde, J.R., Alonso, J., Palacios, I., and Pestaña, A. (2005). RB1 gene mutation up-date, a meta-analysis based on 932 reported mutations available in a searchable database. BMC Genet. *6*, 53.

Venkatraman, E.S., and Olshen, A.B. (2007). A faster circular binary segmentation algorithm for the analysis of array CGH data. Bioinformatics *23*, 657–663.

Vrabec, T., Arbizo, V., Adamus, G., McDowell, J.H., Hargrave, P.A., and Donoso, L.A. (1989). Rod cell-specific antigens in retinoblastoma. Arch. Ophthalmol. (Chicago, Ill. 1960) *107*, 1061–1063.

Watanabe, A., Ogiwara, H., Ehata, S., Mukasa, A., Ishikawa, S., Maeda, D., Ueki, K., Ino, Y., Todo, T., Yamada, Y., et al. (2011). Homozygously deleted gene DACH1 regulates tumor-initiating activity of glioma cells. Proc. Natl. Acad. Sci. *108*, 12384–12389.

Wu, K., Li, A., Rao, M., Liu, M., Dailey, V., Yang, Y., Di Vizio, D., Wang, C., Lisanti, M.P., Sauter, G., et al. (2006). DACH1 Is a Cell Fate Determination Factor That Inhibits Cyclin D1 and Breast Tumor Growth. Mol. Cell. Biol. *26*, 7116–7129.

Wu, K., Liu, M., Li, A., Donninger, H., Rao, M., Jiao, X., Lisanti, M.P., Cvekl, A., Birrer, M., and Pestell, R.G. (2007). Cell Fate Determination Factor DACH1 Inhibits c-Jun-induced Contact-independent Growth. Mol. Biol. Cell *18*, 755–767.

Wu, K., Katiyar, S., Witkiewicz, A., Li, A., McCue, P., Song, L.-N., Tian, L., Jin, M., and Pestell, R.G. (2009). The Cell Fate Determination Factor Dachshund Inhibits Androgen Receptor Signaling and Prostate Cancer Cellular Growth. Cancer Res. *69*, 3347–3355.

Xu, X.L., Fang, Y., Lee, T.C., Forrest, D., Gregory-Evans, C., Almeida, D., Liu, A., Jhanwar, S.C., Abramson, D.H., and Cobrinik, D. (2009). Retinoblastoma has properties of a cone precursor tumor and depends upon cone-specific MDM2 signaling. Cell *137*, 1018–1031.

Xu, X.L., Singh, H.P., Wang, L., Qi, D.-L., Poulos, B.K., Abramson, D.H., Jhanwar, S.C., and Cobrinik, D. (2014). Rb suppresses human cone-precursor-derived retinoblastoma tumours. Nature.

Yang, H., and Wang, K. (2015). Genomic variant annotation and prioritization with ANNOVAR and wANNOVAR. Nat. Protoc. *10*, 1556–1566.

Yoshihara, K., Wang, Q., Torres-Garcia, W., Zheng, S., Vegesna, R., Kim, H., and Verhaak, R.G.W. (2015). The landscape and therapeutic relevance of cancer-associated transcript fusions. Oncogene *34*, 4845–4854.

Zhang, J., Benavente, C.A., McEvoy, J., Flores-Otero, J., Ding, L., Chen, X., Ulyanov, A., Wu, G., Wilson, M., Wang, J., et al. (2012). A novel retinoblastoma therapy from genomic and epigenetic analyses. Nature *481*, 329–334.

Zhong, X., Li, Y., Peng, F., Huang, B., Lin, J., Zhang, W., Zheng, J., Jiang, R., Song, G., and Ge, J. (2007). Identification of tumorigenic retinal stem-like cells in human solid retinoblastomas. Int. J. Cancer *121*, 2125–2131.

Zhu, X., Dunn, J.M., Goddard, A.D., Squire, J.A., Becker, A., Phillips, R.A., and Gallie, B.L. (1992). Mechanisms of loss of heterozygosity in retinoblastoma. Cytogenet. Genome Res. *59*, 248–252.

CHAPTER 2

TFF1 GENE IN RETINOBLASTOMA

Index

TFF1 GENE IN RETINOBLASTOMA 96

INTRODUCTION 99

THE TREFOIL FACTOR FAMILY 99

BIOLOGICAL ROLES OF TFF PEPTIDES 100

TFF EXPRESSION IN NORMAL TISSUES AND CANCER 100

REGULATION OF TFF EXPRESSION 101

TFF1: TUMOR SUPPRESSOR GENE OR ONCOGENIC FACTOR? 101

TFF1 IN NORMAL RETINA AND RETINOBLASTOMA 102

MATERIALS AND METHODS 104

TRANSCRIPTOME ANALYSIS AND DIFFERENTIALLY EXPRESSED GENES BETWEEN RETINOBLASTOMAS OF SUBTYPE 1 AND SUBTYPE 2 104

METHYLATION STATUS OF *TFF1* GENE 104

CELL CULTURE 104

RNA INTERFERENCE ASSAY 104

IN VITRO CELL VIABILITY ASSAY 105

Cell viability after transient knock down of *TFF1* gene 105

Cell viability after treatment with human recombinant TFF1 protein 105

TOTAL RNA ISOLATION AND REVERSE TRANSCRIPTION PCR (RT-PCR) 105

REAL-TIME QUANTITATIVE PCR (qPCR) 105

WESTERN BLOTTING 106

IMMUNOHISTOCHEMICAL ANALYSIS OF PRIMARY TUMORS 106

IMAGING OF RETINOBLASTOMA CELLS 107

IN VITRO CELL MIGRATION EXPERIMENTS 107

IN VITRO CELL INVASION EXPERIMENTS 108

Spheroids embedded in Matrigel 108

Spheroids embedded in collagen type 1 108

IMMUNOFLUORESCENCE CELL STAINING 109

Coverslip preparation for non-adherent cells 109

Immunofluorescence staining protocol used for spheroid cells and cells attached to coverslips 109

STATISTICAL ANALYSIS 110

RESULTS 111

TFF1 IS THE GENE THE MOST DIFFERENTIALLY EXPRESSED BETWEEN RETINOBLASTOMAS SUBTYPES 111

EXPRESSION AND METHYLATION STATUS OF THE *TFF1* GENE ARE NEGATIVELY CORRELATED 112

TFF1 IS A SECRETED PROTEIN THAT CAN BE FIND IN THE NUCLEOUS, CITOPLASM AND THE EXTRACELLULAR SPACE OF RETINOBLASTOMA CELL LINES 114

TFF1 IS EXPRESSED IN CELLS INVADING THE POSTLAMINAR REGION OF THE OPTIC NERVE IN SUBTYPE 2 RETINOBLASTOMA PRIMARY TUMORS 115
ASSESSING THE ENDOGENOUS AND EXOGENOUS EFFECT OF TFF1 ON CELL VIABILITY *IN VITRO* 117
MOTILITY OF RETINOBLASTOMA CELL LINES 118
EVALUATION A POSSIBLE ROLE OF *TFF1* ON CELL MIGRATION AND CELL INVASION *IN VITRO* 119
TFF1 IS ACTIVELY TRANSCRIBED IN RETINOBLASTOMAS AND ITS EXPRESSION IS DOWNREGULATED FOLLOWING TREATMENT WITH BET BROMODOMAIN INHIBITORS 121
DISCUSSION AND CONCLUSIONS 124
THE ONCOGENIC ROLE OF TFF1 IN RETINOBLASTOMA IS STILL UNCOVERED 124
BIBLIOGRAPHY 128

Figures

FIGURE 1. TREFOIL FACTOR FAMILY OF PEPTIDES 99
FIGURE 2. MICRODEVICE USED IN CELL MIGRATION ASSAY 107
FIGURE 3. CULTURE PLATES USED FOR THE IN VITRO INVASION ASSAY 108
FIGURE 4. TFF1 EXPRESSION IN PRIMARY RETINOBLASTOMAS, CELL LINES AND PDX MODELS 112
FIGURE 5. TFF1 METHYLATION STATUS AND GENE EXPRESSION 113
FIGURE 6. CELLULAR LOCALIZATION OF TFF1 IN RETINOBLASTOMA CELLS 115
FIGURE 7. OPTIC NERVE INVASION IN THE 50 RETINOBLASTOMA-COHORT FROM THE GARRAHAN HOSPITAL 116
FIGURE 8. IMMUNOHISTOCHEMICAL STAINING OF POSTLAMINAR OPTIC NERVE INVASION 117
FIGURE 9. ENDOGENOUS AND EXOGENOUS EFFECT OF TFF1 ON CELL VIABILITY IN VITRO 118
FIGURE 10. EXTRACELLULAR MATRIX CONTENT OF THE HUMAN HUMOR VITREOUS AND OPTIC NERVE 119
FIGURE 11. CL-RB247 CELL CLUSTER EMBEDDED IN MATRIGEL 120
FIGURE 12. CL-RB247 CELL SPHEROIDS EMBEDDED IN COLLAGEN I 121
FIGURE 13. PUBLICLY AVAILABLE CHROMATIN IMMUNOPRECIPITATION SEQUENCING DATA OF TFF1 GENE IN FETAL RETINA, PRIMARY HUMAN RETINOBLASTOMA AND XENOGRAFT 122
FIGURE 14. EFFECT OF BET INHIBITORS ON TFF1 MRNA AND PROTEIN EXPRESSION 123

Tables

TABLE 1. TFF1 OVEREXPRESSION IN CANCER AND PROPOSED ONCOGENIC ROLE 102
TABLE 2. *ANTIBODIES USED IN IMMUNOHISTOCHEMICAL STAINING* 126
TABLE 3. SCORE OF SPEARMAN CORRELATION BETWEEN TFF1 METHYLATION AND EXPRESSION 126
TABLE 4. TUMOR GROUP CLASSIFICATION AND HISTOPATHOLOGICAL CHARACTERISTICS OF ENUCLEATED EYES FROM THE GARRAHAN HOSPITAL 126

INTRODUCTION

THE TREFOIL FACTOR FAMILY

The trefoil factor family (TFF) of proteins consists of three small, thermostable and protease-resistant polypeptides, which are secreted from the mucous-producing cells of the gastrointestinal tract of mammalian adults. The family was named for the disulphide bond configuration of the trefoil domain (or P-domain) which forms a three-leaved structure analogous to a trefoil or clover leaf (**Figure 1**) (Taupin and Podolsky, 2003; Thim and May, 2005). Each trefoil domain comprises 42–43 amino acids containing six cysteine amino acid residues, which form disulphide bonds resulting in the characteristic trefoil structure. Whereas TFF1 (6.5kDa) and TFF3 (6.6kDa) contain single trefoil domains, TFF2 (12kDa) consists of two such domains. TFF1 and TFF3 contain a seventh cysteine residue in the carboxy-terminal region that facilitates both homodimerization and intermolecular interactions with other proteins (Thim and May, 2005).

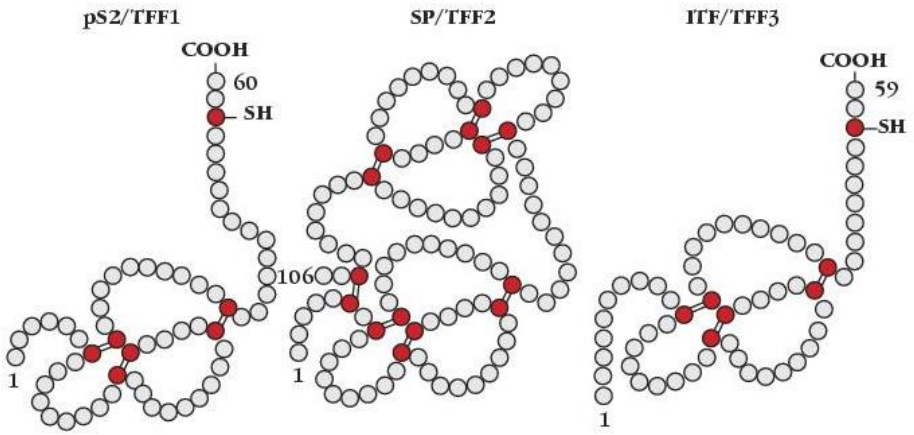


Figure 1. Trefoil factor family of peptides
TFF1 peptide has a molecular weight of approximately 6.5kDa, contains 60 amino acids, and one trefoil domain. TFF1 also exist naturally as a dimer of approximately 14kDa. TFF2 peptide contains 106 amino acids (12kDa) residing in two homologous trefoil domains, probably derived by genomic duplication. TFF3 contains one trefoil domain, 59 amino acids and has a molecular weight of approximately 6.6kDa (monomer) or 13kDa (dimer). Image adapted from (Mathelin et al., 2005).

The TFFs were discovered more than thirty years ago and recognized as new family of growth factor-like peptides (Thim, 1989). TFF2 the first TFF molecule to be discovered, was found in porcine pancreas during purification of insulin (Jørgensen et al., 1982b). Initial experiments showed that it had an inhibitory effect on gastric motility and acid secretion, and it was therefore termed pancreatic spasmolytic polypeptide (PSP) (Jørgensen et al., 1982a). TFF1 was the second TFF member to be discovered and was initially described as human breast cancer associated peptide 2 (hpS2), since it was discovered in a search for genes regulated by estrogen in the breast cancer cell line MCF-7

(Masiakowski et al., 1982; Prud'homme et al., 1985). The last described mammalian member of the family was TFF3. The peptide was cloned from rat intestinal epithelial cells during a search for proteins that contributed to the regulation of proliferation and differentiation among intestinal epithelial populations, and was consequently named intestinal trefoil factor (ITF) (Suemori et al., 1991). The human homologue was subsequently cloned and termed hP1.B in line with a classification system for P-domain peptides (Hauser et al., 1993; Podolsky et al., 1993).

BIOLOGICAL ROLES OF TFF PEPTIDES

TFFs have been implicated in protection of the gastrointestinal tract against mucosal damage and have an important role in its subsequent repair (Taupin and Podolsky, 2003). They are rapidly upregulated and secreted in an autocrine fashion in response to mucosal damage of the gastrointestinal tract. TFFs may not only participate in the early phase of epithelial repair known as restitution (marked by increased cell migration), but also play an important role in the subsequent, protracted phase of glandular renewal (marked by cell proliferation) (Nie et al., 2003). TFF peptides can also function as pro-angiogenic factors, which have beneficial effects on wound repair and mucosal protection (Rodrigues et al., 2003). In addition, TFFs are potent inhibitors of apoptosis and prevent anoikis (cell death induced by anchorage independence) during the cell migration process (Taupin and Podolsky, 2003). Many of the functional properties reported for the TFFs suggest a receptor-mediated mode of action, however signaling pathways that mediate TFF's effects have not been fully elucidated, and no definitive functional receptors have been identified for these peptides (Baus-Loncar and Giraud, 2005).

TFF EXPRESSION IN NORMAL TISSUES AND CANCER

All three human TFF genes are clustered on chromosome 21q22.3 within a 50-kb region (Chinery et al., 1996; Tomasetto et al., 1992). TFF peptides are major constituents of the mucosa. TFF1 and TFF2 are expressed in gastric epithelia and TFF3 expression was detected in all tissues containing mucus-secreting cells (Kjellev, 2009). Besides their prominent expression in mucous epithelia, TFF peptides are also synthesized in the central nervous system of rodents (Belovari et al., 2015; Hirota et al., 1995). Tff1 was found to be uniformly expressed in all brain regions, whereas Tff3 expression was limited to the hippocampus, the temporal cortex and the cerebellum. Tff3 mRNA was found mainly in neurons and not in glia cells (Hinz et al., 2004). TFF1 and TFF3 mRNA expression has also been detected in healthy human cornea, whereas only TFF3 was immunohistochemically detected in different corneal diseases (Steven et al., 2004) and involvement of Tff3 in corneal wound re-epithelialization was demonstrated *in vivo* (Paulsen et al., 2008).

Next to their best known physiological role in the gastrointestinal tract, they seem to display divergent effects depending on the patho-physiological state of the tissue they are expressed (Emami

et al., 2004). TFF expression has been described in several cancer cell lines. In the current literature, TFF peptides are discussed to act as tumor suppressors or as oncogenic factors (Perry et al., 2008). On the one hand, TFF peptides are overexpressed in several human solid tumors (Emami et al., 2004). TFF3 overexpression is frequently observed in gastric cancer where is considered a marker of poor prognosis (Leung et al., 2002), pancreatic cancer (Terris et al., 2002), hepatocellular carcinomas (where correlates with the tumor grade) (Okada et al., 2005), colon carcinoma (Uchino et al., 2000) and breast cancer (May and Westley, 1997; Poulsom et al., 1997). On the other hand, TFF1 has been described as a tumor suppressor gene in gastric carcinoma (Feng et al., 2014) given that TFF1-knockout mice develop gastric carcinomas and adenomas (Yio et al., 2006) and tumors of patients with gastric cancer usually display reduced TFF1 levels.

REGULATION OF TFF EXPRESSION

Trefoil factors are classical estrogen-regulated genes, and *TFF1* has been used as a marker of estrogen gene regulation by various environmental estrogens (Olsen et al., 2003; Ren et al., 1997). Estrogen acts to regulate *TFF1* gene expression through both activating protein 1 (AP1) and estrogen response elements (ERE) in the *TFF1* promoter (Baus-Loncar and Giraud, 2005). Paradoxically, the selective estrogen receptor modulator, tamoxifen, used to abrogate recurrence of estrogen receptor-positive breast cancer, has been demonstrated to enhance both *TFF1* and *TFF3* mRNA levels in human MCF-7 mammary carcinoma cells (Johnson et al., 1989; Kannan et al., 2007; Prest et al., 2002).

TFF gene expression is also regulated by several other growth factors that are clearly involved in the initiation and progression of cancer. These include autocrine human growth hormone (hGH) (Jackerott et al., 2006; Xu et al., 2005), insulin-like growth factor- 1 (IGF-1), transforming growth factor-b (TGF-b), epidermal growth factor (EGF) and fibroblast growth factor (FGF) (Baus-Loncar and Giraud, 2005). In addition, *TFF1* is regulated by the human epidermal growth factor receptor-2, HER-2 (Wilson et al., 2002). Furthermore, TFF gene expression is increased by hypoxia through hypoxia inducible factor-1 and by X-rays, phorbol esters, arachidonic acid and hydrogen peroxide (Baus-Loncar and Giraud, 2005; Emami et al., 2004). *TFF1* and *TFF3* also coregulate each other in a positive feedback loop (Taupin et al., 1999). Additionally, epigenetic mechanisms have been demonstrated to be involved in the regulation of TFFs in cancer (Baus-Loncar and Giraud, 2005; Emami et al., 2004; Philippeit et al., 2014).

TFF1: TUMOR SUPPRESSOR GENE OR ONCOGENIC FACTOR?

To date, the TFF1 function during malignant processes is not clearly defined, as epithelial cell transformation might lead to downregulation of TFF1 expression (in the stomach) or to the induction of TFF1 expression. It has been suggested that TFF1 might be a Janus factor in cancers depending on

the tissue. On the one hand, TFF1 acts as a gastric tumor suppressor gene. Accordingly, TFF1 expression is reduced in human gastric carcinomas due to TFF1 gene alterations (Katoh, 2003; Ribieras et al., 1998; Shi et al., 2006). Besides, a deficiency in TFF1 has been reported to increase the tumorigenicity of human breast cancer cells, thus supporting a tumor suppressor role (Buache et al., 2011). On the other hand, in different type of cancers, TFF1 expression is not downregulated but strongly induced (**Table 1**) suggesting a possible function as an oncogene (Perry et al., 2008).

Table 1. TFF1 overexpression in cancer and proposed oncogenic role

Cancer type	Overexpression in human tissue	*TFF1* action	*in vitro*	*in vivo*	Reference
Breast		migration stimulation of human breast cancer cells	X		(Prest et al., 2002)
	X	associated with breast cancer metastatic to bone			(Smid et al., 2006)
Prostate	X	may contribute to progression of prostate cancer cells			(Liu and Jin, 2015)
		promotes prostate cancer cell migration and invasion *in vitro* and metastasis *in vivo*	X	X	(Bougen et al., 2013)
Pancreas		motility stimulation of normal and cancer cells; increased metastasis *in vivo*	X	X	(Arumugam et al., 2011)
Kidney and colonic	X	cellular scattering and invasion in kidney and colonic cancer cells	X		(Emami et al., 2001)

TFF1 IN NORMAL RETINA AND RETINOBLASTOMA

The role of TFF1 in retinoblastoma tumorigenesis and underlying mechanisms have been sparsely studied so far. *TFF1* is not expressed in normal retina (Zhang et al., 2012) but has been found to be overexpressed in retinoblastoma cell lines and primary tumors (Weise and Dünker, 2013; Zhang et al., 2012). In 2013, Weise and Dünker (2013) reported a possible tumor suppressor role for *TFF1* in retinoblastoma, given that *TFF1* expression levels was negatively correlated with retinoblastoma cell's growth kinetics. In this work, they showed that retinoblastoma cell lines with high *TFF1* expression had increased cyclin-dependent kinase (CDK) inhibitor levels and downregulation of cyclin-dependent kinase (CDK) 6, thus suggesting a tumor suppressor role for *TFF1*. In 2017, the same group reported that forced *TFF1* expression induced apoptosis and decreased proliferation and tumor growth of human retinoblastoma cell lines in a p53- and caspase-dependent manner with implicated miR-18a regulation, further supporting a tumor suppressor function of *TFF1* in retinoblastoma (Busch et al., 2017a). Contradictory results from the same group were published months later, where the authors aimed to correlate TFF1 protein expression in primary tumors with different clinical parameters to evaluate involvement of TFF1 in tumor development and progression (Busch et al., 2017b). This retrospective study, based on immunohistochemical analysis, reported

that poorly differentiated unilateral tumors at a higher clinical tumor-node-metastasis stage expressed significantly higher levels of TFF1 than differentiated tumors at lower tumor-node-metastasis stages. In this case, results pointed to a possible oncogenic role of TFF1 in retinoblastoma tumorigenesis.

No clear functional role for *TFF1* in retinoblastoma tumorigenesis has been established to date, and the few published works on the subject are still contradictory.

Here we present the results performed in order to gain insights into a possible functional role of *TFF1* in retinoblastoma. For this purpose, we have performed *in vitro* experiments related to cell survival, cell migration and cell invasion.

MATERIALS AND METHODS

TRANSCRIPTOME ANALYSIS AND DIFFERENTIALLY EXPRESSED GENES BETWEEN RETINOBLASTOMAS OF SUBTYPE 1 AND SUBTYPE 2

Expression profiling was performed with the Human Genome U133 Plus 2.0 Array as previously described in **chapter 1**.

METHYLATION STATUS OF *TFF1* GENE

Methylation array data from 66 DNA samples were hybridized on Infinium HumanMethylation450 BeadChip arrays (Illumina, San Diego, CA), as described in **chapter 1**.

CELL CULTURE

Retinoblastoma cells were cultured in a humidified 37°C incubator with 5% CO2 in their respective culture media. WERI and Y79 cell lines were grown in RPMI 1640 (Life Technologies) supplemented with 10% fetal bovine serum (FBS) (Lonza), 100 U/mL Penicillin-Streptomycin (Gibco). CL-RB247 cell line was cultured in Iscove's Modified Dulbecco's Medium (IMDM) with 25 mM HEPES and L-glutamine (Life Technologies) supplemented with 10% FBS, 100 U/mL Penicillin-Streptomycin (Gibco), 10 mg/L insulin (Sigma) and 0.0005% (v/v) β-mercaptoethanol (Sigma).

RNA INTERFERENCE ASSAY

Retinoblastoma cell lines were transiently transfected using Lipofectamine RNAiMAX (Invitrogen) transfection reagent, according to the manufacturer's instructions in Opti-MEM (Gibco) or culture media without antibiotics. For gene silencing, 20nM of pre-designed short interfering RNA (siRNA) sequences targeting exon 2 of *TFF1* gene was used (s14034, ThermoFisher Scientific) and one siRNA against Luciferase GL2 gene (1022070, Qiagen) was used as control.

For RNA and protein extraction, cells were seeded in sterile 6-well plates at $1x10^6$ cells per well in 2.75mL of culture media. siRNA mix or lipofectamine alone were added, resulting in a total volume of 3mL per well. Final concentrations of BETi ranged from 300nM to 2.5µM. The cells were collected after 24h, 48h, 72h or 96h for further experiments. Three independent experiments were run for each cell line.

IN VITRO CELL VIABILITY ASSAY

Cell viability after transient knock down of *TFF1* gene

For cell viability assay, cells were seeded in a sterile 96-well black culture plate with transparent bottom at $2x10^4$ cells per well in 50µL of medium containing 10% FBS without antibiotics, in triplicates. siRNA mix or lipofectamine alone were added to the cells, resulting in a total volume of 100µL per well. After incubation for 24h, 48h, 72h and 96h at 37 °C, cell viability was assessed using the CellTiter-Glo Luminescent Cell Viability Assay (Promega) following manufacturer's instructions. Luminescence was measured using the FLUOstar OPTIMA plate reader (BMG LABTECH). Measurements were normalized with respect to the average signal for siRNA control wells, which represented 100% viability. Three independent experiments were run for each cell line.

Cell viability after treatment with human recombinant TFF1 protein

Cells were seeded in a sterile 96-well black culture plate with transparent bottom at 2x104 cells per well in 50µL of medium containing 10% FBS without antibiotics, in duplicates. Recombinant human TFF1 protein (MBL International, JM-4893) was used in a range of different final concentrations (12,5-0,001µg/mL), and water was used as control in a total volume of 100µL per well. After incubation for 48h and 72h, cell viability was assessed using the CellTiter-Glo Luminescent Cell Viability Assay, as described above.

TOTAL RNA ISOLATION AND REVERSE TRANSCRIPTION PCR (RT-PCR)

The total mRNA was isolated from transfected cells using the RNAeasy kit (Qiagen). Five-hundreds micrograms of total RNA was reverse-transcribed in 1X RT Buffer using the High-Capacity cDNA Reverse Transcription kit (Applied Biosystems) in a final volume of 20µL containing 1X dNTP Mix (4mM), 1X RT Random Primers, RNase Inhibitor (1U/µl) and MultiScribe RT (2.5U/µl). Reaction was run in a Mastercycler pro PCR System (Eppendorf) as follows: 25°C (10sec), 37°C (120min), 85°C (5sec).

REAL-TIME QUANTITATIVE PCR (qPCR)

Primer design was performed using Primer3 plus software. RT-qPCR was carried out in a LightCycler 480 Instrument (Roche) in a final volume of 20µL containing forward and reverse primers, 1X LightCycler480 SYBR Green I Master (Roche) and 10ng of cDNA. Thermal cycling conditions included a pre-incubation step at 95°C (5min), followed by 45 cycles at 95°C (20sec), 60°C (15sec) and 72°C (15sec). Melting curve analysis confirmed that each product was homogeneous and specific. Analysis was perfomed with the LightCycler 480 Software. Fold differences were calculated according to the $2^{-\Delta\Delta Ct}$ method and normalized against the endogenous expression of GAPDH gene.

Sequences of primers used are described below:

Gene	Forward 5'- 3'	Reverse 5'- 3'	Final Concentration
TFF1	CACCATGGAGAACAAGGTGA	AGCCCTTATTTGCACACTGG	700nM/500nM
GAPDH	AGCCACATCGCTCAGACAC	GCCCAATACGACCAAATCC	500nM/500nM

WESTERN BLOTTING

Protein extracts were obtained using lysis buffer (50mM Tris-HCl (pH 6.8), 2% SDS, 5% glycerol, DTT 2mM, 2.5mM EDTA, 2.5mM EGTA) freshly supplemented with Protease and phosphatase inhibitor (Roche). Cell lysates were clarified by centrifugation. Protein concentration was determined with a BCA Protein Assay-Reducing Agent Compatible kit (ThermoFischer). As TFF1 is a secreted protein, we collected conditioned culture media and filtered before performing wester blotting. A standard curve with known protein concentration was built in order to determine the amount of secreted protein. Analysis was performed using the Image Lab Software (BioRad).

Ten micrograms of protein or conditioned media[1] were loaded on SDS-polyacrylamide gels using 4-15% Tris-glycine precast gels (Biorad) and transferred to nitrocellulose membranes using a Trans-Blot Turbo transfer system (Biorad). Membranes were stained with 1x Naphthol Blue Black for rapid staining of protein bands (AmidoBlack staining, Sigma) and then blocked for 1h with 5% non-fat milk at room temperature. Next, membranes were incubated with the primary antibody overnight at 4°C: anti-TFF1 in 1:1000 dilution (HPA003425, Sigma), anti-βactin (A2228, Sigma). Secondary antibodies were horse anti-mouse IgG (7076s, Cell Signaling) or goat anti-rabbit IgG (7074, Cell Signaling) used in 1:3000 dilution, incubated for 1h at room temperature. Both primary and secondary antibodies were diluted in 5% non-fat milk PSBT (Phosphate Buffered Saline Tween 0.1%). Signal detection was performed using SuperSignal West Femto (ThermoFisher) or Clarity Western ECL (BioRad) substrates followed by exposure on X-ray film (ThermoFischer) or using the BioRad ChemiDoc MP instrument. Image analysis was performed using the Image Lab Software (BioRad).

IMMUNOHISTOCHEMICAL ANALYSIS OF PRIMARY TUMORS

Primary tumors were fixed in alcohol-formaldehyde-acetic acid (AFA) or buffered formol and then paraffin-embedded and process into 5µm thick cuts and placed on glass slides. Hematoxylin Erythrosine Saffron (HES) staining was performed according to classical histologic procedures. Immunostaining was performed in 5µm thick paraffin-embedded sections using the following anitbodies: anti-CRX (ab140603, Abcam), anti-ARR3 (111 00-2-AP, EUROMEDEX), anti-EBF3

[1] Conditioned media was loaded according recommended volume for the gel type. Protein and conditioned media were loaded in equal volume.

(H00253738-M05, Abnova), anti-TFF1 (HPA03425, Sigma), anti-KI67 (ab15580, Abcam). Dilutions and protocol are described in **Table 2** (page 126). The presence of histopathological risk factors (optic nerve invasion, choroidal infiltration, anterior segment invasion and scleral infiltration) was assessed by experienced pathologist specialized in retinoblastoma.

IMAGING OF RETINOBLASTOMA CELLS

Before performing *in vitro* migration and invasion experiments, cells were imaged with a video-microscope (Inverted microscope Nikon Ti-E, camera CCD 1392x1040 CoolSnap HQ2 (pixel:6.45µm) Photometrics) equipped with an environmental chamber that provides the desired environmental conditions for the cell culture (37°C temperature, 5% CO_2 and humidity), in order to detect cell motility. Retinoblastoma cells in their normal culture conditions were imaged overnight and at different time points.

IN VITRO CELL MIGRATION EXPERIMENTS

Cell migration was carried out using fabricated micro-channels as described in Vargas et al. (Vargas et al., 2014, 2016). This method allows the study of cell migration under confinement in one dimension. In this system cells migrate along microchannels into which they enter spontaneously. Once inside channels, cells have only two possibilities: move forward or backward (**Figure 2**).

Micro-channels were kindly provided by Pablo Vargas and group. Micro-channels were prepared 24h before it use. Their surface was coated with 10 µg/ml bovine plasma fibronectin (Sigma) or collagen type I (Corning) for 1 h and then washed 3 times with PBS before introduction of cells in complete medium. $5x10^4$ cells in 50µL of complete media were introduced in the entry hole of the channels. Microchips were incubate for 30 min at 37 °C, and then 2mL of complete medium was added to the experiment dish. Cell were allowed to migrate for up to 72h.

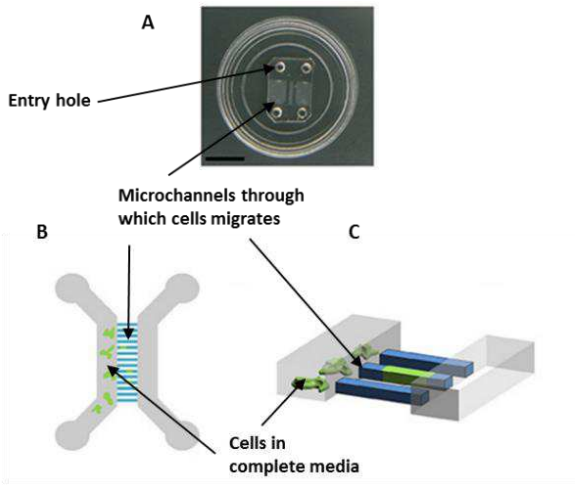


Figure 2. Microdevice used in cell migration assay

A) The assembled chip provided with variable size (10µm-20µm) of microchannels on top of a glass dish. B) Top view of the schematic representation of the device. C) Side view. Green objects represent cells in or out channels (blue). Scale bar= 1 cm. (Adapted from (Vargas et al., 2014)).

IN VITRO CELL INVASION EXPERIMENTS

Retinoblastoma cell invasion was assessed by embedding cells whether in matrigel or collagen, and followed them over time for invasion detection. CL-RB247 cells ($5x10^3$) were seeded in a 96-well plate containing cell culture media in a final volume of 100µL and spheroids were left to form for 2-3 days.

Spheroids embedded in Matrigel

A 24-well plate was pre-coated with 100µL of matrigel in a final concentration of 5mg/ml (Matrigel Growth Factor Reduced (GFR) Basement Membrane Matrix, Corning #354230). One spheroid contained in 30µl of IMDM culture media was transferred per well and embedded in 270µl of matrigel. Once solidified, 500µL of IMDM was added. Embedded cell spheroids were incubated in normal culture conditions (as described above); culture media was changed every 48 hours. Spheroids were photographed using a Leica microscope provided with a camera, and videotaped overnight the first 12 hours after being embedded, using the video-microscope described above.

Spheroids embedded in collagen type 1

30-mm^2 tissue culture plates were specifically fashioned for the invasion assay as described in Attieh et al. (Attieh et al., 2017). Briefly, three holes of 3-4mm in diameter were drilled in a plate and widened around the edges using a scalpel. The bottom of the dish was covered with epoxy (Loctite), and 20×20mm square coverslips were glued to the dish overnight at RT. Before the experiments, the dishes were washed extensively with ethanol and let dried before using (**Figure 3**).

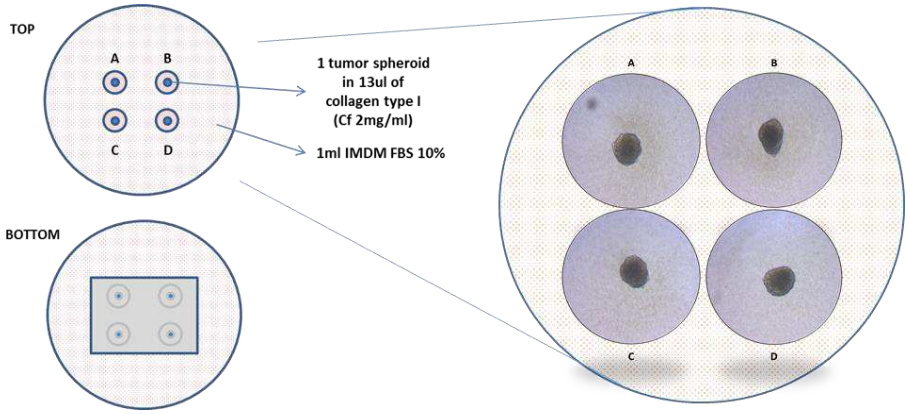


Figure 3. Culture plates used for the in vitro invasion assay
Top and side view of the culture plates containing cell spheroids. The zoomed view shows CL-RB247 spheroids embedded in collagen I.

Rat tail type 1 collagen (Corning, #354236) was prepared in IMDM, PBS 10X and NaOH 1M to a pH of 7, at a final concentration of 2 mg/ml. The solution was kept on ice to avoid collagen polymerization. Spheroids were embedded in 13µl of collagen drops and positioned in the hole of the culture plate. After filling all three or four holes, the plate was turned every 30 seconds for 5 minutes in order for the cells to stay in the middle of the collagen drop (preventing sedimentation of spheroids to the glass or to the collagen/air interface). Collagen was left to polymerize for an additional 15 minutes at RT before 3ml IMDM supplemented with 10% FBS and 1% antibiotics were added. Cancer cells were photographed the day zero, at 24h, at day 6, day 8 and day 11. Spheroids were left to invade for 23 days before fixing and staining.

IMMUNOFLUORESCENCE CELL STAINING

Coverslip preparation for non-adherent cells

Glass coverslips were coated with 10µg/mL of Poly-D-Lysine (PDL) (Sigma, #P6407) for 10 minutes at room temperature, in order to cells to adhere. Excess of PDL solution was aspirated and coverslips were allowed to dry completely, for about 2 hours in sterile hood. Pre-treated coverslips were transferred to the bottom of wells of a 24-well plate. Cells (10^5 or $5x10^4$) were then transferred to the plate in 1mL of culture media per well, and incubated until the cells have adhered to the coverslips.

Immunofluorescence staining protocol used for spheroid cells and cells attached to coverslips

Cells were fixed in 4% paraformaldehyde (PFA) for 10 minutes at room temperature, washed two times in PBS 1X and then permeabilized for 5 minutes in PBS Triton 0.5%. Two additional washed were performed in a shaker at 80 rpm. Blocking was performed for 1 hour in BSA 5% PBS Triton 0.1% at room temperature, and then washed with PBS-Tween. Cells were incubated with the primary antibody for 1 hour. Anti-TFF1 (HPA03425, Sigma) was used in 1:100 dilution, in PBS Triton 0.1% BSA 1%. Afterwards, washing was performed three times with PBS 1X. Secondary antibody Alexa Fluor 488 Goat Anti-Rabbit IgG (H+L) (Life Technologies, a11034) was used in 1:500 dilution (PBS Triton 0.1% BSA 1%). Cells were incubated for 30 minutes and then washed with PBS 1X. DAPI nuclear staining (ThermoFischer Scientific, D1306) was performed for 5 minutes, then washed two times. Coverslips containing attached cells were mounted to glass slides using Mowiol medium (81381, Sigma). Cells and spheroids were imaged using an epifluorescence microscope (Upright microscope, Leica DM6000) provided with a camera (CCD 1392x1040 CoolSnap HQ (pixel:6.45 µm), Photometrics). Images were analyzed using the ImageJ software.

STATISTICAL ANALYSIS

We used GraphPad Prism (version 7.03) for generating graph and analysis of data. Unpaired two-tailed t-test (using Welch's adjustment for heteroscedasticity when necessary) was used to compare: *TFF1* expression in retinoblastomas subtypes, fetal retina, cell lines and PDX models; differences in cell viability and gene expression (control siRNA (siC) vs siRNA TFF1 (si034)). Person's correlation was used for *TFF1* mRNA expression and methylation correlation. P-values indicating significant differences were noted as follows: ns (not significant); * ($p<0.05$); ** ($p<0.01$); *** ($p<0.005$); **** ($p<0.0001$).

RESULTS

TFF1 IS THE GENE THE MOST DIFFERENTIALLY EXPRESSED BETWEEN RETINOBLASTOMAS SUBTYPES

Differentially expressed genes between the two retinoblastomas subtypes were identified using Limma in tumor samples for which the transcriptome was available (N=59), and for which a tumor subtype had been assigned (N=27 subtype 1 tumors, N=32 subtype 2 tumors). A total of 6699 genes were differentially expressed between subtypes (fold change 2 with adjusted pvalue <0.05). Photoreceptor cone cell-related genes like *GUCA1C*, *GUCA1B*, *GNAT2*, *ARR3*, *GNGT2*, *GUCA1A*, *PDE6C* and *PDE6H* (Kaewkhaw et al., 2015; Rodgers et al., 2016) were among the most significantly upregulated genes in subtype 1 tumors, together with the epidermal growth factor peptide coding gene *EGF*. In the other hand, retinal ganglion cell-related genes like *EBF3*, *GAP43*, *STMN2* and *POU4F2* (Aldiri et al., 2017; Gill et al., 2014; Kaewkhaw et al., 2015; Völkner et al., 2016) were among the most significantly upregulated genes in subtype 2 tumors, together with *CD24* and *TFF1* (**Figure 4A**).

TFF1 was the most upregulated gene in subtype 2, and the most significant differentially expressed gene between subtype 1 and subtype 2 retinoblastomas. *TFF1* expression distribution allows a good separation of both subtypes (**Figure 4B**). Different levels of *TFF1* expression are detected in subtype 2 tumors, and no significant differences exist when comparing to expression levels of cell lines (p=0.1006) and PDX models (p=0.3530). *TFF1* is expressed in retinoblastoma cell lines (CL-HSJD-RBT2 > CL-RB247 > CL-HSJD-RBVS10 > CL-HSJD-RBT5 > WERI > CL-RB1021 > Y79 > CL-HSJD-RBT7) and PDX models (RBX109 > RBX102 > RBX111 > RBX210 > RBX200 > RBX218 > RBX215 > RBX206 > RBX202) (**Figure 4C** and **Figure 4D**), impliyng that these models derived from C2 retinoblastomas. On the other hand, *TFF1* is not expressed in fetal retinas (weak ages: 27, 24 and 20) and virtually in none of tumors of the subtype 1 (**Figure 4C** and **Figure 4D**).

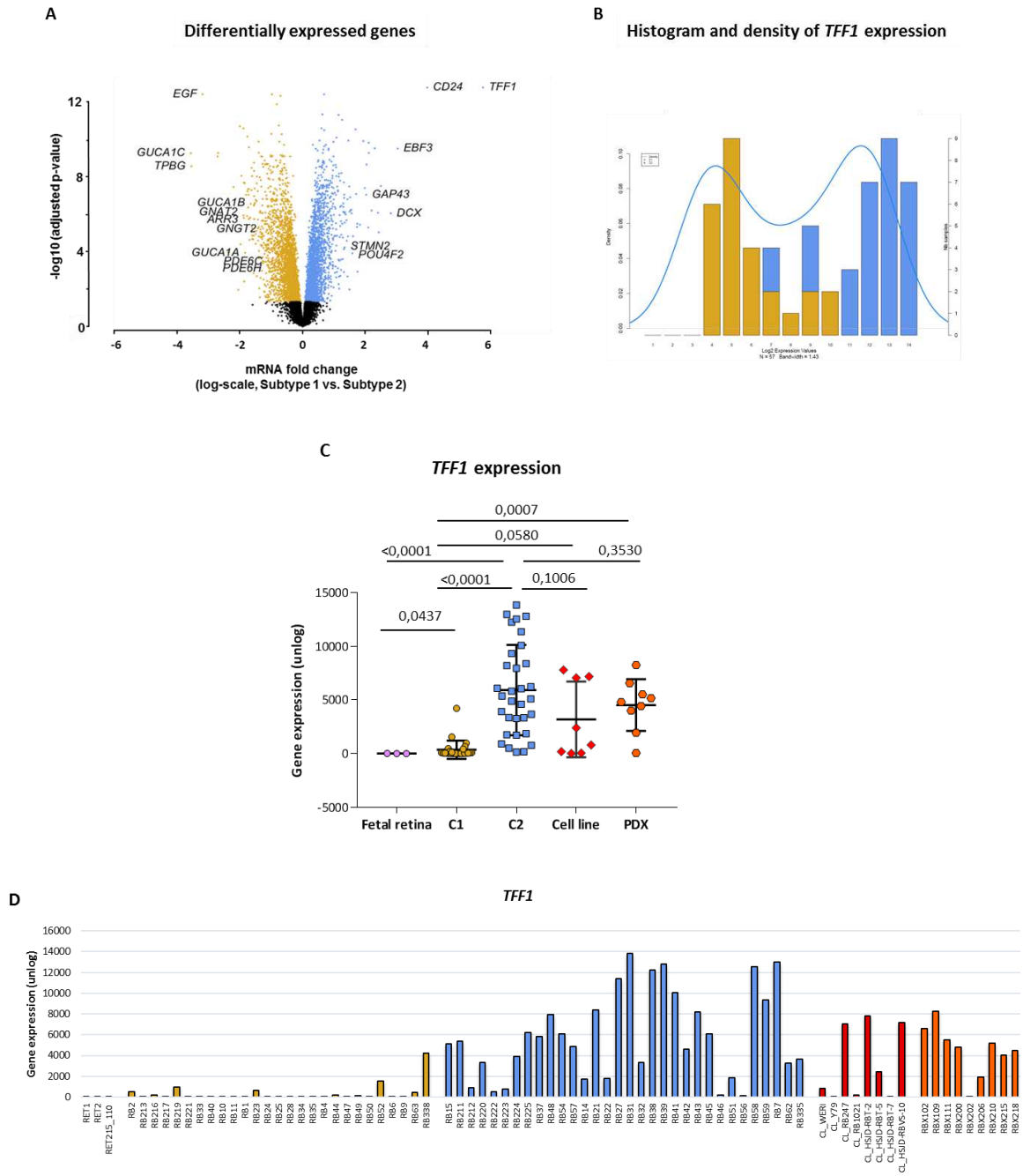


Figure 4. TFF1 expression in primary retinoblastomas, cell lines and PDX models

A) Volcano plot depicting differentially expressed genes in subtype 1 (gold) and subtype 2 (blue) retinoblastomas. The most upregulated genes in each subtypes are EGF and TFF1, respectively. The genes highlighted are those related to photoreceptor's cone cells in the subtype 1, and to retinal ganglion cells in the subtype 2. B) Histogram and density plot of TFF1 expression across retinoblastomas. C) Statistical differences between TFF1 mRNA expression in fetal retinas, C1 tumors, C2 tumors, cell lines and PDX models. D) Levels of TFF1 mRNA expression in fetal retinas, C1 tumors, C2 tumors, cell lines and PDX models.

EXPRESSION AND METHYLATION STATUS OF THE *TFF1* GENE ARE NEGATIVELY CORRELATED

Analysis of our own methylomic data (N=22 C2 tumors, N=19 C1 tumors, N=2 cell lines, N=2 fetal retinas, N=2 PDX models) revealed a significant negative correlation between gene methylation and

level of *TFF1* expression (Pearson's correlation R= -0,9022, p<0,0001) (**Table 3**). The fetal retina and tumors of the subtype 1 have a greater proportion of methylation in the *TFF1* gene, consistent with low values of *TFF1* expression, and the two PDX models analyzed (RBX102 and RBX111) has the lowest values of gene methylation, as tumors from the subtype 2 (**Figure 5A** and **Figure 5B**). Y79, the cell line expressing the lowest values of *TFF1* expression presents with high levels of gene methylation, contrary to what is seen in WERI cell line (**Figure 5C**).

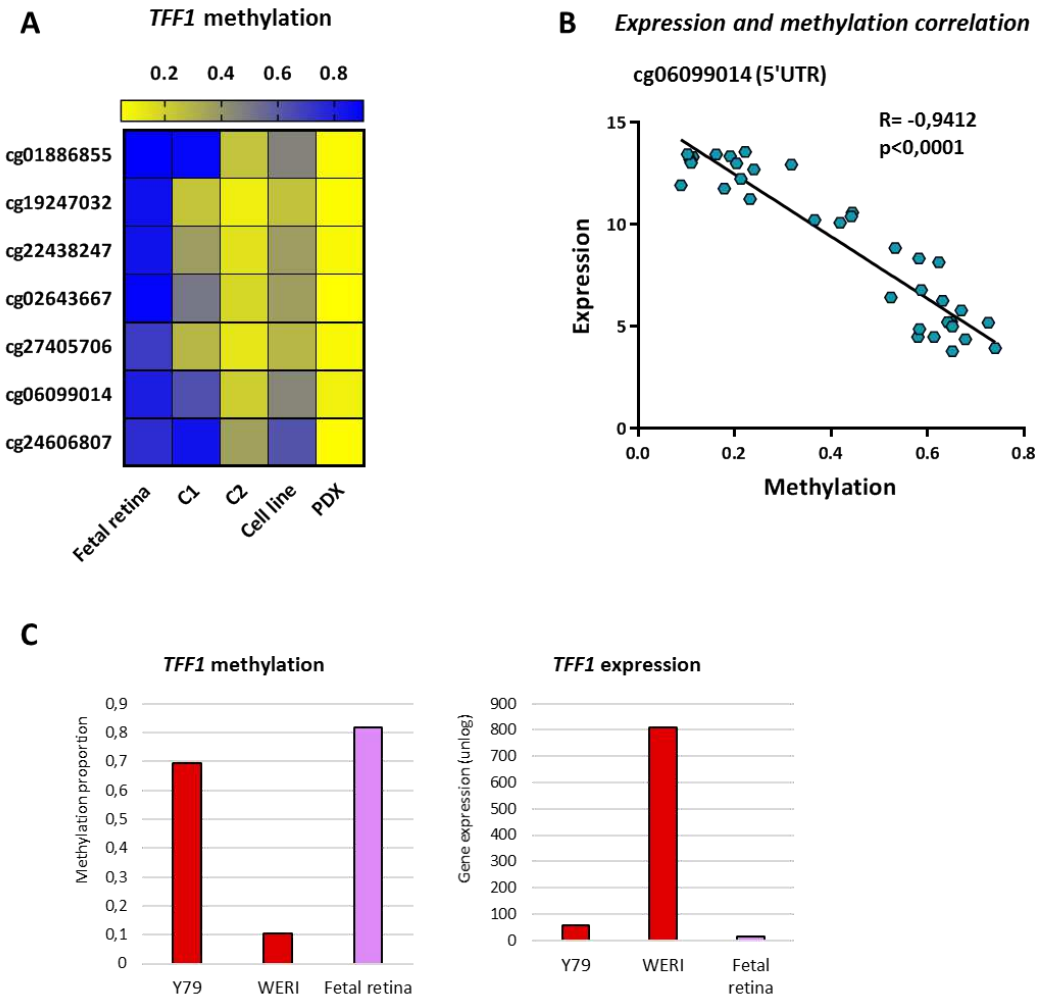
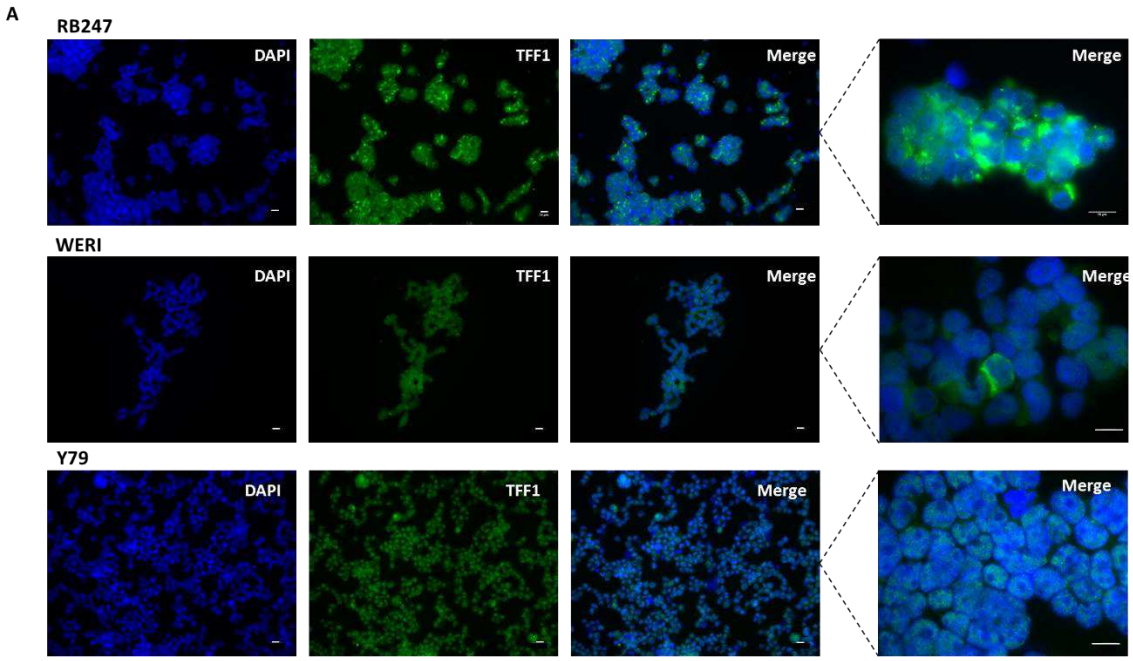
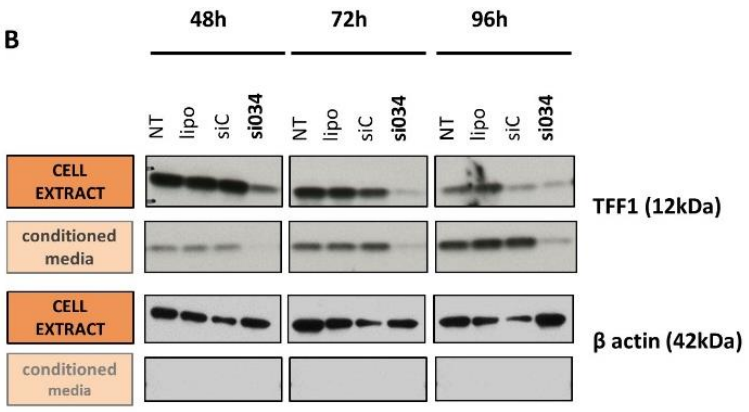


Figure 5. TFF1 methylation status and gene expression
A) *TFF1* methylation status in fetal retina, C1 and C2 tumors, cell lines and PDX models. *TFF1* is highly methylated in fetal retinas and highly hypomethylated in PDX and C2 tumors. B) Significant negative correlation between *TFF1* expression and methylation status of the CpG the most significant correlated (Pearson's correlation R= -0,9412, 95% confidence interval -0,9698 to -0,8868, two-tailed P value <0,0001). C) Negative correlation between TFF1 expression and overall methylation in two cell lines for which the methylome was available. Y79 and fetal retinas have similar levels of *TFF1* methylation.

TFF1 IS A SECRETED PROTEIN THAT CAN BE FIND IN THE NUCLEUS, CYTOPLASM AND THE EXTRACELLULAR SPACE OF RETINOBLASTOMA CELL LINES

TFF1 is reported to be a secreted peptide that can be fond in the intracellular (nuclear or cytoplasmatic) as well as the extracellular space of human cells (Binder et al., 2014; Thul et al., 2017). In order to detetec intracellular localization of TFF1 protein in retinoblastoma cells, we have performed immunofluorescense staining in CL-RB247, WERI and Y79 cell lines (**Figure 6A**). TFF1 was found mostly in the cytoplasm of CL-RB247 and WERI cells, with stronger signals in cell-cell junctions. In the other hand, Y79 cells seemed to have a weak nuclear signal for TFF1, with no detectable cytoplasmatic expression of the protein. Besides, TFF1 could be detected in the conditioned media of CL-RB247 and WERI cells and seemed to be regulated in a reciprocal way related to the intracellular content (**Figure 6B**). Absolute quantification of secreted TFF1 protein was performed and values ranging from 0.3-2.4µg were found in conditioned media of CL-RB247 cells.





standard curve					48h				72h				96h				
21µg	14µg	7µg	3µg	1µg	NT	lipo	siC	si034	NT	lipo	siC	si034	NT	lipo	siC	si034	sample
21	14	7	3	1	0,9	0,5	0,3	N/A	1,3	1,8	0,9	N/A	1,7	2,4	1,9	N/A	absolut quantification(µg)

Figure 6. Cellular localization of TFF1 in retinoblastoma cells
A) Immunolocalization of TFF1 in CL-RB247, WERI and Y79 cells. TFF1 is mostly localized in the cytoplasm of CL-RB247 and WERI cells, while a faint nuclear localization is seen in Y79 cells. Nuclear DAPI staining (blue), TFF1 staining (green). Scale bar 10µm. B) Western blotting showing intracellular (cell extract) and extracellular (conditioned media) of TFF1 in CL-RB247. TFF1 is downregulated after transient gene knock down from 48h after transfection using a siRNA against TFF1 (siRNA: si034). TFF1 in conditioned media increase over time, while a decrease is observed in cell extract, as if cells were producing and secreting TFF1 to the media. Absolute quantification of secreted protein is indicated in the table below the blot. NT: non treated cells; lipo: lipofectamine control; siC: control siRNA; si034: siRNA against TFF1.

TFF1 IS EXPRESSED IN CELLS INVADING THE POSTLAMINAR REGION OF THE OPTIC NERVE IN SUBTYPE 2 RETINOBLASTOMA PRIMARY TUMORS

Given that overexpression of *TFF1* has beeen implicated in disease progression of several types of cancer (**Table 1**, page 102), and mainly implicated in migration and invasion of the tumoral cells, we have analyzed a series of 50 fixed retinoblastomas blocks from the Garrahan Hospital. The great majority of these tumors presented with optic nerve invasion (N=41, 82%) in the prelaminar (N=19) or in the postlaminar (retrolaminar) region (N=22). Many of these patients presented along/or with choroidal infiltration (N=42), anterior segment invasion (N=6), and scleral infiltration (N=10) (**Table 4**, page 126). Massive invasion of the choroid, optic nerve, sclera, and ciliary body are considered to be high-risk features of extraocular relapse in patients with retinoblastoma (Chantada et al., 2007a; Kaliki et al., 2013). When the tumor invades through the lamina cribosa (postlaminar invasion), the risk for extraocular relapse increases significantly, especially if the resection margin is invaded by tumor, since microscopic disease is left behind after enucleation (Chantada et al., 2007b). Therefore, in order to correlate the presence of retrolaminar invasion to the tumor subtype and the phenotype of the invading cells (TFF1+ positive or ARR3+ positive), we analyzed the series of 50 retinoblastomas by immunohistochemical staining.

We assigned a tumor subtype based on our pyrosequencing signature (when tumoral DNA was available) and/or by immunohistochemical TFF1 staining. From the 22 tumors presenting with retrolaminar optic nerve invasion, fifteen could be classed in the subtype 2 (N=15/22, 68%) and six tumors in the subtype 1 (N=6/22, 27%) (**Figure 7A**). One tumoral sample could not be attributed to any subtype since DNA to performed pyrosequencing analysis was not available and extent of TFF1 staining could not be determined due to faint staining.

We then analyzed the phenotype of cells invading into the retrolaminar region of the optic nerve. Retrolaminar invasion in subtype 1 tumors were evidently ARR3+, given that no or a small percentage of TFF1 positive cells are detected in this subtype. On the other hand, we found that cells invading the optic nerve of subtype 2 tumors were positive for TFF1 (N=9/15) (**Figure 7B**). One example of tumors with TFF1+ cells in the retrolaminar region of the optic nerve is shown in **Figure 8A**. Only one C2 tumor (RB593, pyrosequencing-based classification) presented only ARR3 positive cells in the optic nerve. This tumor had low percentages of TFF1+ (10%), while most tumor was ARR3+ comprising the closest area to the optic nerve (**Figure 8B**). Very likely, this tumor is actually a C1 with some expression of TFF1. For the remaining 5 cases with postlaminar optic nerve invasion, we could not concluded if cells invading were positive for TFF1 or ARR3, given that either the optic nerve head was no present in the tumoral slide or the IHQ staining was doubtable or weak, so these cases remained "elusive".

Even though TFF1 is heterogeneously expressed in subtype 2 tumors, we found in nine out of fifteen cases, tumoral cells systematically expressing TFF1 in the invaded area of the optic nerve. This observation of TFF1+ cells associated with postlaminar optic nerve invasion led us to hypothesized that *TFF1* could be involved in the ability of cell to invade, suggesting an oncogenic role for *TFF1* in cell survival or in cell migration and/or invasion.

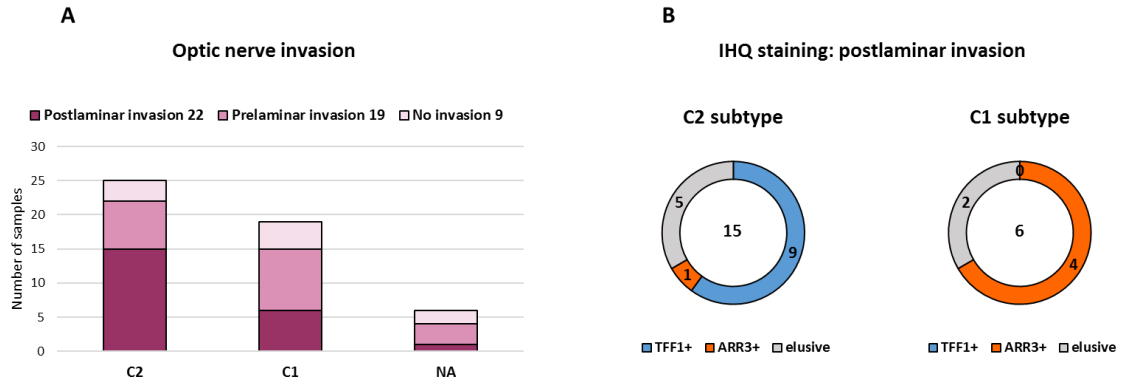


Figure 7. Optic nerve invasion in the 50 retinoblastoma-cohort from the Garrahan Hospital
A) Although not reaching significance (p= 0.107, Fisher's Exact Test), postlaminar optic nerve invasion was predominantly found in enucleated eyes that were classed in the C2 subtype, while prelaminar invasion was mostly found in C1 subtype tumors. B) Fifteen C2 tumors presented with retrolaminar invasion that was positive for TFF1 staining in nine tumor samples. Six C1 tumor samples presented postlaminar optic nerve invasion, positive for ARR3 staining.

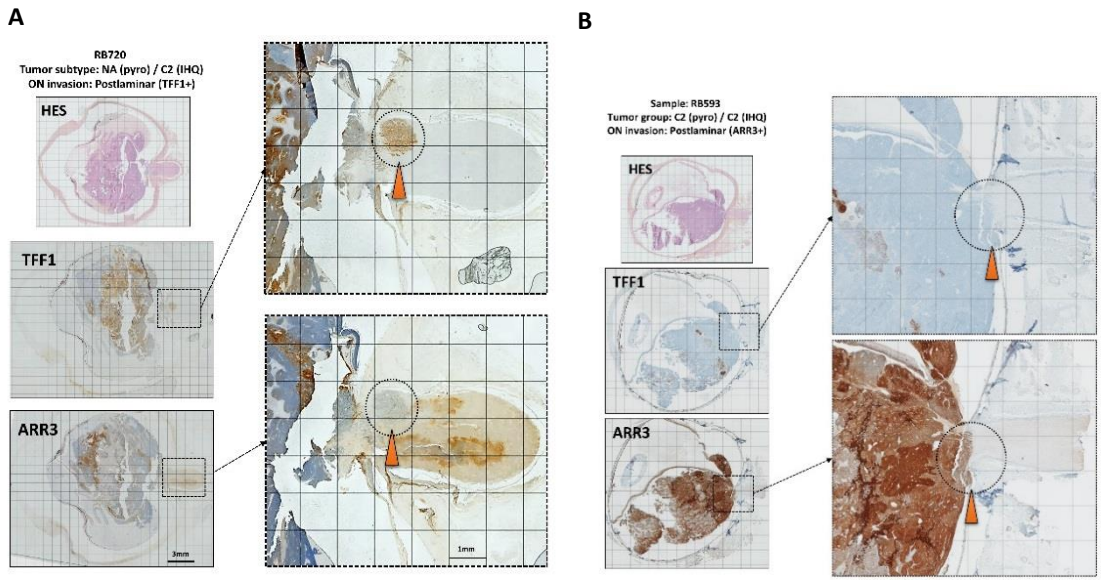


Figure 8. Immunohistochemical staining of postlaminar optic nerve invasion
TFF1 and ARR3 staining for (A) RB720 sample corresponding to a C2 tumor (based on IHQ) with positive TFF1 staining in cells invading the optic nerve and (B) RB593 sample classed in C2 subtype (based on pyrosequencing signature classification) with ARR3 positive cells in the invasion area.

ASSESSING THE ENDOGENOUS AND EXOGENOUS EFFECT OF TFF1 ON CELL VIABILITY *IN VITRO*

With the purpose of uncovering a possible role of *TFF1* on cell survival, we transiently knocked down the *TFF1* gene in CL-RB247 and WERI cell lines. Among the four cell lines available, we chose CL-RB247 and WERI cells, expressing high and low levels of TFF1 gene and protein, respectively (**Figure 9**). The siRNA against TFF1 used (si034) produced a high inhibitory effect on TFF1 expression both at the mRNA and intracellular and secreted protein levels (**Figure 9B** and **Figure 9C**). We performed transient transfection for 48h, 72h and 96h and assessed effect on cell viability using the CeltiterGlo method. No effect on cell viability was appreciated in treated cells compared to the siRNA control (**Figure 9D**).

As TFF1 is a secreted protein that can be find in the conditioned media of retinoblastoma cells, its action could be mediated from the extracellular space. In order to assess cell viability in this condition, we treated Y79 cell line (not expressing TFF1) with a human recombinant TFF1 protein (rTFF1) supplemented to the culture media. We used a range of final concentrations comprising the reported biologically active range (0.5-10µg/mL) of the recombinant protein to treat Y79 for 48h and 72h (**Figure 9E**). Following our hypothesis, we were expecting to enhance Y79 viability, but no significant effects were detected.

Overall, we did not detect any effect on cell viability by knocking down the endogenous expression of *TFF1* gene or applying an exogenous TFF1 protein to retinoblastoma cell lines.

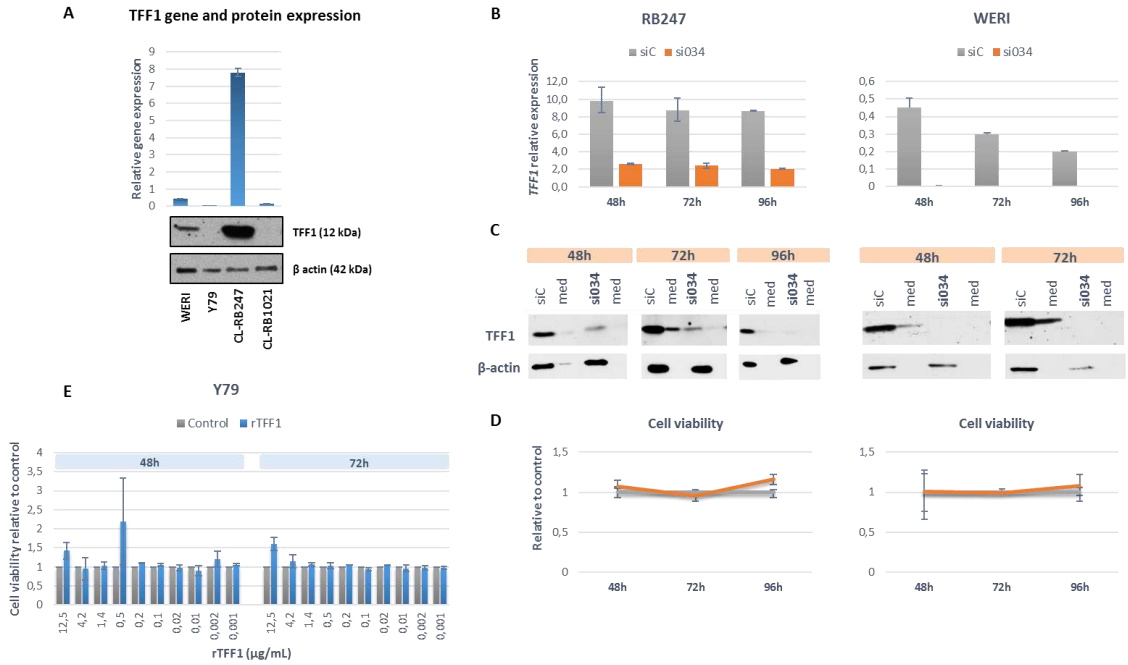


Figure 9. Endogenous and exogenous effect of TFF1 on cell viability in vitro
A) TFF1 gene and protein expression in four retinoblastoma cell lines. TFF1 transient knock down using a siRNA targeting gene exon 2. TFF1 is highly reduced at both the mRNA (B) and the protein level (C) from 48h of transfection, while cell viability is not affected (D) in neither CL-RB247 (left) or WERI (right) cells. Cell viability was neither affected by treating Y79 cells with a human recombinant TFF1 protein (E).

MOTILITY OF RETINOBLASTOMA CELL LINES

Before moving to assess the *in vitro* capacity of migration and invasion of cells expressing *TFF1*, we imaged CL-RB247, WERI and Y79 cell lines in order to see whether cells were motile. Cell were video recorded for 2 hours in their normal culture conditions and in plates coated with collagen I in a videomicroscope provided with a camera ensuring the good condition for cell culture, as described in material and methods. CL-RB247 were the most motile cells, followed by WERI and Y79 (data not shown), assessed by cell movement on a 2D surface. Cells did adhere to the matrix surface used, but did not changed their spherical morphology to an adherent phenotype. The three cell lines displayed bleb-like protrusions, seen as dynamic small rounded protuberances expanding and shrinking from the cell membranes. Blebs are spherical membrane protrusions that are produced by contractions of the actomyosin cortex (Charras and Paluch, 2008). Blebs are often considered to be a hallmark of apoptosis, but are also frequently observed during cytokinesis and during migration in three-dimensional cultures and *in vivo*. For tumor cells and a number of embryonic cells, blebbing migration seems to be a common alternative to the lamellipodium-based motility (Sahai and Marshall, 2003). Given that retinoblastoma cells grows in suspension and do not adhere to matrix substrates in *in vitro* conditions, blebbing could be a way for cells to move or migrate in such conditions.

EVALUATION A POSSIBLE ROLE OF *TFF1* ON CELL MIGRATION AND CELL INVASION *IN VITRO*

We used a microfluidic device to assess cell migration, in which the cells are introduced into microchannels of different µm width. Once inside the channels, cells simply migrates through, forward or backwards, and cell movement can be monitored by live imaging or photographed. According to the general tumoral cell's size, we used channels of 10µm, 12µm, 14µm, 16µm, 18µm and 20µm. CL-RB247, WERI and Y79 cells ($8x10^4$ in 80µL of complete media) were introduced in the entry hole of the channels and allow migrating for 72h. Following our hypothesis of *TFF1* enhancing the cell migration capacity, cells expressing *TFF1* were expected to have an advantage in migration through the microchannels. Y79 were used as control, given that are reported to be a metastatic cell line (Chevez-Barrios et al., 2000). As we were interested in mimicking cell migration through the optic nerve, the microfluidic device was coated with either fibronectin (component of the human optic nerve head) or collagen I (main component of the human optic nerve head and fasciculated segment) (**Figure 10**), in an effort to better represent the natural microenvironment through which cells may migrate. After 72h, the three cell lines have entered into the microchannels but they stayed still, and no migration was appreciated using this *in vitro* assay.

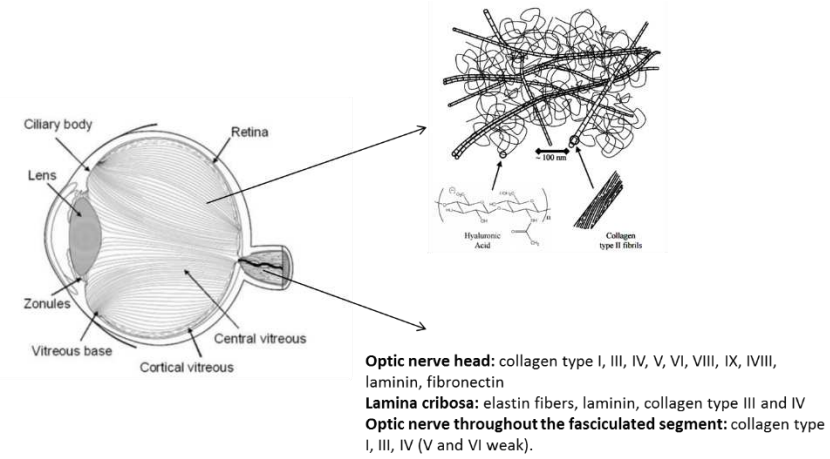


Figure 10. Extracellular matrix content of the human humor vitreous and optic nerve
Vitreous is mainly composed of hyaluronic acid and collagen type II fibrils. The optic nerve head is composed by a mix of collagen type I, III, IV, V, VI, VIII, IX and IVIII, laminin, fibronectin. The lamina cribosa consist of elastin fibers, collagen type III and IV, and laminin. The nerve fibers of the optic nerve are myelinated in the orbital part and rest of optic nerve, but they are unmyelinated in the lamina cribrosa. Throughout the fasciculated segment extending to the central nervous system, the optic nerve is composed by collagen type I, III and IV (V and VI weak).

Thereupon, we decided to move forward to assay the invasion capacity of the highly *TFF1* expressing cell line (CL-RB247). These cells grows in clusters and spontaneously forms tumor cell spheroids (**Figure 3**). Taking advantage of this characteristic, we first embedded these cell clusters in matrigel (5mg/ml) in a 24-well plate, and monitored them for 72h (**Figure 11**). The main components of the matrigel matrix are laminin, collagen IV and entactin (nidogen), similar to the human optic nerve

head composition (**Figure 10**). After 72h, we found that cell cluster did grow and expand, but no cells were found to invade through the matrix. At this time point, we also video-recorded the cell cluster embedded during 12h. In the video, the expansion of cell cluster due to cell grow was better-appreciated (**Figure 11**).

Next, we decided to carry out another experiment for evaluating cell invasion *in vitro*, this time using a different matrix. We seeded $5x10^3$ CL-RB247 cells in 100µL of complete culture media in a 96-well plate, in order to generate smaller spheroids that could be embedded in collagen I (2mg/ml), as described in materials and methods. Eight tumoral spheroids were embedded and followed up to 20 days. Spheroid were found to grow and expand in the collagen matrix, but do not invade throughout (**Figure 12**). At day 20, we performed immunofluorescence staining of the spheroids in order to detect TFF1 expression. TFF1 was mainly expressed in the necrotic center of the spheroids, while DAPI staining was detected in the periphery of the spheroid (**Figure 12**), consisting with the presence of living cells.

Taking together, using the *in vitro* approaches aforementioned, we were not able to confirm our hypothesis that TFF1 was involved in the retinoblastoma cell migratory and/or invasive capacity. For future experiments, it would be interesting to assess the role of TFF1 in *in vivo* approaches given that the eye microenvironment could be an important determinant of *TFF1* function that is not possible to analyze in artificial *in vitro* experiments.

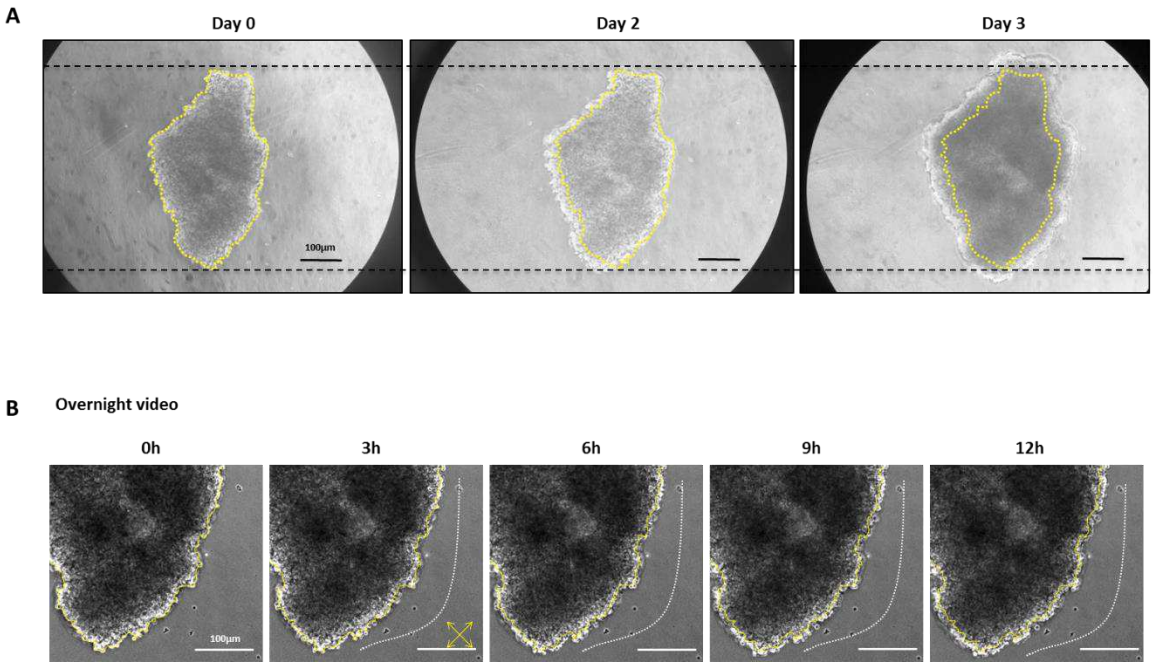


Figure 11. CL-RB247 cell cluster embedded in matrigel
A) Cell cluster proliferates and expands over time, but no cells invade throughout the matrix. B) Live imaging of the cell cluster during 12h showed clearly that cells expand pushing the matrix but not invading through.

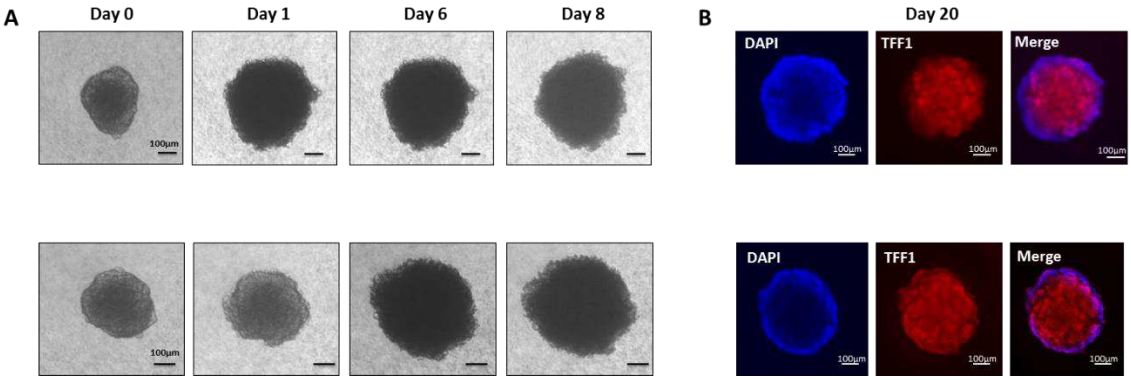


Figure 12. CL-RB247 cell spheroids embedded in collagen I
A) Two cell spheroids are shown. They were followed up to 8 days and found to grow and expand the diameter of the spheroid, but no cells were detect to invade through the collagen matrix up to 20 days. B) Immunofluorescence staining of cell spheroids at day 20. The necrotic center of the spheroids is TFF1+ while nuclear staining is seen in the periphery of the spheroid, corresponding to living cells. DAPI nuclear staining (blue), TFF1 (red). Scale bar 100µm.

TFF1 IS ACTIVELY TRANSCRIBED IN RETINOBLASTOMAS AND ITS EXPRESSION IS DOWNREGULATED FOLLOWING TREATMENT WITH BET BROMODOMAIN INHIBITORS

We have recently analyzed the publicly available chromatin immunoprecipitation sequencing data (ChIP-seq) of four fetal retinas, one retinoblastoma sample and one PDX model (Aldiri et al., 2017). Aldiri and colleagues had built a Chromatin hidden Markov modeling (chromHMM) in order to enable a systematic annotation of the epigenetic states (**Figure 13A**). Public data showed that *TFF1* has epigenetic marks consistent to an actively transcribed gene in the retinoblastoma sample and the PDX model, but not in the fetal retinas (**Figure 13B**). Consistent with this, ChIP-seq tracks for BRD4 were identified in the promotor region of *TFF1* in the retinoblastoma sample, but not in that of the fetal retinas (**Figure 13C**).

Consistent with these observations and to the general understanding that the inhibition of BET proteins target transcription of actively transcribed genes, such as MYC or MYCN (see **chapter 3**), we have noticed that following treatment with either JQ1 or OTX015 (2.5µM), *TFF1* expression was downregulated and completely inhibited within 24 hours of treatment (**Figure 14**). TFF1 is not detected at the protein level in Y79 cells, but even its low mRNA levels were affected after BET inhibition (**Figure 14A**). In CL-RB247 cell line, the effect on mRNA is a complete downregulation at 24h, and the effect is reflected at the protein level from 24h and maintained up to 96h after treatment (**Figure 14B**).

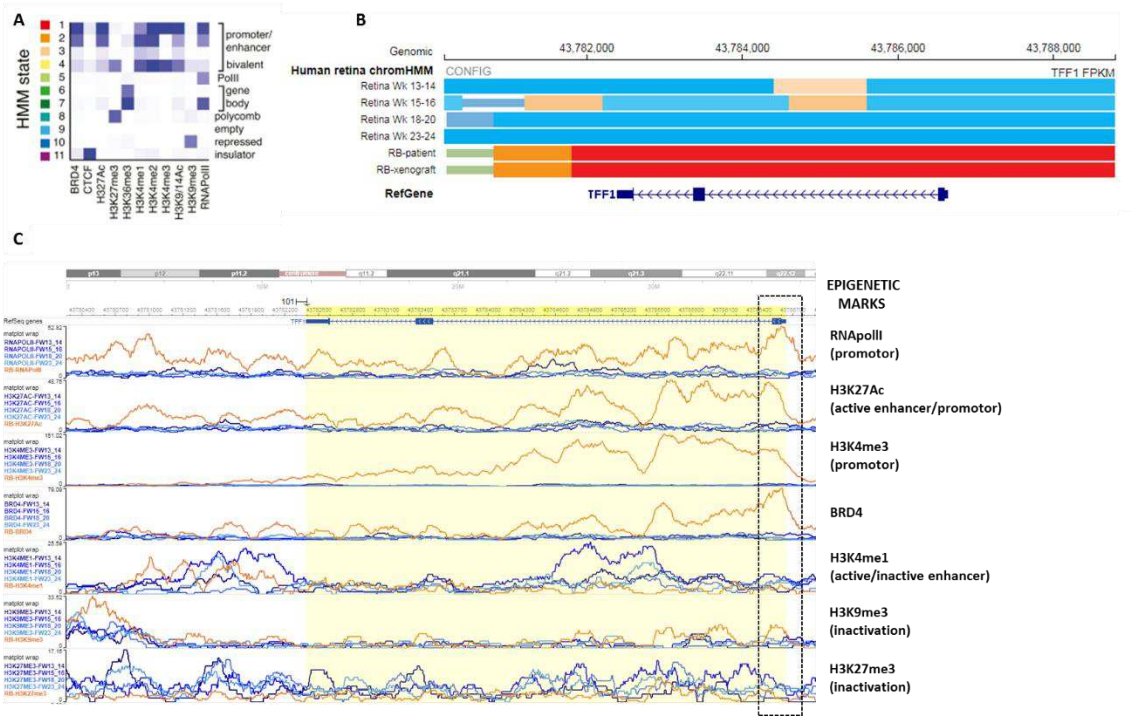


Figure 13. Publicly available chromatin immunoprecipitation sequencing data of tff1 gene in fetal retina, primary human retinoblastoma and xenograft

A) Chromatin hidden Markov modeling (HMM state) built from ChIP-seq data. ChromHMM depicting annotation of the epigenetic states: state 1 (red) has epigenetic marks consistent with actively transcribed genes, states 2 (orange) and 3 are predominantly enhancers, and state 4 identifies bivalent promoters. State 5 is primarily defined by PolII binding, and states 6 and 7 are consistent with gene bodies (H3K36me3). State 8 represents polycomb-repressed chromatin (H3K27me3) outside of the promoter or enhancers, state 9 empty chromatin, and state 10 the H3K9me3-repressed chromatin. Finally, state 11 is marked by the insulator protein CTCF. B) Epigenetic state of TFF1 gene in four fetal retinas (light blue), one retinoblastoma sample and one xenograft model (orange and red). The image shows that TFF1 is actively transcribed in retinoblasma samples and not in the fetal retinas. C) Epigenetic marks in TFF1 gene in fetal retinas (blue) and retinoblastoma (orange). Graph depicts binding of RNA PolII and BRD4 to TFF1 promotor in the retinoblastoma sample but not in fetal retinas. A and B images were adapted from Aldiri et al. 2017, and C image was generated with the Washu Epigenome Browser using publicly available data.

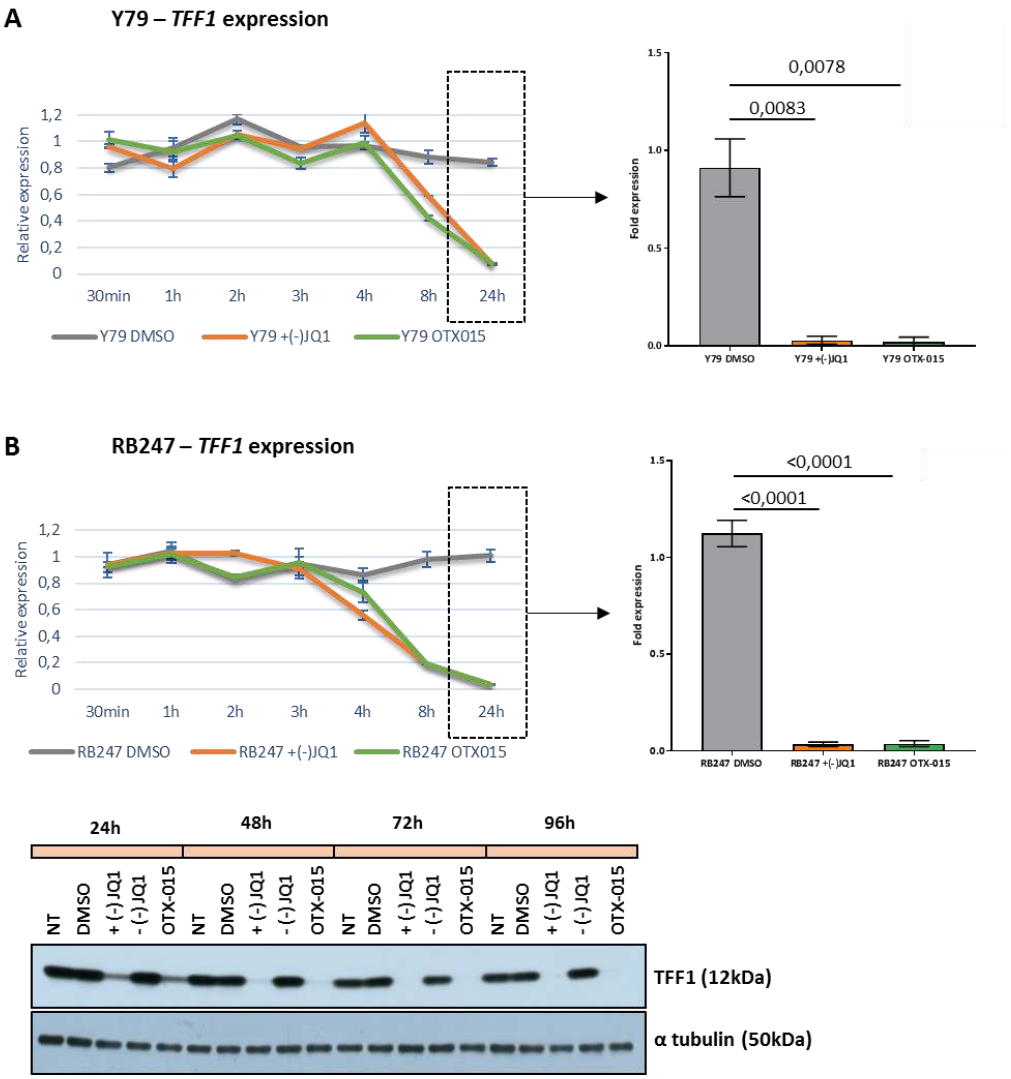


Figure 14. Effect of bet inhibitors on TFF1 mRNA and protein expression

A) TFF1 is downregulated at 8h of treatment, and mRNA is completely knocked down at 24h in Y79 cells. B) The same effect is seen in CL-RB247 cells and also reflected at the protein level of cells treated with either JQ1 or OTX015 compounds. Experiments were performed in triplicates. One representative result is shown for western blotting. NT: non treated cells; DMSO: control; (+)-JQ1: active BET inhibitor compound; (-)-JQ1: inactive form of JQ1 used as control; OTX015: active BET inhibitor compound.

DISCUSSION AND CONCLUSIONS

The analysis of the transcriptome of our retinoblastoma cohort revealed that *TFF1* was the most differentially expressed gene in terms of fold change between our molecular subtypes, and the most significantly upregulated gene in subtype 2 tumors. Upregulation of *TFF1* is also present in retinoblastoma cell and PDX models. The role of *TFF1* in different types of cancer has been largely investigated, and appears to have a pivotal role depending on the tissue where is expressed. It has been propose to act as a tumor suppressor gene in gastric carcinoma, given that its expression is reduced or lost in gastric tumoral cells. In the other hand, overexpression of *TFF1* is found in several solid tumors, where an oncogenic role has been proposed mainly related to promotion of cancer cell migration and invasion, but the role of *TFF1* upregulation in retinoblastoma has not yet been clarified.

THE ONCOGENIC ROLE OF TFF1 IN RETINOBLASTOMA IS STILL UNCOVERED

We hypothesized that *TFF1* could have an oncogenic role in retinoblastoma given that: 1) is upregulated in subtype 2 retinoblastomas, cell lines and PDX, while no expression is detected in the fetal retina, and 2) is expressed by the cells invading the retrolaminar region of the optic nerve of subtype 2 retinoblastomas. Besides, analysis of public ChIP-seq data showed that *TFF1* has epigenetic marks consistent to an actively transcribed gene, which may indicate that the tumoral cells need it for survival. Consistent with the notion of a highly transcribed gene, its expression is abrogated by the treatment with BET proteins inhibitors, as seen in other active oncogenes such as *MYC* or *MYCN* (see **chapter 3**). Our first attempt to investigate a possible role of *TFF1* on retinoblastoma cell survival by inducing a transient knock down of the gene, demonstrated that cell viability was not affected, and the same result was observed by treating Y79 cells with a recombinant rTFF1 protein. Our observation that tumors with retrolaminar optic nerve invasion expressed TFF1, led us to investigate how TFF1 could be involved in retinoblastoma cell migration and invasion. The different *in vitro* approaches used did not show that cells expressing high levels of TFF1 had an advantage in migration nor in invasion through matrigel or collagen matrix. At this point, two different interpretations could be made:

First, the experimental interpretation. The *in vitro* experiments performed may not be appropriated to investigate such role in view of the special natural microenvironment where the retinoblastoma develops. This point could be improved by performing organotypic culture or *in vivo* experiments. In the first case, a recently enucleated mouse eye could be used in culture to study cell migration through a native optic nerve, by tracking stably transfected cells. Although these culture formats enable optical access to the tissue and experimental interventions within native stromal tissues, it

can be challenging to maintain tissue viability. In the second case, orthotopic subretinal injenction of retinoblastoma transfected cells can be performed and let cells to proliferate and invade the mouse eye.

Second, the biological interpretation. Little is known about transcriptional regulation of *TFF1* in the retinoblastoma context. Several signaling pathways have been proposed to mediate the action of TFF peptides, but no receptor for TFF1 has been identified. The 5' flanking region of *TFF1* contains an enhancer region responsive to estrogens and to EGF (Wright et al., 1990). Estrogens were reported to be responsible for *TFF1* upregulation in breast cancer (Ren et al., 1997), but is not the case of retinoblastoma. Paradoxically, EGF is the most upregulated gene (in terms of fold change) in subtype 1 retinoblastomas, but EGF receptor is not expressed in neither of the two subtypes. Besides, no critical neighboring genes are found in the flanking regions of *TFF1* that could explain upregulation by a genetic or epigenetic hitchhiking effect.

At the moment, we haven't been able to get any new clues about the functional role of *TFF1* in retinoblastoma. We have focused our attention on this gene due to its specific upregulation in the retinoblastoma molecular subtype 2 and because it has been implicated in disease progression in other cancer types, but it might just be a surrogate marker in retinoblastoma.

Table 2. Antibodies used in immunohistochemical staining

Antibody	Unmasking pH	Dilution for AFA	Dilution for formol	Exposition time	Detection	Exposition time	Chromogen
CRX	pH9	1/300	1/500	60min	N-histofine	30 min	DAB
ARR3	pH6	1/150	1/300	60 min	N-histofine	30 min	DAB
EBF3	pH6	1/800	1/800	60 min	N-histofine	30 min	DAB
TFF1	pH6	1/1000	1/1000	30 min	N-histofine	30 min	DAB
KI67	pH6	ene-00	1/2500	60 min	N-histofine	25+25 min	DAB

DAB: 3,3'-diaminobenzidine

Table 3. Score of spearman correlation between TFF1 methylation and expression

CpG	Spearman correlation's score	NM_003225	Reference to gene
cg01886855	-30,40332	TFF1	promoter sequence
cg19247032	-20,586241	TFF1	promoter sequence
cg02643667	-28,283937	TFF1	promoter sequence
cg22438247	-27,225105	TFF1	promoter sequence
cg27405706	-26,23212	TFF1	promoter sequence
cg06099014	-35,987242	TFF1	5'UTR and first exon
cg24606807	-12,028487	TFF1	3'UTR

Score: -log(pvalue)*R

Table 4. Tumor group classification and histopathological characteristics of enucleated eyes from the Garrahan Hospital

Sample ID	*Tumor group (pyroseq)*	*Tumor group (IHQ)*	*Optic nerve invasion*	*Choroidal infiltration*	*Anterior segment invasion*	*Scleral infiltration*	*Cell in the optic nerve*
RB589	ND	C1	postlaminar	yes	yes	yes	elusive
RB590	C2	C2	postlaminar	yes	no	no	TFF1+
RB593	C2	C2	postlaminar	yes	no	no	ARR3+
RB594	ND	C1	postlaminar	yes	yes	no	ARR3+
RB598	C2	C2	postlaminar	yes	no	no	TFF1+
RB603	C1	C1	postlaminar	yes	no	no	ARR3+
RB617	C2	C2	postlaminar	no	no	no	TFF1+
RB620	NA	NA	postlaminar	no	no	no	elusive
RB625	C1	NA	no	no	yes	no	
RB629	ND	C2	prelaminar	yes	no	yes	
RB630	NA	C2	prelaminar	no	no	no	
RB632	C2	C1	prelaminar	yes	yes	no	
RB634	C1	C2	prelaminar	yes	no	no	
RB635	C2	NA	prelaminar	yes	no	no	
RB647	C2	C2	no	yes	no	no	
RB659	C2	C2	prelaminar	no	no	no	

RB663	C1	NA	prelaminar	yes	na	no	
RB671	C1	C1	prelaminar	no	na	no	
RB672	ND	C1	prelaminar	yes	na	no	
RB701	ND	C2	postlaminar	yes	no	no	elusive
RB702	ND	C2	postlaminar	yes	no	yes	TFF1+
RB703	ND	C2	postlaminar	yes	no	no	TFF1+
RB704	C2	C2	postlaminar	yes	no	no	elusive
RB705	ND	NA	no	yes	no	yes	
RB706	ND	C2	postlaminar	yes	no	yes	TFF1+
RB707	C2	C2	postlaminar	yes	no	no	elusive
RB708	C2	C1	prelaminar	yes	no	no	
RB709	ND	C1	postlaminar	yes	no	no	ARR3+
RB710	ND	C1	no	yes	no	no	
RB711	ND	C2	prelaminar	yes	no	yes	
RB713	NA	C1	postlaminar	yes	yes	yes	ARR3+
RB714	C1	C1	postlaminar	yes	no	no	elusive
RB716	C2	C2	postlaminar	yes	no	no	TFF1+
RB720	ND	C2	postlaminar	yes	no	yes	TFF1+
RB721	ND	C2	no	yes	no	no	
RB722	ND	C1	no	yes	no	no	
RB723	ND	C2	prelaminar	yes	no	no	
RB724	ND	C2	no	yes	no	no	
RB725	ND	C1	prelaminar	yes	yes	no	
RB726	ND	C2	postlaminar	yes	no	no	TFF1+
RB727	ND	C1	no	yes	no	no	
RB729	ND	C2	prelaminar	yes	no	no	
RB730	ND	C2	postlaminar	yes	no	yes	elusive
RB731	ND	NA	prelaminar	no	no	no	
RB732	ND	C2	postlaminar	yes	no	yes	elusive
RB733	ND	C1	prelaminar	yes	no	no	
RB735	ND	C1	no	yes	no	no	
RB736	ND	C1	prelaminar	yes	no	no	
RB737	ND	C1	prelaminar	no	no	no	
RB738	ND	C1	prelaminar	yes	no	no	

ND: not DNA available, not studied; NA: analyzed, not assigned to any subtype; Elusive: due to faint staining, image missing or problematic interpretation

BIBLIOGRAPHY

Aldiri, I., Xu, B., Wang, L., Chen, X., Hiler, D., Griffiths, L., Valentine, M., Shirinifard, A., Thiagarajan, S., Sablauer, A., et al. (2017). The Dynamic Epigenetic Landscape of the Retina During Development, Reprogramming, and Tumorigenesis. Neuron *94*, 550–568.e10.

Arumugam, T., Brandt, W., Ramachandran, V., Moore, T.T., Wang, H., May, F.E., Westley, B.R., Hwang, R.F., and Logsdon, C.D. (2011). Trefoil factor 1 stimulates both pancreatic cancer and stellate cells and increases metastasis. Pancreas *40*, 815–822.

Attieh, Y., Clark, A.G., Grass, C., Richon, S., Pocard, M., Mariani, P., Elkhatib, N., Betz, T., Gurchenkov, B., and Vignjevic, D.M. (2017). Cancer-associated fibroblasts lead tumor invasion through integrin-β3-dependent fibronectin assembly. J. Cell Biol. *216*, 3509–3520.

Baus-Loncar, M., and Giraud, A.S. (2005). Multiple regulatory pathways for trefoil factor (TFF) genes. Cell. Mol. Life Sci *62*, 2921–2931.

Belovari, T., Bijelić, N., Levak, M.T., and Lončar, M.B. (2015). Trefoil factor family peptides TFF1 and TFF3 in the nervous tissues of developing mouse embryo. Bosn. J. Basic Med. Sci. *15*, 33–37.

Binder, J.X., Pletscher-Frankild, S., Tsafou, K., Stolte, C., O'Donoghue, S.I., Schneider, R., and Jensen, L.J. (2014). COMPARTMENTS: Unification and visualization of protein subcellular localization evidence. Database *2014*.

Bougen, N.M., Amiry, N., Yuan, Y., Kong, X.J., Pandey, V., Vidal, L.J.P., Perry, J.K., Zhu, T., and Lobie, P.E. (2013). Trefoil factor 1 suppression of E-CADHERIN enhances prostate carcinoma cell invasiveness and metastasis. Cancer Lett. *332*, 19–29.

Buache, E., Etique, N., Alpy, F., Stoll, I., Muckensturm, M., Reina-San-Martin, B., Chenard, M.P., Tomasetto, C., and Rio, M.C. (2011). Deficiency in trefoil factor 1 (TFF1) increases tumorigenicity of human breast cancer cells and mammary tumor development in TFF1-knockout mice. Oncogene *30*, 3261–3273.

Busch, M., Große-Kreul, J., Wirtz, J.J., Beier, M., Stephan, H., Royer-Pokora, B., Metz, K., and Dünker, N. (2017a). Reduction of the tumorigenic potential of human retinoblastoma cell lines by TFF1 overexpression involves p53/caspase signaling and miR-18a regulation. Int. J. Cancer *141*, 549–560.

Busch, M., Metz, K., Beier, M., Biewald, E., and Dünker, N. (2017b). Trefoil Factor Family 1 expression correlates with clinical outcome in patients with Retinoblastoma. Retina *0*, 1–7.

Chantada, G.L., Dunkel, I.J., Antoneli, C.B.G., de Dávila, M.T.G., Arias, V., Beaverson, K., Fandiño, A.C., Chojniak, M., and Abramson, D.H. (2007a). Risk factors for extraocular relapse following enucleation after failure of chemoreduction in retinoblastoma. Pediatr. Blood Cancer *49*, 256–260.

Chantada, G.L., Casco, F., Fandiño, A.C., Galli, S., Manzitti, J., Scopinaro, M., Schvartzman, E., and de Dávila, M.T.G. (2007b). Outcome of Patients with Retinoblastoma and Postlaminar Optic Nerve Invasion. Ophthalmology *114*, 2083–2089.

Charras, G., and Paluch, E. (2008). Blebs lead the way: How to migrate without lamellipodia. Nat. Rev. Mol. Cell Biol. *9*, 730–736.

Chevez-Barrios, P., Hurwitz, M.Y., Louie, K., Marcus, K.T., Holcombe, V.N., Schafer, P., Aguilar-Cordova, C.E., and Hurwitz, R.L. (2000). Metastatic and nonmetastatic models of retinoblastoma. Am. J. Pathol. *157*, 1405–1412.

Chinery, R., Williamson, J., and Poulsom, R. (1996). The Gene Encoding Human Intestinal Trefoil Factor (TFF3) Is Located on Chromosome 21q22.3 Clustered with Other Members of the Trefoil Peptide Family. Genomics *32*, 281–284.

Emami, S., LE FLOCH, N., BRUYNEEL, E., THIM, L., MAY, F., WESTLEY, B., RIO, M.-C., MAREEL, M., and GESPACH, C. (2001). Induction of scattering and cellular invasion by trefoil peptides in src- and RhoA-transformed kidney and colonic epithelial cells. FASEB J. *15*, 351–361.

Emami, S., Rodrigues, S., Rodrigue, C.M., Le Floch, N., Rivat, C., Attoub, S., Bruyneel, E., and Gespach, C. (2004). Trefoil factor family (TFF) peptides and cancer progression. Peptides *25*, 885–898.

Feng, G., Zhang, Y., Yuan, H., Bai, R., Zheng, J., Zhang, J., and Song, M. (2014). DNA methylation of trefoil factor 1 (TFF1) is associated with the tumorigenesis of gastric carcinoma. Mol. Med. Rep. *9*, 109–117.

Gill, K.P., Hewitt, A.W., Davidson, K.C., Pébay, A., and Wong, R.C.B. (2014). Methods of Retinal Ganglion Cell

Differentiation From Pluripotent Stem Cells. Transl. Vis. Sci. Technol. *3*, 2.

Hauser, F., Poulsom, R., Chinery, R., Rogers, L.A., Hanby, A.M., Wright, N.A., and Hoffmann, W. (1993). hP1.B, a human P-domain peptide homologous with rat intestinal trefoil factor, is expressed also in the ulcer-associated cell lineage and the uterus. Proc. Natl. Acad. Sci. U. S. A. *90*, 6961–6965.

Hinz, M., Schwegler, H., Chwieralski, C.E., Laube, G., Linke, R., Pohle, W., and Hoffmann, W. (2004). Trefoil factor family (TFF) expression in the mouse brain and pituitary: changes in the developing cerebellum. Peptides *25*, 827–832.

Hirota, M., Awatsuji, H., Sugihara, Y., Miyashita, S., Furukawa, Y., and Hayashi, K. (1995). Expression of pS2 gene in rat brain. Biochem. Mol. Biol. Int. *35*, 1079–1084.

Jackerott, M., Lee, Y.C., Møllgård, K., Kofod, H., Jensen, J., Rohleder, S., Neubauer, N., Gaarn, L.W., Lykke, J., Dodge, R., et al. (2006). Trefoil Factors Are Expressed in Human and Rat Endocrine Pancreas: Differential Regulation by Growth Hormone. Endocrinology *147*, 5752–5759.

Johnson, M.D., Westley, B.R., and May, F.E. (1989). Oestrogenic activity of tamoxifen and its metabolites on gene regulation and cell proliferation in MCF-7 breast cancer cells. Br. J. Cancer *59*, 727–738.

Jørgensen, K., Diamant, B., Jørgensen, K., and Thim, L. (1982a). Pancreatic spasmolytic polypeptide (PSP): III. Pharmacology of a new porcine pancreatic polypeptide with spasmolytic and gastric acid secretion inhibitory effects. Regul. Pept. *3*, 231–243.

Jørgensen, K.H., Thim, L., and Jacobsen, H.E. (1982b). Pancreatic spasmolytic polypeptide (PSP): I. Preparation and initial chemical characterization of a new polypeptide from porcine pancreas. Regul. Pept. *3*, 207–219.

Kaewkhaw, R., Kaya, K.D., Brooks, M., Homma, K., Zou, J., Chaitankar, V., Rao, M., and Swaroop, A. (2015). Transcriptome Dynamics of Developing Photoreceptors in Three-Dimensional Retina Cultures Recapitulates Temporal Sequence of Human Cone and Rod Differentiation Revealing Cell Surface Markers and Gene Networks. Stem Cells *33*, 3504–3518.

Kaliki, S., Shields, C.L., Rojanaporn, D., Al-Dahmash, S., McLaughlin, J.P., Shields, J.A., and Eagle, R.C. (2013). High-Risk Retinoblastoma Based on International Classification of Retinoblastoma: Analysis of 519 Enucleated Eyes. Ophthalmology *120*, 997–1003.

Kannan, N., Grandison, P.M., Kumarasamypet, M., Amiry, N., Mertani, H., Miller, L., Liu, E., and Lobie, P. (2007). Mediation of tamoxifen resistance in mammary carcinoma cells by trefoil factor-3 (Waverly Press).

Katoh, M. (2003). Trefoil factors and human gastric cancer (review). Int. J. Mol. Med. *12*, 3–9.

Kjellev, S. (2009). The trefoil factor family – small peptides with multiple functionalities. Cell. Mol. Life Sci. *66*, 1350–1369.

Leung, W.K., Yu, J., Chan, F.K.L., To, K.F., Chan, M.W.Y., Ebert, M.P.A., Ng, E.K.W., Sydney Chung, S.C., Malfertheiner, P., and Sung, J.J.Y. (2002). Expression of trefoil peptides (TFF1, TFF2, and TFF3) in gastric carcinomas, intestinal metaplasia, and non-neoplastic gastric tissues. J. Pathol. *197*, 582–588.

Liu, M., and Jin, R. (2015). [Expressions of TFF1 and TFF3 in prostate cancer and prostatic intraepithelial neoplasia and their clinical significance]. Zhonghua Nan Ke Xue *21*, 315–319.

Masiakowski, P., Breathnach, R., Bloch, J., Gannon, F., Krust, A., and Chambon, P. (1982). Cloning of cDNA sequences of hormone-regulated genes from the MCF-7 human breast cancer cell line. Nucleic Acids Res. *10*, 7895–7903.

Mathelin, C., Tomasetto, C., and Rio, M.-C. (2005). [Trefoil factor 1 (pS2/TFF1), a peptide with numerous functions]. Bull. Cancer *92*, 773–781.

May, F.E.B., and Westley, B.R. (1997). Expression of human intestinal trefoil factor in malignant cells and its regulation by oestrogen in breast cancer cells. J. Pathol. *182*, 404–413.

Nie, S.-N., Qian, X.-M., Wu, X.-H., Yang, S.-Y., Tang, W.-J., Xu, B.-H., Huang, F., Lin, X., Sun, D.-Y., Sun, H.-C., et al. (2003). Role of TFF in healing of stress-induced gastric lesions. World J. Gastroenterol. *9*, 1772–1776.

Okada, H., Kimura, M.T., Tan, D., Fujiwara, K., Igarashi, J., Makuuchi, M., Hui, A.-M., Tsurumaru, M., and Nagase, H. (2005). Frequent trefoil factor 3 (TFF3) overexpression and promoter hypomethylation in mouse and human hepatocellular carcinomas. Int. J. Oncol. *26*, 369–377.

Olsen, C.M., Meussen-Elholm, E.T.M., Samuelsen, M., Holme, J.A., and Hongslo, J.K. (2003). Effects of the environmental oestrogens bisphenol A, tetrachlorobisphenol A, tetrabromobisphenol A, 4-hydroxybiphenyl and 4,4'-

dihydroxybiphenyl on oestrogen receptor binding, cell proliferation and regulation of oestrogen sensitive proteins in the human breast cancer cell line MCF-7. Pharmacol. Toxicol. *92*, 180–188.

Paulsen, F.P., Woon, C.-W., Varoga, D., Jansen, A., Garreis, F., Jäger, K., Amm, M., Podolsky, D.K., Steven, P., Barker, N.P., et al. (2008). Intestinal Trefoil Factor/TFF3 Promotes Re-epithelialization of Corneal Wounds. J. Biol. Chem. *283*, 13418–13427.

Perry, J.K., Kannan, N., Grandison, P.M., Mitchell, M.D., and Lobie, P.E. (2008). Are trefoil factors oncogenic? Trends Endocrinol. Metab. *19*, 74–81.

Philippeit, C., Busch, M., and Dünker, N. (2014). Epigenetic Control of Trefoil Factor Family (TFF) Peptide Expression in Human Retinoblastoma Cell Lines. Cell. Physiol. Biochem. *34*, 1001–1014.

Podolsky, D.K., Lynch-Devaney, K., Stow, J.L., Oates, P., Murgue, B., DeBeaumont, M., Sands, B.E., and Mahida, Y.R. (1993). Identification of human intestinal trefoil factor. Goblet cell-specific expression of a peptide targeted for apical secretion. J. Biol. Chem. *268*, 6694–6702.

Poulsom, R., Hanby, A.M., Lalani, E., Hauser, F., Hoffmann, W., and Stamp, G.W.H. (1997). Intestinal trefoil factor (TFF 3) and pS2 (TFF 1), but not spasmolytic polypeptide (TFF 2) mRNAs are co-expressed in normal, hyperplastic, and neoplastic human breast epithelium. J. Pathol. *183*, 30–38.

Prest, S.J., May, F.E.B., and Westley, B.R. (2002). The estrogen-regulated protein, TFF1, stimulates migration of human breast cancer cells. FASEB J. *16*, 592–594.

Prud'homme, J.-F., Fridlansky, F., Le cunff, M., Atger, M., Mercier-Bodart, C., Pichon, M.-F., and Milgrom, E. (1985). Cloning of a Gene Expressed in Human Breast Cancer and Regulated by Estrogen in MCF-7 Cells. DNA *4*, 11–21.

Ren, L., Marquardt, M.A., and Lech, J.J. (1997). Estrogenic effects of nonylphenol on pS2, ER and MUC1 gene expression in human breast cancer cells-MCF-7. Chem. Biol. Interact. *104*, 55–64.

Ribieras, S., Tomasetto, C., and Rio, M.-C. (1998). The pS2/TFF1 trefoil factor, from basic research to clinical applications. Biochim. Biophys. Acta - Rev. Cancer *1378*, F61–F77.

Rodgers, H.M., Belcastro, M., Sokolov, M., and Mathers, P.H. (2016). Embryonic markers of cone differentiation. Mol. Vis. *22*, 1455–1467.

Rodrigues, S., Van aken, E., Van Bocxlaer, S., Attoub, S., Nguyen, Q., Bruyneel, E., Westley, B.R., May, F. e. B., Thim, L., Mareel, M., et al. (2003). Trefoil peptides as proangiogenic factors in vivo and in vitro: implication of cyclooxygenase-2 and EGF receptor signaling. FASEB J. *17*, 7–16.

Sahai, E., and Marshall, C.J. (2003). Differing modes of tumour cell invasion have distinct requirements for Rho/ROCK signalling and extracellular proteolysis.

Shi, S.-Q., Cai, J.-T., and Yang, J.-M. (2006). Expression of trefoil factors 1 and 2 in precancerous condition and gastric cancer. World J. Gastroenterol. *12*, 3119–3122.

Smid, M., Wang, Y., Klijn, J.G.M., Sieuwerts, A.M., Zhang, Y., Atkins, D., Martens, J.W.M., and Foekens, J.A. (2006). Genes Associated With Breast Cancer Metastatic to Bone. J. Clin. Oncol. *24*, 2261–2267.

Steven, P., Schäfer, G., Nölle, B., Hinz, M., Hoffmann, W., and Paulsen, F. (2004). Distribution of TFF peptides in corneal disease and pterygium. Peptides *25*, 819–825.

Suemori, S., Lynch-Devaney, K., and Podolsky, D.K. (1991). Identification and characterization of rat intestinal trefoil factor: tissue- and cell-specific member of the trefoil protein family. Proc. Natl. Acad. Sci. U. S. A. *88*, 11017–11021.

Taupin, D., and Podolsky, D.K. (2003). Erratum: Trefoil factors: initiators of mucosal healing. Nat. Rev. Mol. Cell Biol. *4*, 721–732.

Taupin, D., Wu, D.-C., Jeon, W.-K., Devaney, K., Wang, T.C., and Podolsky, D.K. (1999). The trefoil gene family are coordinately expressed immediate-early genes: EGF receptor– and MAP kinase–dependent interregulation. J. Clin. Invest. *103*, R31–R38.

Terris, B., Dubois, S., Buisine, M.-P., Sauvanet, A., Ruszniewski, P., Aubert, J.-P., Porchet, N., Couvelard, A., Degott, C., and Fléjou, J.-F. (2002). Mucin gene expression in intraductal papillary-mucinous pancreatic tumours and related lesions. J. Pathol. *197*, 632–637.

Thim, L. (1989). A new family of growth factor-like peptides. 'Trefoil' disulphide loop structures as a common feature in breast cancer associated peptide (pS2), pancreatic spasmolytic polypeptide (PSP), and frog skin peptides (spasmolysins). FEBS Lett. *250*, 85–90.

Thim, L., and May, F.E.B. (2005). Structure of mammalian trefoil factors and functional insights. Cell. Mol. Life Sci *62*, 2956–2973.

Thul, P.J., Åkesson, L., Wiking, M., Mahdessian, D., Geladaki, A., Ait Blal, H., Alm, T., Asplund, A., Björk, L., Breckels, L.M., et al. (2017). A subcellular map of the human proteome. Science (80-.). *356*, eaal3321.

Tomasetto, C., Rockel, N., Mattei, M.G., Fujita, R., and Rio, M.C. (1992). The gene encoding the human spasmolytic protein (SML1/hSP) is in 21q 22.3, physically linked to the homologous breast cancer marker gene BCEI/pS2. Genomics *13*, 1328–1330.

Uchino, H., Kataoka, H., Itoh, H., Hamasuna, R., and Koono, M. (2000). Overexpression of intestinal trefoil factor in human colon carcinoma cells reduces cellular growth in vitro and in vivo. Gastroenterology *118*, 60–69.

Vargas, P., Terriac, E., Lennon-Duménil, A.-M., and Piel, M. (2014). Study of Cell Migration in Microfabricated Channels. J. Vis. Exp. 1–8.

Vargas, P., Maiuri, P., Bretou, M., Saéz, P.J., Pierobon, P., Maurin, M., Chabaud, M., Lankar, D., Obino, D., Terriac, E., et al. (2016). Innate control of actin nucleation determines two distinct migration behaviours in dendritic cells. Nat. Cell Biol. *18*, 43–53.

Völkner, M., Zschätzsch, M., Rostovskaya, M., Overall, R.W., Busskamp, V., Anastassiadis, K., and Karl, M.O. (2016). Retinal Organoids from Pluripotent Stem Cells Efficiently Recapitulate Retinogenesis. Stem Cell Reports *6*, 525–538.

Weise, A., and Dünker, N. (2013). High trefoil factor 1 (TFF1) expression in human retinoblastoma cells correlates with low growth kinetics, increased cyclin-dependent kinase (CDK) inhibitor levels and a selective down-regulation of CDK6. Histochem. Cell Biol. *139*, 323–338.

Wilson, K.S., Roberts, H., Leek, R., Harris, A.L., and Geradts, J. (2002). Differential Gene Expression Patterns in HER2/neu-Positive and -Negative Breast Cancer Cell Lines and Tissues. Am. J. Pathol. *161*, 1171–1185.

Wright, N.A., Poulsom, R., Stamp, G.W.H., Hall, P.A., Jeffery, R.E., Longcroft, J.M., Rio, M.-C., Tomasetto, C., and Chambon, P. (1990). Epidermal growth factor (EGF/URO) induces expression of regulatory peptides in damaged human gastrointestinal tissues. J. Pathol. *162*, 279–284.

Xu, X.Q., Emerald, B.S., Goh, E.L.K., Kannan, N., Miller, L.D., Gluckman, P.D., Liu, E.T., and Lobie, P.E. (2005). Gene expression profiling to identify oncogenic determinants of autocrine human growth hormone in human mammary carcinoma. J. Biol. Chem. *280*, 23987–24003.

Yio, X., Diamond, M., Zhang, J., Weinstein, H., Wang, L., Werther, L., and Itzkowitz, S. (2006). Trefoil Factor Family-1 Mutations Enhance Gastric Cancer Cell Invasion Through Distinct Signaling Pathways. Gastroenterology *130*, 1696–1706.

Zhang, J., Benavente, C.A., McEvoy, J., Flores-Otero, J., Ding, L., Chen, X., Ulyanov, A., Wu, G., Wilson, M., Wang, J., et al. (2012). A novel retinoblastoma therapy from genomic and epigenetic analyses. Nature *481*, 329–334.

CHAPTER 3

MYC, *MYCN* AND BROMODOMAIN INHIBITORS IN RETINOBLASTOMA

Index

INTRODUCTION 135

TARGETING THE CANCER EPIGENOME 135

THE *MYC* PROTO-ONCOGENE FAMILY 136

MYCN ONCOGENE DURING NORMAL DEVELOPMENT AND TUMORIGENESIS 137

RECURRENT GENOMIC COPY NUMBER ALTERATIONS IN RETINOBLASTOMA 138

MYCN amplifications in retinoblastoma 138

MATERIALS AND METHODS 140

GENOMIC COPY NUMBER ANALYSIS 140

TRANSCRIPTOME ANALYSIS AND DIFFERENTIALLY EXPRESSED GENES AND PATHWAYS 140

CELL CULTURE 140

BET INHIBITORS (BETi) COMPOUNDS 140

In vitro BETi treatment 141

RNA INTERFERENCE ASSAY 141

TOTAL RNA ISOLATION AND REVERSE TRANSCRIPTION PCR (RT-PCR) 142

REAL-TIME QUANTITATIVE PCR (qPCR) 142

RT-qPCR reaction efficiencies 142

WESTERN BLOTTING 142

STATISTICAL ANALYSIS 143

RESULTS 144

MYCN/MYCNOS CLUSTER AMPLIFICATION IN RETINOBLASTOMA PRIMARY TUMORS 144

MYC PATHWAY UPREGULATION IN RETINOBLASTOMA SUBTYPE 2 147

SENSITIVITY OF RETINOBLASTOMA CELL LINES TO BROMODOMAIN INHIBITORS COMPOUNDS 149

Effect of JQ1 and OTX015 on *c-MYC* and *MYCN* expression in retinoblastoma cell lines 151

BET INHIBITION OUTCOME ON C-MYC/MYCN DOWNSTREAM TARGET GENES 154

TRANSIENT KNOCKDOWN OF C-MYC AND MYCN DO NOT RECAPITULATE THE BET INHIBITION EFFECTS 156

COMPLEX DYNAMICS OF C-MYC AND MYCN GENE EXPRESSION FOLLOWING JQ1 AND OTX015 TREATMENT 157

DISCUSSION AND CONCLUSIONS 160

MYCN AMPLIFICATIONS AND *MYC* SIGNALING ARE RELATED TO RETINOBLASTOMA MOLECULAR SUBTYPE 2 160

MYC SIGNALING AS A THERAPEUTIC TARGET IN RETINOBLASTOMA 161

Retinoblastoma cell's viability is significantly reduced by the use of BET inhibitors 161

MYC/MYCN downregulation induced by BETi treatment 162

BIBLIOGRAPHY 167

Figures

FIGURE 1. BROMODOMAIN INHIBITORS 136
FIGURE 2. GENOMIC COPY NUMBER CHANGES DETECTED IN OUR 102 RETINOBLASTOMA COHORT 145
FIGURE 3. AMPLIFICATIONS OF THE MYCN/MYCNOS LOCUS 146
FIGURE 4. MYCN GENE EXPRESSION DOWNREGULATION AFTER TRANSIENT KNOCKDOWN OF MYCNOS 147
FIGURE 5. HIERARCHICAL CLUSTERING OF THE DIFFERENTIALLY EXPRESSED GENES BETWEEN SUBTYPE 1 AND SUBTYPE 2 RETINOBLASTOMAS 148
FIGURE 6. MYC AND MYCN EXPRESSION IN RETINOBLASTOMA CELL LINES AND SENSITIVITY TO A RANGE CONCENTRATIONS OF BETI COMPOUNDS 150
FIGURE 7. Y79 RESPONSE TO BET INHIBITORS TREATMENT 152
FIGURE 8. CL-RB247 RESPONSE TO BET INHIBITORS TREATMENT 153
FIGURE 9. WERI RESPONSE TO BET INHIBITORS TREATMENT 154
FIGURE 10. Y79 MYCN GENE AND PROTEIN EXPRESSION AND DOWNSTREAM TARGET GENES 155
FIGURE 11. CL-RB247 MYC GENE AND PROTEIN EXPRESSION AND DOWNSTREAM TARGET GENES 156
FIGURE 12. TRANSIENT TRANSFECTION USING PREDESIGNED SIRNA AGAINST MYC AND MYCN GENES 157
FIGURE 13. DYNAMICS OF GENE EXPRESSION FOLLOWING JQ1 AND OTX015 TREATMENT 159
FIGURE 14. NUMBER OF CODING MUTATIONS, GENOMIC INSTABILITY, AND OVERALL DNA METHYLATION IN RETINOBLASTOMA 160
FIGURE 15. PROPOSED MECHANISM OF BRD4 INHIBITION IN NEUROBLASTOMA. 162
FIGURE 16. CHIP-SEQ PUBLICLY AVAILABLE DATA OF FETAL RETINAS AND ONE RETINOBLASTOMA SAMPLE 163

Tables

TABLE 1. PRIMERS USED IN RT-QPCR 164
TABLE 2. FOCAL AMPLIFICATIONS ON 2P24.3 IN THE SERIES OF 102 RETINOBLASTOMAS 164
TABLE 3. GENE SET ENRICHMENT USE FOR HIERARCHICAL CLUSTERING 165

INTRODUCTION

TARGETING THE CANCER EPIGENOME

An important epigenetic determinant of chromatin structure and function is the presence of post-translational modifications (PTMs) on histones. Histone PTMs were first reported more than 50 years ago with the discovery of histone acetylation and methylation (Allfrey et al., 1964). The acetylation of lysine residues within histone N-terminal tails is generally associated with the so-called open chromatin, accessible to DNA and RNA polymerases and transcription factors to activate gene transcription (Allfrey et al., 1964). Histone acetylation is a highly dynamic process regulated by two families of enzymes: the "chromatin writers" histone acetyltransferases (HATs) that produce acetylation marks and the "chromatin erasers" histone deacetylases (HDACs) that catalyze the removal of acetylation marks (Kuo and Allis, 1998). Bromodomain-containing (BRD) proteins are "epigenetic readers" of histone acetylation that specifically recognize and binds to acetylation marks (Musselman et al., 2012). BRDs plays crucial roles in transcriptional regulation, functioning as a scaffold for the assembly of macromolecular complexes that alter chromatin accessibility to transcription factors and allowing the recruitment or activation of the RNA polymerases (Sanchez and Zhou, 2009). BRDs proteins are structurally divided into bromodomain and extra-terminal (BET) or non-BET protein families. The BET family comprises four proteins: BRD2, BRD3, and BRD4, which are ubiquitously expressed, and BRDT, which is testis-specific (Jain and Barton, 2016).

Epigenetic regulators that maintain aberrant cell states have emerged as accessible entry points for targeted therapies (Jones et al., 2016). Among these, BET bromodomain inhibitors (BETi) have shown activity in preclinical models of leukemia and several solid tumor cancers (Jones et al., 2016; Shi and Vakoc, 2014), yet the underlying mechanisms remain poorly understood. Although BETi interfere with multiple BET proteins, therapeutic effects have mainly been attributed to displacement of BRD4 from acetylated histones and repression of its target genes (**Figure 1**). By interfering with BRD4 regulation, BETi arrest the transcription of genes involved in cell proliferation, including many proto-oncogenes such as *MYC* (Ferri et al., 2016), an oncogenic transcription factor that is overexpressed in up to 70% of human cancers (Dang, 2012). This effect was first described in multiple myeloma (Delmore et al., 2011) and later in medulloblastoma (Henssen et al., 2013). In addition to *MYC*, independent reports have shown repression of *MYCN* and MYCN target genes to inhibit tumor growth in preclinical models of neuroblastoma (Henssen et al., 2016; Puissant et al., 2013), pancreatic neuroendocrine tumors (Fielitz et al., 2016) and medulloblastoma (Bandopadhayay et al., 2014; Henssen et al., 2013).

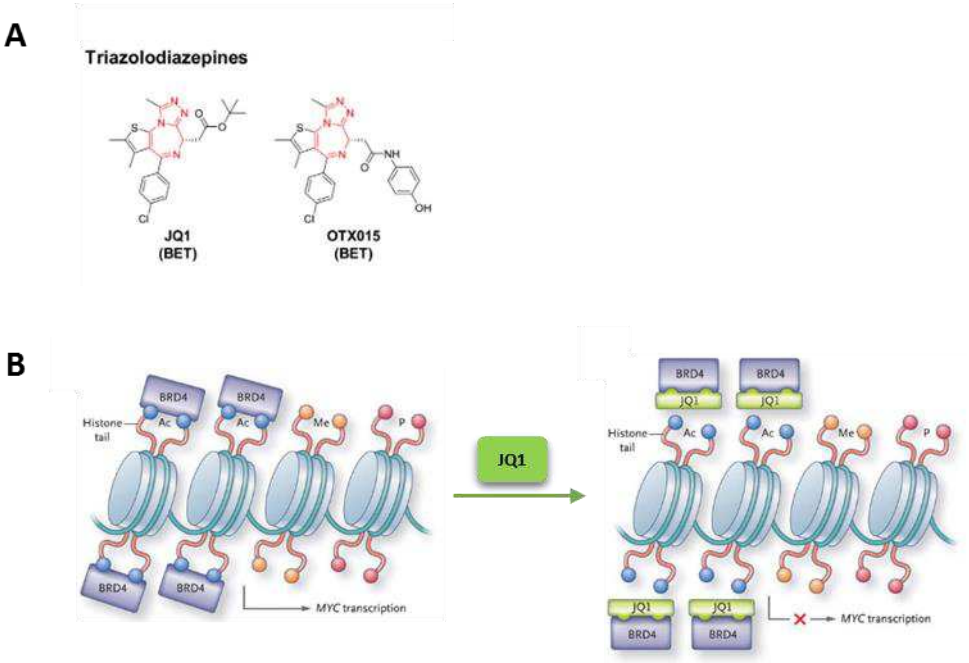


Figure 1. Bromodomain inhibitors

A) Chemical structures of representative JQ1 and OTX015 triazolothienodiazepines. The design of JQ1 (Filippakopoulos et al., 2010) was based on a patent by Mitsubishi Pharmaceuticals, in which triazolothienodiazepines discovered in anti-inflammatory phenotypic screens that monitored the activity of Apolipoprotein A-1 (ApoA1) were reported to inhibit BET BRDs and have anti-tumor properties. JQ1 was shown to be selective for the BET family, with stronger affinity for BRD4 (Luger et al., 1997). OTX015 (Oncoethix) was originally developed for the treatment of inflammatory bowel disease. Is the first BET inhibitor to have moved into the clinic, with three phase Ib clinical trials initiated for various malignancies (Adult Myeloid Leukemia, Diffuse Large B-Cell Lymphoma: NCT01713582 phase I; Nut-Midline Carcinoma, castrate-resistant prostate cancer: NCT02259114 phase Ib; Glioblastoma Multiforme: NCT02296476 phase Iia) (Ferri et al., 2016). b) Like all BETi, JQ1 and OTX015 interact with the BRD pocket in a competitive manner with acetylated peptide binding, resulting in the displacement of BET proteins from acetylated chromatin in cells exposed to these inhibitors, and thus repressing gene transcription. An example with JQ1 inhibitor and MYC repression is depicted (adapted from N Engl J Med. 2012 Mar 8;366(10):960-1)

THE *MYC* PROTO-ONCOGENE FAMILY

The MYC gene family members, *MYC*, *MYCN* and *MYCL*, are transcription factors that control the expression of many target genes, which in turn regulate fundamental cellular processes including proliferation, cell growth, protein synthesis, metabolism, apoptosis and differentiation (Eilers and Eisenman, 2008). They encode basic helix-loop-helix leucine zipper proteins that are found as heterodimers with their partner protein, MAX (Amati et al., 1993). The MYC-MAX heterodimer binds to DNA consensus core binding sites E-boxes (5'-CACGTG-3' or variants) which preferentially leads to transcriptional activation of target genes, recruiting transcriptional co-factors such as TRRAP-containing complexes with either GCN5 or TIP60 histone acetyl transferases or the p300/CBP acetyl transferase. This in turn stimulates histone acetylation leading to an open chromatin structure that provides docking sites for additional proteins that promote transcription (Westermark et al., 2011). Factors such as P-TEFb and TFII-H that stimulate transcriptional elongation through phosphorylation

or RNA pol II can also be recruited to the MYC/MAX dimer. MYC induces a broad repertoire of targets including genes involved in metabolism, protein synthesis, cell cycle promotion as well as in mitochondrial biogenesis and function (Dang et al., 2006). The MYC proteins can also repress gene expression by binding to other transcription factors such as Miz-1 (ZBTB17) and SP1 and thereby inhibiting transcription of their downstream targets. *MYCN* can in this way repress many negative cell cycle regulators and genes involved in cell adhesion (Kleine-Kohlbrecher et al., 2006).

MYC family members are among the most frequently amplified oncogenes in human cancers. Enhanced activity of *MYC* transcription factors contributes to almost every aspect of tumor formation: unrestricted cell proliferation, inhibition of differentiation, cell growth, angiogenesis, reduced cell adhesion, genomic instability and metastasis (Adhikary and Eilers, 2005).

MYCN ONCOGENE DURING NORMAL DEVELOPMENT AND TUMORIGENESIS

While biochemical properties, dimerization with MAX, DNA binding and transforming capacity are very similar for MYC and MYCN proteins, their pattern of expression in normal tissues differs significantly. While MYC is expressed in all proliferating tissues in the adult, MYCN expression is restricted to certain tissues in the developing embryo and is very low or absent in adult tissues (Hirvonen et al., 1990). *MYCN*, but not *MYC*, is essential for the rapid proliferation of progenitor cells during the development of the central nervous system (Knoepfler et al., 2002). The *MYCL* gene is less well characterized, and is expressed in both neonatal and adult lung tissue (Brägelmann et al., 2017). In many cases, *MYCN* or *MYC*–driven tumors appear to arise from cell lineages that express *MYCN* or *MYC* during normal development, but their roles in tumor biology, sometimes differs within a specific lineage (Rickman et al., 2018). For example, in the hematopoietic system, *MYCN* is expressed in self-renewing, quiescent stem cells, but their expression switches to *MYC* upon differentiation to transit-amplifying progenitors (King et al., 2016). Likewise, in some solid tumors (e.g., prostate), enhanced *MYCN* expression drives a neuroendocrine tumor type that differs from the *MYC*–driven tumors in histology and response to therapies. In the case of prostate cancer, evidence suggests that *MYCN* may play a role in lineage switching from an epithelial origin to a more neuroendocrine one (Lee et al., 2016).

MYCN gene (V-myc myelocytomatosis viral-related oncogene, neuroblastoma derived [avian]) was first discovered in neuroblastoma cell lines as amplified DNA with homology to viral myc (Schwab et al., 1983). *MYCN* amplification are found in non-neuronal tumors like castration-resistant prostate cancer and neuroendocrine prostate cancer, hematologic malignancies and rhabdomyosarcoma, among others (Beltran et al., 2011; Hirvonen et al., 1993; Williamson et al., 2005), but is more commonly amplified in tumors derived from the nervous system such as retinoblastoma, neuroblastoma, medulloblastoma, astrocytoma and glioblastoma multiforme (Bjerke et al., 2013;

Estiar et al., 2017; Lee et al., 1984; Marees et al., 2008; Massimino et al., 2016; Westermark et al., 2011). In neuroblastoma, *MYCN* is critically involved in tumor aggressiveness and resistance to therapy. Neuroblastoma is a pediatric solid tumor derived from the sympathetic nervous system. The prognosis is highly variable and is associated with clinical parameters such as age at diagnosis, dissemination at time of diagnosis, tumor stage, and grade of differentiation of the primary tumor (Park et al., 2010). Neuroblastoma stages 1 and 2 have a very good prognosis, but survival in stage 4 neuroblastoma is below 30%. Amplification of *MYCN* is associated with poor outcome, occurring in about 20% of the tumors and is confined to high-stage neuroblastoma (Maris et al., 2007). High MYC-signaling is also correlated to poor prognosis, not only in the high-risk stratification group, but also in intermediate- or low-risk patient (Fredlund et al., 2008).

RECURRENT GENOMIC COPY NUMBER ALTERATIONS IN RETINOBLASTOMA

Most retinoblastomas are believed to initiate with biallelic inactivation of the retinoblastoma susceptibility gene (*RB1*) which is rate limiting for tumorigenesis (Knudson, 1971). Over the past decades since the *RB1* gene was cloned, researchers have focused on identifying genetic lesions in retinoblastoma that contribute to tumor progression following RB1 inactivation (Corson and Gallie, 2007). Specifically, cytogenetic and array comparative genome hybridization (aCGH) studies have led to the identification of regions of the genome that are recurrently gained (chromosomes 1q, 2p and 6p) or lost (chromosomes 13q and 16q) in retinoblastomas and that may contribute to tumorigenesis (Corson and Gallie, 2007). Indeed, candidate oncogenes and tumor suppressor genes have been identified whereby copy number variations (CNV) correlate with changes in gene expression. Candidate oncogenes in the retinoblastoma genome include *MDM4* (Laurie et al., 2006) and *KIF14* (Corson et al., 2005) on chromosome 1q32, *MYCN* on chromosome 2p34 (Bowles et al., 2007), and *DEK* and *E2F3* (Grasemann et al., 2005; Orlic et al., 2006) on chromosome 6p22. In addition, there are *CDH11* (Marchong et al., 2004), and *RBL2* (Bellan et al., 2002; Tosi et al., 2005) as a candidate tumor suppressor genes on chromosome 16q21 and 16q12.2, respectively.

MYCN amplifications in retinoblastoma

One of the recurrent copy number variation in retinoblastoma is the amplification of a region on chromosome 2p spanning the *MYCN* oncogene. *MYCN* amplifications have long been known to occur in human retinoblastoma (Lee et al., 1984) and is also amplified in the archetypal retinoblastoma cell line Y79 (Squire et al., 1986). This amplification is present in approximately 10% of retinoblastomas (Kooi et al., 2016; Rushlow et al., 2013a). How *MYCN* amplification contributes to human retinoblastomas that harbor *RB1* mutations is not known, but genetically engineered retinoblastoma mouse models suggest a role in metastasis (MacPherson et al., 2007). Rushlow et al. (Rushlow et al., 2013b) proposed that approximately 1.5% of human retinoblastomas have wild-type *RB1*, and the

tumors are initiated by *MYCN* amplifications (≥10 copies). In this study, the authors demonstrated that $RB1^{+/+}$ $MYCN^{A}$ tumors expressed functional RB1 protein, had fewer overall genomic copy number changes in genes characteristic of retinoblastoma than did $RB1^{-/-}$, and that these patients were diagnosed at very early ages (4.5 months) compared to children with non-familial unilateral $RB1^{-/-}$ retinoblastoma (24.5 months).

In this chapter, taking advantage of known *MYCN* amplification occurring in retinoblastoma, and after having discovered MYC signaling upregulation in subtype 2 retinoblastomas, we decided to test the efficacy of BET inhibitors as a possible treatment for this pediatric cancer.

MATERIALS AND METHODS

GENOMIC COPY NUMBER ANALYSIS

Analysis of copy number variation of primary tumors was described in Chapter 1. Overall genomic instability score (GNL (Gain=1/Normal=0/Loss=-1) copy number data are aggregated by chromosome as the proportion of features with an aberration (i.e. Gain or Loss). The final score corresponds to mean score across all chromosomes.

TRANSCRIPTOME ANALYSIS AND DIFFERENTIALLY EXPRESSED GENES AND PATHWAYS

Expression profiling was performed with the Human Genome U133 Plus 2.0 Array as previously described (**chapter 1**).

We compared the transcriptome of the two retinoblastomas subtypes (C1=26; C2=31) using the Limma R package (Smyth, 2005) and identified 5991 differentially expressed genes (adjusted p-value<0.05). Pathway enrichment analyses were performed using hypergeometric tests, for differentially expressed genes either under-expressed (ratio < 2/3) or overexpressed (ratio > 1.5) in subtype 1 versus subtype 2. We focused on gene sets corresponding to retinal cell population markers and on REACTOME and HALLMARK pathways from the Molecular Signatures Database (Subramanian et al., 2005).

CELL CULTURE

Retinoblastoma cells grow in suspension. Cells were cultured in a humidified 37°C incubator with 5% CO2 in their respective media. WERI and Y79 cell lines were grown in RPMI 1640 (Life Technologies) supplemented with 10% fetal bovine serum (FBS) (Lonza), 100 U/mL Penicillin-Streptomycin (Gibco). CL-RB247 cell line was cultured in Iscove's Modified Dulbecco's Medium (IMDM) with 25 mM HEPES and L-glutamine (Life Technologies) supplemented with 10% FBS, 100 U/mL Penicillin-Streptomycin (Gibco), 10 mg/L insulin (Sigma) and 0.0005% (v/v) β-mercaptoethanol (Sigma). WERI and Y79 were obtained from the ATCC. CL-RB247 was kindly provided by Brenda Gallie (Impact Genetics, Canada).

BET INHIBITORS (BETi) COMPOUNDS

The bromodomain inhibitors OTX015 ($C_{25}H_{22}ClN_5O_2S$) (HY-15743), active (+)-JQ1 ($C_{23}H_{25}ClN_4O_2S$) (HY-13030) and inactive (-)-JQ1 ($C_{23}H_{25}ClN_4O_2S$) stereoisomer of (+)-JQ1 (HY-13030A) were purchased from MedChemExpress. All compounds were obtained in powder, dissolved in dimethyl sulfoxide

(DMSO; 10mM stock solution) and stored at -20°C. Aliquots were thawed and diluted in water in the desired concentrations immediately before use.

In vitro BETi treatment

Retinoblastoma cells were counted using 0.4% Trypan blue stain (Invitrogen) in an automated cell counter Countess (Invitrogen).

For RNA and protein extraction, cells were seeded in a sterile 6-well plate at $1x10^6$ cells per well in 2.96mL of culture media. Diluted compounds or an equivalent volume of DMSO (0.02%) were added to the cells, resulting in a total volume of 3mL per well. Final concentrations of BETi ranged from 300nM to 2.5µM. The cells were collected after 24h, 48h, 72h or 96h for further experiments. Three independent experiments were run for each cell line.

For cell viability assay, cells were seeded in a sterile 96-well black culture plate with transparent bottom at $2x10^4$ cells per well in 98µL of medium containing 10% FBS. Diluted compounds or an equivalent volume of DMSO (0.02%) were added to the cells, resulting in a total volume of 100µL per well. Final (+)-JQ1 and (-)-JQ1 concentrations ranged from 300nM to 10µM, whereas OTX015 concentrations ranged from 300nM to 10µM. Each compound and DMSO-only control had three replicates per dose. After incubation for 24h to 96h at 37 °C, cell viability was assessed using the CellTiter-Glo Luminescent Cell Viability Assay (Promega) following manufacturer's instructions. Luminescence was measured using the FLUOstar OPTIMA plate reader (BMG LABTECH). Measurements were normalized with respect to the average signal for DMSO-only control wells, which represented 100% viability. Three independent experiments were run for each cell line.

RNA INTERFERENCE ASSAY

Retinoblastoma cell lines were transiently transfected using Lipofectamine RNAiMAX (Invitrogen) transfection reagent, according to the manufacturer's instructions in Opti-MEM (Gibco) or culture media without antibiotics. For gene silencing, 20nM of pre-designed short interfering RNA (siRNA) sequences targeting different regions of *MYC*, *MYCN* or *MYCNOS* genes were used. All were purchased from Qiagen: siRNA Luciferase GL2 (1022070), HS-MYC-si5 (SI00300902), Hs-MYC-si7 (SI02662611), Hs-MYCNOS-si12 (SI05463493), Hs-MYCN-si6 (SI03087518), Hs-MYCN-si7 (SI03113670). The cells were collected after 48h, 72h or 96h for further experiments. siRNA Luciferase was used as control.

Cell viability was assessed as described previously. Measurements were normalized with respect to the average signal for siRNA control wells, which represented 100% viability. Three independent experiments were run for each cell line.

TOTAL RNA ISOLATION AND REVERSE TRANSCRIPTION (RT)

The total mRNA was isolated from transfected or treated cells using the RNAeasy kit (Qiagen). Five-hundreds micrograms of total RNA was reverse-transcribed in 1X RT Buffer using the High-Capacity cDNA Reverse Transcription kit (Applied Biosystems) in a final volume of 20µL containing 1X dNTP Mix (4mM), 1X RT Random Primers, RNase Inhibitor (1U/µl) and MultiScribe RT (2.5U/µl). Reaction was run in a Mastercycler pro PCR System (Eppendorf) as follows: 25°C (10sec), 37°C (120min), 85°C (5sec).

REAL-TIME QUANTITATIVE PCR (qPCR)

Primer design was performed using Primer3 plus software. RT-qPCR was carried out in a LightCycler 480 Instrument (Roche) in a final volume of 20µL containing forward and reverse primers (300nM or 500nM or 700nM), 1X LightCycler480 SYBR Green I Master (Roche) and 10ng of cDNA. Thermal cycling conditions included a pre-incubation step at 95°C (5min), followed by 45 cycles at 95°C (20sec), 60°C (15sec) and 72°C (15sec). Melting curve analysis confirmed that each product was homogeneous and specific. Analysis was performed with the LightCycler 480 Software. Fold differences were calculated according to the $2^{-\Delta\Delta Ct}$ method and normalized against the endogenous expression of TBP gene. The primer's sequences are described in **Table 1** (page 164).

RT-qPCR reaction efficiencies

PCR efficiency for each pair of primers was determined by preparing a dilution series of known cDNA content. The CT values obtained after the RT-qPCR reaction were plotted against the logarithm of the template amount used. One hundred percent efficiency corresponds to a slope value of-3.32. Efficiency was calculated with the formula: (10(-1/slope)-1)*100. The tolerated slope values were -3.32 +/- 0.3, in order to have similar efficiencies values between target and reference genes.

WESTERN BLOTTING

Protein extracts were obtained using lysis buffer (50mM Tris-HCl (pH 6.8), 2% SDS, 5% glycerol, DTT 2mM, 2.5mM EDTA, 2.5mM EGTA) freshly supplemented with protease and phosphatase inhibitor (Roche). Cell lysates were clarified by centrifugation. Protein concentration was determined with a BCA Protein Assay-Reducing Agent Compatible kit (ThermoFischer).

Ten micrograms of protein were loaded on SDS-polyacrylamide gels using 4-15% or 7.5% Tris-glycine precast gels (Biorad) and transferred to nitrocellulose membranes using a Trans-Blot Turbo transfer system (Biorad). Membranes were stained with 1x Naphthol Blue Black for rapid staining of protein bands (AmidoBlack staining, Sigma) and then blocked for 1h with 5% non-fat milk at room temperature. Next, membranes were incubated with the primary antibody overnight at 4°C: anti-

MYC in 1:1000 dilution (5605S, Cell Signaling), anti- MYCN in 1:1000 dilution (sc-53993, Santa Cruz), anti-α tubulin in 1:20000 dilution (T9026, Sigma), anti-TOP2A (1826-1, Epitomics), anti-BUB1B (4116, Cell Signaling), anti-BIRC5 (2808, Cell Siganling), anti-AURKA (14475, Cell Signaling). Secondary antibodies were horse anti-mouse IgG (7076s, Cell Signaling) or goat anti-rabbit IgG (7074, Cell Signaling) used in 1:3000 dilution, incubated for 1h at room temperature. Both primary and secondary antibodies were diluted in 5% non-fat milk PSBT (Phosphate Buffered Saline Tween 0.1%). Signal detection was performed using SuperSignal West Femto (ThermoFisher) or Clarity Western ECL (BioRad) substrates followed by exposure on X-ray film (ThermoFischer).

In order to quantify protein expression, densitometry analysis was done using Image J software. Relative protein expression was calculated by the ratio of the target (MYC, MYCN) to that of the loading control (alpha tubulin). Data was normalized to the non-treated cells and analyzed to the control (DMSO).

STATISTICAL ANALYSIS

We used GraphPad Prism (version 7.03) for generating graph and analysis of data. Unpaired two-tailed t-test (using Welch's adjustment for heteroscedasticity when necessary) was used to compare differences in gene expression; cell viability and gene and protein expression: control (DMSO) vs JQ1; DMSO vs OTX015; gene expression after siRNA transfection: control (siC) vs si5; siC vs si7. P-values indicating significant differences were noted as follows: ns (not significant); * ($p<0.05$); ** ($p<0.01$); *** ($p<0.005$); **** ($p<0.0001$).

RESULTS

MYCN/MYCNOS CLUSTER AMPLIFICATION IN RETINOBLASTOMA PRIMARY TUMORS

We have previously analyzed the copy number variation data of our cohort of 102 primary tumors. Focal high level amplifications encompassing the *MYCN* gene (2p24.3) were found in 11% of samples analyzed (N=11/102) (**Table 2**-page 164, **Figure 2**). Interestingly, ten out of the eleven *MYCN* amplified tumors were classed in the subtype 2, while the remaining sample (HSJD-RBT3) could not be attributed to any subtype. One of this *MYCN* amplified tumors (RB222) had no detectable alterations in *RB1* gene (**Figure 2C**). Clinically, patients with tumors presenting *MYCN* amplification were significantly younger at diagnosis (15.9 months; N=10; range 5.7-25.8 months) than the rest of $RB1^{-/-}$ patients with subtype 2 tumors (27.1 months; N=47; range 11.2-85.4 months) (Unpaired t test with Welch's correction, p<0,0001) (**Figure 2B**). As most of tumors classed in the subtype 2, retinoblastoma $MYCN^{A}$ patients were non-familial cases and mostly unilateral (N=7/10) (**Table 1, chapter 1**).

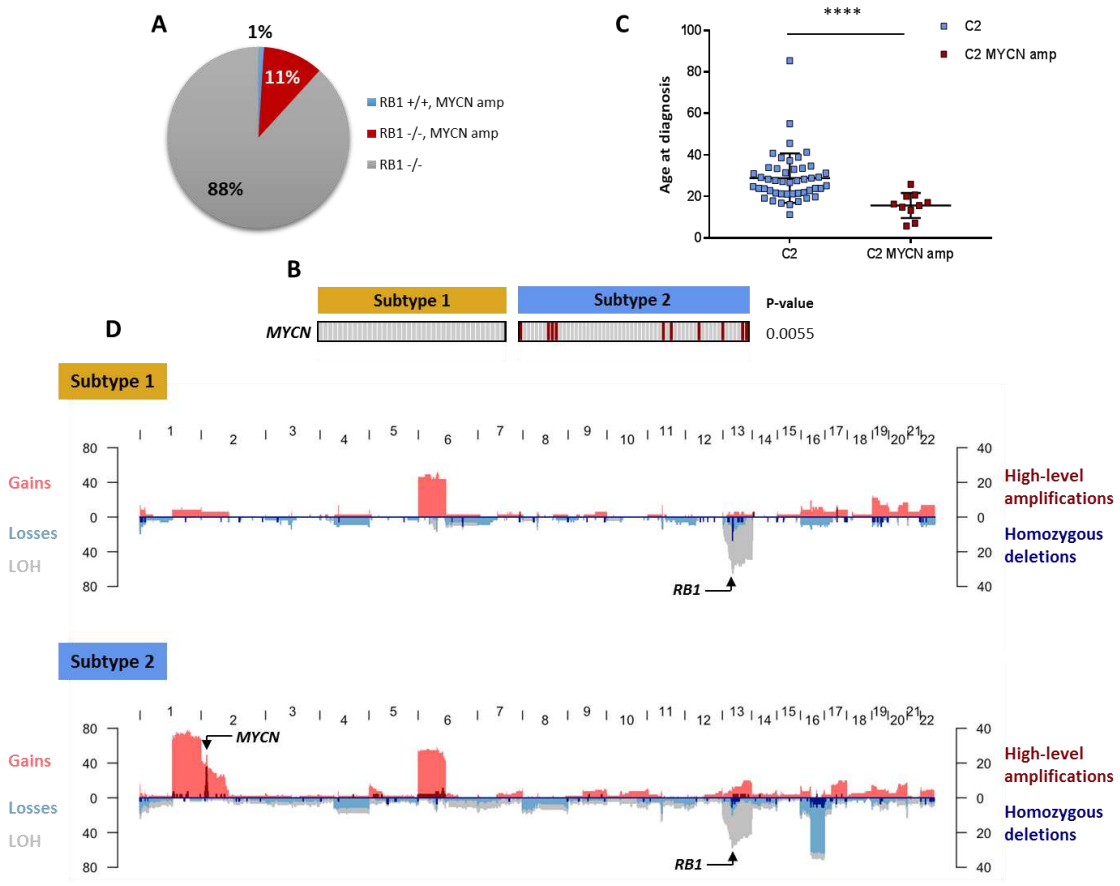


Figure 2. Genomic copy number changes detected in our 102 retinoblastoma cohort
A) Eleven percent of tumors analyzed had *MYCN* amplifications together with mutations in the *RB1* gene. One *MYCN* amplified sample (RB222) had no detectable *RB1* mutations. B) *MYCN* amplified tumors were only found in in the molecular subtype 2. C) Age at diagnosis is significantly different between the C2 *MYCN* amplified tumors (15.9 months) compared to the non-amplified C2 tumors (27.1 months). D) Genomic characteristics of the two tumor subtypes, using their copy number profiles. 1q gains, 2p gains (MYCN), 6p gains, 13q losses/LOH (RB1), and 16q losses/LOH are the most frequent alterations observed in our retinoblastoma cohort, but not equally distributed between tumor subtypes: 1q gains, 2p gains and 16q losses are mostly found in subtype 2 tumors (Fisher's exact test p-values <0.01). Besides, *MYCN* gains or amplifications are found in 50% of mixed tumors.

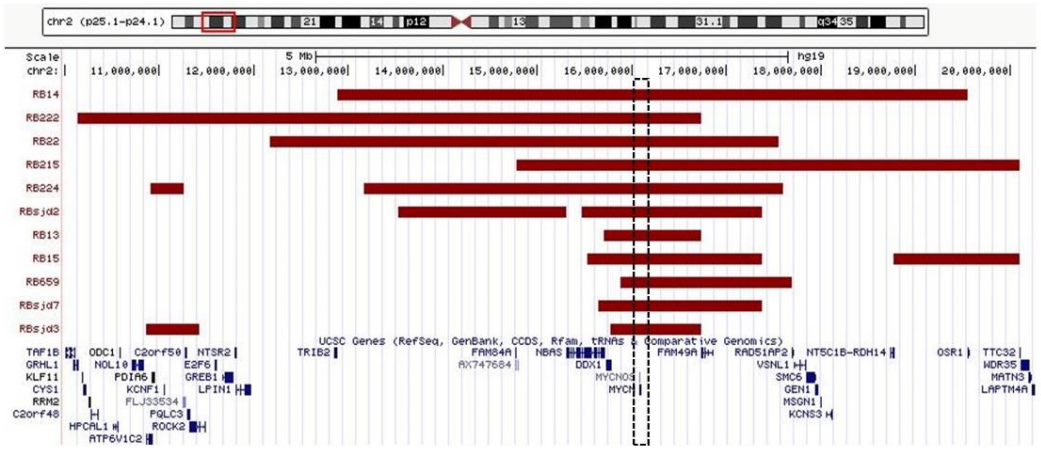
We identified five genes that were frequently co-amplified with *MYCN* (

Figure *3***A** and

Figure *3***B**). Of interest, *MYCNOS* gene (*MYCN* Opposite Strand) was the only gene found to be systematically co-amplified and co-upregulated with *MYCN* (

Figure *3***C**). *MYCNOS* is transcribed from the opposite DNA strand to *MYCN* and overlaps its 5'-end. This was an interesting gene to investigate since it has been involved in the aggressiveness of *MYCN*-amplified neuroblastoma, acting both as a protein that stabilize the MYCN protein and as an antisense RNA that regulates *MYCN* transcription (Suenaga et al., 2014; Vadie et al., 2015; Zhao et al., 2016).

A



B

Gene symbol	Location	Start	End	n	Sample ID	Gene Function	Involvement in cancer	PMID
FAM84A	2p24.3	14772810	14790933	5	RBsjd2, RB224, RB22, RB14, RB222	Unknown	Not reported	
NBAS	2p24.3	15307032	15701454	5	RB224, RB215, RB22, RB14, RB222	Involved in Golgi-to-endoplasmic reticulum (ER) retrograde transport	Not reported	
DDX1	2p24.3	15731302	15771235	9	RB13, RB15, RBSjd7, RBsjd2, RB224, RB215, RB22, RB14, RB222	Acts as an ATP-dependent RNA helicase	Protumorigenic and tumor suppressor roles	193989532 5176654
MYCNOS	2p24.3	16061159	16082371	11	RB13, RBsjd3, RB659, RB15, RBSjd7, RBsjd2, RB224, RB215, RB22, RB14, RB222	As a protein stabilize the MYCN protein; as an antisense RNA participate in the transcriptional regulation of MYCN	Facilatates MYCN expression	26549029
MYCN	2p24.3	16080686	16087129	11	RB13, RBsjd3, RB659, RB15, RBSjd7, RBsjd2, RB224, RB215, RB22, RB14, RB222	Transcription factor	Involved in several cancers including retinoblastomas and neuroblastomas	15975048
FAM49A*	2p24.2	16730727	16847599	8	RB659, RB15, RBSjd7, RBsjd2, RB224, RB215, RB22, RB14*	Unknown	Not reported	19398953

***RB14 presents a translocation t(1;2)(q23.3;p24.2) (fusion in frame NUF2_FAM49A) (Table 9, chapter 1)**

C

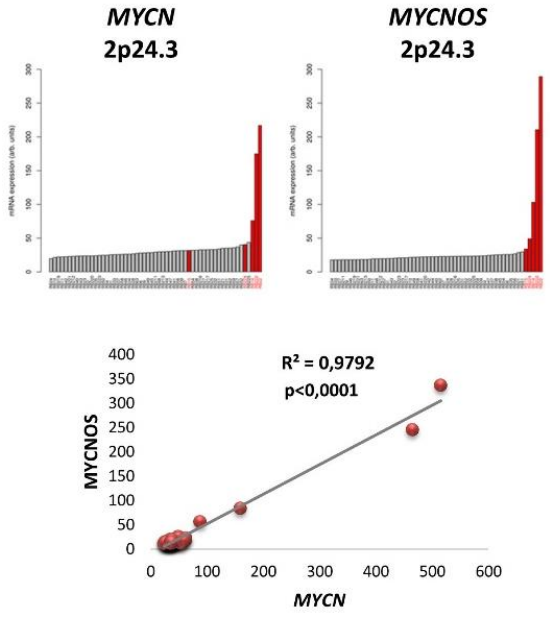


***Figure 3. Amplifications of the MYCN/MYCNOS* locus**
A) Amplified regions spanning the *MYCN/MYCNOS* locus (2p24.3) in eleven samples (RB13, RB14, RB15, RB22, RB215, RB222, RB224, RB659, HSJD-RBT2, HSJD-RBT3, HSJD-RBT7). For each tumor, the regions presenting amplification are shown in dark red. The black dotted rectangle indicate the location of *MYCN/MYCNOS*. B) Characteristics and description of genes located around the amplified MYCN locus. For each gene, "n" is the number of tumors displaying amplification. C) Relationship between expression and amplification of *MYCN* and *MYCNOS* genes. Tumors are classified according to their *MYCN* (left panel) or *MYCNOS* (right panel) mRNA expression (N=59/102 tumors). Red bars indicate the five tumors with MYCN/MYCNOS amplification. *MYCN* and *MYCNOS* expression correlation is shown below graphs (Pearson's correlation R=0,9792, p<0,0001).

Therefore, in order to test a possible role of *MYCNOS* gene in retinoblastoma, we transiently knocked down *MYCNOS* in one retinoblastoma cell line. We transfected the Y79 *MYCN*-amplified cell line with a pre-designed short interfering RNA (siRNA) against *MYCNOS*-exon 3. Targeted sequence was specific for *MYCNOS* and did not overlap to that of *MYCN* gene. Targeting *MYCNOS* reduced ~70% of *MYCN* gene expression from 48h of treatment and was maintained up to 96h post-transfection (**Figure 4**). As it was shown for neuroblastoma (Vadie et al., 2015; Zhao et al., 2016), the expression of *MYCNOS* is related to the expression of *MYCN* in the retinoblastoma context. As no available antibody exists for MYCNOS, we could not assessed its effect at the protein level. Given that *MYC* family of oncogenes are typically expressed in rapidly dividing cells, we evaluated a possible effect of *MYCNOS* on cell viability. Although lipofectamine used in transient transfection entailed some toxicity, no effect on cell viability was appreciated after transient transfection at 24h, 48h, 72h or 96h compared to the siRNA control (data not shown).

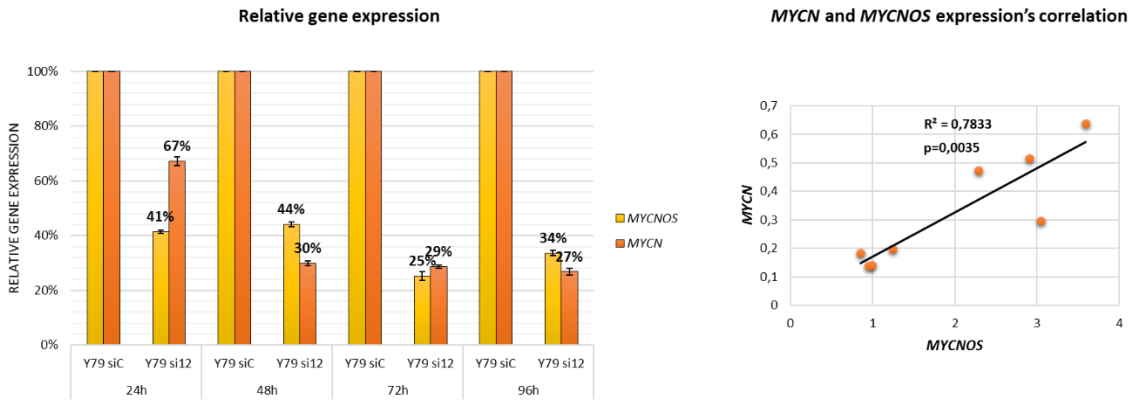
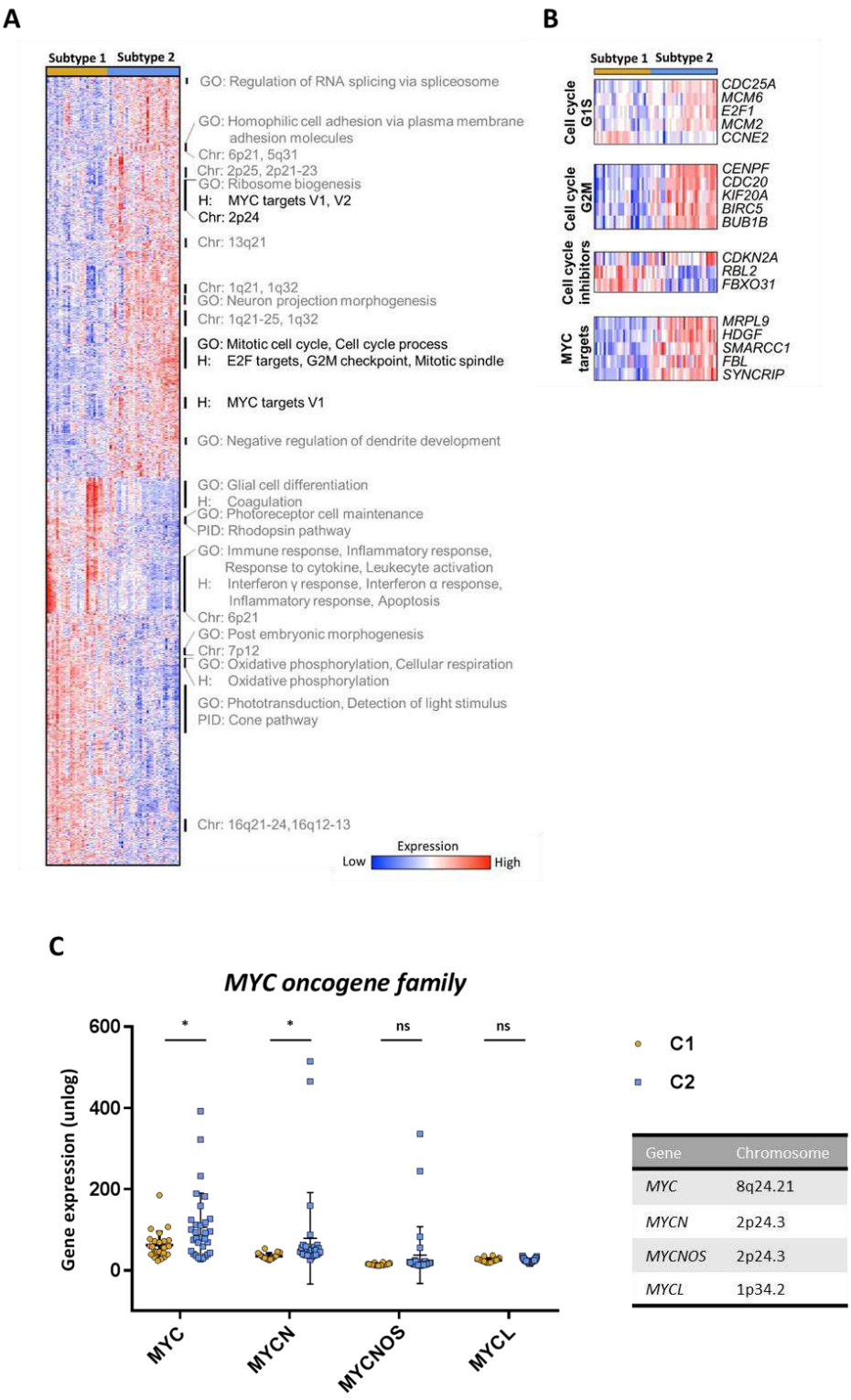


Figure 4. MYCN gene expression downregulation after transient knockdown of MYCNOS
Transient transfection at 24h, 48h, 72h and 96h. *MYCN* and *MYCNOS* expression correlation is shown at the left (Pearson's correlation R=0,7833, p=0,0035).

MYC PATHWAY UPREGULATION IN RETINOBLASTOMA SUBTYPE 2

To identify differentially expressed genes between the retinoblastoma subtypes we used Limma analysis in the classified tumor samples, for which the transcriptome was available (N=26 subtype 1; N=31 subtype 2). Hierarchical clustering of the differentially expressed genes was used to identified gene clusters enrichment for Gene Ontology Biological Processes, and we used Hallmark genesets to

identified differentially expressed gene pathways (**Figure 5A**). We found that subtype 2 tumors overexpressed cell-cycle-associated genes and targets of *E2F* transcription factors. In addition, we detected an upregulation of cell cycle genes involved in both G1/S and G2/M transitions, with stronger upregulation of genes involved in the latter. In **Figure 5B** are shown the most differentially expressed genes between both subtypes and for each category. In line with this pro-proliferative state, *MYC* target genes were found to be significantly upregulated in the subtype 2 (**Table 3**, page 165). *MYC* and *MYCN* genes are significantly differentially expressed between both subtypes (**Figure 5C**).



Gene	Chromosome
MYC	8q24.21
MYCN	2p24.3
MYCNOS	2p24.3
MYCL	1p34.2

Figure 5. Hierarchical clustering of the differentially expressed genes between subtype 1 and subtype 2 retinoblastomas

A) Hierarchical cluster analysis of 6699 significantly differentially expressed genes. Clusters significantly enriched for biological functions in gene ontology (GO), clusters significantly enriched for pathways in HALLMARK (H) or Pathway Interaction Database (PID) and clusters significantly enriched for human chromosome and cytogenetic band (Chr) are described at the right of the heatmap. Highlighted in black are those related to cell cycle and *MYC* signaling pathways. B) Heatmap of differentially expressed genes in the selected pathways. G2/M cell cycle genes were more strongly

upregulated than those of G1/S in the subtype 2, while cell cycle inhibitors were strongly upregulated in subtype 1. MYC target genes are upregulated in subtype 2 tumors. C) Gene expression (transcriptome) of the MYC-oncogen family members. *MYC* and *MYCN* are differentially expressed between subtype 1 and subtype 2 tumors (*MYC* C1 vs C2: p=0,0104; *MYCN* C1 vs C2: p=0,0369; *MYCNOS* C1 vs C2: p=0,0760; *MYCL* C1 vs C2: p=0,8796).

SENSITIVITY OF RETINOBLASTOMA CELL LINES TO BROMODOMAIN INHIBITORS COMPOUNDS

Bromodomain inhibitor compounds (BETi) are synthetic small molecules that targets the BET bromodomain proteins BRD2/3/4. They have been shown to have strong antitumor activity against a range of cell lines derived from hematologic malignancies and solid tumors (Coudé et al., 2015; Henssen et al., 2016), modulating transcriptional repression pathways characteristic of MYC functioning. Given that *MYC* pathway was found to be overexpressed and that we mostly found *MYCN* amplifications in the mixed subtype of primary retinoblastoma tumors, we hypothesized that retinoblastoma cell lines representative of subtype 2 would be susceptible to BRD inhibition. For that purpose, we chose three cell lines with different molecular backgrounds: Y79 classed as subtype 2, with *MYCN* amplification and showing high expression of *MYCN* gene and protein; CL-RB247 classed as subtype 2, showing *MYC* gene and protein expression; and WERI, which could not be attributed to any subtype, having moderate *MYCN* gene and protein expression (**Figure 6A** and **Figure 6A**). Basal expression of *BRD2*, *BRD3* and *BRD4* genes are similar for the cell lines chosen (**Figure 6C**). Retinoblastoma cell line's molecular classification was assessed by centroid classification based on transcriptomic data and by pyrosequencing. Molecular aspects of retinoblastoma cell and animal models will be discussed in details in **chapter 4**.

The effect of (+)-JQ1 and OTX015 compounds was evaluated on the three cell lines *in vitro,* with doses ranging from 300nM to 10µM. DMSO was used as control as well as the inactive stereoisomer ((-)-JQ1) of the active (+)-JQ1. Cell viability was assessed using the Celltiter Glo assay at 72h post-treatment. Cell viability was reduced in the three cell models used. WERI response was dose-dependent, reaching to approximately 75% of viability inhibition at the highest concentration (10µM), while Y79 and CL-RB247 showed a maximum effect at the lowest concentration used (312nM) reaching an inhibition plateau of near 50% at higher concentrations (**Figure 6D**). Both compounds (+)-JQ1 and OTX015 had similar effects on cell viability.

Together, JQ1 and OTX015 induced inhibition of cell viability in the three cell lines. Nevertheless, effect on Y79 and CL-RB247 seemed to be more specific, as viability was affected at lower concentrations. WERI cells response increased with higher concentrations of BET inhibitors. This observation led us to suppose that viability of WERI cells was more probably affected by toxicity rather than by a specific action of the treatment.

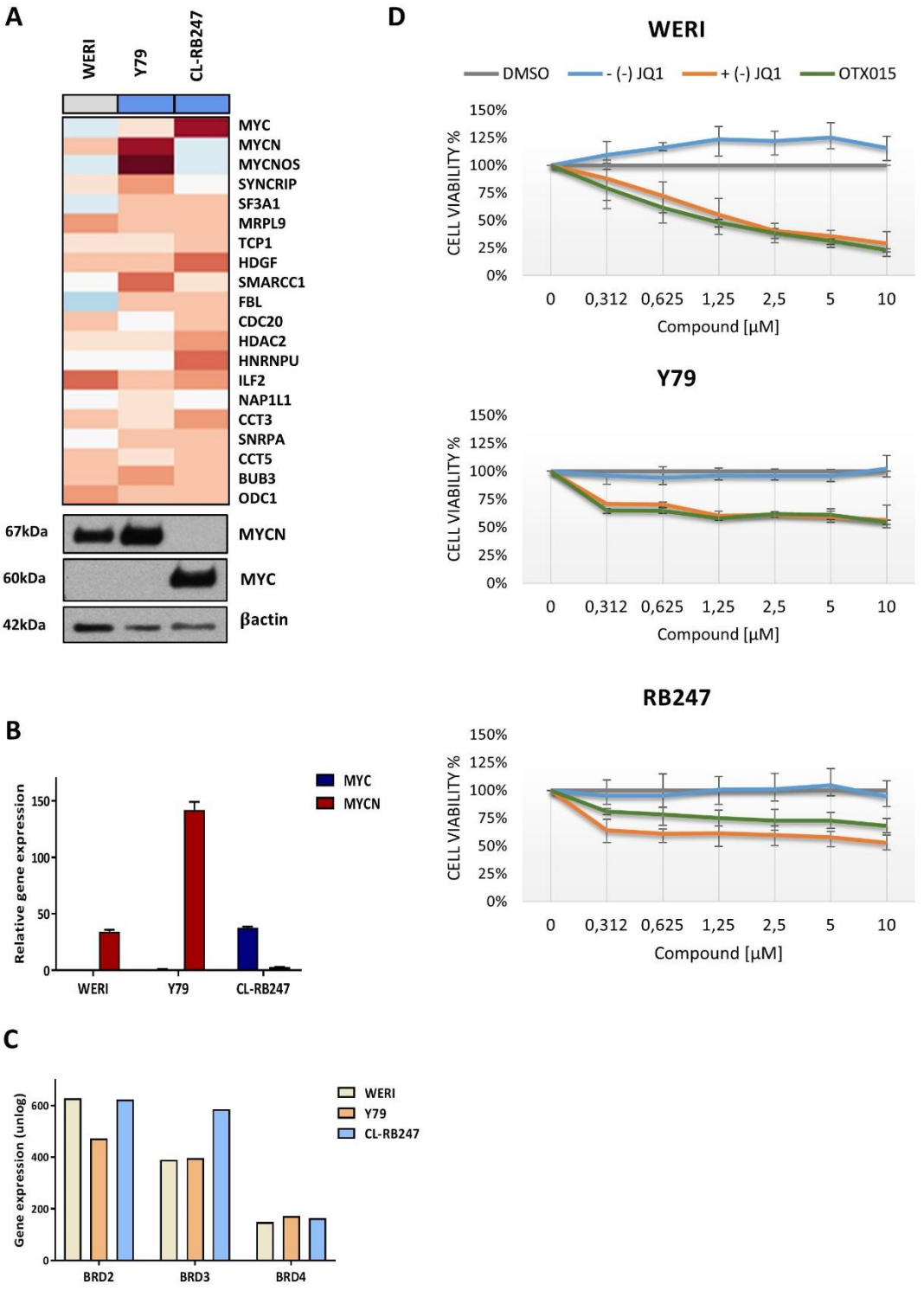


Figure 6. MYC and MYCN expression in retinoblastoma cell lines and sensitivity to a range concentrations of BETi compounds

A) WERI is indicated in gray (not classed) and Y79 and CL-RB247 in blue (subtype 2). *MYC*, *MYCN* and target genes expression assessed by transcriptome array. MYC and MYCN protein expression assessed by western blot. B) Relative gene expression of *MYC* (blue) and MYCN (dark red) assessed by RT-qPCR in the three cell lines selected. C) Gene expression of bromodomains (BRD2 in light yellow, BRD3 in light orange and BRD4 in light blue) assessed by transcriptome array in the three selected retinoblastoma cell lines. D) Dose–response curve at 72h with increasing OTX015 (green) and JQ1 (orange) concentrations. Data was normalized to the control (DMSO).

Effect of JQ1 and OTX015 on *MYC* and *MYCN* expression in retinoblastoma cell lines

We then performed a time-response curve treatment in the purpose of evaluating, in addition to cell viability, the effect on MYC and MYCN mRNA and protein expression levels. Treatment was performed in triplicates for 24h, 48h, 72h and 96h at a high JQ1 and OTX015 dose (2.5µM), based on the previous observation of 50% cell viability inhibition for the three cell lines at 72h.

Following exposure to OTX015 and JQ1, the three cell lines showed significantly reduced cell inhibition over time, but effects on gene and protein expression were different for the highly expressing MYCN and MYC cell lines, Y79 and CL-RB247, respectively, compared to WERI cells with a moderate MYCN expression. Relative gene expression was assessed by RT-qPCR using TBP as the reference gene. Immunoblotting was performed and relative protein expression was calculated as described in material and methods.

Y79 cell line

A significant cell viability effect was observed from 24h (JQ1) and 48h (OTX015) of treatment in Y79 cells (**Figure 7A**) (DMSO vs (+)-JQ1: 24h, p=0,0450 ; 48h, p=0,0173; 72h, p=0,0052; 96h, p=0,0232. DMSO vs OTX015: 24h, p= 0,0503; 48h, p= 0,0013; 72h, p=0,0014; 96h, p=0,0144, unpaired t-test), accompanied by *MYCN* gene downregulation (**Figure 7B**). At the protein level, MYCN was downregulated at 24h, continued to decrease to 72h and then recovered to expression's levels detected at 24h (**Figure 7C**). Relative protein expression was calculated relative to DMSO control, as described in material and methods. Effects of JQ1 and OTX015 on cell viability and gene expression were significantly correlated (Cell viability: Pearson's correlation R=0,8448, p<0,0001; Gene expression: Pearson's correlation R=0,9779, p<0,0001) (**Figure 7D**).

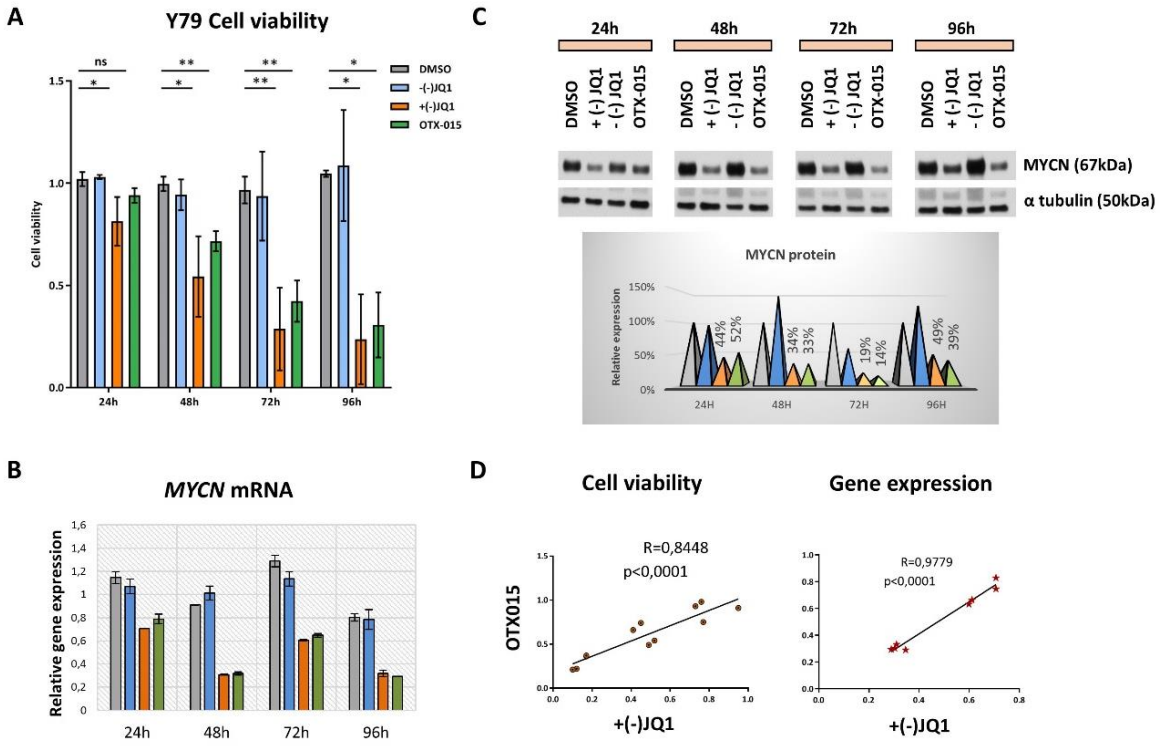


Figure 7. Y79 response to BET inhibitors treatment
A) Cell viability time-response following JQ1 and OTX015 (2.5µM) treatment. A significant cell viability effect was observed from 48h after treatment. B) *MYCN* gene expression assessed by RT-qPCR showed downregulation from 24h of treatment, effect that was maintained up to the end pf the treatment. C) *MYCN* protein expression assessed by western blot at the indicated time points. Alpha tubulin was used as control. D) Response on cell viability and *MYCN* gene expression was significantly correlated with both BET inhibitors used. One representative experiment is shown for B) and C).

CL-RB247 cell line

Cell viability of CL-RB247 cells was significantly reduced as early as 24h, and effect continued for the next days of treatment, increasingly affecting cell viability (DMSO vs (+)-JQ1: 24h, p=0,0010; 48h, 0,0007; 72h, p<0,0001; 96h, p=0,0014. DMSO vs OTX015: 24h, p=0,0083; 48h, 0,0005; 72h, p<0,0001; 96h, p=0,0012) (**Figure 8A**) and *MYC* mRNA expression (**Figure 8B**). At the protein level, a MYC decrease was also observed from 24h and sustained to the end of treatment (**Figure 8C**). Effects of JQ1 and OTX015 on cell viability and gene expression were significantly correlated (**Figure 8D**) (Cell viability: Pearson's correlation R=0,9384, p<0,0001; Gene expression: Pearson's correlation R=0,8345, p<0,0001).

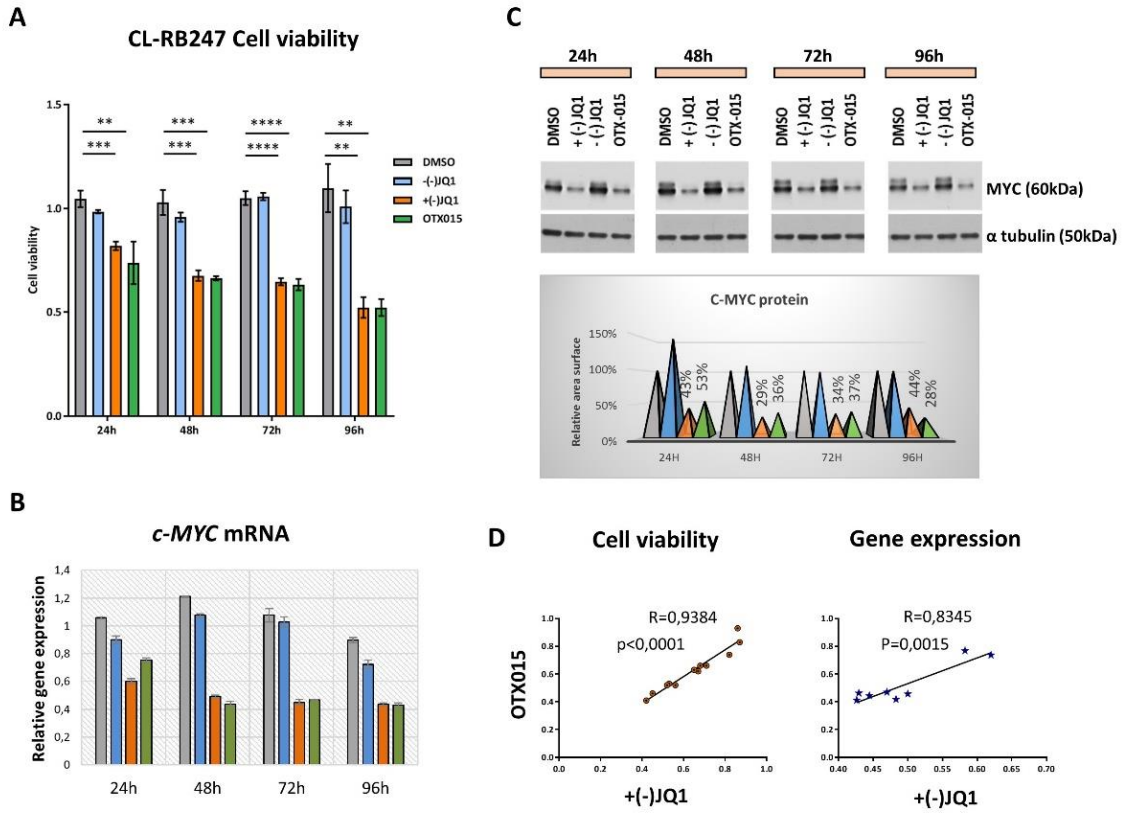


Figure 8. CL-RB247 response to BET inhibitors treatment
A) Cell viability time-response following JQ1 and OTX015 (2.5µM) treatment. A significantly effect on cell viability reduction was observed as early as 24h after treatment. B) *MYC* gene expression assessed by RT-qPCR showed downregulation from 24h of treatment, and effect that was maintained up to the end of the treatment. C) MYC protein expression assessed by western blot at the indicated time points. Alpha tubulin was used as control. D) Response on cell viability and *MYC* gene expression was significantly correlated with both BET inhibitors used. One representative experiment is shown for B) and C).

WERI cell line

As first observed, WERI cells were the most affected by the treatment at 2.5µM, reaching up to 90% of viability inhibition at 96h (DMSO vs (+)-JQ1: 24h, p=0,0017 ; 48h, p=0,0002 ; 72h, p= 0,0023 ; 96h, p= 0,0010. DMSO vs OTX015: 24h, p=0,0016 ; 48h, p=0,0003 ; 72h, p= 0,0024 ; 96h, p= 0,0010. Unpaired t-test) (**Figure 9A**). We did not detected a MYCN gene or protein downregulation as observed for Y79 and CL-RB247. Moreover, *MYCN* gene was upregulated after the treatment (**Figure 9B**). MYCN protein was initially downregulated at 24h with OTX015 treatment, but then restored. Due to a high cell viability inhibition at 72h and 96h, the loading protein control used in the immunoblotting was also decreased, thus not possible to analyze MYCN protein expression at that time points (**Figure 9C**). This observation also supports the idea of a highly induced toxicity, non-specific to the treatment.

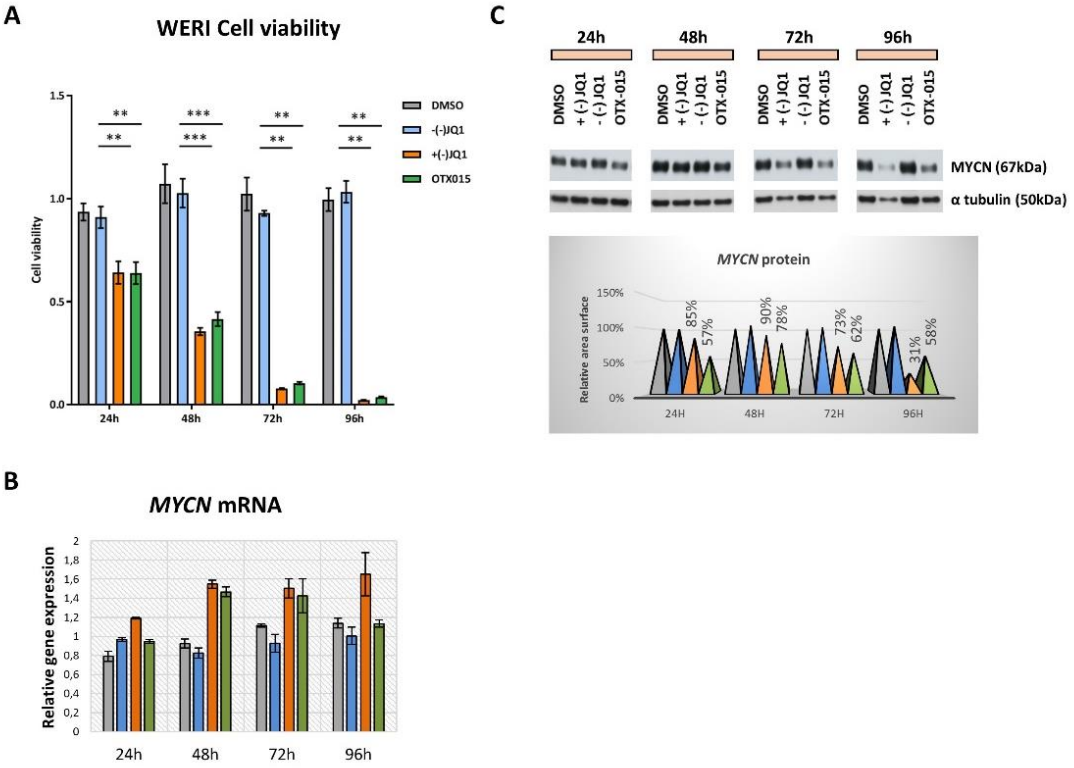


Figure 9. WERI response to BET inhibitors treatment
A) Cell viability time-response following JQ1 and OTX015 (2.5µM) treatment. A significant cell viability effect was observed as early as 24h after treatment and cell inhibition increased over time. B) Relative *MYCN* gene expression was not downregulated but upregulated after the treatment. C) MYCN protein was initially downregulated at 24h with OTX015, but then restores its expression levels. The loading control was also affected with the treatment at 72h and 96h (probably due to high cell inhibition) therefore not analyzable at these time points. One representative experiment is shown for B) and C).

BET INHIBITION OUTCOME ON MYC/MYCN DOWNSTREAM TARGET GENES

Our results showed that JQ1 and OTX015 treatment leads to a significant decrease in cell viability and to MYC and MYCN downregulation in CL-RB247 and Y79 cells. In order to confirm the direct MYC/MYCN transcriptional repression, a series of known downstream target genes were selected to evaluate its expression after the treatment. Six target genes (*AURKB*, *CCND2*, *DUSP7*, *SKP2*, *FBL* and *MRPL9*) were chosen based on publicly available data (Bouchard et al., 1999; Chappell et al., 2013; Evans et al., 2015; den Hollander et al., 2010; Morrish and Hockenbery, 2014; Raetz et al., 2003) and our own transcriptomic data.

Expression of target genes was evaluated by RT-qPCR in Y79 and CL-RB247 cells exposed to JQ1 and OTX015 (2.5µM) or inactive JQ1 and DMSO (0.02%) for 24h. Experiments were performed in triplicates. Data was normalized to non-treated cells and analyzed relative to control (DMSO). Four target genes, *AURKB*, *CCND2*, *DUSP7* and *FBL*, were found to be significantly downregulated in both Y79 cells (**Figure 10**) and CL-RB247 (**Figure 11**).

Taken together, BET inhibition not only lead to the downregulation of MYC and MYCN genes (and protein) but also to its target genes.

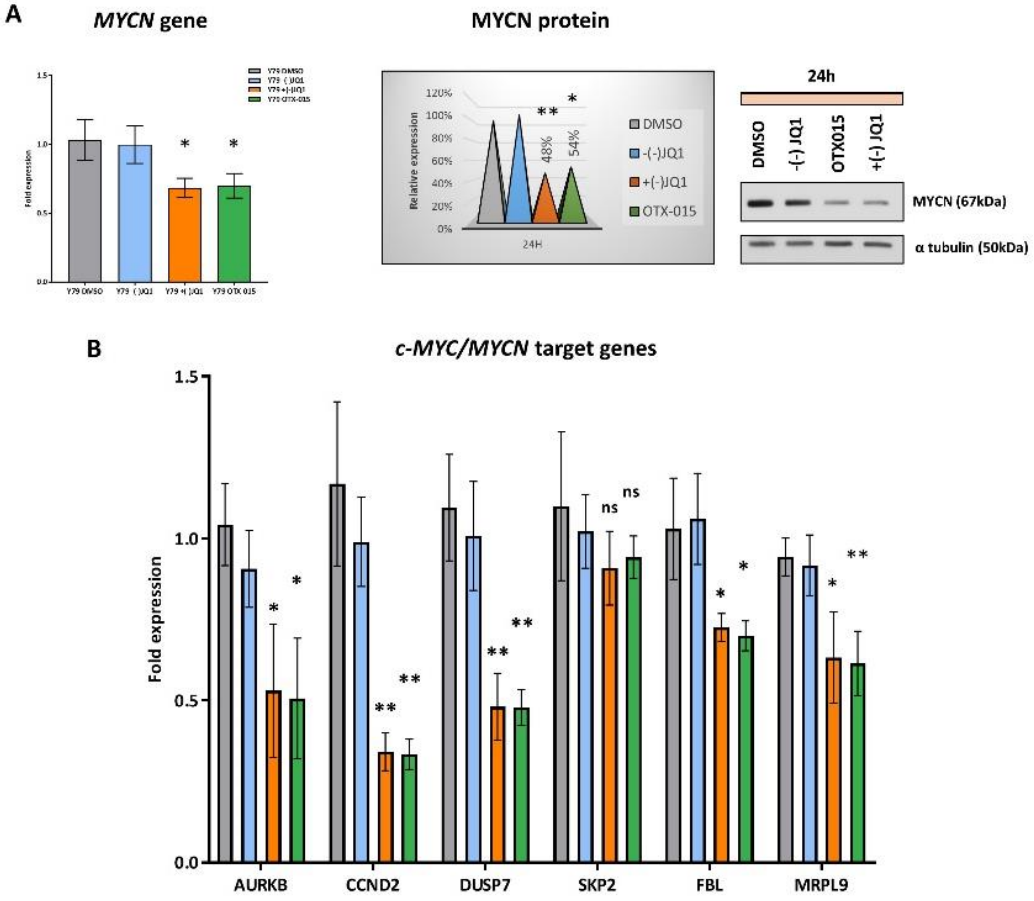


Figure 10. Y79 MYCN gene and protein expression and downstream target genes

A) Significant downregulation of MYCN gene and protein and its B) downstream target genes (b) following BET inhibition treatment (2.5µM) at 24h. Experiments were performed in triplicates. One representative experiment is show for immunoblotting. Difference in gene expression for SKP2 was not significant by non of the inhibitors used. Gene expression. DMSO vs (+)-JQ1 at 24h: MYCN, p=0,0211 ; AURKB, p=0,0212 ; CCND2, p=0,0053; DUSP7, p=0,0054; SKP2, p=0,2661; FBL, p=0,0313; MRPL9, p=0,0242. DMSO vs OTX015 at 24h: MYCN, p=0,0287; AURKB, p=0,0145 ; CCND2, p=0,0050; DUSP7, p=0,0035; SKP2, p=0,3177; FBL, p=0,0246; MRPL9, p=0,0078. Protein. DMSO vs (+)-JQ1 at 24h: MYCN, p=0,0061. DMSO vs OTX015 at 24h: MYCN, p=0,0173.

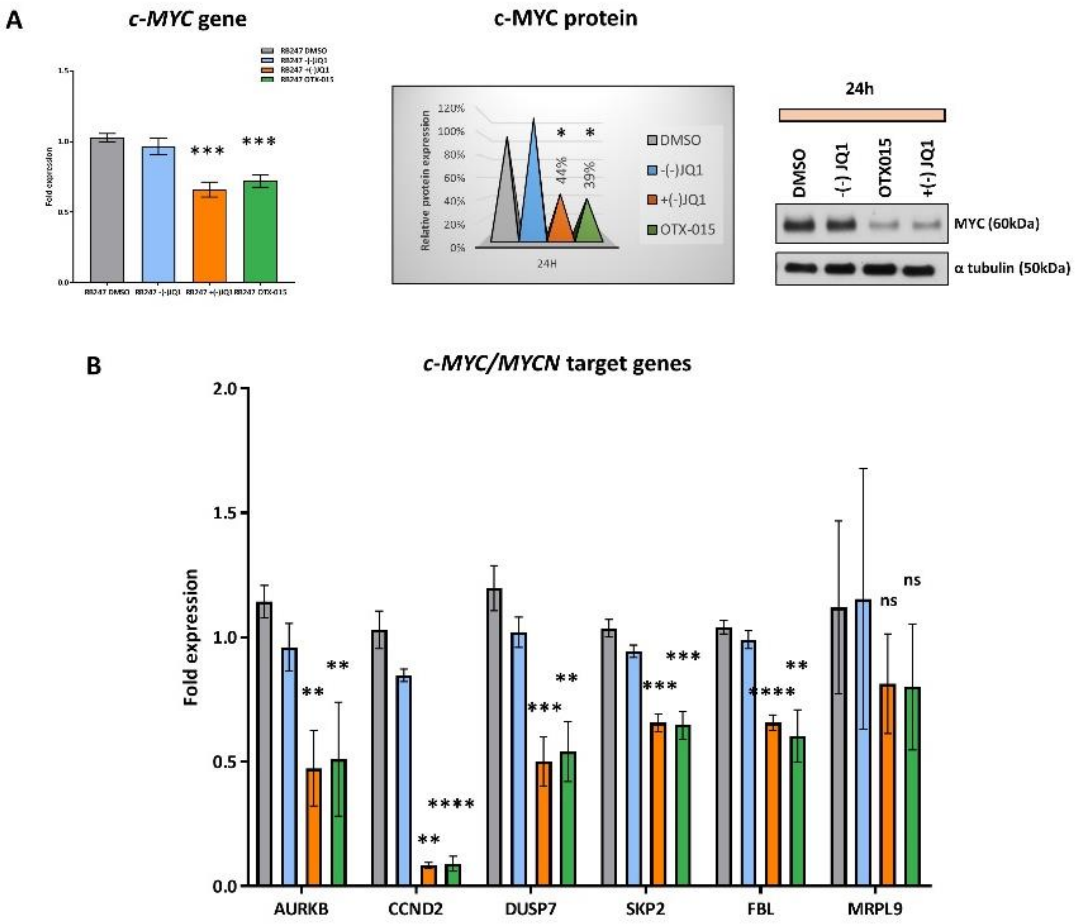


Figure 11. CL-RB247 MYC gene and protein expression and downstream target genes
A) Significant downregulation of MYC gene and protein and B) downstream target genes following BET inhibitors treatment (2.5µM) at 24h. Experiments were performed in triplicates. One representative experiment is show for immunoblotting. Difference in gene expression for *MRPL9* was not significant by none of the inhibitors used. Gene expression. DMSO vs (+)-JQ1 at 24h: c-MYC, p=0,0005 ; AURKB, p=0,0021 ; CCND2, p=0,0017; DUSP7, p=0,0008; SKP2, p=0,0002; FBL, p<0,0001; MRPL9, p=0,2555. DMSO vs OTX015 at 24h: MYC, p=0,0006 ; AURKB, p=0,0100; CCND2, p<0,0001; DUSP7, p=0,0016; SKP2, p=0,0005; FBL, p=0,0022; MRPL9, p=0,2667. Protein. DMSO vs (+)-JQ1 at 24h: MYC, p=0,0202. DMSO vs OTX015 at 24h: MYC, p=0,0274.

TRANSIENT KNOCKDOWN OF MYC AND MYCN DO NOT RECAPITULATE THE BET INHIBITION EFFECTS

In order to uncover whether deregulation of this series of genes was a direct consequence of MYC/MYCN repression, we performed a transient siRNA transfection against MYC in CL-RB247 cells. Transfection was performed for 96h with two pre-designed siRNA against MYC exon 3 (si5) and exon 2 (si7) at a final concentration of 30nM. Experiments were performed in triplicates. Data was normalized to non-treated cells and analyzed relative to control (siC: siRNA against luciferase). MYC gene was significantly downregulated, with 60% (si5) and 40% (si7) of gene expression inhibition (**Figure 12A**). At the protein level, MYC expression was reduced by almost 50% with both siRNAs (**Figure 12B**). Regarding MYC target genes, *DUSP7* was the only significantly downregulated after transfection with one of the siRNA used (si5) (**Figure 12C**). In summary, our results of transient

downregulation of *MYC* gene did not recapitulate results of BET inhibition treatment. This could in part suggest that both MYC and its target genes are direct BET targets. Direct downregulation effect was only seen for DUSP7 after MYC knock down in CL-RB247.

In parallel, we aimed to uncover a possible direct role of MYC/MYCN on cell viability inhibition. For this purpose, we performed cell viability assays in Y79 and CL-RB247 cells for 48h, 72h and 96h after transient siRNA transfection. CL-RB247 cells were transfected with si5 and si7 against MYC as described above. Y79 cells were transfected with two siRNA targeting MYCN-exon 3 (si6 and si7) at a final concentration of 30nM. *MYCN* was highly reduced at the gene (-60% using si6 and -90% using si7) and the protein level (**Figure 12E** and **Figure 12F**). Nevertheless, changes in cell viability (**Figure 12D** and **Figure 12G**) were not detected when compared to the control. We noticed that transfection by itself entailed toxicity, reducing cell viability considerably for control and transfected cells, though difficult to interpret. Improvements in transfection need to be made in order to obtain interpretable results.

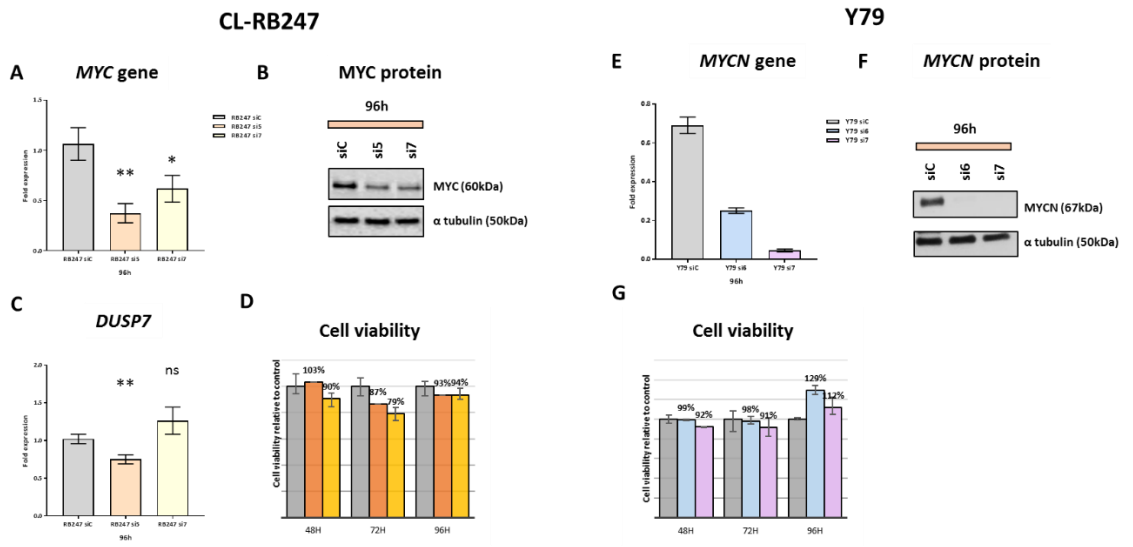


Figure 12. Transient transfection using predesigned siRNA against c-MYC and MYCN genes
A) MYC gene was significantly downregulated in CL-RB247 at 96h of transfection, using two different siRNA (siC vs si5: p=0,0032; siC vs si7: p=0,0212). B) MYC protein expression showed a downregulation of ~50% with both siRNAs. C) DUSP7 was the only target gene significantly downregulated after transfection with one of the siRNA used (si5) (siC vs si5: p=0,0057; siC si7: p=0,0915). D) No changes in CL-RB247 cell viability were detected after 48h, 72h, and 96h of transient transfection. E) *MYCN* was highly reduced after transfection in Y79 cells: 60% of gene downregulation using si6 and 90% using si7) at 96h. F) MYCN protein expression was inhibited after treatment with both siRNAs. G) No changes in Y79 cell viability were detected after 48h, 72h, and 96h of transient transfection. Experiments were performed in triplicates for CL-RB247. One experiment was run in Y79 cells.

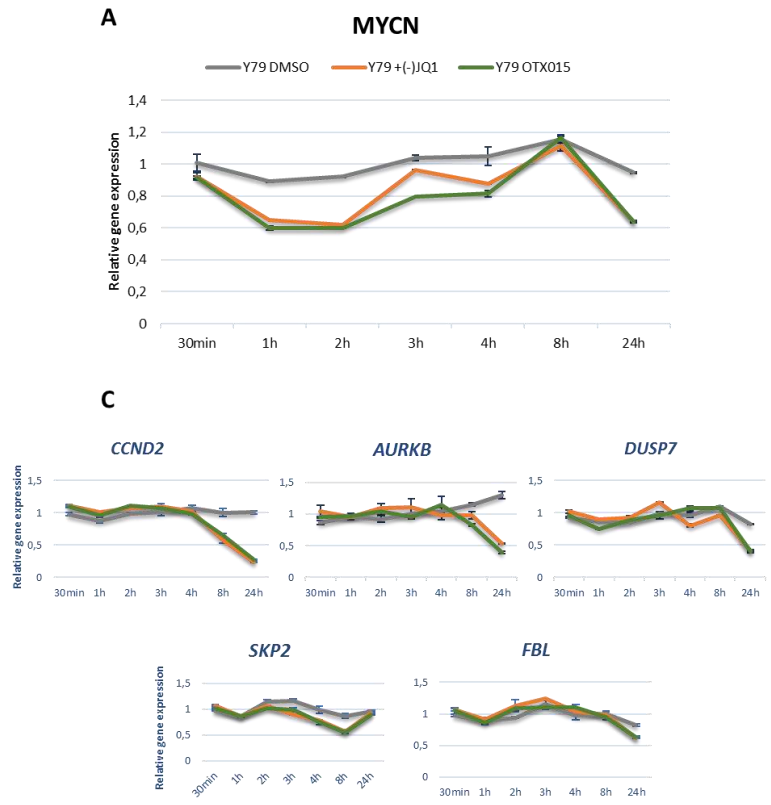
COMPLEX DYNAMICS OF MYC AND MYCN GENE EXPRESSION FOLLOWING JQ1 AND OTX015 TREATMENT

We have shown that *MYC* and *MYCN* genes were significantly downregulated as early as 24h post-treatment in both cell lines. To the gain insights in the dynamics of *MYC* and *MYCN* gene deregulation

following BET inhibition, we performed a time-response curve treatment at shorter times than previous experiments. Y79 and CL-RB247 cells were treated for 30 minutes, 1h, 2h, 3h, 4h, 8h and 24h at 2.5µM dose. Relative gene expression was assessed by RT-qPCR using TBP as the gene of reference. Values were normalized to the non-treated cells.

Following treatment, both *MYCN* and *MYC* gene expression showed an intricate pattern of gene regulation with both compounds. *MYCN* was downregulated as fast as 1h after treatment, maintained its repression the following hour, then upregulated up to 8h and finally going down reaching the expression' level found at 2 hours of treatment (**Figure 13A**). A similar pattern was observed for *MYC* in CL-RB247 cells (**Figure 13B**). We then looked for the expression of the series of target genes previously described. In Y79 cells, *CCND2* was downregulated after 4h of treatment and continued up to 24h. *AURKB*, *DUSP7* and *FBL* showed a decreased expression from 8h to 24h. SKP2 was downregulated from 2h to 8h, and then upregulated (**Figure 13C**). In CL-RB247 cells, *CCND2* was deregulated early in time, since 1h after treatment with decreasing levels of expression over time. *AURKB*, *DUSP7* and *FBL* showed downregulation from 4h to 24h. *SKP2* was downregulated from 4h and, unlike Y79 cells, maintained up to 24h (**Figure 13D**).

In summary, c-MYC/MYCN showed a complex pattern of gene expression following BET inhibition, with inhibitory peaks at 1-2h and then upregulated. This pattern was very similar for Y79 and CL-RB247 cells, both for *MYCN* and *c-MYC* as well as for their target genes.



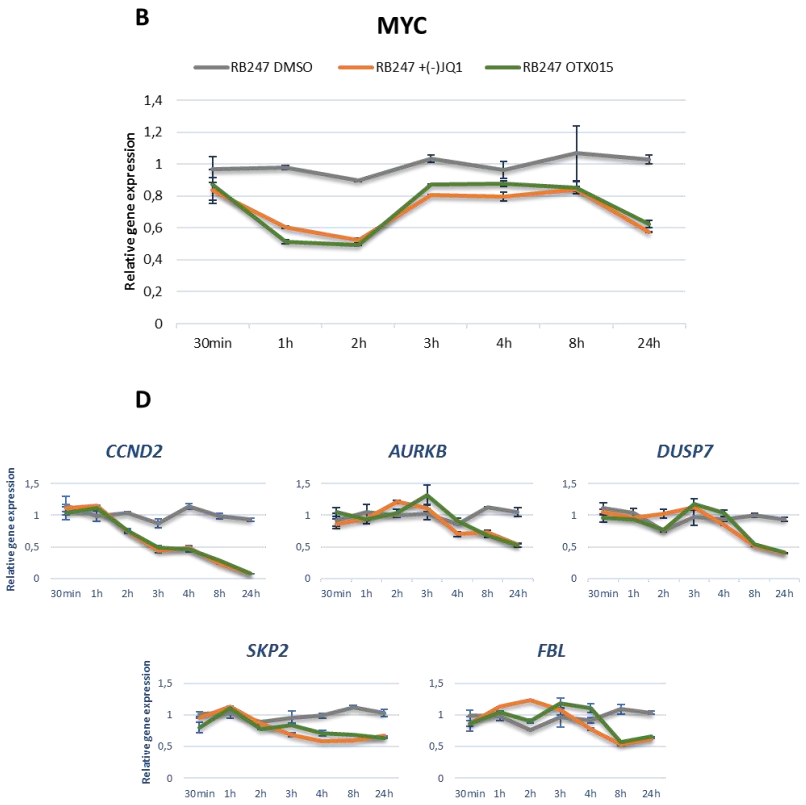


Figure 13. Dynamics of gene expression following JQ1 and OTX015 treatment

MYCN (a) and *MYC* (b) were downregulated 1h after treatment and maintained its repression the following hour. Then, an upregulation occurred up to 8h, and finally expression went down reaching similar expression levels to that found after 2 hours of treatment. Both genes followed the same expression pattern. C) In Y79 cells, *CCND2* was downregulated after 4h of treatment, increasing over time up to 24h. *AURKB*, *DUSP7* and *FBL* showed downregulation from 8h. *SKP2* was slightly downregulated from 2h to 8h, and then upregulated at 24h. D) In CL-RB247 cells, *CCND2* was deregulated early in time, since 1h after treatment with decreasing levels of expression over time. *AURKB*, *DUSP7* and *FBL* showed downregulation from 4h. SKP2 was downregulated from 4h and this downregulation was maintained up to 24h. All experiments were run in duplicates.

DISCUSSION AND CONCLUSIONS

MYCN AMPLIFICATIONS AND *MYC* SIGNALING ARE RELATED TO RETINOBLASTOMA MOLECULAR SUBTYPE 2

MYCN amplifications have long been known to occur in retinoblastoma, often together with retinoblastoma gene loss (10% of cases) or not (1.5% of cases), and were reported to have distinct clinical onset, histopathological features and less overall genomic copy-number changes (Rushlow et al., 2013b). Analysis in our cohort, indeed suggest that they may represent a distinct molecular subgroup within the subtype 2, for several reasons. First, all patients carrying a *MYCN* amplification (11%) were diagnosed at earlier ages compared to the non-amplified subtype 2 tumors (15.9 months vs 27.1 months, p<0,0001). Second, they present a significant lower genomic instability score (p=0.014). Seven out of the eleven *MYCN*-amplified tumors presented with only chromosome 2p amplifications as copy number variations, whereas four samples presented in addition 1 or 2 more genomic changes (RB14: 1q gain, 16q loss; RB215: 13q loss, 17q loss; HSJD-RBT2: 12q loss; HSJD-RBT3: 8p loss). Third, *MYCN* amplified tumors were globally hypomethylated compared to both non-amplified subtype 2 and subtype 1 tumors (p=0.0038, p=0.0016) (**Figure 14**). This latter feature is in line with reported observations in mice, where Mycn disruption led to large-scale changes in histone modifications associated with chromatin inactivation, including altered methylation (Knoepfler et al., 2006).

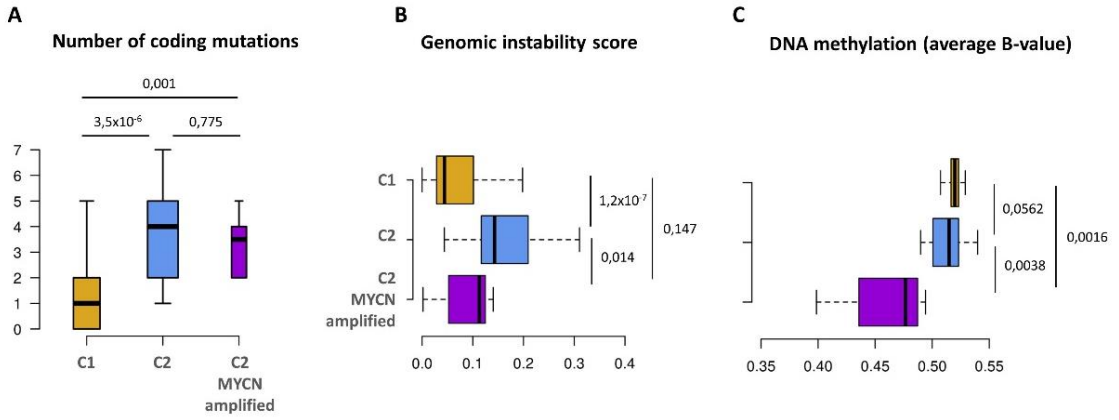


Figure 14. Number of coding mutations, genomic instability, and overall DNA methylation in retinoblastoma
Subtype 1 (gold), non-amplified (blue) and *MYCN*-amplified (violet) subtype 2 retinoblastomas. A) The distribution of exon coding mutations (SNV and indels) identified by whole-exome sequencing is not significant different between *MYCN* amplified and non-amplified subtype 2 retinoblastomas , but they are both significantly different to subtype 1 tumors. B) Overall genomic instability score recapitulating the amount of copy number alterations in retinoblastomas subtypes. Non-amplified subtype 2 tumors has the highest instability score, significantly different to that of *MYCN*-amplified subtype 2 tumors and subtype 1. C) *MYCN* amplified tumors are significantly hypomethylated compared to the non-amplified C2 tumors and the C1 retinoblastoma subtype. P-values for each comparison is indicated above (A) and to the right of groups compared (B) and (C).

MYCN role in retinoblastoma onset and progression is not fully understood, but is believed to possibly provide a selective growth advantage to human retinoblastoma cells (McEvoy and Dyer, 2015), and a role in metastasis has been suggested in genetically engineered retinoblastoma mouse models (MacPherson et al., 2007). Besides *MYCN* amplifications, here we reported a significant activation of *MYC* signaling pathway and upregulation of hallmark *MYC* target genes in subtype 2 tumors, consistent with an oncogenic related proliferation state of these tumors. In neuroblastoma, a transcriptional *MYCN/MYC* signature, originally described for disease outcome prediction (Valentijn et al., 2012; Westermann et al., 2008), recognized not only neuroblastomas *MYCN*-amplified, but also an equally large group of tumors without *MYCN* amplification, similar to what we have found in our series.

MYC SIGNALING AS A THERAPEUTIC TARGET IN RETINOBLASTOMA

Our observations of *MYCN* amplifications and upregulation of *MYC* target genes, together with the knowledge that BET inhibitors have shown activity against proliferation and tumor growth in preclinical models characterized by an upregulation of the MYC/MYCN signaling, led us to test this treatment in retinoblastoma cell models *in vitro.*

Retinoblastoma cells' viability is significantly reduced by the use of BET inhibitors

OTX015 and JQ1 treatment strongly reduced viability of three retinoblastoma cell lines *in vitro*. The choice of these cell lines was based on their MYC/MYCN expression patterns. Responsiveness to BRD4 inhibition in neuroblastoma, has been previously attributed to the extent of endogenous *MYCN* expression and *MYCN* amplification, given that cell lines highly expressing *MYC* (for example SK-N-AS) were rather resistant to OTX015 treatment (Henssen et al., 2016; Puissant et al., 2013). Our results on cell viability *in vitro* showed independence of the MYC/MYCN endogenous expression status, as the three cell lines were affected by the treatment. At this point two major observations have to be done. First, we worked at micromolar (high) concentrations, and most published (*in vitro*) works have shown efficacy of the treatment at the submicromolar level. This imply that our results could be masked by non-specific responses to the treatment. Second, WERI cells' response was dose-dependent but the extremely high response (near 90% of cell viability inhibition) may be more probably due to a general cytotoxic effect rather than a specific one. Still, our dose-response curve results, showed that at the lowest concentration (300nM) WERI viability was inhibited in ~30%, while Y79 and CL-RB247 showed its maximum effect (~50%) at these low concentrations.

MYC/MYCN downregulation induced by BETi treatment

The effect of bromodomain protein inhibition on cell viability has been attributed to MYC signaling repression (Delmore et al., 2011; Henssen et al., 2016; Mertz et al., 2011). Supporting these findings, we observed a significant MYC/MYCN gene and protein downregulation in CL-RB247 and Y79 cell lines, following JQ1 and OTX015 treatment. On the other hand, effect on WERI cell's viability was independent of *MYCN* downregulation. Of interest, both cell lines attributed to the subtype 2 (Y79 and CL-RB247) showed similar responses following treatment, while WERI cells (that could not be attributed to any subtype) seemed to behave in a different way in terms of *MYCN* downregulation. These results could suggest that, at least in WERI cells, BET inhibition regulated pro-proliferative and/or survival genes others than *MYCN,* and raise the question about other therapeutically important BRD4 targets in retinoblastoma.

We observed that JQ1 and OTX015 treatment not only induced *MYC* and *MYCN* gene downregulation, but also significantly affected the expression of its target genes. By transiently transfecting CL-RB247, we could only confirm a significant downregulation of one out of the six target genes assessed, as a *MYC* target. These findings could be explained by the model proposed by Henssen and colleagues (Henssen et al., 2016). They showed that genes transcriptionally repressed after OTX015 treatment were enriched for *MYCN* targets in both *MYCN*-amplified neuroblastoma cells and in one neuroblastoma cell line ectopically expressing *MYCN,* meaning that BRD4 inhibition directly suppresses *MYCN*-target gene transcription even in the presence of high *MYCN* levels (**Figure 15**). We lastly analyzed publicly available chromatin immunoprecipitation sequencing data (ChIP-seq) of four fetal retinas and one retinoblastoma sample (Aldiri et al., 2017) and, supporting the model proposed for neuroblastoma, ChIP-seq tracks for BRD4 were noted in *MYC* and *MYCN* promoters, as well as for their target genes (**Figure 16**).

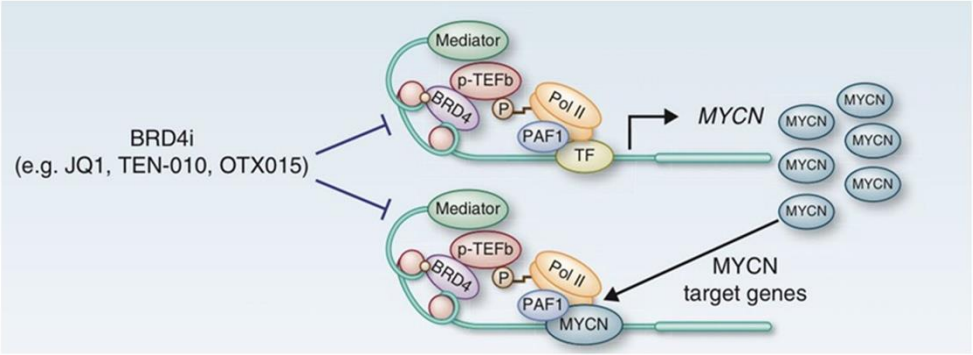


Figure 15. Proposed mechanism of BRD4 inhibition in neuroblastoma
BRD4 is recruited to super-enhancer complexes of the *MYCN* gene (top). MYCN acts as a transcription factor at MYCN target gene promoters and enhancer sites where BRD4 is also recruited to (bottom). BRD4 inhibition by OTX015

therefore not only indirectly leads to decreased expression of MYCN target genes by inhibiting MYCN expression, but also suppressed MYCN activity at its target genes directly. Image adapted from (Henssen et al., 2016).

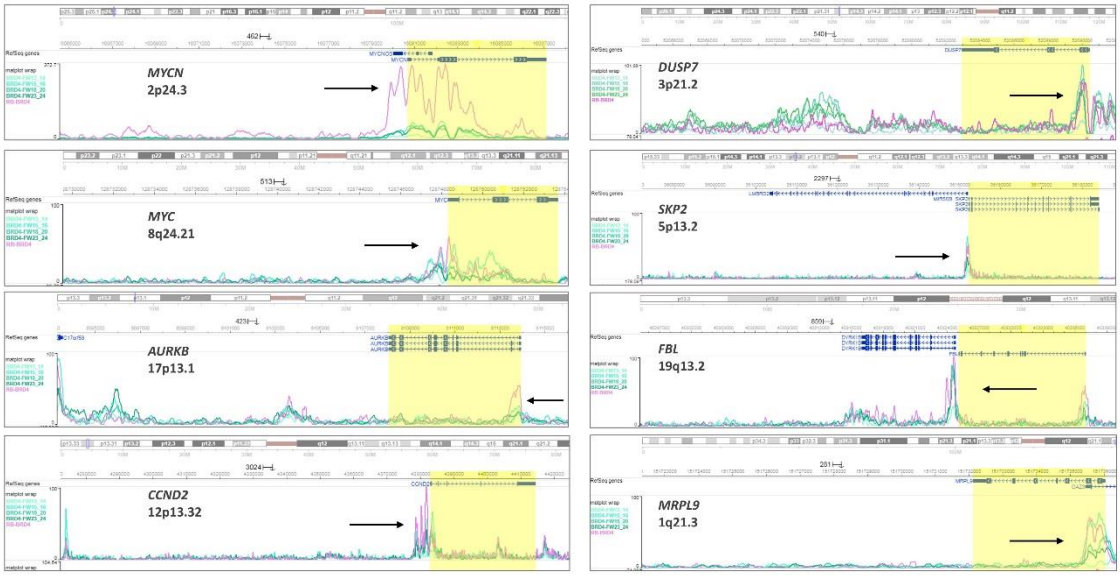


Figure 16. ChIP-seq publicly available data of fetal retinas and one retinoblastoma sample
BRD4 binding tracks are indicated with black arrows at *MYCN* and *MYC* promoters, as well as for the target genes analyzed in this chapter. In a growing gradient of green color are shown the four fetal retinas (fetal weeks 13-14, 15-16, 18-20 and 23-24). The retinoblastoma tumor sample is represented by the rose line. In yellow are highlighted the mapping genes. All genes are shown using the same scale, except for *MYCN* (higher scale).

We hereby provide preliminary results to explore this new therapeutic avenue of BET proteins inhibition in retinoblastoma. Understanding the underlying mechanisms is essential for a possible future clinical application of OTX015 and other BRD4 inhibitors. Even though retinoblastoma current therapies are highly efficient in saving children's eyes and life, BET inhibitors might be a therapeutic option for a subset of chemoresistant retinoblastomas. Given that cell viability inhibition was independent of *MYCN* downregulation in one cell model, this therapy could extend the small subset (10%) that *MYCN*-amplified represents within all cases of retinoblastomas.

Further experiments are needed in order to test specificity of BETi treatment at lower concentrations, *in vitro* and *in vivo*. Besides, it would be interesting to analyze the gene expression profiling following exposure to BETi to explore the underlying mechanisms affecting cell viability and the alternative targets that BET proteins could have in the retinoblastoma context.

Table 1. Primers used in RT-qPCR

Gene	Forward 5'- 3'	Reverse 5'- 3'	Final C (nM)
MYC	CACCAGCAGCGACTCTGA	GATCCAGACTCTGACCTTTTGC	500/300
MYCN	TGAGCGATTCAGATGATGAAG	AGGCATCGTTTGAGGATCAG	700/700
MYCNOS	GGCACCCTTTGGAGAAGAAC	TGGCTTCTGCGAAAAGAAAT	700/700
AURKB	GGACACCCGACATCTTAACC	TTCTCCCGAGCCAAGTACAC	300/300
CCND2	TGGGGAAGTTGAAGTGGAAC	CTTAAAGTCGGTGGCACACA	700/500
DUSP7	GCTGCCAGGCCTACTACCTC	GAGGAAGAGCTGTCCACGTT	700/500
FBL	CTCGATTTCGGAAGGAGATG	CGGTTTGATGTGGATCTGGT	500/500
SKP2	AGCCCGACAGTGAGAACATC	CCCATGAAACACCTGGAAAG	500/500
MRPL9	GCAGTCGGTGGAGAATGTTA	AGTCCCTGAGGAAGGAGTCG	500/500
TBP	TTGCTGCGGTAATCATGAGG	TTTTCTTGCTGCCAGTCTGG	500/500

Table 2. Focal amplifications on 2p24.3 in the series of 102 retinoblastomas

ID	Genomic alteration	Chr	N° genes	Start pos	End pos	length (kbp)	Start cyto	End cyto	Platform
RB13	focal amplification	2	3	15701497	16734178	1032,7	2p24.3	2p24.2	WES
RB13	focal amplification	2	4	15701497	16734178	1032,7	2p24.3	2p24.2	WES
RB14	focal amplification	2	14	12882856	19551246	6668,4	2p24.3	2p24.1	WES
RB14	focal amplification	2	16	12882856	19551246	6668,4	2p24.3	2p24.1	WES
RB15	focal amplification	2	4	15534498	17377898	1843,4	2p24.3	2p24.2	WES
RB15	focal amplification	2	5	15534498	17377898	1843,4	2p24.3	2p24.2	WES
RB215	focal amplification	2	14	14776447	20097629	5321,2	2p24.3	2p24.1	WES
RB215	focal amplification	2	16	14776447	20097629	5321,2	2p24.3	2p24.1	WES
RB22	focal amplification	2	7	12173642	17554158	5380,5	2p25.1	2p24.2	BAC array
RB22	focal amplification	2	7	12173642	17554158	5380,5	2p25.1	2p24.2	BAC array
RB222	focal amplification	2	24	10142411	16733900	6591,5	2p25.1	2p24.2	WES
RB222	focal amplification	2	26	10142411	16733900	6591,5	2p25.1	2p24.2	WES
RB224	focal amplification	2	6	13168232	17594283	4426,1	2p24.3	2p24.2	SNP array
RB224	focal amplification	2	6	13168232	17594283	4426,1	2p24.3	2p24.2	SNP array

RB659	focal amplification	2	3	15883672	17692045	1808,4	2p24.3	2p24.2	WES
RB659	focal amplification	2	4	15883672	17692045	1808,4	2p24.3	2p24.2	WES
HSJD-RBT2	focal amplification	2	4	15470914	17377898	1907	2p24.3	2p24.2	WES
HSJD-RBT2	focal amplification	2	5	15470914	17377898	1907	2p24.3	2p24.2	WES
HSJD-RBT3	focal amplification	2	2	15771055	16734178	963,1	2p24.3	2p24.2	WES
HSJD-RBT3	focal amplification	2	4	15771055	16734178	963,1	2p24.3	2p24.2	WES
HSJD-RBT7	focal amplification	2	4	15651499	17377898	1726,4	2p24.3	2p24.2	WES
HSJD-RBT7	focal amplification	2	5	15651499	17377898	1726,4	2p24.3	2p24.2	WES

Table 3. Gene set enrichment use for hierarchical clustering

subtype	GO_term	nº genes in the cluster	Mean expression	P value
1	chr16q22	37	-0,39193569	5,07E-259
1	GO_IMMUNE_RESPONSE	171	-0,67181042	7,34E-194
1	HALLMARK_INTERFERON_GAMMA_RESPONSE	72	-0,6977419	3,78E-103
1	chr16q12	14	-0,56125193	1,53E-102
1	chr16q24	13	-0,43404298	2,71E-77
1	HALLMARK_INTERFERON_ALPHA_RESPONSE	43	-0,69897095	4,50E-73
1	GO_INFLAMMATORY_RESPONSE	65	-0,63762528	5,56E-69
1	chr16q23	9	-0,46765995	1,80E-67
1	GO_RESPONSE_TO_CYTOKINE	92	-0,70354597	2,00E-67
1	HALLMARK_INFLAMMATORY_RESPONSE	48	-0,53625874	8,21E-60
1	GO_LEUKOCYTE_ACTIVATION	59	-0,52638423	9,16E-54
1	chr16q13	6	-0,47411327	2,00E-28
1	GO_GLIAL_CELL_DIFFERENTIATION	17	-0,71998539	3,08E-24
1	PID_CONE_PATHWAY	10	-1,57749786	3,92E-22
1	GO_OXIDATIVE_PHOSPHORYLATION	6	-0,17848673	2,63E-20
1	chr7p12	2	-0,72108994	4,46E-20
1	HALLMARK_OXIDATIVE_PHOSPHORYLATION	10	-0,2403712	3,17E-19
1	GO_PHOTOTRANSDUCTION	12	-1,32228922	9,21E-18
1	HALLMARK_COAGULATION	13	-0,76148668	2,59E-16
1	GO_CELLULAR_RESPIRATION	7	-0,20803885	1,98E-15
1	GO_POST_EMBRYONIC_MORPHOGENESIS	2	-0,47146217	2,77E-15

1	chr6p21	26	-0,90619074	3,47E-15
1	GO_DETECTION_OF_LIGHT_STIMULUS	12	-1,32228922	1,35E-13
1	HALLMARK_APOPTOSIS	20	-0,68367952	2,28E-11
1	GO_PHOTORECEPTOR_CELL_MAINTENANCE	3	-1,0923994	5,90E-11
1	chr16q21	3	-0,43087334	7,62E-10
1	PID_RHODOPSIN_PATHWAY	2	-0,4853431	5,27E-07
2	GO_MITOTIC_CELL_CYCLE	104	0,56046062	1,54E-164
2	GO_CELL_CYCLE_PROCESS	114	0,5610809	8,08E-156
2	HALLMARK_E2F_TARGETS	55	0,50897136	5,72E-151
2	HALLMARK_G2M_CHECKPOINT	55	0,57144005	4,90E-135
2	chr1q21	33	0,43803555	8,56E-128
2	chr6p21	23	0,36408998	1,20E-118
2	GO_RIBOSOME_BIOGENESIS	44	0,2743482	2,08E-87
2	chr1q22	13	0,52357764	2,49E-73
2	chr1q23	14	0,49698039	2,72E-70
2	chr2p25	8	0,37004371	7,20E-46
2	chr1q25	12	0,4671302	2,82E-44
2	chr13q21	3	0,38948151	2,54E-40
2	HALLMARK_MITOTIC_SPINDLE	27	0,61457144	4,66E-37
2	chr2p23	9	0,31036552	4,38E-35
2	GO_HOMOPHILIC_CELL_ADHESION_VIA_PLASMA_MEMBRANE_ADHESION_MOLECULES	10	0,78012409	7,65E-35
2	chr1q21	13	0,41367452	3,74E-31
2	chr1q32	10	0,58432137	3,39E-29
2	chr1q32	13	0,46216763	5,27E-29
2	HALLMARK_MYC_TARGETS_V1	14	0,461477	4,24E-24
2	chr1q24	6	0,60074111	3,60E-23
2	chr2p21	5	0,32055057	4,74E-22
2	chr2p22	5	0,29121868	4,74E-22
2	chr5q31	9	0,84565474	2,75E-21
2	HALLMARK_MYC_TARGETS_V1	20	0,29150065	8,43E-19
2	GO_REGULATION_OF_MRNA_SPLICING_VIA_SPLICEOSOME	5	0,29462195	1,44E-16
2	GO_NEGATIVE_REGULATION_OF_DENDRITE_DEVELOPMENT	3	1,45427333	7,03E-16
2	GO_NEURON_PROJECTION_MORPHOGENESIS	12	0,80121979	3,33E-12
2	chr2p13	4	0,22136304	4,56E-11
2	HALLMARK_MYC_TARGETS_V2	8	0,30990657	1,57E-09
2	chr2p24	5	0,45349001	6,99E-07

BIBLIOGRAPHY

Adhikary, S., and Eilers, M. (2005). Transcriptional regulation and transformation by Myc proteins. Nat. Rev. Mol. Cell Biol. *6*, 635–645.

Allfrey, V.G., Faulkner, R., and Mirsky, A.E. (1964). Acetylation and methylation of histones and their possible role in the regulation of RNA synthesis. Proc. Natl. Acad. Sci. U. S. A. *51*, 786–794.

Amati, B., Brooks, M.W., Levy, N., Littlewood, T.D., Evan, G.I., and Land, H. (1993). Oncogenic activity of the c-Myc protein requires dimerization with Max. Cell *72*, 233–245.

Bandopadhayay, P., Bergthold, G., Nguyen, B., Schubert, S., Gholamin, S., Tang, Y., Bolin, S., Schumacher, S.E., Zeid, R., Masoud, S., et al. (2014). BET Bromodomain Inhibition of MYC-Amplified Medulloblastoma. Clin. Cancer Res. *20*, 912–925.

Bellan, C., De Falco, G., Tosi, G.M., Lazzi, S., Ferrari, F., Morbini, G., Bartolomei, S., Toti, P., Mangiavacchi, P., Cevenini, G., et al. (2002). Missing expression of pRb2/p130 in human retinoblastomas is associated with reduced apoptosis and lesser differentiation. Invest. Ophthalmol. Vis. Sci. *43*, 3602–3608.

Beltran, H., Rickman, D.S., Park, K., Chae, S.S., Sboner, A., MacDonald, T.Y., Wang, Y., Sheikh, K.L., Terry, S., Tagawa, S.T., et al. (2011). Molecular characterization of neuroendocrine prostate cancer and identification of new drug targets. Cancer Discov. *1*, 487–495.

Bjerke, L., Mackay, A., Nandhabalan, M., Burford, A., Jury, A., Popov, S., Bax, D.A., Carvalho, D., Taylor, K.R., Vinci, M., et al. (2013). Histone H3.3. mutations drive pediatric glioblastoma through upregulation of MYCN. Cancer Discov. *3*, 512–519.

Bouchard, C., Thieke, K., Maier, A., Saffrich, R., Hanley-Hyde, J., Ansorge, W., Reed, S., Sicinski, P., Bartek, J., and Eilers, M. (1999). Direct induction of cyclin D2 by Myc contributes to cell cycle progression and sequestration of p27.

Bowles, E., Corson, T.W., Bayani, J., Squire, J.A., Wong, N., Lai, P.B.-S., and Gallie, B.L. (2007). Profiling genomic copy number changes in retinoblastoma beyond loss ofRB1. Genes, Chromosom. Cancer *46*, 118–129.

Brägelmann, J., Böhm, S., Guthrie, M.R., Mollaoglu, G., Oliver, T.G., and Sos, M.L. (2017). Family matters: How MYC family oncogenes impact small cell lung cancer. Cell Cycle *16*, 1489–1498.

Chappell, J., Sun, Y., Singh, A., and Dalton, S. (2013). MYC/MAX control ERK signaling and pluripotency by regulation of dual-specificity phosphatases 2 and 7. Genes Dev. *27*, 725–733.

Corson, T.W., and Gallie, B.L. (2007). One Hit , Two Hits , Three Hits , More ? Genomic Changes in the Development of Retinoblastoma. Genes. Chromosomes Cancer *46*, 617–634.

Corson, T.W., Huang, A., Tsao, M.-S., and Gallie, B.L. (2005). KIF14 is a candidate oncogene in the 1q minimal region of genomic gain in multiple cancers. Oncogene *24*, 4741–4753.

Coudé, M.-M., Braun, T., Berrou, J., Dupont, M., Bertrand, S., Masse, A., Raffoux, E., Itzykson, R., Delord, M., Riveiro, M.E., et al. (2015). BET inhibitor OTX015 targets BRD2 and BRD4 and decreases c-MYC in acute leukemia cells. Oncotarget *6*.

Dang, C. V (2012). Leading Edge Review MYC on the Path to Cancer.

Dang, C. V., O'Donnell, K.A., Zeller, K.I., Nguyen, T., Osthus, R.C., and Li, F. (2006). The c-Myc target gene network. Semin. Cancer Biol. *16*, 253–264.

Delmore, J.E., Issa, G.C., Lemieux, M.E., Rahl, P.B., Shi, J., Jacobs, H.M., Kastritis, E., Gilpatrick, T., Paranal, R.M., Qi, J., et al. (2011). BET bromodomain inhibition as a therapeutic strategy to target c-Myc. Cell *146*, 904–917.

Eilers, M., and Eisenman, R.N. (2008). Myc's broad reach. Genes Dev. *22*, 2755–2766.

Estiar, M.A., Javan, F., Zekri, A., Mehrazin, M., and Mehdipour, P. (2017). Prognostic significance of MYCN gene amplification and protein expression in primary brain tumors: Astrocytoma and meningioma. Cancer Biomarkers *19*, 341–351.

Evans, L., Chen, L., Milazzo, G., Gherardi, S., Perini, G., Willmore, E., Newell, D.R., and Tweddle, D.A. (2015). SKP2 is a direct transcriptional target of MYCN and a potential therapeutic target in neuroblastoma. Cancer Lett. *363*, 37–45.

Ferri, E., Petosa, C., and Mckenna, C.E. (2016). Bromodomains: Structure, function and pharmacology of inhibition. Biochem. Pharmacol. *106*, 1–18.

Fielitz, K., Althoff, K., De Preter, K., Nonnekens, J., Ohli, J., Elges, S., Hartmann, W., Klöppel, G., Knösel, T., Schulte, M., et al. (2016). Characterization of pancreatic glucagon-producing tumors and pituitary gland tumors in transgenic mice overexpressing MYCN in hGFAP-positive cells. Oncotarget *7*, 74415–74426.

Filippakopoulos, P., Qi, J., Picaud, S., Shen, Y., Smith, W.B., Fedorov, O., Morse, E.M., Keates, T., Hickman, T.T., Felletar, I., et al. (2010). Selective inhibition of BET bromodomains. Nature *468*, 1067–1073.

Fredlund, E., Ringnér, M., Maris, J.M., and Påhlman, S. (2008). High Myc pathway activity and low stage of neuronal differentiation associate with poor outcome in neuroblastoma. Proc. Natl. Acad. Sci. U. S. A. *105*, 14094–14099.

Grasemann, C., Gratias, S., Stephan, H., Schüler, A., Schramm, A., Klein-Hitpass, L., Rieder, H., Schneider, S., Kappes, F., Eggert, A., et al. (2005). Gains and overexpression identify DEK and E2F3 as targets of chromosome 6p gains in retinoblastoma. Oncogene *24*, 6441–6449.

Henssen, A., Althoff, K., Odersky, A., Beckers, A., Koche, R., Speleman, F., Schäfers, S., Bell, E., Nortmeyer, M., Westermann, F., et al. (2016). Targeting MYCN-driven transcription by BET-bromodomain inhibition. Clin. Cancer Res. *22*, 2470–2781.

Henssen, A.G., Thor, T., Odersky, A., Heukamp, L., El-Hindy, N., Beckers, A., Slpeleman, F., Althoff, K., Schäfers, S., Schramm, A., et al. (2013). BET bromodomain protein inhibition is a therapeutic option for medulloblastoma. Oncotarget *4*, 2080–2095.

Hirvonen, H., Mäkelä, T.P., Sandberg, M., Kalimo, H., Vuorio, E., and Alitalo, K. (1990). Expression of the myc proto-oncogenes in developing human fetal brain. Oncogene *5*, 1787–1797.

Hirvonen, H., Hukkanen, V., Salmi, T.T., Pelliniemi, T.T., and Alitalo, R. (1993). L-myc and N-myc in hematopoietic malignancies. Leuk. Lymphoma *11*, 197–205.

den Hollander, J., Rimpi, S., Doherty, J.R., Rudelius, M., Buck, A., Hoellein, A., Kremer, M., Graf, N., Scheerer, M., Hall, M.A., et al. (2010). Aurora kinases A and B are up-regulated by Myc and are essential for maintenance of the malignant state. Blood *116*, 1498–1505.

Jain, A.K., and Barton, M.C. (2016). Bromodomain Histone Readers and Cancer.

Jones, P.A., Issa, J.-P.J., and Baylin, S. (2016). Targeting the cancer epigenome for therapy. Nat. Publ. Gr. *17*.

King, B., Boccalatte, F., Moran-Crusio, K., Wolf, E., Wang, J., Kayembe, C., Lazaris, C., Yu, X., Aranda-Orgilles, B., Lasorella, A., et al. (2016). The ubiquitin ligase Huwe1 regulates the maintenance and lymphoid commitment of hematopoietic stem cells. Nat. Immunol. *17*, 1312–1321.

Kleine-Kohlbrecher, D., Adhikary, S., and Eilers, M. (2006). Mechanisms of transcriptional repression by Myc. Curr. Top. Microbiol. Immunol. *302*, 51–62.

Knoepfler, P.S., Cheng, P.F., and Eisenman, R.N. (2002). N-myc is essential during neurogenesis for the rapid expansion of progenitor cell populations and the inhibition of neuronal differentiation. Genes Dev. *16*, 2699–2712.

Knoepfler, P.S., Zhang, X., Cheng, P.F., Gafken, P.R., McMahon, S.B., and Eisenman, R.N. (2006). Myc influences global chromatin structure. EMBO J. *25*, 2723–2734.

Knudson, A.G. (1971). Mutation and Cancer: Statistical Study of Retinoblastoma.

Kooi, I.E., Mol, B.M., Massink, M.P.G., De Jong, M.C., De Graaf, P., Van Der Valk, P., Meijers-Heijboer, H., Kaspers, G.J.L., Moll, A.C., Te Riele, H., et al. (2016). A Meta-Analysis of Retinoblastoma Copy Numbers Refines the List of Possible Driver Genes Involved in Tumor Progression.

Kuo, M.-H., and Allis, C.D. (1998). Roles of histone acetyltransferases and deacetylases in gene regulation. BioEssays *20*, 615–626.

Laurie, N.A., Donovan, S.L., Shih, C.S., Zhang, J., Mills, N., Fuller, C., Teunisse, A., Lam, S., Ramos, Y., Mohan, A., et al. (2006). Inactivation of the p53 pathway in retinoblastoma. Nature *444*, 61–66.

Lee, J.K., Phillips, J.W., Smith, B.A., Park, J.W., Stoyanova, T., McCaffrey, E.F., Baertsch, R., Sokolov, A., Meyerowitz, J.G., Mathis, C., et al. (2016). N-Myc Drives Neuroendocrine Prostate Cancer Initiated from Human Prostate Epithelial Cells. Cancer Cell *29*, 536–547.

Lee, W.H., Murphree, A.L., and Benedict, W.F. (1984). Expression and amplification of the N-myc gene in primary retinoblastoma. Nature *309*, 458–460.

Luger, K., Mäder, A.W., Richmond, R.K., Sargent, D.F., and Richmond, T.J. (1997). Crystal structure of the nucleosome core particle at 2.8 Å resolution. Nature *389*, 251–260.

MacPherson, D., Conkrite, K., Tam, M., Mukai, S., Mu, D., and Jacks, T. (2007). Murine bilateral retinoblastoma exhibiting rapid-onset, metastatic progression and N-myc gene amplification. EMBO J. *26*, 784–794.

Marchong, M.N., Chen, D., Corson, T.W., Lee, C., Harmandayan, M., Bowles, E., Chen, N., and Gallie, B.L. (2004). Minimal 16q genomic loss implicates cadherin-11 in retinoblastoma. Mol. Cancer Res. *2*, 495–503.

Marees, T., Moll, A.C., Imhof, S.M., de Boer, M.R., Ringens, P.J., and van Leeuwen, F.E. (2008). Risk of second malignancies in survivors of retinoblastoma: more than 40 years of follow-up. J. Natl. Cancer Inst. *100*, 1771–1779.

Maris, J.M., Hogarty, M.D., Bagatell, R., and Cohn, S.L. (2007). Neuroblastoma. Lancet *369*, 2106–2120.

Massimino, M., Biassoni, V., Gandola, L., Garrè, M.L., Gatta, G., Giangaspero, F., Poggi, G., and Rutkowski, S. (2016). Childhood medulloblastoma. Crit. Rev. Oncol. Hematol. *105*, 35–51.

McEvoy, J.D., and Dyer, M.A. (2015). Genetic and Epigenetic Discoveries in Human Retinoblastoma. Crit. Rev. Oncog. *20*, 217–225.

Mertz, J.A., Conery, A.R., Bryant, B.M., Sandy, P., Balasubramanian, S., Mele, D.A., Bergeron, L., and Sims Iii, R.J. (2011). Targeting MYC dependence in cancer by inhibiting BET bromodomains. Proc. Natl. Acad. Sci. *108*, 16669–16674.

Morrish, F., and Hockenbery, D. (2014). MYC and Mitochondrial Biogenesis. Cold Spring Harb Perspect Med *4*, 1–16.

Musselman, C.A., Lalonde, M.-E., Côté, J., and Kutateladze, T.G. (2012). Perceiving the epigenetic landscape through histone readers.

Orlic, M., Spencer, C.E., Wang, L., and Gallie, B.L. (2006). Expression analysis of 6p22 genomic gain in retinoblastoma. Genes, Chromosom. Cancer *45*, 72–82.

Park, J.R., Eggert, A., and Caron, H. (2010). Neuroblastoma: Biology, Prognosis, and Treatment. Hematol. Oncol. Clin. North Am. *24*, 65–86.

Puissant, A., Frumm, S.M., Alexe, G., Bassil, C.F., Qi, J., Chanthery, Y.H., Nekritz, E.A., Zeid, R., Gustafson, W.C., Greninger, P., et al. (2013). Targeting MYCN in Neuroblastoma by BET Bromodomain Inhibition. Cancer Discov. *3*, 308–323.

Raetz, E.A., Kim, M.K.H., Moos, P., Carlson, M., Bruggers, C., Hooper, D.K., Foot, L., Liu, T., Seeger, R., and Carroll, W.L. (2003). Identification of genes that are regulated transcriptionally by Myc in childhood tumors. Cancer *98*, 841–853.

Rickman, D.S., Schulte, J.H., and Eilers, M. (2018). The expanding world of N-MYC-driven tumors. Cancer Discov. *8*, 150–164.

Rushlow, D.E., Mol, B.M., Kennett, J.Y., Yee, S., Pajovic, S., Thériault, B.L., Prigoda-Lee, N.L., Spencer, C., Dimaras, H., Corson, T.W., et al. (2013a). Characterisation of retinoblastomas without RB1 mutations: genomic, gene expression, and clinical studies. Lancet Oncol. *14*, 327.

Rushlow, D.E., Mol, B.M., Kennett, J.Y., Yee, S., Pajovic, S., Thériault, B.L., Prigoda-Lee, N.L., Spencer, C., Dimaras, H., Corson, T.W., et al. (2013b). Characterisation of retinoblastomas without RB1 mutations: Genomic, gene expression, and clinical studies. Lancet Oncol. *14*, 327–334.

Sanchez, R., and Zhou, M.-M. (2009). The role of human bromodomains in chromatin biology and gene transcription. Curr. Opin. Drug Discov. Devel. *12*, 659–665.

Schwab, M., Alitalo, K., Klempnauer, K.H., Varmus, H.E., Bishop, J.M., Gilbert, F., Brodeur, G., Goldstein, M., and Trent, J. (1983). Amplified DNA with limited homology to myc cellular oncogene is shared by human neuroblastoma cell lines and a neuroblastoma tumour. Nature *305*, 245–248.

Shi, J., and Vakoc, C.R. (2014). The Mechanisms behind the Therapeutic Activity of BET Bromodomain Inhibition. Mol. Cell *54*, 72–736.

Smyth, G.K. (2005). limma: Linear Models for Microarray Data. In Bioinformatics and Computational Biology Solutions Using R and Bioconductor, (New York: Springer-Verlag), pp. 397–420.

Squire, J., Goddard, A.D., Canton, M., Becker, A., Phillips, R.A., and Gallie, B.L. (1986). Tumour induction by the retinoblastoma mutation is independent of N-myc expression. Nature *322*, 555–557.

Subramanian, A., Tamayo, P., Mootha, V.K., Mukherjee, S., Ebert, B.L., Gillette, M.A., Paulovich, A., Pomeroy, S.L., Golub, T.R., Lander, E.S., et al. (2005). Gene set enrichment analysis: a knowledge-based approach for interpreting genome-wide expression profiles. Proc. Natl. Acad. Sci. U. S. A. *102*, 15545–15550.

Suenaga, Y., Islam, S., Alagu, J., Kaneko, Y., and Kato, M. (2014). NCYM, a Cis-Antisense Gene of MYCN, Encodes a De Novo Evolved Protein That Inhibits GSK3b Resulting in the Stabilization of MYCN in Human Neuroblastomas. PLoS Genet *10*.

Tosi, G.M., Trimarchi, C., Macaluso, M., La Sala, D., Ciccodicola, A., Lazzi, S., Massaro-Giordano, M., Caporossi, A., Giordano, A., and Cinti, C. (2005). Genetic and epigenetic alterations of RB2/p130 tumor suppressor gene in human sporadic retinoblastoma: implications for pathogenesis and therapeutic approach. Oncogene *24*, 5827–5836.

Vadie, N., Saayman, S., Lenox, A., Ackley, A., Clemson, M., Burdach, J., Hart, J., Vogt, P.K., and Morris, K. V. (2015). MYCNOS functions as an antisense RNA regulating MYCN. RNA Biol. *12*, 893–899.

Valentijn, L.J., Koster, J., Haneveld, F., Aissa, R.A., van Sluis, P., Broekmans, M.E.C., Molenaar, J.J., van Nes, J., and Versteeg, R. (2012). Functional MYCN signature predicts outcome of neuroblastoma irrespective of MYCN amplification. Proc. Natl. Acad. Sci. *109*, 19190–19195.

Westermann, F., Muth, D., Benner, A., Bauer, T., Henrich, K.O., Oberthuer, A., Brors, B., Beissbarth, T., Vandesompele, J., Pattyn, F., et al. (2008). Distinct transcriptional MYCN/c-MYC activities are associated with spontaneous regression or malignant progression in neuroblastomas. Genome Biol. *9*.

Westermark, U.K., Wilhelm, M., Frenzel, A., and Henriksson, M.A. (2011). The MYCN oncogene and differentiation in neuroblastoma. Semin. Cancer Biol. *21*, 256–266.

Williamson, D., Lu, Y.-J., Gordon, T., Sciot, R., Kelsey, A., Fisher, C., Poremba, C., Anderson, J., Pritchard-Jones, K., and Shipley, J. (2005). Relationship between MYCN copy number and expression in rhabdomyosarcomas and correlation with adverse prognosis in the alveolar subtype. J. Clin. Oncol. *23*, 880–888.

Zhao, X., Li, D., Pu, J., Mei, H., Yang, D., Xiang, X., Qu, H., Huang, K., Zheng, L., and Tong, Q. (2016). CTCF cooperates with noncoding RNA MYCNOS to promote neuroblastoma progression through facilitating MYCN expression. Oncogene *35*, 3565–3576.

CHAPTER 4

MOLECULAR CLASSIFICATION OF RETINOBLASTOMA PRECLINICAL MODELS

Index

MOLECULAR CLASSIFICATION OF RETINOBLASTOMA PRECLINICAL MODELS 172

INTRODUCTION 177

PRECLINICAL MODELS IN CANCER RESEARCH 177

METHODOLOGICAL ASPECTS OF DEVELOPING PDX MODELS 178

PDX IN PEDIATRIC CANCER RESEARCH 178

A SHORT STORY OF PRECLINICAL MODELS IN RETINOBLASTOMA RESEARCH 179

Cell lines 179

Animal models 179

SIGNIFICANCE OF PRECLINICAL MODELS IN RETINOBLASTOMA 180

BOX 1 182

RETINOBLASTOMAS FROM SUBTYPE 2 ARE HETEROGENEOUS WHILE SUBTYPE 1 ARE RATHER HOMOGENOUS 182

MATERIALS AND METHODS 184

PRECLINICAL MODELS INCLUDED IN THIS STUDY 184

Retinoblastoma patient-derived xenografts 184

Retinoblastoma cellular models 185

SHORT TANDEM REPEAT ANALYSIS: FINGERPRINTING OF RETINOBLASTOMA MODELS 185

RB1 GENETIC AND EPIGENETIC ANALYSIS 186

RNA EXTRACTION 186

MOLECULAR CLASSIFICATION OF PRECLINICAL MODELS 187

IMMUNOHISTOCHEMICAL ANALYSIS OF PRIMARY TUMORS AND PRECLINICAL MODELS 187

DIFFERENTIALLY EXPRESSED GENES AND PATHWAYS 187

PROTEIN PROFILING ASSESSED BY WESTERN BLOTTING 187

RESULTS 189

HETEROTOPIC PDX DEVELOPMENT AND CLINICAL CHARACTERISTICS 189

CELLULAR MODELS 191

SHORT TANDEM REPEATS (STRs) DNA FINGERPRINTING 191

RB1 MUTATIONS AND *MYCN* AMPLIFICATION STATUS IN PDX AND CELL MODELS 192

MOLECULAR CLASSIFICATION OF PRECLINICAL MODELS 192

IMMUNOHISTOCHEMICAL CHARACTERIZATION ON PDX AND PRIMARY TUMORS 194

PDX models show characteristics of undifferentiated retinoblastoma 194

ARR3, CRX, EBF3 and TFF1 immunohistochemical characterization 194

IMMUNOHISTOCHEMICAL ANALYSIS OF CELL LINES REVEALED THEY ARE PHENOTYPICALLY HETEROGENEOUS 196

GENOMIC PROFILING 197

Paired PDX and primary tumor samples 197
FINAL CLASSIFICATION OF PRECLINICAL MODELS 199
PROTEIN PROFILING 200
PDX protein profiling 202
Cell lines protein profiling 203
TRANSCRIPTOME-BASED CHARACTERIZATION OF PDX AND CELLULAR MODELS OF RETINOBLASTOMA 203
Upregulated genes and pathways in models 205
Downregulated genes and pathways in models 206
Retinal-cell-differentiation-associated genes 207
DISCUSSION AND CONCLUSIONS 210
DNA PROFILING PROVIDES IDENTITY TO PRECLINICAL MODELS 210
RB1 MUTATIONS AND *MYCN* AMPLIFICATION STATUS 210
RETINOBLASTOMA PRECLINICAL MODELS MOSTLY DERIVE FROM TUMORS CLINICALLY CLASSED IN THE SUBTYPE 2 210
PRECLINICAL MODELS CLASSED IN THE RETINOBLASTOMA MOLECULAR SUBTYPE 2 211
IMMUNOHISTOCHEMICAL ANALYSIS REVEALED THAT MOST PDXs DO NOT RETAIN THE INTRA-TUMORAL HETEROGENEITY FOUND IN SUBTYPE 2 RETINOBLASTOMAS 211
PDXs AND CELL LINES EXPRESS MYC AND MYCN PROTEINS AND SHOW UPREGULATION OF *MYC* SIGNALING-RELATED PATHWAYS 212
UPREGULATED PATHWAYS IN RETINOBLASTOMA SUBTYPES AND PRECLINICAL MODELS 213
PRECLINICAL MODELS EXPRESS GENES RELATED TO EARLY-CONE-PHOTORECEPTORS AND RETINAL GANGLION CELLS 214
BIBLIOGRAPHY 228

Figures

FIGURE 1. WORKFLOW OF CELLULAR AND PDX MODELS INCLUDED IN THIS STUDY 184
FIGURE 2. STR LOCI ANALYZED IN DNA FINGERPRINTING 186
FIGURE 3. RETINOBLASTOMA PDX ENGRAFTMENT EFFICIENCY IN THE CURIE INSTITUTE 189
FIGURE 4. PDX MODELS CATEGORIZATION BY TUMOR LATERALITY, AGE AT DIAGNOSIS AND GENDER OF PATIENTS FROM WHICH THEY DERIVED 190
FIGURE 5. HISTOGRAM RECAPITULATING THE DISTRIBUTION OF AGE AT DIAGNOSIS OF THE 102-RETINOBLASTOMA COHORT OF PRIMARY TUMORS 191
FIGURE 6. MOLECULAR CLASSIFICATION OF THE RETINOBLASTOMA PRECLINICAL MODELS AND ITS ORIGINAL TUMORS 194
FIGURE 7. IMMUNOCHARACTERIZATION OF RB335 AND ITS PDX RBX202 196
FIGURE 8. IMMUNOCHARACTERIZATION OF RB338, ITS PDX RBX211 AND THE CELL LINE DERIVED CL-RBX211 197
FIGURE 9. COPY NUMBER CHANGES ASSOCIATED TO RETINOBLASTOMA SUBTYPES 198
FIGURE 10. GENOMIC COPY NUMBER ALTERATIONS IN PRIMARY TUMORS AND MATCHED PDX 199
FIGURE 11. FINAL CLASSIFICATION OF PRECLINICAL MODELS AND PRIMARY TUMORS 200
FIGURE 12. TFF1, EBF3 AND EBF1 EXPRESSION IN PRIMARY RETINOBLASTOMA TUMORS 201
FIGURE 13. IMMUNOBLOTTING PROFILING FOR PDX AND CELLULAR MODELS 202
FIGURE 14. EBF3 AND EBF1 EXPRESSION IN PDX MODELS AND CELL LINES 203
FIGURE 15. PRINCIPAL COMPONENT ANALYSIS OF TRANSCRIPTOME DATA SETS 204
FIGURE 16. MTORC1 SIGNALING IS UPREGULATED IN RETINOBLASTOMA CELL LINES 205
FIGURE 17. WNT/B-CATENIN IS UPREGULATED IN PDXS AND CELL LINES 206
FIGURE 18. ERK1/ERK2 CASCADE AND APOPTOSIS PATHWAY ARE UPREGULATED IN SUBTYPE 1 TUMORS 207
FIGURE 19. RETINAL-CELL-DIFFERENTIATION-ASSOCIATED GENES 208
FIGURE 20. HEATMAP OF DIFFERENTIALLY EXPRESSED GENES IN RETINOBLASTOMAS AND PRECLINICAL MODELS 209
FIGURE 21. INTRA-TUMORAL HETEROGENEITY IS OFTEN LOST IN PDXS MODELS 212

Tables

TABLE 1. CLINICAL CHARACTERISTICS OF PRECLINICAL RETINOBLASTOMA MODELS AND PRIMARY TUMORS 215
TABLE 2. ANALYSIS AND TECHNOLOGIES PERFORMED FOR THE CHARACTERIZATION OF PRECLINICAL MODELS 216
TABLE 3. DNA FINGERPRINTING FOR MODELS AND THEIR CORRESPONDING PRIMARY TUMOR 217
TABLE 4. RB1 MUTATIONS AND MYCN STATUS IN PRECLINICAL MODELS AND ITS ORIGINAL TUMORS 219
TABLE 5. ANTIBODIES USED IN IMMUNOHISTOCHEMICAL STAINING 220
TABLE 6. HISTOLOGICAL CHARACTERIZATION OF PDX AND PRIMARY TUMOR ASSOCIATED 220
TABLE 7. IMMUNOHISTOCHEMICAL ANALYSIS OF PRIMARY TUMORS AND PDX DERIVED 221
TABLE 8. IMMUNOHISTOCHEMICAL STAINING PERFORMED ON CELL LINES 222
TABLE 9. FINAL MOLECULAR CLASSIFICATION OF PDX, CELL LINES AND PRIMARY TUMOR ASSOCIATED 223
TABLE 10. GENE ONTOLOGY AND PATHWAYS ANALYSIS OF GENES DIFFERENTIALLY EXPRESSED IN PDX 224
TABLE 11. GENE ONTOLOGY AND PATHWAYS ANALYSIS OF GENES DIFFERENTIALLY EXPRESSED IN CELL LINES 225
TABLE 12. STATISTICAL SIGNIFICANCE OF THE MESTASCORE CONSTRUCTED FROM THE GENES INCLUDED IN THE DIFFERENTIALLY EXPRESSED GENE SETS 227

INTRODUCTION

PRECLINICAL MODELS IN CANCER RESEARCH

The use of preclinical *in vitro* or *in vivo* models is essential in translational cancer research. Over the last 50 years, this preclinical input has permitted better understanding of tumor biology, providing new treatment strategies for targeted drug development (Boyd, 1997; Venditti et al., 1984). Although the *in vitro* and *in vivo* experiments with cultured cell lines have led to significant advances in cancer biology, these cell lines have adapted to growth in artificial culture conditions, thereby developing genetic and phenotypic changes which may hinder the translational purpose (Daniel et al., 2009; Tentler et al., 2012). Evidence suggests that the process of generating cancer cell lines results in major and irreversible alterations in biological properties, including gain and loss of genetic information, alteration in growth and invasion properties, and loss of specific cell populations (Gillet et al., 2011). In addition, cell lines are usually established from the more aggressive tumors and hence are not representative of complex tumor heterogeneity evident in the clinic. Cell lines usually represent the first steps in preclinical drug development by virtue of convenience and ease of use, but have important limitations (Johnson et al., 2001).

Tumor grafts developed in mice from patient tumor tissues, generally known as patient-derived xenografts (PDXs), were developed as an alternative to better represent the biology of the original tumor and provide a better platform for testing new treatments with higher probability of success when translated to patients (Hidalgo et al., 2011; Stewart et al., 2017). Histologic, mutational, and gene expression analyses have demonstrated that PDX preserves the patient's tumor genomic profile, including gene amplification, genomic architecture, gene expression, histopathology, and cancer stem cell biology. They also maintain the tridimensional architecture and human microenvironment of the tumor, since transplanted tissue fragments contain not only malignant cells but also tumoral stroma, thereby mimicking the human tumor environment (Daniel et al., 2009; Stewart et al., 2017).

PDX models were first generated in the early 80's and were mainly used to characterize and compared responses with several drugs between tumor models and patients (Fiebig et al., 1985; Fujita et al., 1980; Houghton et al., 1982; Shorthouse et al., 1980). These first studies reported a high degree of similarity between the xenograft and the original human tumors, providing an early evidence of the validity and interest of PDX models.

METHODOLOGICAL ASPECTS OF DEVELOPING PDX MODELS

The methodology of PDX generation is based on the direct transplantation of fresh patient tumors samples into immunocompromised mice. Tumor pieces could be obtained from patients during biopsy, surgery or even from bone marrow, fluids drained from malignant ascites, pleural effusions or circulating tumor cells (Gao et al., 2014; Zarzosa et al., 2017). Samples are minced in small fragments (maintaining tridimensional structure) and/or enzymatically processed and implanted into immunocompromised mice either alone or embedded in semi-solid matrixes (such as matrigel) or mixed with human fibroblasts or mesenchymal stem cells (Siolas and Hannon, 2013). Depending on the transplantation location in the mouse, there are two types of xenografted models: orthotopic and heterotopic. Orthotopic transplants are implanted in the same organ as the original tumor while in heterotopic PDX models, tumors are mostly implanted subcutaneously in the back of the mice (Zayed et al., 2015). Orthotopic models are considered to be more similar to human tumors as the tumor develops in the same anatomical microenvironment, and are thought to better predict patient tumor progression and response to treatment (Vidal et al., 2012).

PDX IN PEDIATRIC CANCER RESEARCH

One barrier to identifying and validating biomarkers that predict sensitivity to molecularly targeted therapeutics is the lack of preclinical models that capture the diversity of pediatric solid tumors. In addition, pharmaceutical companies have little financial incentive to develop therapies for childhood cancers because pediatric patients represent only 1% of all patients with cancer (Dyer et al., 2005). For adult cancers, important advances have been made in developing patient-derived organoids for colon, prostate and pancreatic cancers (Boj et al., 2015; Gao et al., 2014; van de Wetering et al., 2015), leading to an international collaboration called the Human Cancer Model Initiative for developing cancer and normal organoids for the research community. There are also international efforts to develop PDXs for adult leukemias and solid tumors, including the EuroPDX consortium, the Public Repository of Xenografts, and the National Cancer Institute Patient-Derived Models Repository (Bruna et al., 2016; Gao et al., 2015; Klco et al., 2014; Townsend et al., 2016). Pediatric solid tumors are rare compared to adult cancers, and this represents the main obstacle to the access of samples for developing pediatric organoids or PDX models of solid tumors (Zarzosa et al., 2017).

A recent initiative called the Childhood Solid Tumor Network (CSTN), established by St. Jude Children's Research Hospital, has been created in order to improve quality and repository of pediatric preclinical models (Stewart et al., 2016). This network also includes genomic and other molecular data, cell lines, patient-derived orthotopic xenografts, and genetically engineered mouse models of childhood solid tumor. Sixty-seven orthotopic PDX models from 12 different pediatric solid tumor were successfully established, including neuroblastoma, osteosarcoma, rhabdomyosarcoma and

retinoblastoma (Stewart et al., 2017). Pediatric PDX have also begun to be incorporated into a large PDX repository (the EurOPDX Consortium). The EurOPDX displays currently over 1900 subcutaneous or orthotopic models for more than 30 different solid tumour types, including 12 models of pediatric cancer[1].

A SHORT STORY OF PRECLINICAL MODELS IN RETINOBLASTOMA RESEARCH

Cell lines

The first human retinoblastoma cell line established was Y79 (Reid et al., 1974). These cells were derived from the tumor of a two-and-a-half year old Caucasian girl with a strong maternal history of retinoblastoma. The original tumor was mostly undifferentiated and, although intraocularly invasive, no extraocular extensions were evident. A few years later, WERI-Rb1, the second established retinoblastoma cell line was characterized (McFall et al., 1977). The WERI-Rb1 cells were derived from the tumor of a one-year-old Caucasian girl with no family history of retinoblastoma. The primary tumor was also essentially undifferentiated and, although it had invaded the optic nerve head, there was no evidence of tumor at any distal site. Since the 70's until to date, these two cell lines have been widely used in retinoblastoma research, both *in vitro* and *in vivo* approaches. Intraocular injections of Y79 cells into immunodeficient mice have shown to closely resemble human tumors with aggressive behavior and metastatic potential, given that mouse optic nerve invasion and brain dissemination was observed (Chevez-Barrios et al., 2000; Pascual-Pasto et al., 2016). In the other hand, the WERI-Rb1 model behaved as a localized tumor that invaded only the anterior structures of the eye without extraocular spread or metastasis (Chevez-Barrios et al., 2000).

Many other different retinoblastoma cell lines has been established and characterized from the 80's until today. These cell models were characterized regarding their genotype, karyotype, genomic copy number and cell properties such as their ability to migrate or invade and give metastasis, as well as for testing the efficacy of existing and new chemotherapeutic agents (Bejjani et al., 2012; Dalgard et al., 2008; Gallie et al., 1982; Griegel et al., 1990; Inomata et al., 1994; Kooi et al., 2016; Madreperla et al., 1991; Pascual-Pasto et al., 2016; Rodríguez-cruz et al., 2005). However, despite this vast variety of published cell lines, no repository exists today. Only Y79 and WERI-RB1 can be obtained commercially, which explains its wide use in retinoblastoma research.

Animal models

The first mouse model of retinoblastoma was generated in 1990 by ectopically expressing the SV40 large T antigen (TAg) in the developing retina (O'Brien et al., 1990). The oncogenic protein code by the virus bind to the retinoblastoma gene product, perturbs its normal function and animals carrying

[1] The EurOPDX consortium. 2018. http://europdx.eu/. Accessed 06 October 2018.

this genetic alteration developed multifocal retinal tumors. The limitation of this model was that the SV40 T antigen may disrupt other pathways that are not deregulated in human retinoblastoma, and thus treatments that are effective in this model could have little clinical impact. In 1992, genetically engineered mouse models (GEMMs) carrying an inactivated *Rb1* gene were generated by three groups (Clarke et al., 1992; Jacks et al., 1992; Lees et al., 1992). Unlike children with germline *RB1* mutations, heterozygous mice failed to develop retinoblastoma. In 1998, chimeric mouse studies demonstrated that *p107* (*Rbl1*), a gene related to *RB1*, was involved in preventing retinal tumor formation in mice (Robanus-Maandag et al., 1998). In 2004, three research groups generated the first knockout mouse models of retinoblastoma by conditionally inactivating Rb^{Lox} in the developing retina of p107-deficient mice using Nestin-Cre, Pax6-Cre, and Chx10-Cre (Chen et al., 2004; MacPherson et al., 2004; Zhang et al., 2004). Inactivation of Rb and p130 (Rbl2) also led to retinoblastoma (MacPherson et al., 2004) showing for the first time that p130 can suppress retinoblastoma in mice. Although GEMMs faithfully recapitulated the histopathology, molecular, cellular, morphometric, neuroanatomical and neurochemical features of human retinoblastoma, data suggest there are important differences between mouse and human retinoblastomas with respect to the mechanism of tumor progression (Benavente et al., 2013; Singh et al., 2018). Similar to human retinoblastoma, mouse tumors have low rates of single nucleotide variations. However, mouse retinoblastomas have higher rates of aneuploidy and regional and focal copy number changes that vary depending on the genetic lesions that initiate tumorigenesis in the developing murine retina. Furthermore, the epigenetic landscape in mouse retinoblastoma was shown to be significantly different from human tumors and some pathways that had been proposed to be candidates for molecular targeted therapy for human retinoblastoma such as *SYK* (spleen tyrosine kinase) and *MCL1* (myeloid cell leukemia sequence) (Zhang et al., 2012) were not found to be deregulated in GEMMs (Benavente et al., 2013). These differences mentioned above were instrumental in shifting away from GEMMs for preclinical testing of pediatric solid tumors (Dyer, 2016). Although GEMMs are still useful for testing genetic hypotheses and elucidating fundamental biological processes, PDX models are better suited by providing translational relevance for new putative therapies to treat pediatric solid tumors (Brennan et al., 2011).

SIGNIFICANCE OF PRECLINICAL MODELS IN RETINOBLASTOMA

Retinoblastoma was one of the first pediatric solid tumor grown as an orthotopic PDX, retaining molecular, cellular, and genetic features of a patient's tumor (Zhang et al., 2012). Still, retinoblastoma represent a special case for modeling orthotopic PDX given the anatomical site where tumor develops. Disadvantages are related to the small size of mice eyeballs, leaving little material to work with later. Relative to the development of the orthotopic models itself, based on the injection of tumoral cells directly into the intraocular cavity of mice, the inoculation could be either

in the vitreous or in the subretinal space (Lemaitre et al., 2017; Pascual-Pasto et al., 2016). Human retinoblastoma tumors can develop into the vitreous (endophytic pattern) or into the retina (exophytic pattern) or both (mixed pattern), and the way in which tumoral cells are inoculated in mice could not represent the real nature of progression and disease dissemination. In the other hand, even if heterotopic subcutaneous PDX models have been shown to retain cellular, genomic and genetic features of its original tumor (Aerts et al., 2010), microenvironment is very different. The unique anatomy and physiology of the eye creates an environment where cancer remains contained and represent a barrier to drug delivery, therefore pointing to orthotopic models to be more suitable for translational research (Stewart et al., 2017).

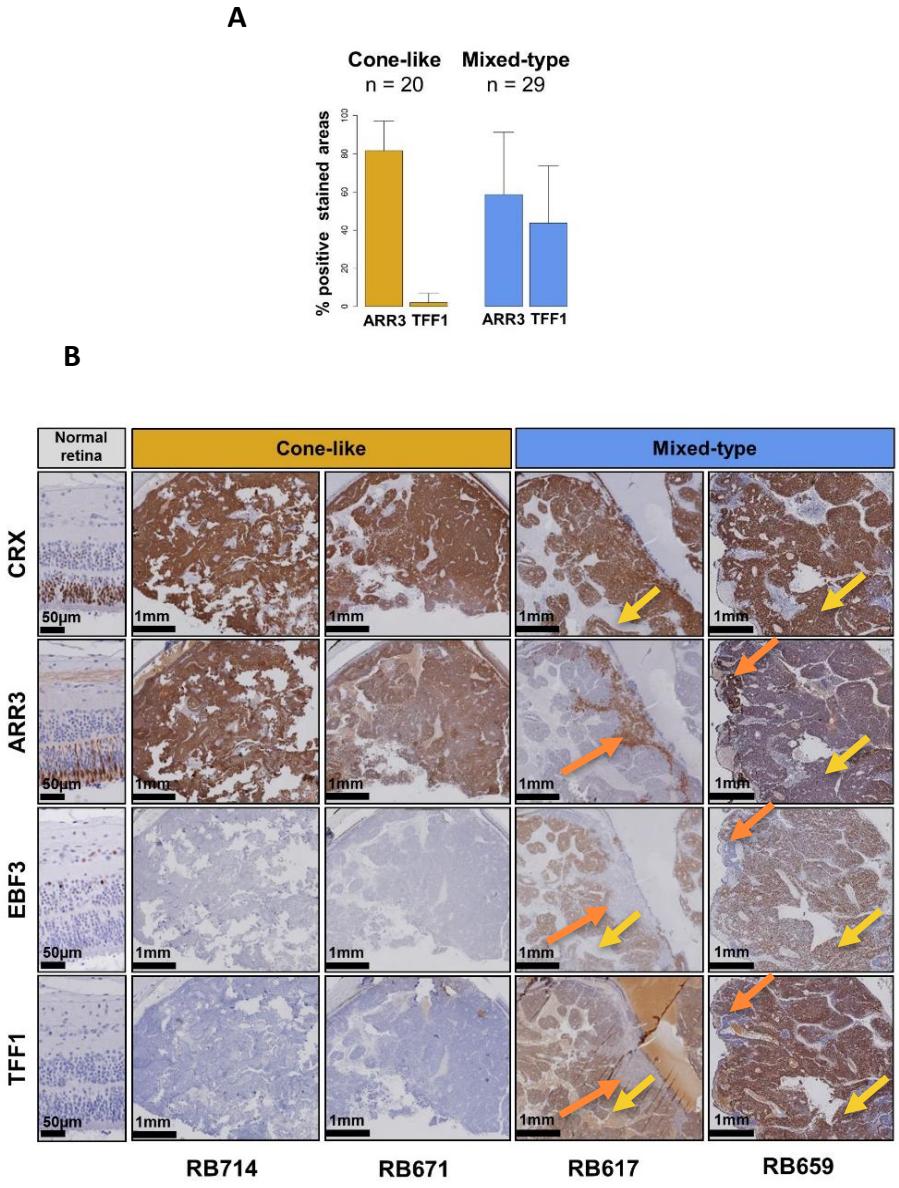
One of the reasons that research on retinoblastoma and RB1 pathway has not had a greater effect on retinoblastoma treatment has been the lack of preclinical models that faithfully recapitulate genetic and histopathologic features of childhood retinoblastoma (Dyer et al., 2005). Animal models of rare childhood malignancies are essential for identifying new therapies. Preclinical models can optimize information regarding pharmacokinetics, best doses and schedules, which can be then translated into front-line or salvage treatments. The importance of this approach cannot be underestimated, particularly in rare malignancies like retinoblastoma, where large scale clinical trials are difficult to carry out (Zhang et al., 2004).

Therefore, the development of preclinical models that recapitulate the molecular, genetic and cellular characteristics of retinoblastoma are essential to identify new-targeted therapies as well as to validate the hypotheses of basic research. Models widely used in retinoblastoma research have not yet been characterized or classified at the molecular level, from where our interest in studying the existing preclinical models. In this chapter, cellular and PDX retinoblastoma models will be analyzed following the same approach as we have done for primary tumors in terms of their transcriptome, the pyrosequencing-based classification (9CpG-tool), the immunohistochemical characterization and copy number alteration data.

BOX 1

RETINOBLASTOMAS FROM SUBTYPE 2 ARE HETEROGENEOUS WHILE SUBTYPE 1 ARE RATHER HOMOGENOUS

Immunohistochemistry analysis assessed by four protein markers revealed an intra-tumoral heterogeneity in subtype 2, while tumors from subtype 1 are rather homogenous.



Using immunohistochemistry, we studied the pattern of expression of four proteins: two photoreceptor cone-cell markers (CRX[1-3] and ARR3[4-5]), one retinal ganglion-cell marker (EBF3[6]) and TFF1[7], the most differentially expressed gene between both subtypes which expression correlated with that of several ganglion markers, notably EBF3. Immunohistochemistry staining was performed on fixed paraffin samples for 20 primary tumors of subtype 1 and 29 of subtype 2.

Tumors from subtype 1 showed uniformly high positive cell percentages for ARR3 and CRX, and displayed no EBF3- or TFF1-positive cells. Tumors of subtype 2 revealed an intra-tumoral heterogeneity. Different patterns were detected in this subtype: i) tumors showing positive areas for either ARR3 or TFF1/EBF3 in a mutually exclusive pattern, ii) tumors displaying a co-expression of the different markers, and iii) tumors displaying both patterns in different areas of the tumor. CRX expression is positive in all tumors. The proportion of tumor areas positively stained for either ARR3 or TFF1 varied across subtype 2 tumors.

Based on this phenotypic difference between tumors, we attributed a name for each subtype. To those uniformly expressing CRX and ARR3 cone markers, were called "the cone-like" subtype. To those heterogeneous tumors expressing both the cone (CRX/ARR3) and the ganglion associated-markers (EBF3/TFF1) were referred as "the mixed-type" subtype.

C1 tumors, homogeneously expressing CRX and ARR3, were referred as the "cone-like" subtype

C2 tumors, heterogeneously expressing CRX/ARR3 and EBF3/TFF1, were referred as the "mixed-type" subtype

Figure box 3. Immunohistochemistry patterns in retinoblastoma.

A) Cone-like tumors showed no positive stained cells for TFF1, marker that was positive in the mixed-subtype tumors. Proportions of ARR3/TFF1 stained areas varied across the mixed-subtype tumors. B) Four representative tumors displaying the different immunohistochemical patterns. **RB714** and **RB671** are cone-like tumors showing positive tumor areas for CRX and ARR3, and negative staining for TFF1 and EBF3 proteins. **RB617** is a mixed-type tumor showing co-expression of CRX and ARR3, and positive areas for ARR3 that are negatives for either TFF1 or EBF3, and vice versa (orange arrow; mutually exclusive pattern or mirror image). This tumor also display a co-expressed area for CRX and TFF1/EBF3 (yellow arrow). **RB659** is another mixed-type tumor showing the mutually exclusive pattern between ARR3 and EBF3/TFF1 (orange arrow) and a co-expression of CRX and TFF1/EBF3 (yellow arrow).

BIBLIOGRAPHY

1. Chen, S. et al. Crx, a novel Otx-like paired- homeodomain protein, binds to and transactivates photoreceptor cell-specific genes. Neuron 19, 1017–1030 (1997).
2. Furukawa, T., Morrow, E. M. & Cepko, C. L. Crx, a novel otx-like homeobox gene, shows photoreceptor-specific expression and regulates photoreceptor differentiation. Cell 91, 531–541 (1997).
3. Freund, C. L. et al. Cone-rod dystrophy due to mutations in a novel photoreceptor-specific homeobox gene (CRX) essential for maintenance of the photoreceptor. Cell 91, 543–553 (1997).
4. Craft, C.M. Whitmore, D.H. & Wiechmann, A.F. Cone arrestin identified by targeting expression of a functional family. J. Biol. Chem. 269, 4613-4619 (1994).
5. Kubo, M. Hirano, T. & Kakinuma, M. Molecular cloning and sequence analysis of cDNA and genomic DNA for the human cone transducin alpha subunit. FEBS Lett. 291, 245-248 (1991).
6. Trimarchi, J.M. et al. Molecular heterogeneity of developing retinal ganglion and amacrine cells revealed through single cell gene expression profiling. J. Comp. Neurol. 502, 1047-1065 (2007).
7. Zhang, J. et al. A novel retinoblastoma therapy from genomic and epigenetic analyses. Nature 481, 329-334 (2012).

MATERIALS AND METHODS

PRECLINICAL MODELS INCLUDED IN THIS STUDY

Workflow of developed models included the current study are shown in **Figure 1**, and clinical data are described in **Table 1** (page 215).

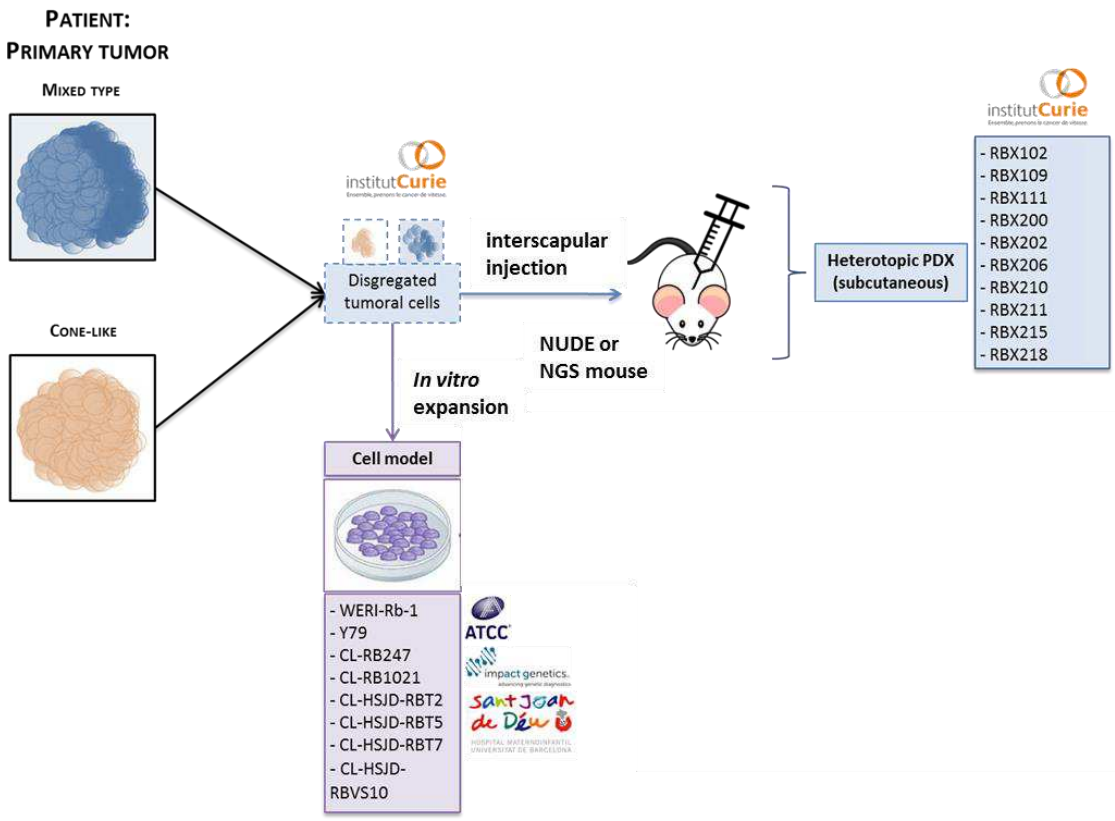


Figure 1. Workflow of cellular and PDX models included in this study

Retinoblastoma patient-derived xenografts

Human retinoblastoma samples were obtained from enucleated patients without prior treatment at the Curie Hospital. Informed consent for the development of animal models was signed by the family of the affected child.

Heterotopic patient-derived xenografts are established by subcutaneous implantation of human retinoblastoma fragments directly into the scapular fat pad area of anesthetized NSG[2] mice, as described in Aerts et al. (Aerts et al., 2010). Once the tumor grows, subsequent passages are made

[2] NSG: NOD/SCID/IL2λ- receptor null mice strain; characterized by the absence of mature T, B and NK cells and defective dendritic cells and macrophages. NOD: non-obese diabetic; SCID: severe combined immunodeficiency disorder; NK: natural killer. (The Jackson Laboratory (JAX) tumor model repository: https://www.jax.org/)

in nude[3] mice. After the third passage, it is considered that the model is established. Ten established PDX were included in this study.

Retinoblastoma cellular models

Eight cellular models were selected for their molecular characterization. All cell models grow in suspension. WERI (RRID[4]:CVCL_1792) and Y79 (RRID:CVCL_1893) were obtained commercially from the ATCC[5]. CL-RB247 (RRID:CVCL_2704) and CL-RB1021 (RRID:CVCL_S624) were kindly provided by Brenda Gallie (Impact Genetics, Canada). Four cell models (CL-HSJD-RBT2, CL-HSJD-RBT5, CL-HSJD-RBT7 and CL-HSJD-RBVS10) were kindly provided by and Ángel Montero Carcaboso (Sant Joan de Déu Hospital –HSJD– Spain). The establishment of these four primary retinoblastoma cultures are described in Pascual-Pasto et al. (2016).

SHORT TANDEM REPEAT ANALYSIS: FINGERPRINTING OF RETINOBLASTOMA MODELS

DNA from patients' primary tumors, PDX tumors (at passage ranging from p3 to P5+1) and cell lines was extracted using a standard phenol-chloroform protocol. DNA concentration was determined by Qubit Fluorometer quantitation assay (Thermo Fisher Scientific). Integrity and purity of samples were assessed by 1% agarose gel electrophoresis.

STR analysis was performed by the Genomic platform of the Curie Institute. One nanogram of DNA samples were subjected to short tandem repeat (STR) DNA fingerprinting using the PowerPlex 16HS (Promega) that amplifies 15 unique STR loci and the Amelogenin gender-determining marker (**Figure 2**), according to manufacturer instructions. All sixteen loci are amplified simultaneously in a single tube and analyzed in a single capillary injection. Internal Lane Standard 600 was used as internal control. PCR products were separated by capillary electrophoresis on a 3730xl DNA Analyzer (Applied Biosystems, Life Technologies) and results analyzed using the GeneMapper software.

[3] Nude mice strain: characterized by the absence of mature T cells. (The Jackson Laboratory (JAX) tumor model repository: https://www.jax.org/)
[4] RRID: Resource Identifiers
[5] American Type Culture Collection

STR Locus	Label	Chromosomal Location	GenBank® Locus and Locus Definition	Repeat Sequence[1] 5′→ 3′
Penta E	FL	15q	NA	AAAGA
D18S51	FL	18q21.3	HUMUT574	AGAA (21)
D21S11	FL	21q11–21q21	HUMD21LOC	TCTA Complex (21)
TH01	FL	11p15.5	HUMTH01, human tyrosine hydroxylase gene	AATG (21)
D3S1358	FL	3p	NA	TCTA Complex
FGA	TMR	4q28	HUMFIBRA, human fibrinogen alpha chain gene	TTTC Complex (21)
TPOX	TMR	2p24–2pter	HUMTPOX, human thyroid peroxidase gene	AATG
D8S1179	TMR	8q24.13	NA	TCTA Complex (21)
vWA	TMR	12p13.31	HUMVWFA31, human von Willebrand factor gene	TCTA Complex (21)
Amelogenin[2]	TMR	Xp22.1–22.3 and Y	HUMAMEL, human Y chromosomal gene for Amelogenin-like protein	NA
Penta D	JOE	21q	NA	AAAGA
CSF1PO	JOE	5q33.3–34	HUMCSF1PO, human c-fms proto-oncogene for CSF-1 receptor gene	AGAT
D16S539	JOE	16q24.1	NA	GATA
D7S820	JOE	7q11.21–22	NA	GATA
D13S317	JOE	13q22–q31	NA	TATC
D5S818	JOE	5q23.3–32	NA	AGAT

[1]The August 1997 report (23,24) of the DNA Commission of the International Society for Forensic Haemogenetics (ISFH) states, "1) for STR loci within coding genes, the coding strand shall be used and the repeat sequence motif defined using the first possible 5′ nucleotide of a repeat motif; and 2) for STR loci not associated with a coding gene, the first database entry or original literature description shall be used".

[2]Amelogenin is not an STR.

TMR = carboxy-tetramethylrhodamine

FL = fluorescein

JOE = 6-carboxy-4′,5′-dichloro-2′,7′-dimethoxyfluorescein

NA = not applicable

Figure 2. STR loci analyzed in DNA fingerprinting

RB1 GENETIC AND EPIGENETIC ANALYSIS

Primary retinoblastoma tumors were analyzed by the Genetic Service of the Curie Institute, for diagnostic purpose. Developed PDX were screened in order to verify their origin. Briefly, all *RB1* coding sequence and flanking intronic junctions were captured and then sequenced using an array-based platform (Illumina, Santa Clara, CA, USA) in order to identify point mutations and large rearrangements. Microsatellite and methylation analyses were used for loss of heterozygosity (LOH) and promoter methylation assessment, respectively. Two intragenic microsatellite markers (D13S153 and Rbi4) and three extragenic markers on both centromeric and telomeric parts were used for LOH determination. Tumor DNA was digested with the methylation-sensitive enzyme HpaII, using corresponding normal DNA as control, and following analysis by fluorescent quantitative multiplex PCR.

RNA EXTRACTION

Total RNA was extracted using Qiazol (Qiagen, Courtaboeuf, France) according to the manufacturer instructions and purified using miRNeasy Mini kit (Qiagen). RNA concentration was determined with a NanoVue Plus spectrophotometer (Dutscher) and/or Qubit Fluorometer quantitation assay (Thermo Fisher Scientific). The RNA quality was assessed by capillary electrophoresis (Bio- analyzer;

Agilent, Inc., Santa Clara, CA, USA) based on the RNA 6000 Pico LabChip kit (Agilent) that assigns per sample quantification and integrity.

MOLECULAR CLASSIFICATION OF PRECLINICAL MODELS

Molecular classification of samples was performed by the transcriptome-based centroid method described in **chapter 1** (using 33 genes) and by the methylome-based pyrosequencing signature (using 9CpG loci), as described in **chapter 1**.

IMMUNOHISTOCHEMICAL ANALYSIS OF PRIMARY TUMORS AND PRECLINICAL MODELS

Primary tumors were fixed in alcohol-formaldehyde-acetic acid (AFA), PDX tumors and cells were fixed in buffered formol. Tumors and cells were paraffin-embedded and process into 5µm thick cuts and placed on glass slides. Hematoxylin Erythrosine Saffron (HES) staining was performed according to classical histologic procedures. Immunostaining was performed in 5µm thick paraffin-embedded sections using the following antibodies: CRX (ab140603, Abcam), ARR3 (111 00-2-AP, EUROMEDEX), EBF3 (H00253738-M05, Abnova), TFF1 (HPA03425, Sigma), KI67 (ab15580, Abcam). Dilutions and protocol are described in **Table 5** (page 220). Analysis was performed by an experienced pathologist specialized in retinoblastoma.

DIFFERENTIALLY EXPRESSED GENES AND PATHWAYS

Expression profiling was performed with the Human Genome U133 Plus 2.0 Array as previously described (**chapter 1**). We compared the transcriptome of the PDX models and cell lines against primary tumors (C1=26; C2=31) using the Limma R package (Smyth, 2005). We used adjusted p-value<0.05 for identifying differentially expressed genes between models and primary tumors. Pathway enrichment analyses were performed using hypergeometric tests, for differentially expressed genes either under-expressed (ratio < 2/3) or overexpressed (ratio > 1.5) in models versus primary tumors, and in models versus subtype 1 only or subtype 2 only.

PROTEIN PROFILING ASSESSED BY WESTERN BLOTTING

Protein extracts were obtained using lysis buffer (50mM Tris-HCl (pH 6.8), 2% SDS, 5% glycerol, DTT 2mM, 2.5mM EDTA, 2.5mM EGTA) freshly supplemented with protease and phosphatase inhibitor (Roche). Cell lysates were clarified by centrifugation. Protein concentration was determined with a BCA Protein Assay-Reducing Agent Compatible kit (ThermoFischer).

Ten micrograms of protein were loaded on SDS-polyacrylamide gels using 4-15% or 7.5% Tris-glycine precast gels (Biorad) and transferred to nitrocellulose membranes using a Trans-Blot Turbo transfer system (Biorad). Membranes were stained with 1x Naphthol Blue Black for rapid staining of protein

bands (AmidoBlack staining, Sigma) and then blocked for 1h with 5% non-fat milk at room temperature. Membranes were incubated with the primary antibody overnight at 4°C. The following antibodies were used: anti-MYC in 1:1000 dilution (5605S, Cell Signaling); anti-MYCN in 1:1000 dilution (sc-53993, Santa Cruz); anti-CRX in 1:500 dilution (ab140603, Abcam); anti-ARR3 in 1:1000 (ab180912, Abcam); anti-EBF3 in 1:1000 dilution (H00253738-M05, Abnova); anti-EBF1 in 1:1000 dilution (ab108369, Abcam); anti-TFF1 in 1:1000 dilution (HPA003425, Sigma); anti-RB1 N-terminal in 1:1000 dilution (ab1113, Abcam); anti-RB1 C-terminal in 1:1000 dilution (#9309, Cell Signaling); anti-Phospho RB1 (Phospho-Rb (Ser780)) in 1:2000 dilution (#9307, Cell Signaling); anti-α tubulin in 1:20000 dilution (T9026, Sigma), anti-βactin in 1:20000 dilution (A2228, Sigma). Secondary antibodies were horse anti-mouse IgG (7076s, Cell Signaling) or goat anti-rabbit IgG (7074, Cell Signaling) used in 1:3000 dilution, incubated for 1h at room temperature. Signal detection was performed using SuperSignal West Femto (ThermoFisher) or Clarity Western ECL (BioRad) substrates followed by exposure on X-ray film (ThermoFischer).

Membrane incubation and antibody dilution were performed in 5% non-fat milk using TBS-tween for Phospo-RB1, ARR3 and EBF1 antibodies. For the remaining antibodies 5% non-fat milk in PBS-tween was used.

RESULTS

HETEROTOPIC PDX DEVELOPMENT AND CLINICAL CHARACTERISTICS

Since 2002, the Preclinical Investigation Laboratory (LIP) of the Curie Institute has engrafted subcutaneously 77 primary retinoblastoma tumors in NGS mice in an effort to establish retinoblastoma PDX models. Primary retinoblastoma tumors were obtained directly from patients who underwent enucleation at the Curie Hospital, and xenografted subcutaneously into the scapular area of NSG mice. Up to day, 15 PDX have been successfully established (N=15/77, 20%) and there is one more engrafted mice ongoing (mice-passage below three) (**Figure 3A**). Establishment of a PDX is considered when four successive passages in mice are achieved. Established PDX derived from patients who had no received chemotherapy or radiotherapy before enucleation.

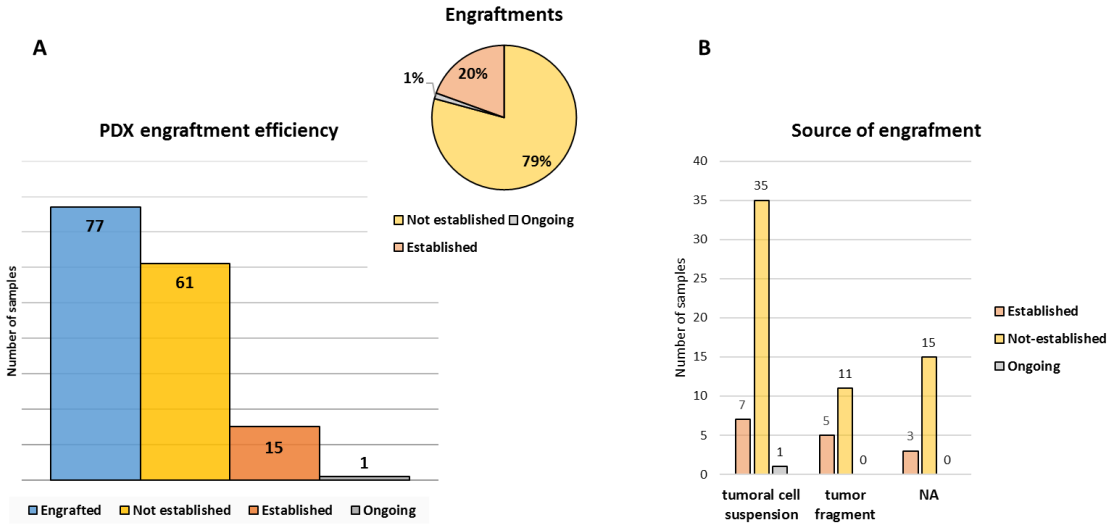


Figure 3. Retinoblastoma PDX engraftment efficiency in the Curie Institute
A) Since 2002, 77 freshly tumoral samples has been injected in NSG mice (engrafted, in blue) from which 15 PDX models has been established (established, in orange). One PDX model is ongoing, but not yet established (ongoing, in gray). B) The source of engraftments was either a suspension of tumoral cells or fragments of solid tumor. NA: data not available.

PDX were generated from either fragments of solid tumors (N=5/15) or from tumoral cell suspension (N=7/15), based on material availability (no data was available for three models). Thirty-five non-successful engraftments had been derived from tumoral cell suspension (N=35/61) and eleven from solid tumor fragments (N=11/61) (no data was available for 15 models) (**Figure 3B**). No significant differences existed between the source of material injected in mice and the successful of the engraftment (p= 0.2811, Fisher's exact test). The latency period for all models established (the time between engraftment and tumor growth) was between 1.5 and 3.5 months. There were no

significant differences between the latency period of models established from tumoral cell suspension or solid tumor fragments (p= 0.4175, Fisher's exact test). Most subcutaneously injected (N=66/77, 86%) and successfully engrafted tumors (N=14/15, 93%) were developed from unilateral retinoblastomas (**Figure 4**). Before the molecular characterization and subtype assignment of the PDX models, we stratified our PDX cohort according to age at diagnosis (<18 months>) based on the distribution observed in our cohort of primary retinoblastomas (N=102) (**Figure 5**). Most injected (N=47/77, 61%) and established models (N=11/15, 73%) were developed from patients diagnosed after 18 months of age (**Figure 4**). The median age at diagnosis of established PDX was 32.8 months (range 9.8-81.4 months), and 23.5 months (range 2.5-138 months) for the non-established models. Regarding the gender of patients, most engrafted tumors (N=11/15, 73%) were developed from females (**Figure 4**).

Based on material availability, we selected 10 out of the 15 established PDX models to include in this study. Clinical information of patients and technologies used for the characterization of the PDXs can be found in **Table 1** (page 215) and **Table 2** (page 216), respectively.

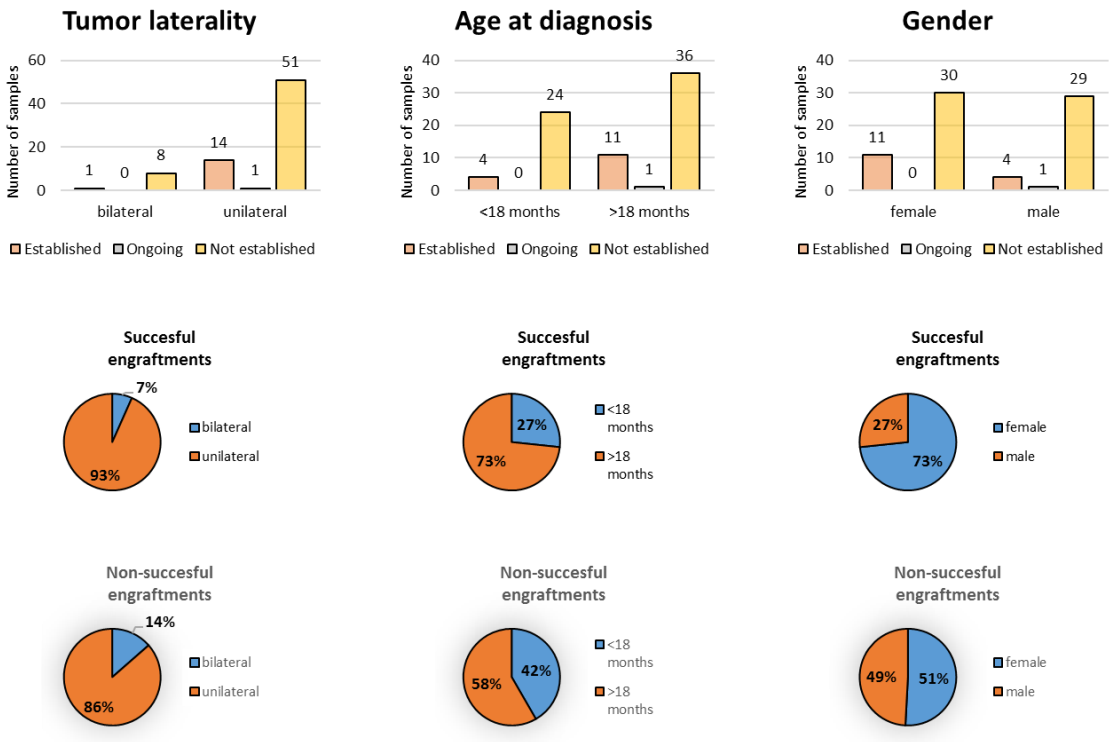


Figure 4. PDX models categorization by tumor laterality, age at diagnosis and gender of patients from which they derived

In the upper part: established models (orange), ongoing model (gray) and non-established models (yellow). At the bottom are indicated the successful engraftments that includes the 15 PDX models established, and the non-successful engraftments (N=61).

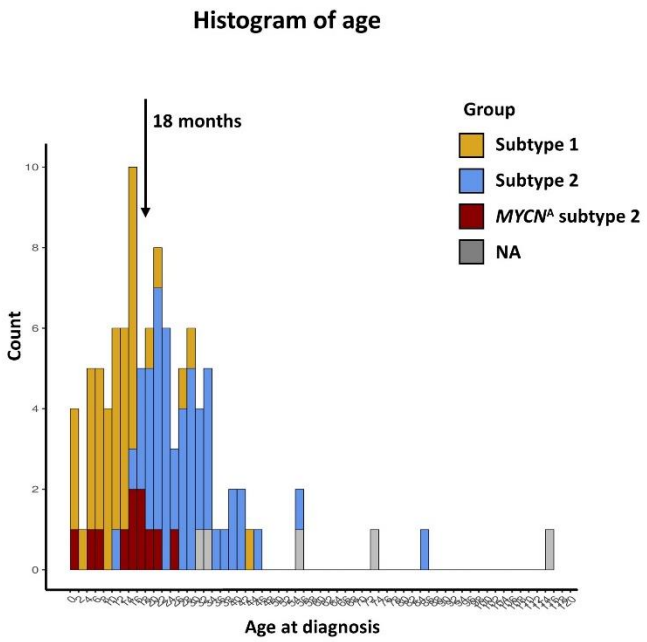


Figure 5. Histogram recapitulating the distribution of age at diagnosis of the 102-retinoblastoma cohort of primary tumors
Most tumors from the subtype 1 are diagnosed at ages below 18 months, while subtypes 2 tumors are diagnosed at older ages. MYCN^A tumors (dark red) are also diagnosed earlier.

CELLULAR MODELS

Eight cellular models were selected for their clinical and molecular characterization. WERI and Y79, the cell lines most commonly used in retinoblastoma research, were obtained commercially (ATCC). The six remaining models, were kindly provided by Brenda Gallie (Impact Genetics, Canada) and Ángel Montero Carcaboso (Sant Joan de Déu Hospital –HSJD– Spain). The cell models provided by HSJD derived from patients diagnosed before the age of 18 months, half of them deriving from unilateral and female patients. Two out of the four cell models (CL-HSJD-RBT2, CL-HSJD-RBT5) were derived from patients having received chemotherapy prior to enucleation.
Clinical information and technologies used for the characterization of the cellular models can be found in **Table 1** (page 215) and **Table 2** (page 216), respectively.

SHORT TANDEM REPEATS (STRs) DNA FINGERPRINTING

In order to characterize the cellular and animal models and to corroborate its origin regarding the original tumor, a STRs analysis was performed for all models included in the study. Procedures and data analysis was carried out by the Genomic platform of the Curie Institute. All PDX models were compared with the primary tumor from which they derive: six PDX were 100% correlated (RBX202, RBX206, RBX210, RBX211, RBX215, RBX218) and four were correlated at 97% (RBX102, RBX109, RBX111, RBX200). Three cellular models from HSJD were correlated at 100% whit its original tumor (CL-HSJD-RBT2, CL-HSJD-RBT7, CL-HSJD-RBVS10). CL-HSJD-RBT2 derived from solid tumor was

compared to DNA from vitreous seeding of the tumor. CL-HSJD-RBVS10 derived from vitreous seeding was analyzed together with the solid and vitreous seeds of the primary tumor. No primary tumor was available for CL-HSJD-RBT5. No data was available for cell lines CL-RB247 and CL-RB1021 to compare with. Y79 was 100% correlated with the STR profile publicly available in Cellosaurus (https://web.expasy.org/cellosaurus/CVCL_1893). WERI was 93% correlated with the STR profile provide by the ATCC described in Cellosaurus (https://web.expasy.org/cellosaurus/CVCL_1792): one allele (allele 12) of the CSF1PO marker was missing in our cells (reported alleles: 11,12,13). Results are described in **Table 3** (page 217).

RB1 MUTATIONS AND *MYCN* AMPLIFICATION STATUS IN PDX AND CELL MODELS

RB1 mutations of PDX and its corresponding original tumors were identified and provided by the Genetic Service of the Curie Hospital. *RB1* mutations were identified in nine out of ten PDX (RBX109 was not studied) and its primary tumors. In total, thirteen mutations were identified: eight of them were SNVs or indels, five were exon-deletions, and one model carried a biallelic promotor methylation. Four PDX models (RBX102, RBX109, RBX211 and RBX215) derived from patients harboring germline *RB1* mutations.

Y79 is a *MYCN*-amplified cell line, harboring two somatic *RB1* mutations (Lee et al., 1984). WERI cells carry a biallelic *RB1* deletion (McFall et al., 1977). *RB1* mutation status for CL-RB247 and CL-RB1021 was described in (Paderova et al., 2007). Two cell models from the HSJD derived from *MYCN*-amplified tumors (CL-HSJD-RBT2, CL-HSJD-RBT7), but the *MYCN* status was not analyzed in the cells. *RB1* mutation screening from HSJD-samples were performed in the constitutional DNA (blood) of patients with diagnostics purpose only (no tumor or cell line have been sequenced).

A table recapitulating the *RB1* mutation and *MYCN*-amplification status of models are described in **Table 4** (page 219).

MOLECULAR CLASSIFICATION OF PRECLINICAL MODELS

In order to attribute a molecular subtype to the available animal and cellular models of retinoblastoma, we used the same approach to the used for classification of primary tumors. We used the centroid-transcriptomic based (based on 483 and 33 genes) and the centroid built from the methylome and assessed by a 9CpG-pyrosequencing signature. Transcriptome was available for nine PDX models and three of their corresponding primary tumors, and for eight cell lines. Pyrosequencing was performed on four primary tumors and four cell lines. We combined results and defined a molecular subtype, shown in **Figure 6**.

Patient-derived xenograft

Six PDX were classified in the molecular subtype 2 (C2, N=6/10, 60%), and one in the molecular subtype 1 (C1, N=1/10, 10%). Two PDX (RB109 LAK, RB218 SI) could not be assigned to any subtype (analyzed by the transcriptomic signature) (NA, N=2/10, 20%) and one (RB211 MY) was not analyzed due to low RNA quality (ND, N=1/10, 10%).

Cell lines

Six cell lines were classified in the molecular subtype 2 (C2, N=6/8, 75%), while two models (WERI, CL-HSJD-RBT7) could not be attributed to any molecular subtype (NA, N=2/8, 25%).

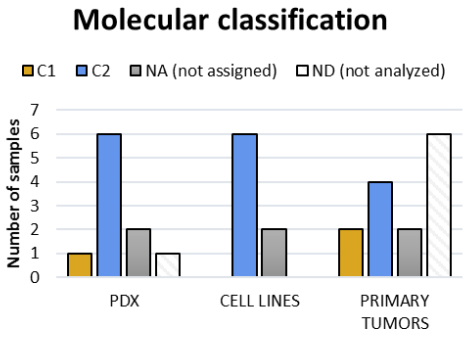
Primary tumors

One primary tumor was classified in subtype 1 (RB338), and RB109 had already been attributed to the subtype 1 based on methylome and copy number alteration's cluster analysis (C1, N=2/14, 14%). Four primary tumors were classified in subtype 2 (C2, N=4/14, 29%), while two could not be assigned to any subtype (NA, N=2/14, 14%). One of the unclassified tumor (RB102) was attributed to the C1 subtype by the transcriptome and to the C2 subtype by the pyrosequencing signature, and thus was left unclassified. This discrepancy could be explained by the intra-tumoral heterogeneity displayed by subtype 2 tumors, and the portion of tumor taken during sampling. The source of the material analyzed was not the same: the RNA used for transcriptomic analysis came from the Biological Resource Centre of the Curie Institute, while the DNA used to performed pyrosequencing was obtained in our lab by scratching tumor block-FFPE slides. The remaining six primary tumors were not analyzed (ND, N=6/14, 43%).

Classified models and their associated primary tumors are shown in **Figure 6B**. From the pairs for which both samples could be analyzed (RBX200/RB327; CL-HSJD-RBT2/HSJD-RBVS2), both were classified in the molecular subtype 2. We were expecting to have primary tumors and model derived grouping in the same subtype, but one discording subtype between model RBX202 (subtype 1) and its original tumor RB335 (subtype 2) was identified.

Taken together, twelve retinoblastoma preclinical models were classed in the molecular subtype 2 (C2, N=12/18, 67%), while only one model was classed in the subtype 1 (C1, N=1/18, 5%). One model was not analyzed (ND=1/18, 5%), and four models remained unclassed (NA, N=4/18, 23%).

A



B

MODEL		PRIMARY TUMOR	
RBX102	C2	RB102	NA
RBX109	NA	RB109	C1
RBX111	C2	RB111	ND
RBX200	C2	RB327	C2
RBX202	C1	RB335	C2
RBX206	C2	RB336	ND
RXB210	C2	RB337	ND
RBX211	ND	RB338	C1
RBX215	C2	RB339	ND
RBX218	NA	RB340	ND
CL-HSJD-RBT2	C2	HSJD-RBVS2	C2
CL-HSJD-RBT5	C2	HSJD-RBT5	ND
CL-HSJD-RBT7	NA	HSJD-RBT7	C2
CL-HSJD-RBVS10	C2	HSJD-RBT10	NA
WERI	NA		
Y79	C2		
CL-RB247	C2		
CL-RB1021	C2		

Figure 6. Molecular classification of the retinoblastoma preclinical models and its original tumors
A) All PDX (N=10), cellular models (N=8) and primary tumors (N=14) included in this study, classified by subtypes. B) Associated preclinical models and primary tumor's classification.

IMMUNOHISTOCHEMICAL CHARACTERIZATION ON PDX AND PRIMARY TUMORS

PDX models show characteristics of undifferentiated retinoblastoma

We performed Hematoxylin Erythrosine Saffron (HES) staining on PDX models and paired primary tumors (**Table 6**, page 220). Microscopic histopathology analysis was performed by an experienced pathologist specialized in retinoblastoma (Dr. Paul Fréneaux; Pathology Service of the Curie Hospital). This analysis confirmed the retinoblastoma histology in all PDX tumors analyzed. Necrosis was present in similar percentages in PDXs (5-50%) and in primary tumors (5-40%). Tumor differentiation was assessed by the extent and presence of typical Homer-Wright rosettes or Flexner-Wintersteiner rosettes, two histopathological features that reflect partially differentiated retinoblastoma cells (Shields et al., 1994; Ts'O et al., 1970). Most primary tumors (N=8/10) were undifferentiated, with percentages of rosettes less than 5%. Two primary tumors, RB327 and RB337, were more differentiated with 40% and 30% of rosettes, respectively. In these cases, differentiation was lost in the PDX models derived. Rosettes were not identified in any PDX model.

ARR3, CRX, EBF3 and TFF1 immunohistochemical characterization

We then performed immunohistochemical (IHQ) analysis using the proteins that had been used for the characterization of primary tumors. The aim was: 1) to attribute a molecular subtype to the unclassed samples, based on the extension of EBF3 and TFF1 stained areas, present only in C2

tumors[6]; 2) to determine whether intra-tumoral heterogeneity detected in primary tumors was also present in PDXs; 3) to analyze the staining pattern in the tumor (mutual exclusive or co-expression, or both); and 4) to compare the percentages of cells positively stained for CRX, ARR3, EBF3 and TFF1 in primary tumors and PDX models, to infer the phenotypic population of cells that grew in mice. Results of the immunohistochemical-based classification, staining pattern and staining percentages are described in **Table 7** (page 221).

Immunostaining-based tumor classification

Given that EBF3 and TFF1 are overexpressed in the mixed-subtype, we used them to attribute a sample to a subtype, based on the extent of the positive staining (>15%). All primary tumors but one (RB338) could be classified in the C2 subtype. Based on the transcriptome, RB338 had already been attributed to the molecular subtype 1. Likewise, all PDX tumors could be classified in subtype 2 except for RBX202, already attributed to the molecular subtype C1 (based on the transcriptome). With two exceptions (RB335/RBX202 and RB338/RBX211) PDX tumors classed in the same subtype that their original tumor. RB335/RBX202 and RB338/RBX211 are shown in **Figure 7** and **Figure 8**, respectively.

Percentage of CRX, ARR3, EBF3 and TFF1 staining varies from primary to the PDX model

CRX staining was positive in all primary tumors and PDXs, with different percentages of positive cells across models and primary tumors. ARR3 was positive in all primary tumors but not all PDXs. In one model (RBX109) derived from a primary tumor with 30% positive for ARR3, no staining was detected in the PDX, while for the rest of the models the proportion of cells positively stained varied from 10% to 100%. Positive EBF3 staining was higher than 70% in primary tumors (except for RB338), and in most of PDXs (N=7/10), except for three: RBX109 (10%), RBX202 (5%) and RBX218 (0%). Finally, TFF1 was positive in more than 50% in most primary tumors (N=8/10) and (except for RB338) and most PDXs (N=6/10) and was negative for RBX202, the model classed in the subtype 1.
In general, proportion of stained cells varied from primary to PDX tumors. No general rules could be made regarding the proportion of cells growing in PDX tumors.

PDX exhibit mostly a co-expression pattern

Most primary tumors (N=7/10) displayed mutual exclusive staining pattern between ARR3 and TFF1/EBF3 in some areas of the tumor, together with a CRX co-expression in other tumoral areas. Most PDX tumors (N=7/10) showed a co-expression for the four markers.

[6] EBF3 and TFF1 staining are mostly exclusive for the subtype 2. Subtype 1 tumors displaying positive staining of these proteins are few and generally displays fewer percentages of staining extends (<10%).

IMMUNOHISTOCHEMICAL ANALYSIS OF CELL LINES REVEALED THEY ARE PHENOTYPICALLY HETEROGENEOUS

Cell lines were paraffin-fixed and analyzed as primary and PDX tumors. Three established cell lines (WERI, Y79 and CL-RB247) in addition to five cell models derived from the PDX tumors (RBX109, RBX111, RBX200, RBX211 and RBX215) were analyzed. This analysis showed that all cell models are composed by a heterogeneous population of cells marked positively for the four markers (**Table 8**, page 222), as is seen in primary tumors and PDX models. Representative IHQ images for cells derived from RBX211 are shown in **Figure 8**, together with the PDX and primary tumor.

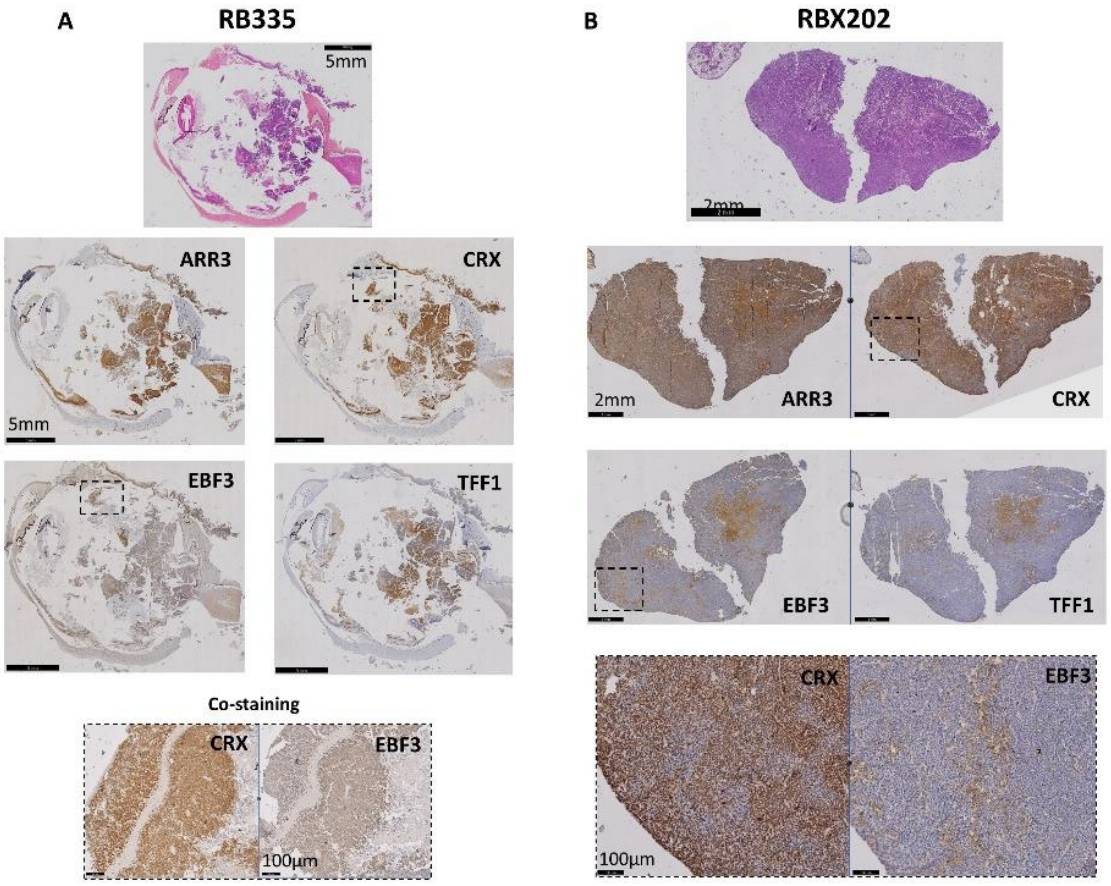


Figure 7. Immunocharacterization of RB335 and its PDX RBX202
A) Primary tumor: HES and immunostaining for the four markers, showing one tumor area displaying co-expression of CRX and EBF3 (bottom). B) PDX: HES and immunostaining. EBF3 is expressed by 5% of tumoral cells while no positive cells are observed for TFF1 marker. A CRX positive/EBF3 negative tumor area is shown at the bottom.
The zoomed areas are indicated with a dotted square. Scale bars are indicated in each figure.

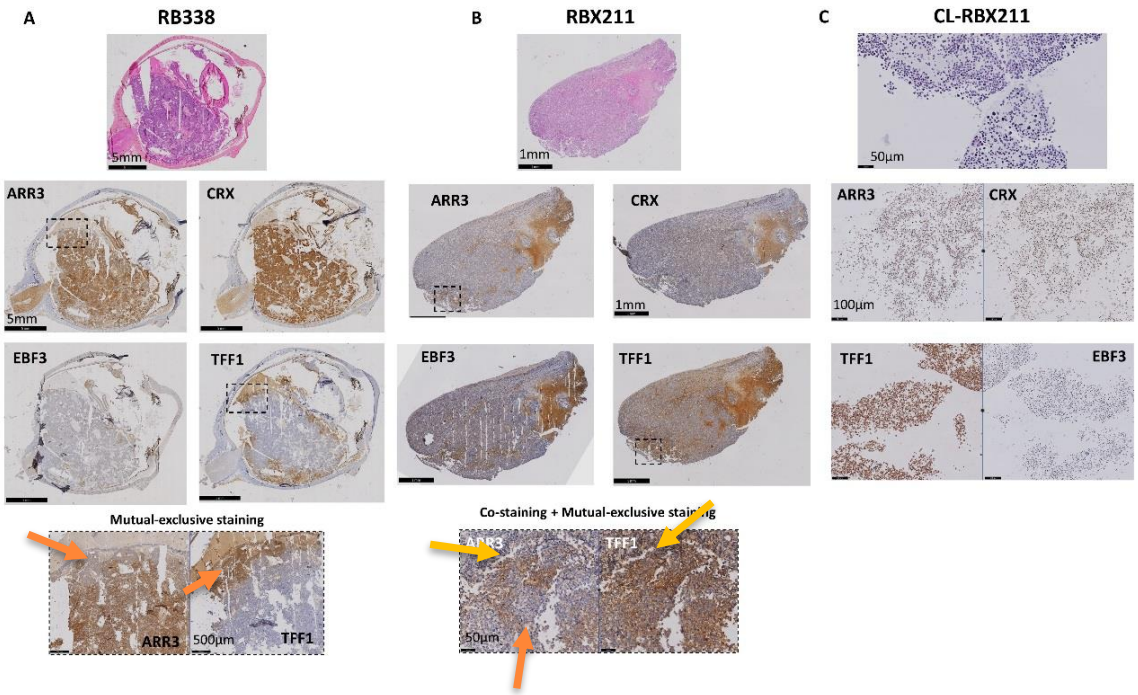


Figure 8. Immunocharacterization of RB338, its PDX RBX211 and the cell line derived CL-RBX211
A) Primary tumor: HES and immunostaining for the four markers, showing one tumor area displaying mutual-exclusive staining pattern for ARR3 and TFF1 (orange arrow). B) PDX: HES and immunostaining. EBF3 is expressed by 20% of tumoral cells, and TFF1 is positive in 80% of the tumor. At the bottom in shown one tumor area displaying co-expression of ARR3 and TFF1 (yellow arrow), as well as a mutual-exclusive pattern (orange arrow). C) Cells derived from the PDX tumor show positive cells for all the four markers. The zoomed areas are indicated with a dotted square. Scale bars are indicated in each figure.

GENOMIC PROFILING

Paired PDX and primary tumor samples

When analyzing the immunohistochemistry of paired primary and PDX tumors, we found two curious cases where PDXs models completely lost the phenotypic immunohistochemical characteristics of the primary tumor, and classified in a different retinoblastoma subtype: RB335 (subtype 2)/RBX202 (subtype 1), and RB338 (subtype 1)/RBX211 (ND, transcriptome; subtype 2, IHQ). In order to determine if theses phenotypic differences observed implied, in addition, genotypic changes we analyzed the genomic copy number for these two pair of samples.

We have previously characterized (**figure 2, chapter 3**) the copy number changes associated to each retinoblastoma subtype: 1q gains together with 16q losses or 2p amplifications are systematically observed in the subtype 2, while 6p gains and 13q losses are observed in both subtypes (**Figure 9**).

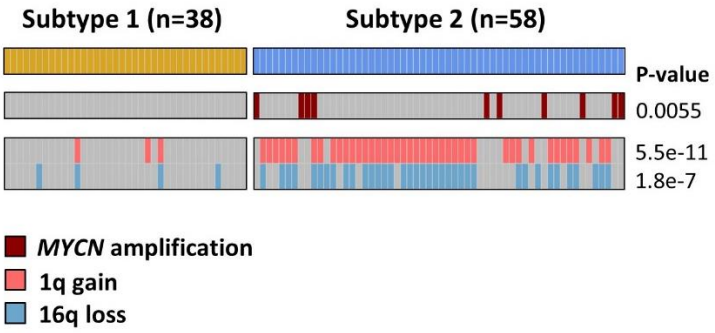


Figure 9. Copy number changes associated to retinoblastoma subtypes
With two exceptions, 1q gains together with 16q losses or 2p amplifications are systematically observed in the subtype 2.

RB335/RBX202

Gain on chromosomes 1q and 2p were detected in both samples, as well as loss on chromosome 16q. These copy number changes indicates that both samples actually belong to the subtype 2. Thus, RBX202 represent a subtype 2 tumor with low expression levels of both EBF3 and TFF1.

Gain on 2p revealed an amplification involving the locus *MYCN/MYCNOS*, with five copies present in RB335 and six copies in RBX202. Other commonalities between primary and PDX tumor were lost of chromosome 1p, 5q and 14q, and gain on chromosomes 19q and 20. Additional changes were detected in the PDX on 1p (gain), 3p (loss), 6p (gain), 11p and 11q (loss), and 17q (gain), that were not present in the original tumor (**Figure 10A**).

RB338/RBX211

Gain on chromosomes 1q and 2p were detected in both samples. These copy number changes would indicate that both samples actually belong to the subtype 2, and that RB338 is one of the subtype 2 tumors displaying low TFF1 and EBF3 staining. Chromosomal 16q loss was detected only in the primary tumor, as well as loss on 17p and 17q (**Figure 10B**). Regarding IHQ staining, ARR3 was lost, and EBF3/TFF1 were gained in the PDX, related to the primary tumor. We were not able to correlate the observed genomic copy number changes to these phenotypical changes observed.

Two additional copy number changes were detected in the PDX in relation to its original tumor: 6p gain and chromosomal gain on 13. This latter could be explained by LOH (duplication of the mutated allele carrying a deletion on *RB1* gene).

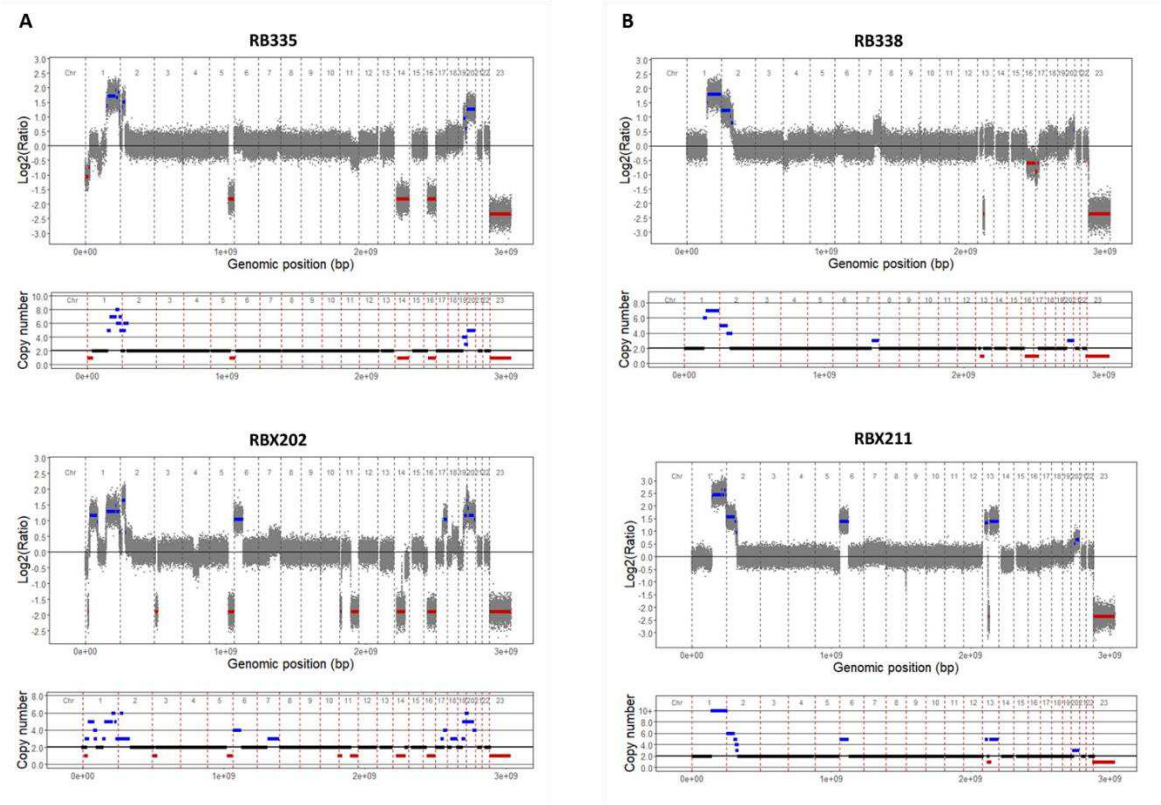


Figure 10. Genomic copy number alterations in primary tumors and matched PDX
A) RB335 primary tumor (top) and its PDX models RBX202 (bottom). B) RB338 primary tumor and its PDX model RBX211 (bottom).

In conclusion, we were not able to associate the phenotypic changes in protein expression to the genomic changes observed. Undoubtedly, more cases like these needs to be studied in order to establish a rule. Additional copy number changes appearing in the PDX models could be explained by either i) the presence of sub-clones in the primary tumors (RB335, RB338), with few cells harboring these alterations, explaining why they were not detected in the original tumors; or ii) the appearance of these chromosomal changes during the establishment of the models.

FINAL CLASSIFICATION OF PRECLINICAL MODELS

Taking into consideration the genomic copy number changes in addition to our previous molecular based-classification, allowed us to reclassified one PDX model and one primary tumor previously classified by the transcriptome in the subtype 1 (RBX202, RB338) to the subtype 2. In addition, we could assign one unanalyzed PDX model (RBX211) to the subtype 2. Sample RB109 (primary tumor) had been already attributed to the subtype 1, based on the methylome and copy number alteration's cluster analysis (**chapter 1, table 5, page 82**).

Taken together, fourteen retinoblastoma preclinical models were classed in the molecular subtype 2 (C2, N=14/18, 78%), and four models remained unclassed (NA, N=4/18, 22%).

Final classification based on the transcriptome and the pyrosequencing signature, including the copy number alterations, are shown in **Figure 11** and are described in **Table 9** (page 223).

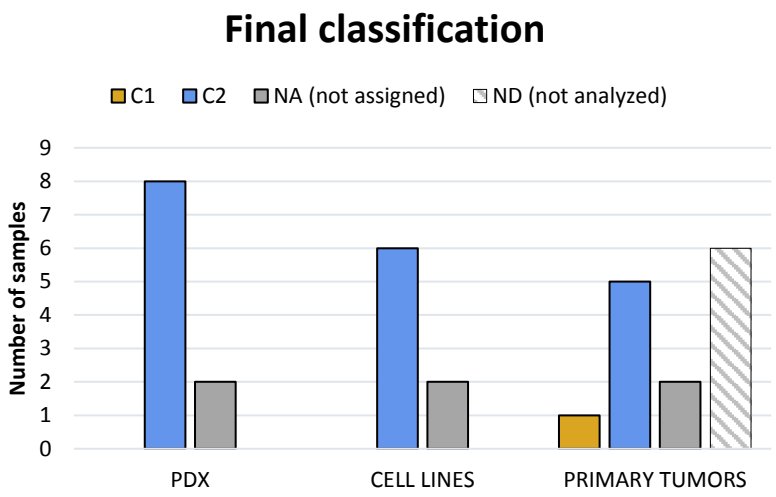


Figure 11. Final classification of preclinical models and primary tumors
Classification based on the transcriptome, the pyrosequencing signature, and taking into consideration genomic copy number changes

PROTEIN PROFILING

Next, we assessed by Western blotting the expression of the four markers used in immunohistochemistry (CRX, ARR3, EBF3, TFF1), in addition to another retinal ganglion cell marker EBF1, which is expressed in a subpopulation of retinal ganglion cells (Kaewkhaw et al., 2015; Trimarchi et al., 2007). *TFF1*, *EBF1* and *EBF3* are significantly differentially expressed between retinoblastoma subtypes (**Figure 12A**). Besides, we have previously seen that expression of *TFF1* and *EBF3* are significantly correlated (**Figure 12B**), and that *EBF1* shows complementary levels of expression to that of *TFF1* and *EBF3* in primary tumors of the molecular subtype 2 (**Figure 12C**). Additionally, we assessed expression of MYC, MYCN, and RB1 protein. Immunoblottings are shown in **Figure 13A** (PDX) and **Figure 13B** (cell lines).

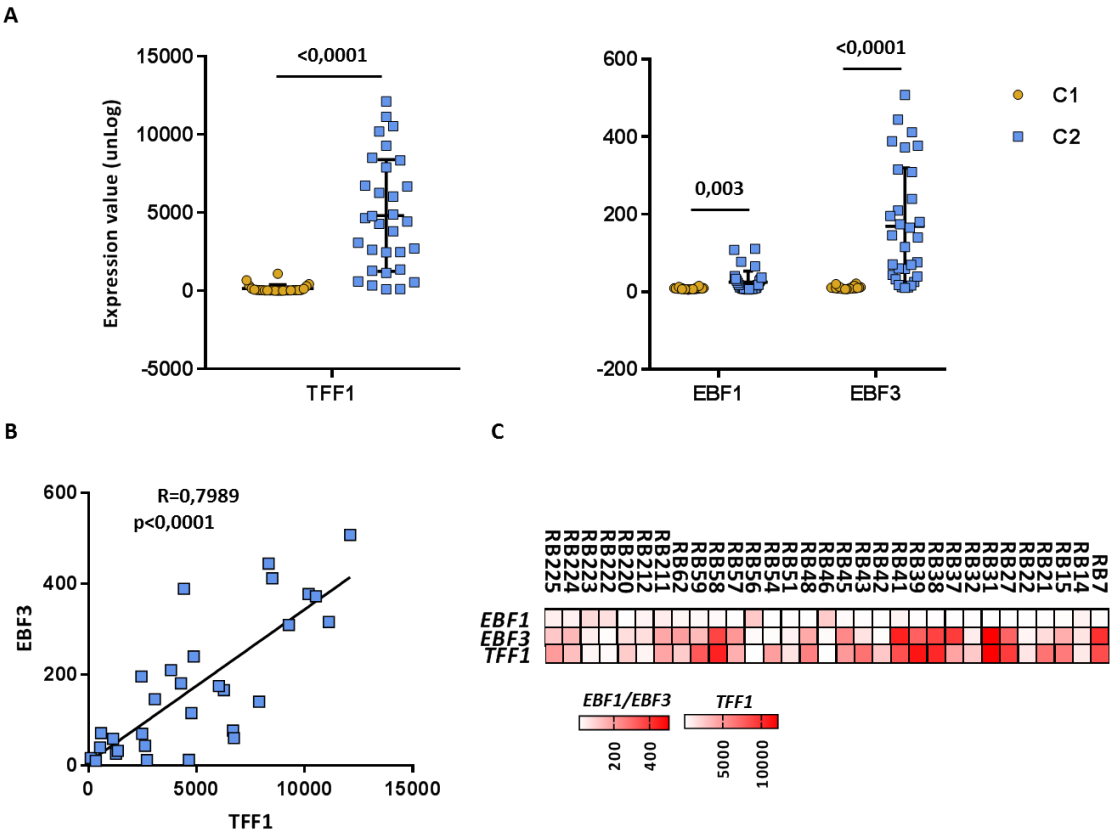
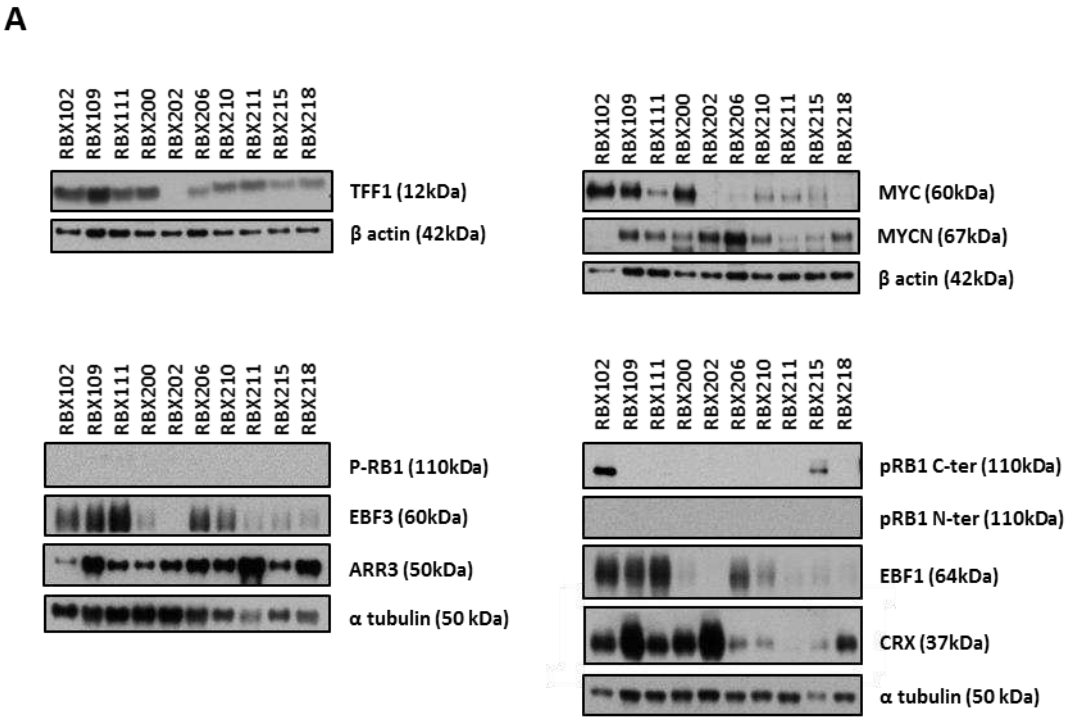


Figure 12. TFF1, EBF3 and EBF1 expression in primary retinoblastoma tumors

A) TFF1, *EBF3* and *EBF1* significantly differentially expressed between subtype 1 (in gold) and subtype 2 (in blue) tumors. B) *EBF3* and *TFF1* expression is significantly correlated in subtype 2 tumors (Pearson's correlation R=0,7989, 95% confidence interval 0,6202 to 0,8988, P (two-tailed) <0,0001). C) *EBF1* is expressed in a complementary way respect to *EBF3* and *TFF1* in subtype 2 tumors: when TFF1 and EBF3 are expressed at low levels, *EBF1* is higher expressed, and vice versa.



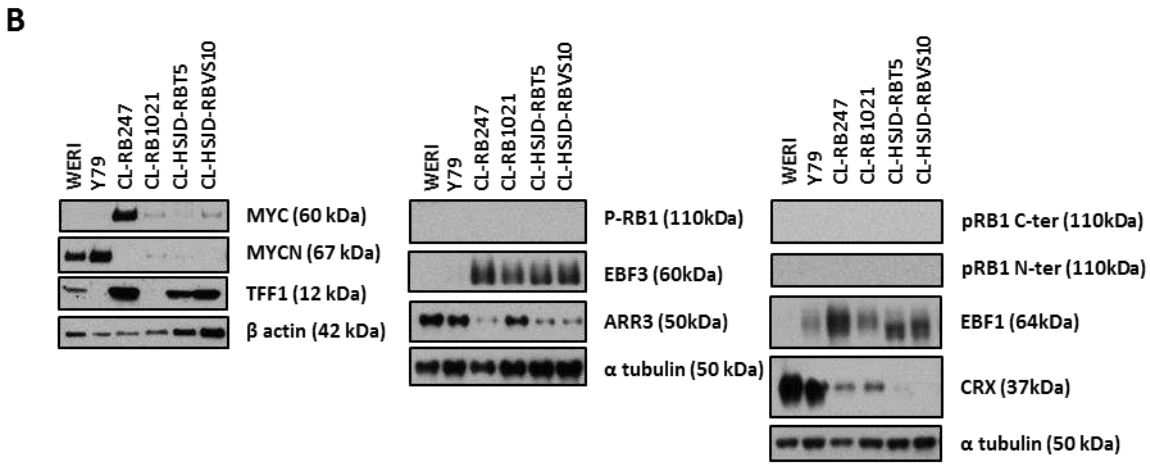


Figure 13. Immunoblotting profiling for PDX and cellular models
A) PDX models. B) Cellular models.

PDX protein profiling

TFF1, EBF3 and EBF1 are expressed in all PDX models (at different levels) except for RBX202, the only model negative for the three markers. Certain differences were found for EBF3 marker between IHQ staining and WB: RBX109 shows low percentages of positively stained cells by IHQ but expression is be higher assessed by WB, and the contrary is seen in models RBX200, RBX211 and RBX215. Similar levels of expression were found for EBF3 and EBF1, contrary to what is seen at the mRNA level (**Figure 14A**), where *EBF1* is not expressed as high as is seen at the protein level. A possible explanation to this could be that the antibody might not be specific.

ARR3 is expressed in all PDX models, but some discrepancies were found with respect to the IHQ staining: RBX102 is 100% positive by IHQ while a faint band is detected by WB, while RBX109 and RBX211 are 0% and 10% positive by IHQ, respectively, and they show high levels of expression by WB. Similar discrepancies were found for CRX: low levels of expression are found by WB (compared to IHQ) in models RBX206, RBX210, RBX211 and RBX215.

All the differences mentioned above could be explained by blind tumor sampling: the selection of a group of tumoral cells that would ultimately be processed for protein extraction, not being representatives of the whole tumor.

We found that MYC and MYCN are expressed in all PDX models, either one or both of them. RBX202 model with a chromosomal 2p gain show expression of MYCN only, while RBX211 model that also has 2p gain shows both MYCN and MYC protein expression. The antibody targeting the C-terminal region of the RB1 protein (pRB1-Cter, targeting amino acids 701-928) was detected in RBX102 and RBX215 models, probably detecting a non-functional protein: RBX102 model harbors a splice-site mutation in exon 14 (theoretically introducing a change from amino acid number 463) and loss of the normal allele (LOH), while RBX215 model harbor a missense mutation in exon 21 (targeting amino

acid 711) and a nonsense mutation in exon 20 (theoretically introducing a change from amino acid number 691).

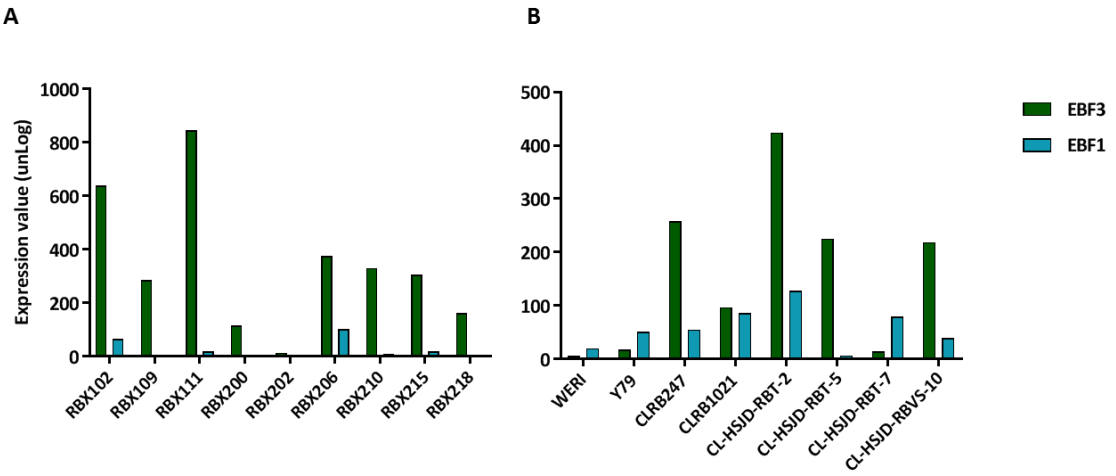


Figure 14. EBF3 and EBF1 expression in PDX models and cell lines
A) PDX models. B) Cellular models

Cell lines protein profiling

TFF1 is expressed in all cell lines except for Y79 and CL-RB1021. EBF3 and EBF1 are expressed by all cell models except for WERI. EBF1 showed complementary level of expression to EBF3 and TFF1 (similar to what is seen in primary tumors) only for Y79 cells, while a co-expression in seen for the rest of the models. Similar discrepancies as seen for PDX models were observed for EBF3 and EBF1 regarding protein and gene expression (**Figure 14B**).

ARR3 is found in all cellular models, at different levels of expression. CRX is strongly expressed in WERI and Y79 cells, moderately expressed in CL-RB247 and CL-RB1021 cells, and poorly expressed in CL-HSJD-RBT5 and CL-HSJD-RBVS10 cells.

Two cell models co-expressed low levels of MYC and MYCN proteins (CL-RB1021 and CL-HSJD-RBT5) while the rest expressed either MYCN (strongly expressed by WERI and Y79-*MYCN* amplified) or MYC (strongly expressed by CL-RB247 cells and poorly expressed by CL-HSJD-RBVS10 cells).

RB1 protein was not detected in any cell model.

TRANSCRIPTOME-BASED CHARACTERIZATION OF PDX AND CELLULAR MODELS OF RETINOBLASTOMA

Transcriptome was available for 59 retinoblastomas (N=27 subtype 1; N=32 subtype 2), 9 PDXs and 8 cell lines. Principal component analysis using the transcriptome data sets allows separation in groups of primary tumors, PDX, cell lines and fetal retina (**Figure 15**). To identify differentially expressed genes between primary tumors and preclinical models we used Limma analysis. Limma analysis was performed comparing: 1) PDX vs all primary tumors, and against each subtype; 2) cell lines vs all primary tumors, and against each subtype; and 3) PDX and cell lines vs all primary tumors,

and against each subtype. We did not include the fetal retina in this analysis given that is composed by a heterogeneous population of different (normal) retinal cells, risking introducing a bias in the analysis. We compared preclinical models against all retinoblastomas and against each retinoblastoma subtype in order to identify the differences or similarities that could exist with each subtype.

Gene set enrichment analysis was performed with the resulting differentially expressed genes to identify enriched gene ontologies (GO) and signaling pathways (Hallmark gene sets) in each group (**Table 10** , page 224, and **Table 11,** page 225). We then selected the most significantly differentially expressed GOs and pathways (FDR-adjusted p-values < 0.05) and built a metascore of all genes included in each gene set category to depict differences between preclinical models and primary retinoblastomas. In addition, we have selected a series of retinal cell-associated genes, based on bibliography and publicly available data, to build retinal-cell-differentiation-signatures related to photoreceptor cells, early/intermediate/late cone photoreceptor cells, rod photoreceptor cells, retinal ganglion cells, and Müller glia cells. Global results are depicted in **Figure 20,** and detailed in **Table 12** (page 227).

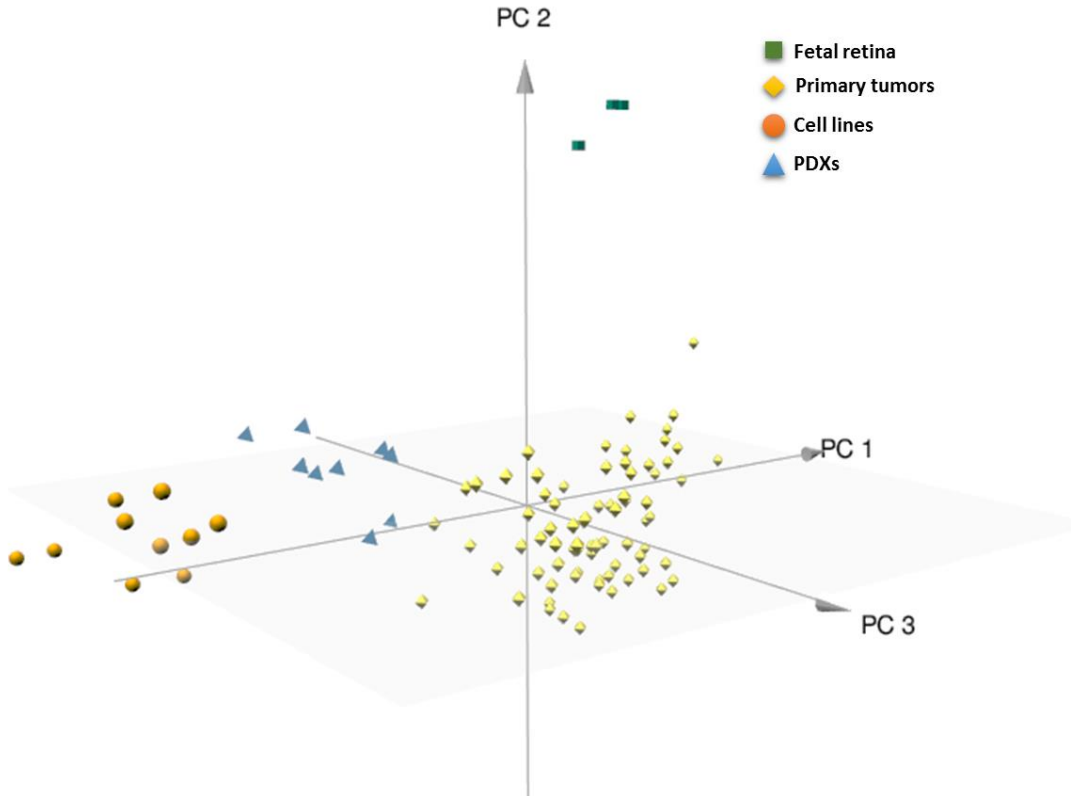


Figure 15. Principal component analysis of transcriptome data sets
Fetal retinas are shown in green squares at the top; primary tumors are shown in yellow diamonds in the center of the plot; PDX tumors in orange balls at the left; cells lines are shown in light blue triangles between PDX and primary tumors.

Upregulated genes and pathways in models

Functional annotation of differentially expressed genes against all primary tumors revealed that the PDX were notably enriched in GO processes like ”DNA packaging complex”, “ribonucleoprotein complex localization”, and cell lines in “translational termination”, “amino acid activation”, consistent with cellular growth. Related to the GO terms identified in cell lines, mTORC1 signaling is upregulated. mTOR complex 1 (mTORC1), is a master growth regulator that senses and integrates diverse nutritional and environmental cues, including growth factors, energy levels, cellular stress, and amino acids. It couples these signals to the promotion of cellular growth by phosphorylating substrates that potentiate anabolic processes such as mRNA translation and lipid synthesis (Laplante and Sabatini, 2012). This pathway may not count for PDX cell growth, as is downregulated in PDX (**Figure 16** and **Figure 20**).

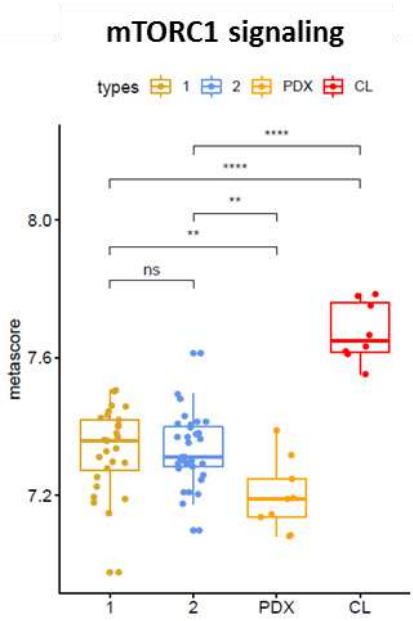


Figure 16. mTORC1 signaling is upregulated in retinoblastoma cell lines
Subtype 1 tumors (gold), subtype 2 tumors (blue), PDXs (orange), cell lines (red).

The most upregulated pathways (Hallmarks gene sets) in PDX when comparing against all primary tumors and subtype 1 tumors only were MYC targets, E2F targets and G2M checkpoint, difference that was not significant when comparing against subtype 2 tumors. When comparing PDX against subtype 1 tumors only, WNT beta catenin signaling appeared significantly upregulated in PDX, in addition to the aforementioned pathways. The metascore built from all genes included in this gene set, revealed that the WNT/beta catenin is in addition upregulated in subtype 2 tumors and cell lines (**Figure 17**).

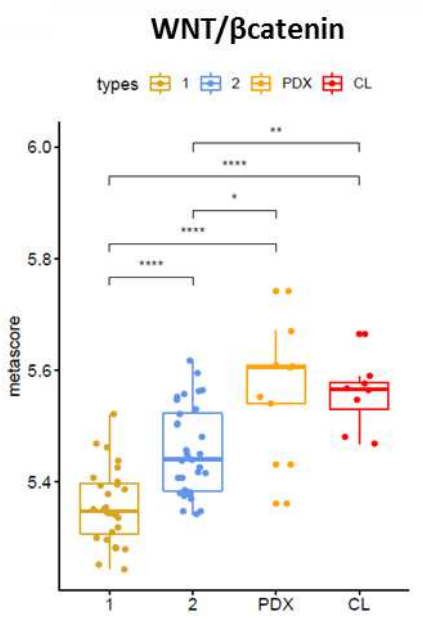


Figure 17. WNT/b-catenin is upregulated in PDXs and cell lines
Subtype 1 tumors (gold), subtype 2 tumors (blue), PDXs (orange), cell lines (red).

Downregulated genes and pathways in models

Significant downregulated GO terms in PDX and cell lines were “photoreceptor outer segment”, “photo-transduction” and “eye photoreceptor cell differentiation”. Another term that appeared downregulated in the models is “extracellular matrix” may be related to developmental processes. When comparing PDX against subtype 2 tumors only, GO term “regulation of ERK1 and ERK2 cascade” appears significantly downregulated in PDX, and is also downregulated in cells lines. The metascore built from all genes included in this gene set, revealed that the ERK1 and ERK2 cascade is upregulated in subtype 1 tumors, in agreement with its possible role in cell differentiation or apoptosis (Wortzel and Seger, 2011): indeed subtype 1 tumors are more differentiated and shows significant upregulation of apoptosis hallmark pathway (**Figure 18**), compared to subtype 2 tumors. Significant downregulated pathways in PDX and cell lines compared to all primary tumors, and to each tumor subtypes, were “hypoxia”, “epithelial mesenchymal transition”, KRAS signaling, TNF alpha signaling via NF-kB, “complement”, and “interferon gamma response”. All these GOs and pathways are not only significantly downregulated in preclinical models but also in subtype 2 tumors (**Table 11**, page 225).

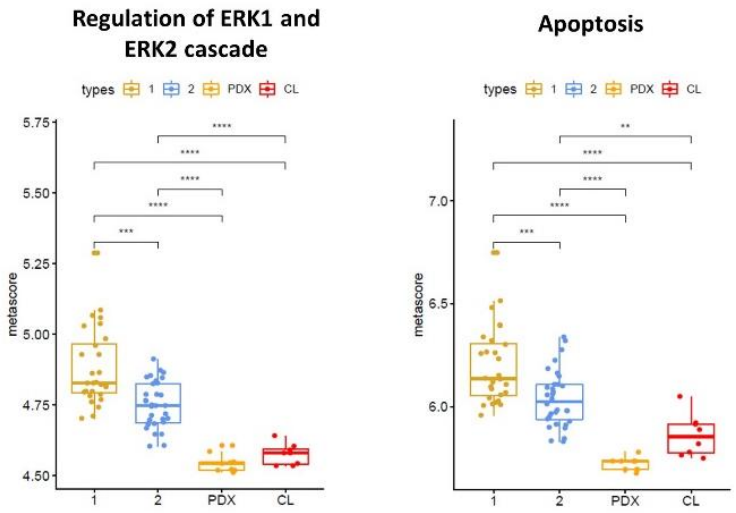


Figure 18. ERK1/ERK2 cascade and apoptosis pathway are upregulated in subtype 1 tumors

Retinal-cell-differentiation-associated genes

Using our retina cell type specific signatures, we aimed to determine those genes differentially expressed between primary retinoblastomas and preclinical models (**Figure 19**). Cone and rod photoreceptor-, late cone-, rod cell-, and Müller glia-associated genes are downregulated both in PDX and cell lines, compared to both subtype 1 and subtype 2 tumors. Early cone-, and intermediate cone-associated genes are upregulated in PDX while downregulated in cell lines. Retinal ganglion cells in PDX and cell lines are upregulated and downregulated when comparing to subtype 1 and subtype 2 tumors, respectively.

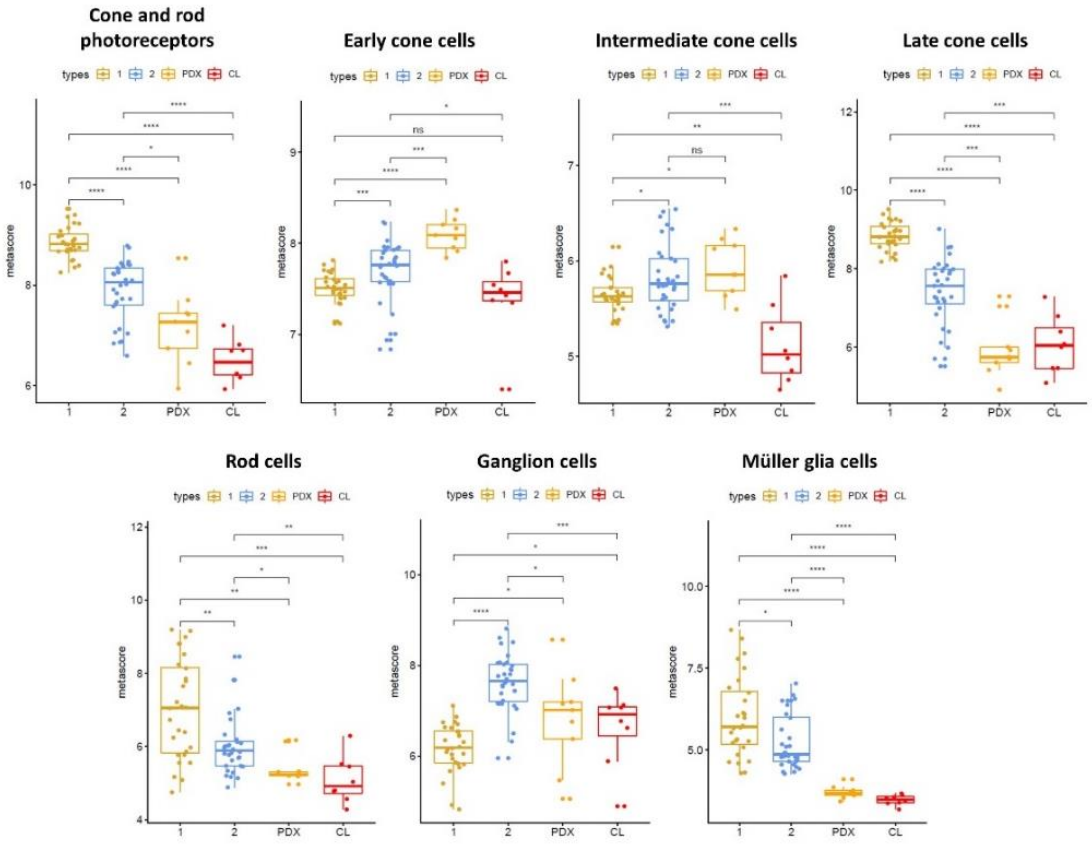


Figure 19. Retinal-cell-differentiation-associated genes
Subtype 1 tumors (gold), subtype 2 tumors (blue), PDX (orange), cell lines (red).

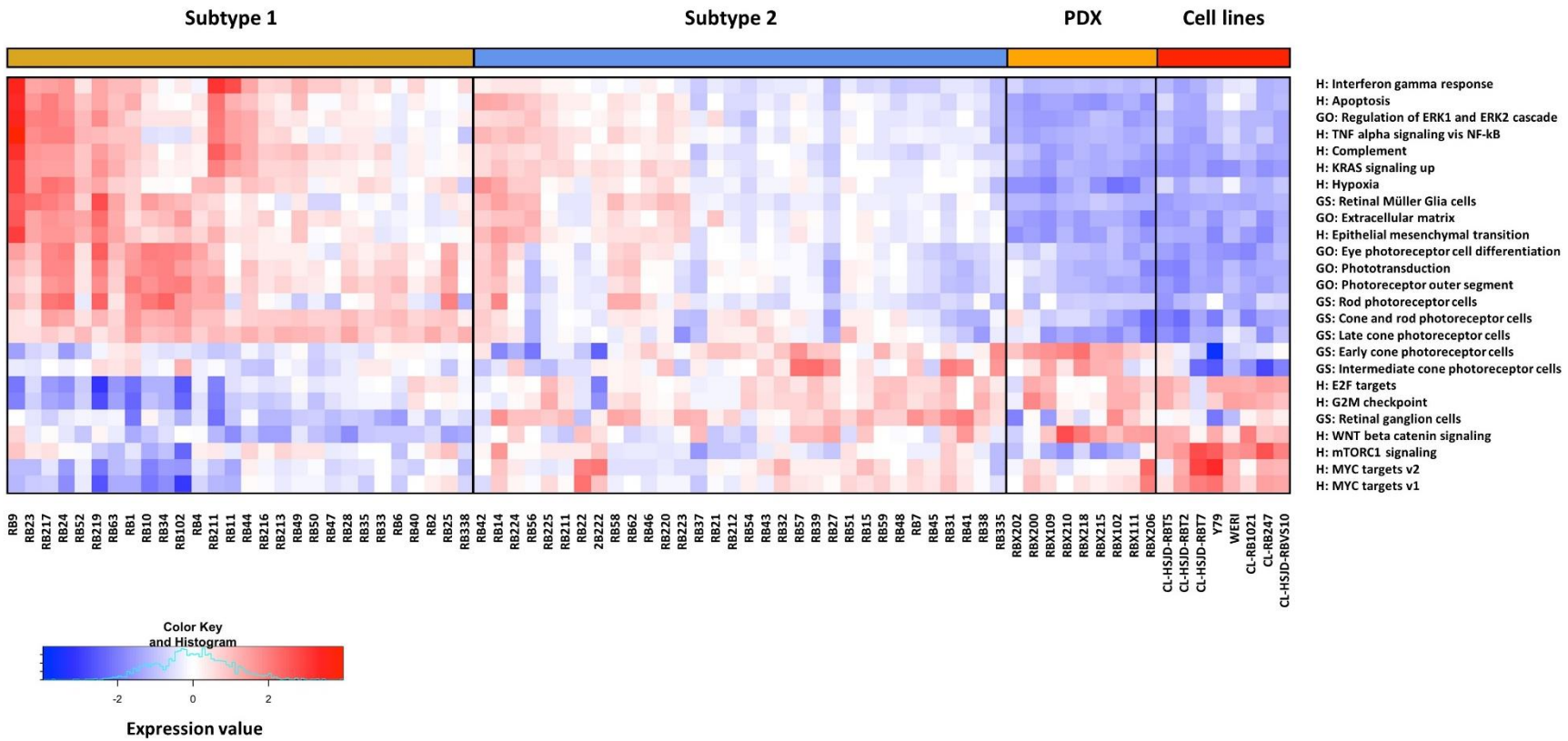


Figure 20. Heatmap of differentially expressed genes in retinoblastomas and preclinical models

Subtype 1 tumors (gold), subtype 2 tumors (blue), PDX (orange), cell lines (red). Gene ontology (GO), pathways in HALLMARK (H) and retinal-cell-gene signature (GS) of genes differentially expressed in primary tumors and in preclinical models of retinoblastoma.

DISCUSSION AND CONCLUSIONS

DNA PROFILING PROVIDES IDENTITY TO PRECLINICAL MODELS

STRs profiling was not only used to confirm the origin of the model to the primary tumor from which is derived, but also provides a unique identity to the model. This would be very useful for researchers in order to know we are working with the right model. Identity of a preclinical model is of importance especially when testing new treatments, given that results would be interpreted based on the molecular or genomic background of the preclinical model of choice. Publicly available data regarding DNA profiling of retinoblastoma cell lines is not exhaustive, being the two cell lines most used in retinoblastoma research (WERI and Y79) the only available ones (https://web.expasy.org/cellosaurus/CVCL_1792; https://web.expasy.org/cellosaurus/CVCL_1893).

RB1 MUTATIONS AND *MYCN* AMPLIFICATION STATUS

RB1 mutational status of preclinical models also provides information about its origin compared to their corresponding primary tumor. For most PDX, *RB1* mutations was assessed and confirm the original mutations found in the primary tumor. No special pattern of mutations was found in the models.

There are two PDXs (RBX202 and RBX211) and one cell model (Y79) with *MYCN* amplifications. Two additional cellular models (CL-HSJD-RBT2 and CL-HSJD-RBT7) derived from *MYCN* amplified tumors, and two PDXs derived (RBX111 and RBX200) from primary tumors with chromosomal 2p gains.

RETINOBLASTOMA PRECLINICAL MODELS MOSTLY DERIVE FROM TUMORS CLINICALLY CLASSED IN THE SUBTYPE 2

Results presented in the previous chapters indicated special clinical and molecular characteristics of subtype 2 tumors. This subtype is enriched in unilateral tumors coming from patients diagnosed later in life, harbored more somatic mutations per sample (included *BCOR* and *ARID1A* mutations), had more genomic instability and overexpressed genes that provide a proliferative advantage to tumoral cells (upregulation of MYC targets and cell cycle genes). In consequence, we have previously hypothesized that PDX and cellular models would mostly derived from this tumor subtype, as they would have an advantage to grow in artificial conditions, and indeed is what we found. Regarding clinical data of primary tumors, all PDX established derived from the mixed-subtype. Seven out of ten PDX included in this study (70%) derived from patients diagnosed after 18 months of age, and almost all of them derived from unilateral tumors (90%) (except RBX215). Regarding cell lines from HSJD, all of them derived from young patients (5-7 months). Two of them (CL-HSJD-RBT2, CL-HSJD-

RBT7) are *MYCN* amplified tumors, and we have seen that these tumors are diagnosed earlier and are molecularly classed in the subtype 2. Cell model CL-HSJD-RBVS10 has been derived from the vitreous seeding of the primary tumor. Vitreous seeding is a feature of tumors growing into the vitreous (Munier, 2014), and we have seen that endophytic tumors are enriched in the subtype 2.

PRECLINICAL MODELS CLASSED IN THE RETINOBLASTOMA MOLECULAR SUBTYPE 2

We have found some discrepancies between the technologies used for the molecular classification of primary tumors and preclinical models. For example, RB102 is classified in the subtype 1 by its transcriptome but is assigned to the subtype 2 by the pyrosequencing signature. In this particular case, we have concluded that tumor sampling in a heterogeneous tumor was the cause: the sample that was used for RNA extraction and subsequently analyzed by its transcriptome came from the Biological Resource Centre of the Curie Institute; while the DNA sample that was used for pyrosequencing was obtained in our lab by tumor- blade scratching, thus comprising all the tumoral surface, and not only a small portion as is usually done. Differences appearing when analyzing heterogeneous solid tumors should be taken into consideration to the assignment of a final subtype. The use of more than one technology helped us to attribute a molecular subtype, taking into consideration the chromosomal copy number changes in addition to our previous transcriptome-based and pyrosequencing-based molecular classification.

Samples with discording molecular subtypes (like RB102) were left unclassified. Eight out of the ten PDX models (80%), and six out of the eight cell models (75%) classified in the subtype 2, confirming our previous hypothesis. WERI cell line could not be attributed to any subtype by either the transcriptome or the pyrosequencing-based classification. Pyrosequencing would be of importance to perform in the PDXs and in four out of the eight cell lines that had not yet been analyzed by this technology. This also apply for the six primary tumors that had not been studied by any technology, and for HSJD-RBT/VS10 primary tumor that remained unclassified by the transcriptome-based classification.

IMMUNOHISTOCHEMICAL ANALYSIS REVEALED THAT MOST PDXs DO NOT RETAIN THE INTRA-TUMORAL HETEROGENEITY FOUND IN SUBTYPE 2 RETINOBLASTOMAS

We have previously identified an intra-tumoral phenotypic heterogeneity in retinoblastomas from the subtype 2, based on the discrete expression of CRX, ARR3, EBF3 and TFF1 proteins. We have hypothesized that PDXs deriving from subtype 2 tumors would retain this heterogeneity. The immunohistochemical-based comparison between primary tumors and PDXs revealed that PDXs are more likely to display a co-expression of the four markers, often losing the “mutual exclusive” pattern characteristic of a subset of subtype 2 tumors (**Figure 21**).

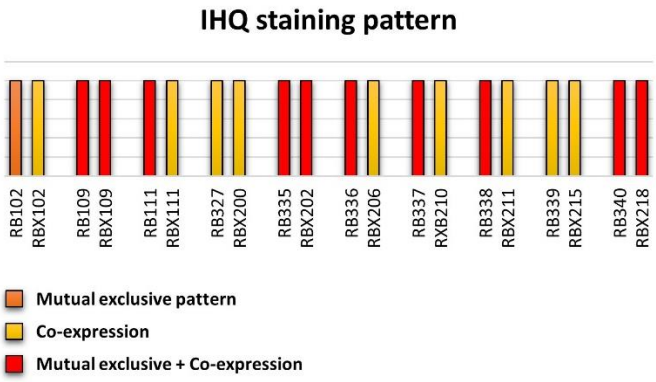


Figure 21. Intra-tumoral heterogeneity is often lost in PDXs models
Only one primary tumor displayed the "mutual exclusive pattern" that was lost in its PDX model (RB102/RBX102). Three PDXs model retained the intra-tumoral heterogeneity of their original tumor (RBX109, RBX202, RBX218), while the rest of the PDXs (N=7/10) displays a co-expression of the four markers (CRX, ARR3, TFF1, EBF3).

Three possible explanations could respond to these observations. First, a tumor sample is taken by inserting a needle into the enucleated eye; considering the intra-tumoral heterogeneity that exists in subtype 2 tumors, this sample could be enriched with a certain population of cells that would eventually grow in the mouse, thus developing a model that is not fully representative of the original tumor. A second possible explanation would be a clone of tumoral cells that does not grow in the PDX model. And third, the microenvironment of the tumor could play a role in the (mutual exclusive) pattern displayed by the primary tumors that is not fully identified in the PDXs, except for small areas of three models (RBX109, RBX202 and RBX218). Analyzing orthotopic models would answer to the question whether the eye microenvironment play a role in the phenotypic expression of the markers used.

Although cell lines analyzed showed expression of CRX, ARR3, EBF3 and TFF1, at different levels, heterogeneity in these models is not possible to analyze, with the techniques that we have used, because of their cellular organization, not tissue-arranged. Single-cell analysis could be performed to analyze a possible heterogeneity.

PDXs AND CELL LINES EXPRESS MYC AND MYCN PROTEINS AND SHOW UPREGULATION OF *MYC* SIGNALING-RELATED PATHWAYS

Gene Set Enrichment Analyses demonstrated that hallmarks MYC targets are upregulated in the preclinical models, as well as in subtype 2 tumors. In line with this, the protein profiling of PDXs and cell lines revealed that models expressed either MYC or MYCN, or both of them (**Figure 13**). We have previously seen that Y79, WERI and CL-RB247 cell lines expressed either MYCN or MYC at the protein level (**chapter 3**), and now, when analyzing a more extended series of models, we noted that a co-expression of both proteins do exist. Since most PDXs expressed MYC and/or MYCN proteins, they represent good candidates for testing the *in vivo* efficacy of BET inhibitors.

UPREGULATED PATHWAYS IN RETINOBLASTOMA SUBTYPES AND PRECLINICAL MODELS

The comparison analysis between PDXs against each retinoblastoma subtype, came up two pathways that are differentially expressed in: i) regulation of ERK1 and ERK2 cascade, when comparing against subtype 2, and ii) the Wnt/beta-catenin signaling, when we have compared against subtype 1 tumors.

Regulation of ERK1 and ERK2 cascade is significantly upregulated in subtype 1 tumors, while is downregulated in preclinical models and subtype 2 primary tumors. The extracellular signal-regulated kinase 1/2 (ERK1/2) cascade is a central signaling pathway that regulates a wide variety of stimulated cellular processes, including mainly proliferation, differentiation, and survival, but apoptosis and stress response as well (Wortzel and Seger, 2011). Subtype 1 tumors are histologically more differentiated than subtype 2 tumors, and also the apoptosis pathway is upregulated in subtype 1 tumors. This pathway is often upregulated in other human tumors and as such represents an attractive target for the development of anticancer drugs (Kohno and Pouyssegur, 2006).

Wnt/beta-catenin signaling in significantly upregulated in preclinical models and subtype 2 tumors, while is downregulated in subtype 1. The Wnt-signaling pathway is a known regulator of stem cell maintenance, cellular proliferation and differentiation, and has also been tightly associated with cancer (Giles et al., 2003). Wnt proteins also play a central role during various stages of retinal development and retinal field establishment (Das et al., 2008; Lad et al., 2009), and deregulation may play a role in retinoblastoma tumorigenesis. Besides, activation of the canonical Wnt/beta-catenin pathway might account for the *MYC* signaling upregulation seen in models and subtype 2 tumors, given that *MYC* is a beta-catenin transcriptional target (He et al., 1998). Deregulated Wnt has been suggested to drive the overexpression of *MYC* in non-*MYCN* amplified high-risk neuroblastomas (Liu et al., 2008). Therefore, subtype 2 tumors may deregulate MYC and other oncogenic genes via altered Wnt/beta-catenin signaling providing a potential candidate pathway for therapeutic inhibition.

Recently, it has been reported an interplay between MAPK/ERK pathway and Wnt/beta-catenin signaling in intestinal homeostasis (Kabiri et al., 2018). The balance between proliferation and differentiation in intestinal stem cells is regulated by Wnt/beta-catenin signaling. This group showed that *in vivo* inhibition of Wnt signaling induced a burst of proliferation in the stem cell compartment of the small intestine with a loss of intrinsic intestinal stem cells self-renewal, and that this process involved MAPK pathway activation, suggesting a role for Wnt signaling in suppressing the MAPK pathway to maintain a pool of intestinal stem cells. The interaction between Wnt and MAPK pathways in retinoblastoma may explain the differences seen in terms of differentiation and proliferation between both subtypes. Undoubtedly, these pathways should be explored in depth in each retinoblastoma tumoral subtype.

PRECLINICAL MODELS EXPRESS GENES RELATED TO EARLY-CONE-PHOTORECEPTORS AND RETINAL GANGLION CELLS

Based on an extended research in retinal-cell-associated genes, we have built a signature for cone and rod photoreceptors, as well as ganglion and Müller glia cells. The aim was to infer cell differentiation in primary tumors, as well as in the preclinical models. From these signatures, we found that PDX and cell lines are more related to subtype 2 tumor's differentiation than to subtype 1 tumors. Rod and Müller glia cell-associated genes were downregulated in preclinical models. These cell types were previously reported not to represent the pool of transformed retinoblastoma cells (Xu et al., 2009). Early-cone related genes (such as *ONECUT1* (Wang and Cepko, 2016), *THRB* and *RXRG* (Rodgers et al., 2016)) and retinal-ganglion related cells (such as *EBF3*, *GAP43* and *ISL1* (Trimarchi et al., 2007)) are upregulated in preclinical models as well as in subtype 2 tumors, while are downregulated in subtype 1 tumors. In the other hand, late-cone related genes associated to a more differentiated cell such as *ARR3* (Wu et al., 2015) and *GUCA1C* (Kaewkhaw et al., 2015) are downregulated in preclinical models as well as in subtype 2 tumors.

Table 1. Clinical characteristics of preclinical retinoblastoma models and primary tumors

Model ID	Tissue of origin	Latency period (months)	Model type	Center	Primary tumor ID	Gender	Age diagnosis (months)	Laterality	Familial	Treatment prior enucleation
RBX102	NA	NA	PDX	Curie	RB102	female	17,8	unilateral	no	no
RBX109	NA	2	PDX	Curie	RB109	female	15,9	unilateral	no	no
RBX111	NA	3,5	PDX	Curie	RB111	female	32,8	unilateral	no	no
RBX200	Tumor fragment	1,5	PDX	Curie	RB327	female	27,6	unilateral	no	no
RBX202	Cell suspension	NA	PDX	Curie	RB335	male	69,3	unilateral	no	no
RBX206	Cell suspension	3	PDX	Curie	RB336	female	57,1	unilateral	no	no
RXB210	Tumor fragment	3	PDX	Curie	RB337	male	40,2	unilateral	no	no
RBX211	Tumor fragment	2	PDX	Curie	RB338	male	16,3	unilateral	no	no
RBX215	Cell suspension	3	PDX	Curie	RB339	female	18,6	bilateral	yes	no
RBX218	Cell suspension	2	PDX	Curie	RB340	female	31,4	unilateral	no	no
WERI-Rb-1	NA		Cell model	ATCC[d]		female	12	NA	no	NA
Y79	NA		Cell model	ATCC[d]		female	30	NA	yes	NA
CL-RB247	NA		Cell model	IG[e]		male	NA	bilateral	NA	yes[a]
CL-RB1021	NA		Cell model	IG[e]		female	NA	bilateral	NA	NA
CL-HSJD-RBT2	Solid tumor		Cell model	HSJD[f]	HSJD-RBVS2	male	7	bilateral	no	yes[b]
CL-HSJD-RBT5	Solid tumor		Cell model	HSJD[f]	HSJD-RBT5	male	7	unilateral	no	yes[c]
CL-HSJD-RBT7	Solid tumor		Cell model	HSJD[f]	HSJD-RBT7	female	6	unilateral	no	no
CL-HSJD-RBVS10	Vitreous seeds		Cell model	HSJD[f]	HSJD-RBT10	female	5	bilateral	no	no

PDX: patient-derived xenograft; Curie: Curie Institute, Paris, France; ATCC: American Type Culture Collection; IG: Impact Genetics, Canada; HSJD: Sant Joan de Déu Hospital, Barcelona, Spain; Tx: treatment

a model derived from retinoblastoma solid tumor (RBT)

b model derived from retinoblastoma vitreal seeds (RBVS), small clusters of cells that are free floating in the vitreous of the eye

c Five doses of topotecan and melphalan in the ophthalmic artery

d Six cycles of systemic carboplatin, etoposide and vincristine, two doses of topotecan and melphalan in the ophthalmic artery, ruthenium brachytherapy

Table 2. Analysis and technologies performed for the characterization of preclinical models

				STRs fingerprinting		Transcriptome array		Pyrosequencing signature		Protein profiling (WB)			IHQ	
Model ID	**Model type**	**Primary tumor ID**	**passage analyzed**	**Model**	**Primary tumor**	**Model**	**Primary tumor**	**Model**	**Primary tumor**	**Model**	**Primary tumor**	**passage analyzed**	**Model**	**Primary tumor**
RBX102	PDX	RB102	p4	yes	yes	yes	yes	no	yes	yes	no	p6+1	yes	yes
RBX109	PDX	RB109	p5+1	yes	yes	yes	no	no	no	yes	no	p2	yes	yes
RBX111	PDX	RB111	p4	yes	yes	yes	no	no	no	yes	no	p3	yes	yes
RBX200	PDX	RB327	p4	yes	yes	yes	no	no	yes	yes	no	p3	yes	yes
RBX202	PDX	RB335	p3	yes	yes	yes	yes	no	no	yes	no	p3	yes	yes
RBX206	PDX	RB336	p5	yes	yes	yes	no	no	no	yes	no	p3	yes	yes
RXB210	PDX	RB337	p3	yes	yes	yes	no	no	no	yes	no	p3	yes	yes
RBX211	PDX	RB338	p3	yes	yes	no	yes	no	no	yes	no	p3	yes	yes
RBX215	PDX	RB339	p3	yes	yes	yes	no	no	no	yes	no	p3	yes	yes
RBX218	PDX	RB340	p3	yes	yes	yes	no	no	no	yes	no	p3	yes	yes
WERI-Rb-1	Cell line			yes		yes		yes		yes			yes	
Y79	Cell line			yes		yes		yes		yes			yes	
CL-RB247	Cell line			yes		yes		yes		yes			yes	
CL-RB1021	Cell line			yes		yes		yes		yes			no	
CL-HSJD-RBT2	Cell line	HSJD-RBVS2		yes	yes	yes	no	no	yes	yes	no		no	no
CL-HSJD-RBT5	Cell line	HSJD-RBT5		yes	no	yes	no	no	no	yes	no		no	no
CL-HSJD-RBT7	Cell line	HSJD-RBT7		yes	yes	yes	no	no	yes	yes	no		no	no
CL-HSJD-RBVS10	Cell line	HSJD-RBT10		yes	yes	yes	yes	no	no	yes	no		no	no

Table 3. DNA fingerprinting for models and their corresponding primary tumor

Sample ID	D3S1358	TH01	D21S11	D18S51	Penta E	D5S818	D13S317	D7S820	D16S539	CSF1PO	Penta D	AMEL	vWA	D8S1179	TPOX	FGA	Correlation
RBX102	14;18	9;9	29;30	12;14	5;11	11;13	11;-	12;13	12;13	12	9;12	X	14;17	10;14	8;11	21;21,2	97%
RB102	14;18	9;9	29;30	12;14	5;11	11;13	11;12	12;13	12;13	12	9;12	X	14;17	10;14	8;11	21;21,2	
RBX109	16;17	7;8	30,2;33,2	13;21	12;14	12;13	13	10	11;-	11;12	5;11	X	14;17	13;14	9;11	23;26	97%
RB109	16;17	7;8	30,2;33,2	13;21	12;14	12;13	13	10	11;12	11;12	5;11	X	14;17	13;14	9;11	23;26	
RBX111	17;19	6;7	30,2;32,2	12;18	11;12	12;13	12	8;10	-;11	10;13	9;12	X	18;19	14	9;12	22	97%
RB111	17;19	6;7	30,2;32,2	12;18	11;12	12;13	12	8;10	9;11	10;13	9;12	X	18;19	14	9;12	22	
RBX200	16;18	6;7	30;31	12;18	12	12	9	8;11	11;-	12	9;10	X	16;18	13;14	8;11	24	97%
RB327	16;18	6;7	30;31	12;18	12	12	9	8;11	11;13	12	9;10	X	16;18	13;14	8;11	24	
RBX202	14;16	6;9,3	28;30	15;20	11;13	10;12	12	10;11	12	13	9;13	X;Y	14;18	10;14	8	21	100%
RB335	14;16	6;9,3	28;30	15;20	11;13	10;12	12	10;11	12	13	9;13	X;Y	14;18	10;14	8	21	
RBX206	15;16	7;9,3	33,2;33,2	12;18	5;14	11;12	12;14	8;11	12;13	12	9;11	X;X	17;18	11;13	8	19;26	100%
RB336	15;16	7;9,3	33,2;33,2	12;18	5;14	11;12	12;14	8;11	12;13	12	9;11	X;X	17;18	11;13	8	19;26	
RBX210	15;17	7;9	29;35	14;20	8;14	12;13	12	8;11	9	7;12	2,2	X;Y	15;16	13;14	8;11	22;25	100%
RB337	15;17	7;9	29;35	14;20	8;14	12;13	12	8;11	9	7;12	2,2	X;Y	15;16	13;14	8;11	22;25	
RBX211	15;17	6	28;32,2	16;18	12;13	10;11	11;13	8;9	12;13	11;12	10;12	X;Y	17;21	14;15	8	21;22	100%
RB338	15;17	6	28;32,2	16;18	12;13	10;11	11;13	8;9	12;13	11;12	10;12	X;Y	17;21	14;15	8	21;22	
RBX215	15;18	9;10	29	16	10;11	10;12	11;12	9;11	11;13	10;11	11;14	X	17	13;15	11	20;24	100%
RB339	15;18	9;10	29	16	10;11	10;12	11;12	9;11	11;13	10;11	11;14	X	17	13;15	11	20;24	
RBX218	16;18	6;8	28;30	12;18	13;17	9;11	13	8;11	11	10;13	11;13	X	14;16	13	8;11	23	100%
RB340	16;18	6;8	28;30	12;18	13;17	9;11	13	8;11	11	10;13	11;13	X	14;16	13	8;11	23	
WERI-Rb-1	14;15	9,3	29	13;19	7;11	11;12	14	10;13	13	10;13	12;13	X	17;18	12;15	8;11	21	93%[a]
Y79	15;16	6;9,3	30;32	13;16	13;18	11;12	11;12	8;9	13;14	11;12	12	X	15;18	13;16	8	20;22	100%[b]
CL-RB247	14;18	8;9,3	28;30	14;17	17	11;13	8;11	10;12	12	12	9	X;Y	16;18	12;13	8;9	23	

CL-RB1021	16	7	29;32,2	13;15	7;10	12;15	13	9;10	13	10;11	12;13	X	16;17	11;14	8;11	23	
CL-HSJD-RBT2	16;17	9,3	30	14;16	10	11;12	11;13	11	11;12	9;12	9;14	X;Y	17;18	13;14	8	22;24	100%
HSJD-RBVS2	16;17	9,3	30	14;16	10	11;12	11;13	11	11;12	9;12	9;14	X;Y	17;18	13;14	8	22;24	
CL-HSJD-RBT5	17;18	9,3	30;32,2	14	7;17	12	12;13	8;11	12	12	9;14	X;Y	16;18	11;16	8;11	19;21	
HSJD-RBT5																	
CL-HSJD-RBT7	14;17	8;9,3	28;30	18;21	13	12	11;14	8;11	12;13	8;10	11;13	X	14;17	14	8;10	19;22	100%
HSJD-RBT7	14;17	8;9,3	28;30	18;21	13	12	11;14	8;11	12;13	8;10	11;13	X	14;17	14	8;10	19;22	
CL-HSJD-RBVS10	14;15	7;9	28;32	13;15	7;13	8;11	14	8;9	11;12	12	13;14	X	15;18	11;13	8;11	23;24	
HSJD-RBT10	14;15	7;9	28;32	13;15	7;13	8;11	14	8;9	11;12	12	13;14	X	15;18	11;13	8;11	23;24	100%
HSJD-RBVS10	14;15	7;9	28;32	13;15	7;13	8;11	14	8;9	11;12	12	13;14	X	15;18	11;13	8;11	23;24	

a Based on ATCC data provided by Cellosaurus, only 1 allele (allele 12) is missing for marker CSF1PO (alleles 10,12,13)

b Based on ATCC provided by Cellosaurus

Table 4. RB1 mutations and MYCN status in preclinical models and its original tumors

Sample ID	Germline	HIT 1		HIT 2		*MYCN*
RBX102		splice site	c.1389+1G>A	LOH		NA
RB102	yes					normal
RBX109		NA		NA		NA
RB109	mosaic	nonsense	c.2233A>T	NA		gain
RBX111		splice site	c.2106+2T>G	LOH		NA
RB111	no					normal
RBX200		prom meth		prom meth		NA
RB327	no					gain
RBX202		frameshift	c.1959del	LOH		amplification
RB335	no					
RBX206		deletion	prom-exon2	deletion	prom-exon17	NA
RB336	no					
RBX210		nonsense	c.751C>T	LOH		NA
RB337	no					
RBX211		deletion	prom-exon27	splice site	c.1498+2T>C	amplification
RB338	yes					
RBX215		missense	c.2132T>A	nonsense	c.2071G>T	NA
RB339	yes			NA		
RBX218		deletion	exon 18-27	deletion	prom-exon27	NA
RB340	no					
WERI-Rb-1	NA	deletion		deletion		normal
Y79	NA	splice site	IVS20+1G>A	deletion	exon 2-6	amplification
CL-RB247	yes	8–base pair deletion within exon 1		NA		normal
CL-RB1021	yes	CGA-TGA substitution in exon 10		NA		normal
CL-HSJD-RBT2		NA		NA		NA
HSJD-RBVS2	yes	splice site	c.1422-2A>G			amplification
CL-HSJD-RBT5		NA		NA		normal
HSJD-RBT5	no					
CL-HSJD-RBT7		NA		NA		NA
HSJD-RBT7	no					amplification
CL-HSJD-RBVS10		NA		NA		no
HSJD-RBT10	yes	frameshift	c.219_220dup			

NA: unknown/not determined; prom meth: gene promotor methylation

Table 5. Antibodies used in immunohistochemical staining

Antibody	Unmasking pH	Dilution for AFA	Dilution for formol	Exposition time	Detection	Exposition time	Chromogen
CRX	pH9	1/300	1/500	60min	N-histofine	30 min	DAB
ARR3	pH6	1/150	1/300	60 min	N-histofine	30 min	DAB
EBF3	pH6	1/800	1/800	60 min	N-histofine	30 min	DAB
TFF1	pH6	1/1000	1/1000	30 min	N-histofine	30 min	DAB
KI67	pH6	ene-00	1/2500	60 min	N-histofine	25+25 min	DAB

DAB: 3,3'-diaminobenzidine

Table 6. Histological characterization of PDX and primary tumor associated

			HES		
	Sample ID	**PDX passage**	**tumor size (mm)**	**necrosis**	**rosettes**
PDX	RBX102	p6+1	6	5%	0%
Primary tumor	RB102		13	20%	5%
PDX	RBX109	p2	12	50%	0%
Primary tumor	RB109		12	10%	5%
PDX	RBX111	p3	6	25%	0%
Primary tumor	RB111		17	5%	1%
PDX	RBX200	p3	2000	15%	0%
Primary tumor	RB327		NA	30%	40%
PDX	RBX202	p3	8	5%	0%
Primary tumor	RB335		12	10%	5%
PDX	RBX206	p3	9	10%	0%
Primary tumor	RB336		12	5%	1%
PDX	RXB210	p3	14	20%	0%
Primary tumor	RB337		NA	40%	30%
PDX	RBX211	p3	5	30%	0%
Primary tumor	RB338		17	15%	20%
PDX	RBX215	p3	13	35%	0%
Primary tumor	RB339		14	40%	1%
PDX	RBX218	p3	18	20%	0%
Primary tumor	RB340		13	20%	5%

NA: not determined

Table 7. Immunohistochemical analysis of primary tumors and PDX derived

				CRX		ARR3		EBF3		TFF1	
	Sample ID	**IHQ subtype**	**Staining pattern**	**positive cells**	**intensity**	**positive cells**	**intensity**	**positive cells**	**intensity**	**positive cells**	**intensity**
PDX	RBX102	C2	C	100%		100%		NA		100%	
Primary tumor	RB102	C2	ME	20%	S/W	20%	S/W	80%	S	80%	S
PDX	RBX109	C2	ME + C	100%		0%		10%		80%	
Primary tumor	RB109	C2	ME + C	70%		30%		70%		60%	
PDX	RBX111	C2	C	80%	W	75%	M	70%		100%	S
Primary tumor	RB111	C2	ME + C	90%		10%	W	90%		90%	
PDX	RBX200	C2	C	90%		90%		90%	S/W	90%	
Primary tumor	RB327	C2	C	70%	S/W	90%	S/W	70%	W	70%	M
PDX	RBX202	C1	ME + C	80%		100%	MD	5%		0%	
Primary tumor	RB335	C2	ME + C	95%	S	90%	M	70%		60%	M
PDX	RBX206	C2	C	100%	WD	100%	W	90%	M	40%	WD
Primary tumor	RB336	C2	ME + C	90%	M/S	50%	M	90%		50%	M
PDX	RBX210	C2	C	30%	W	100%	W/MD	15%	W	10%	W
Primary tumor	RB337	C2	ME + C	90%		70%	D	80%		30%	W/M
PDX	RBX211	C2	C	80%	W	10%	M	20%	W	80%	M
Primary tumor	RB338	NA	ME + C	100%	S	95%	S	10%	M	10%	M
PDX	RBX215	C2	C	100%	WD	30%	W	100%	WD	90%	M
Primary tumor	RB339	C2	C	90%	M	100%	M	100%	M	100%	M
PDX	RBX218	C2	ME + C	40%	W	90%	M	0%		60%	W/M
Primary tumor	RB340	C2	ME + C	90%	S	90%	M	90%	W	90%	M

Code for staining pattern. C: co-expression; ME: mutual exclusive or mirror image. Code for intensity of staining. S: strong; M/S: moderate and strong; S/W: strong and weak; M: moderate; MD: moderate and diffuse W: weak; W/M: weak and moderate; WD: weak and diffuse; D: diffuse

Table 8. Immunohistochemical staining performed on cell lines

		CRX	ARR3	EBF3	TFF1
Sample ID	**IHQ subtype**	**positive cells**	**positive cells**	**positive cells**	**positive cells**
WERI	C2	+++	+++	-	+
Y79	C2	+++	+++	+	-
CL-RB247	C2	+++	+++	+++	+++
CL-RBX109	C2	+++	++	+++	+++
CL-RBX111	C2	+++	++	+++	+++
CL-RBX200	C2	+++	+++	++	+
CL-RBX211	C2	++	++	+	+++
CL-RBX215	C2	+++	+	+++	+++

(-) negative; (+) <25%; (++) 25%-50%; (+++) >50%

Table 9. Final molecular classification of PDX, cell lines and primary tumor associated

	Sample ID	transcriptomic signature (33)	pyrosequencing signature	CNV (1q loss+16q loss or 2p gain)	Final subtype
PDX	RBX102	C2	no	no	**C2**
	RBX109	NA	no	no	**NA**
	RBX111	C2	no	no	**C2**
	RBX200	C2	no	no	**C2**
	RBX202	C1	no	C2	**C2**
	RBX206	C2	no	no	**C2**
	RXB210	C2	no	no	**C2**
	RBX211	no	no	C2	**C2**
	RBX215	C2	no	no	**C2**
	RBX218	NA	no	no	**NA**
Cell lines	WERI-Rb-1	NA	NA	no	**NA**
	Y79	NA	C2	no	**C2**
	CL-RB247	C2	C2	no	**C2**
	CL-RB1021	NA	C2	no	**C2**
	CL-HSJD-RBT2	C2	no	no	**C2**
	CL-HSJD-RBT5	C2	no	no	**C2**
	CL-HSJD-RBT7	NA	no	no	**NA**
	CL-HSJD-RBVS10	C2	no	no	**C2**
Primary tumors	RB102	C1	C2	no	**NA**
	RB109	no	no	C1	**C1**
	RB111	no	no	no	**ND**
	RB327	no	C2	C2	**C2**
	RB335	C2	no	no	**C2**
	RB336	no	no	no	**ND**
	RB337	no	no	no	**ND**
	RB338	C1	no	C2	**C2**
	RB339	no	no	no	**ND**
	RB340	no	no	no	**ND**
	HSJD-RBVS2	no	C2	no	**C2**
	HSJD-RBT5	no	no	no	**ND**
	HSJD-RBT7	no	C2	no	**C2**
	HSJD-RBT10	NA	no	no	**NA**
	HSJD-RBVS10	NA	no		

NA: analyzed, not assigned. ND: not analyzed, not assigned

Table 10. Gene ontology and pathways analysis of genes differentially expressed in PDX

Gene set	SIZE	NES	NOM p-val	FDR q-val
Group comparison: PDX vs Primary tumors				
HALLMARK_MYC_TARGETS_V1	49	2.35	<0,0001	<0,0001
HALLMARK_E2F_TARGETS	59	2.32	<0,0001	<0,0001
HALLMARK_G2M_CHECKPOINT	73	1.86	<0,0001	0,005
GO_DNA_PACKAGING_COMPLEX	23	2.90	<0,0001	<0,0001
GO_RIBONUCLEOPROTEIN_COMPLEX_LOCALIZATION	35	2.42	<0,0001	0,003
HALLMARK_EPITHELIAL_MESENCHYMAL_TRANSITION	88	-2.62	<0,0001	<0,0001
HALLMARK_TNFA_SIGNALING_VIA_NFKB	77	-2.60	<0,0001	<0,0001
HALLMARK_COMPLEMENT	68	-2.59	<0,0001	<0,0001
HALLMARK_HYPOXIA	76	-2.54	<0,0001	<0,0001
HALLMARK_INTERFERON_GAMMA_RESPONSE	70	-2.42	<0,0001	<0,0001
HALLMARK_KRAS_SIGNALING_UP	71	-2.41	<0,0001	<0,0001
HALLMARK_APOPTOSIS	60	-2.36	<0,0001	<0,0001
HALLMARK_MTORC1_SIGNALING	58	-1.89	0,001	0,002
GO_PHOTORECEPTOR_OUTER_SEGMENT	27	-2.59	<0,0001	<0,0001
GO_SENSORY_PERCEPTION_OF_LIGHT_STIMULUS	78	-2.55	<0,0001	<0,0001
GO_EXTRACELLULAR_MATRIX	141	-2.54	<0,0001	<0,0001
Group comparison: PDX vs C2 Primary tumors				
HALLMARK_HYPOXIA	68	-2.68	<0,0001	<0,0001
HALLMARK_TNFA_SIGNALING_VIA_NFKB	79	-2.68	<0,0001	<0,0001
HALLMARK_EPITHELIAL_MESENCHYMAL_TRANSITION	81	-2.58	<0,0001	<0,0001
HALLMARK_KRAS_SIGNALING_UP	60	-2.38	<0,0001	<0,0001
HALLMARK_COMPLEMENT	62	-2.37	<0,0001	<0,0001
HALLMARK_APOPTOSIS	53	-2.32	<0,0001	<0,0001
HALLMARK_INTERFERON_GAMMA_RESPONSE	68	-2.21	<0,0001	<0,0001
HALLMARK_MTORC1_SIGNALING	53	-1.87	<0,0001	0,003
GO_EXTRACELLULAR_MATRIX	134	-2.59	<0,0001	<0,0001
GO_REGULATION_OF_ERK1_AND_ERK2_CASCADE	61	-2.49	<0,0001	<0,0001
Group comparison: PDX vs C1 Primary tumors				
HALLMARK_E2F_TARGETS	101	2.94	<0,0001	<0,0001
HALLMARK_G2M_CHECKPOINT	124	2.63	<0,0001	<0,0001
HALLMARK_MYC_TARGETS_V1	91	2.59	<0,0001	<0,0001
HALLMARK_WNT_BETA_CATENIN_SIGNALING	18	1.93	<0,0001	0,003
HALLMARK_MYC_TARGETS_V2	31	1.92	<0,0001	0,003
HALLMARK_COMPLEMENT	98	-2.77	<0,0001	<0,0001
HALLMARK_INTERFERON_GAMMA_RESPONSE	113	-2.66	<0,0001	<0,0001
HALLMARK_HYPOXIA	100	-2.60	<0,0001	<0,0001
HALLMARK_EPITHELIAL_MESENCHYMAL_TRANSITION	106	-2.60	<0,0001	<0,0001
HALLMARK_KRAS_SIGNALING_UP	103	-2.43	<0,0001	<0,0001
HALLMARK_APOPTOSIS	76	-2.42	<0,0001	<0,0001
GO_PHOTORECEPTOR_OUTER_SEGMENT	40	-2.68	<0,0001	<0,0001
GO_EXTRACELLULAR_MATRIX	178	-2.56	<0,0001	<0,0001
GO_PHOTOTRANSDUCTION	26	-2.55	<0,0001	<0,0001

Table 11. Gene ontology and pathways analysis of genes differentially expressed in cell lines

Gene set	SIZE	NES	NOM p-val	FDR q-val
Group comparison: CL vs Primary tumors				
HALLMARK_E2F_TARGETS	85	2.53	<0,0001	<0,0001
HALLMARK_MTORC1_SIGNALING	114	2.48	<0,0001	<0,0001
HALLMARK_MYC_TARGETS_V1	73	2.39	<0,0001	<0,0001
HALLMARK_G2M_CHECKPOINT	87	2.25	<0,0001	<0,0001
HALLMARK_MYC_TARGETS_V2	31	1.91	<0,0001	0,005
GO_TRANSLATIONAL_TERMINATION	54	2.84	<0,0001	<0,0001
GO_AMINO_ACID_ACTIVATION	30	2.84	<0,0001	<0,0001
HALLMARK_EPITHELIAL_MESENCHYMAL_TRANSITION	86	-3.06	<0,0001	<0,0001
HALLMARK_KRAS_SIGNALING_UP	91	-2.76	<0,0001	<0,0001
HALLMARK_INTERFERON_GAMMA_RESPONSE	84	-2.70	<0,0001	<0,0001
HALLMARK_TNFA_SIGNALING_VIA_NFKB	96	-2.66	<0,0001	<0,0001
HALLMARK_COMPLEMENT	86	-2.54	<0,0001	<0,0001
HALLMARK_HYPOXIA	80	-2.22	<0,0001	<0,0001
HALLMARK_APOPTOSIS	77	-1.99	<0,0001	0,001
GO_PHOTORECEPTOR_OUTER_SEGMENT	34	-2.76	<0,0001	<0,0001
GO_EXTRACELLULAR_MATRIX	144	-2.75	<0,0001	<0,0001
GO_PHOTOTRANSDUCTION	24	-2.69	<0,0001	<0,0001
GO_EYE_PHOTORECEPTOR_CELL_DIFFERENTIATION	21	-2.54	<0,0001	<0,0001
Group comparison: CL vs C2 Primary tumors				
HALLMARK_MTORC1_SIGNALING	107	2.45	<0,0001	<0,0001
HALLMARK_E2F_TARGETS	74	2.03	<0,0001	0,002
HALLMARK_MYC_TARGETS_V1	66	2.01	<0,0001	0,002
HALLMARK_MYC_TARGETS_V2	20	1.74	0,011	0,015
HALLMARK_EPITHELIAL_MESENCHYMAL_TRANSITION	80	-3.04	<0,0001	<0,0001
HALLMARK_KRAS_SIGNALING_UP	82	-2.73	<0,0001	<0,0001
HALLMARK_TNFA_SIGNALING_VIA_NFKB	98	-2.57	<0,0001	<0,0001
HALLMARK_COMPLEMENT	81	-2.43	<0,0001	<0,0001
HALLMARK_INTERFERON_GAMMA_RESPONSE	77	-2.17	<0,0001	<0,0001
HALLMARK_HYPOXIA	80	-2.13	<0,0001	<0,0001
HALLMARK_APOPTOSIS	78	-1.87	<0,0001	0,004
GO_EXTRACELLULAR_MATRIX	131	-2.76	<0,0001	<0,0001
GO_PHOTORECEPTOR_OUTER_SEGMENT	31	-2.70	<0,0001	<0,0001
GO_PHOTOTRANSDUCTION	24	-2.62	<0,0001	<0,0001
Group comparison: CL vs C1 Primary tumors				
HALLMARK_E2F_TARGETS	122	2.83	<0,0001	<0,0001
HALLMARK_MYC_TARGETS_V1	110	2.60	<0,0001	<0,0001
HALLMARK_G2M_CHECKPOINT	140	2.47	<0,0001	<0,0001
HALLMARK_MTORC1_SIGNALING	118	2.29	<0,0001	<0,0001
HALLMARK_MYC_TARGETS_V2	43	2.25	<0,0001	<0,0001
HALLMARK_EPITHELIAL_MESENCHYMAL_TRANSITION	102	-2.78	<0,0001	<0,0001
HALLMARK_INTERFERON_GAMMA_RESPONSE	106	-2.76	<0,0001	<0,0001
HALLMARK_COMPLEMENT	99	-2.72	<0,0001	<0,0001

HALLMARK_KRAS_SIGNALING_UP	111	-2.65	<0,0001	<0,0001
HALLMARK_TNFA_SIGNALING_VIA_NFKB	114	-2.50	<0,0001	<0,0001
HALLMARK_HYPOXIA	88	-2.33	<0,0001	<0,0001
HALLMARK_APOPTOSIS	88	-2.13	<0,0001	<0,0001

CL: cell lines. SIZE: Number of genes in the gene set. NES: Normalized enrichment score; when positive is upregulated in the group, when negative is downregulated. NOM p-value: Nominal p value, the statistical significance of the enrichment score. FDR q-value: False discovery rate, the estimated probability that the normalized enrichment score represents a false positive finding.

Table 12. Statistical significance of the mestascore constructed from the genes included in the differentially expressed gene sets

	C1vsC2		C1vsPDX		C1vsCL		C2vsPDX		C2vsCL	
	pvalue	FDR	pvalue	FDR	pvalue	FDR	pvalue	FDR	pvalue	FDR
HALLMARK_G2M_CHECKPOINT	1,6E-09	6,6E-09	4,1E-06	6,0E-06	3,8E-06	5,0E-06	2,6E-01	3,0E-01	7,6E-03	8,3E-03
HALLMARK_E2F_TARGETS	2,5E-07	6,9E-07	2,2E-04	2,6E-04	2,9E-05	3,4E-05	3,4E-01	3,5E-01	1,1E-03	1,4E-03
HALLMARK_MYC_TARGETS_V1	4,7E-07	1,1E-06	5,6E-06	7,8E-06	1,7E-07	2,7E-07	1,6E-01	1,9E-01	2,0E-04	3,5E-04
HALLMARK_MYC_TARGETS_V2	4,2E-07	1,1E-06	1,2E-04	1,5E-04	5,7E-06	7,1E-06	9,0E-01	9,0E-01	9,6E-03	1,0E-02
HALLMARK_WNT_BETA_CATENIN_SIGNALING	1,5E-05	2,8E-05	1,4E-05	1,8E-05	5,9E-07	8,7E-07	1,1E-02	1,6E-02	2,1E-03	2,3E-03
HALLMARK_MTORC1_SIGNALING	5,9E-01	5,9E-01	3,5E-03	3,8E-03	8,5E-08	1,5E-07	1,9E-03	2,9E-03	1,3E-07	3,6E-07
HALLMARK_EPITHELIAL_MESENCHYMAL_TRANSITION	6,3E-03	7,6E-03	2,1E-08	3,8E-08	8,5E-08	1,5E-07	7,3E-09	2,3E-08	3,3E-08	1,6E-07
HALLMARK_KRAS_SIGNALING_UP	2,9E-04	4,6E-04	2,1E-08	3,8E-08	8,5E-08	1,5E-07	7,3E-09	2,3E-08	3,3E-08	1,6E-07
HALLMARK_TNFA_SIGNALING_VIA_NFKB	5,1E-02	5,5E-02	2,1E-08	3,8E-08	8,5E-08	1,5E-07	7,3E-09	2,3E-08	1,3E-07	3,6E-07
HALLMARK_COMPLEMENT	2,2E-07	6,9E-07	2,1E-08	3,8E-08	8,5E-08	1,5E-07	2,9E-08	8,1E-08	1,3E-07	3,6E-07
HALLMARK_INTERFERON_GAMMA_RESPONSE	4,8E-10	2,4E-09	2,1E-08	3,8E-08	8,5E-08	1,5E-07	2,6E-06	6,6E-06	7,0E-04	9,2E-04
HALLMARK_APOPTOSIS	5,6E-04	7,8E-04	2,1E-08	3,8E-08	2,5E-06	3,5E-06	7,3E-09	2,3E-08	4,9E-04	6,9E-04
HALLMARK_HYPOXIA	1,1E-04	2,0E-04	2,1E-08	3,8E-08	1,7E-07	2,7E-07	7,3E-09	2,3E-08	4,4E-06	8,5E-06
GO_PHOTORECEPTOR_OUTER_SEGMENT	2,6E-10	1,6E-09	2,1E-08	3,8E-08	8,5E-08	1,5E-07	5,9E-04	9,9E-04	9,8E-07	2,2E-06
GO_PHOTOTRANSDUCTION	3,2E-08	1,2E-07	2,1E-08	3,8E-08	8,5E-08	1,5E-07	4,4E-04	7,8E-04	6,2E-07	1,5E-06
GO_EYE_PHOTORECEPTOR_CELL_DIFFERENTIATION	1,4E-06	2,9E-06	4,2E-08	7,1E-08	8,5E-08	1,5E-07	1,7E-05	3,8E-05	3,3E-08	1,6E-07
GO_EXTRACELLULAR_MATRIX	2,2E-03	2,8E-03	2,1E-08	3,8E-08	8,5E-08	1,5E-07	7,3E-09	2,3E-08	3,3E-08	1,6E-07
GO_REGULATION_OF_ERK1_AND_ERK2_CASCADE	1,3E-04	2,1E-04	2,1E-08	3,8E-08	8,5E-08	1,5E-07	7,3E-09	2,3E-08	6,5E-08	2,7E-07
GS_ganglion	1,4E-11	1,1E-10	3,2E-02	3,2E-02	3,7E-02	3,9E-02	1,6E-02	2,1E-02	4,1E-04	6,1E-04
GS_rod	2,0E-03	2,6E-03	2,6E-04	3,0E-04	2,9E-05	3,4E-05	1,3E-02	1,8E-02	1,5E-03	1,8E-03
GS_mullerglia	2,5E-02	2,8E-02	2,1E-08	3,8E-08	8,5E-08	1,5E-07	7,3E-09	2,3E-08	3,3E-08	1,6E-07
GS_cone_early	5,6E-04	7,8E-04	2,1E-08	3,8E-08	5,2E-01	5,2E-01	9,1E-05	1,9E-04	1,9E-02	1,9E-02
GS_cone_intermediate	6,6E-02	6,8E-02	9,8E-03	1,0E-02	1,1E-03	1,2E-03	2,9E-01	3,2E-01	3,5E-04	5,8E-04
GS_cone_late	5,0E-12	6,3E-11	2,1E-08	3,8E-08	8,5E-08	1,5E-07	1,6E-04	3,1E-04	4,1E-04	6,1E-04
GS_cone_rod	5,0E-12	6,3E-11	2,5E-07	4,0E-07	8,5E-08	1,5E-07	1,8E-02	2,2E-02	4,4E-06	8,5E-06

BIBLIOGRAPHY

Aerts, I., Leuraud, P., Blais, J., Pouliquen, A.-L., Maillard, P., Houdayer, C., Couturier, J., Sastre-Garau, X., Grierson, D., Doz, F., et al. (2010). In vivo efficacy of photodynamic therapy in three new xenograft models of human retinoblastoma. Photodiagnosis Photodyn. Ther. *7*, 275–283.

Bejjani, A., Choi, M.R., Cassidy, L., Collins, D.W., Brien, J.M.O., Murray, T., Ksander, R., and Seigel, G.M. (2012). RB116 : An RB1 + retinoblastoma cell line expressing primitive markers. Mol. Vis. *18*, 2805–2813.

Benavente, C.A., McEvoy, J.D., Finkelstein, D., Wei, L., Kang, G., Wang, Y.D., Neale, G., Ragsdale, S., Valentine, V., Bahrami, A., et al. (2013). Cross-species genomic and epigenomic landscape of retinoblastoma. Oncotarget *4*, 844–859.

Boj, S.F., Hwang, C.-I., Baker, L.A., Chio, I.I.C., Engle, D.D., Corbo, V., Jager, M., Ponz-Sarvise, M., Tiriac, H., Spector, M.S., et al. (2015). Organoid Models of Human and Mouse Ductal Pancreatic Cancer. Cell *160*, 324–338.

Boyd, M.R. (1997). The NCI In Vitro Anticancer Drug Discovery Screen. In Anticancer Drug Development Guide, (Totowa, NJ: Humana Press), pp. 23–42.

Brennan, R.C., Federico, S., Bradley, C., Zhang, J., Flores-Otero, J., Wilson, M., Stewart, C., Zhu, F., Guy, K., and Dyer, M.A. (2011). Targeting the p53 pathway in retinoblastoma with subconjunctival Nutlin-3a. Cancer Res. *71*, 4205–4213.

Bruna, A., Rueda, O.M., Greenwood, W., Batra, A.S., Callari, M., Batra, R.N., Pogrebniak, K., Sandoval, J., Cassidy, J.W., Tufegdzic-Vidakovic, A., et al. (2016). A Biobank of Breast Cancer Explants with Preserved Intra-tumor Heterogeneity to Screen Anticancer Compounds. Cell *167*, 260–274.e22.

Chen, D., Livne-Bar, I., Vanderluit, J.L., Slack, R.S., Agochiya, M., and Bremner, R. (2004). Cell-specific effects of RB or RB/p107 loss on retinal development implicate an intrinsically death-resistant cell-of-origin in retinoblastoma. Cancer Cell *5*, 539–551.

Chevez-Barrios, P., Hurwitz, M.Y., Louie, K., Marcus, K.T., Holcombe, V.N., Schafer, P., Aguilar-Cordova, C.E., and Hurwitz, R.L. (2000). Metastatic and nonmetastatic models of retinoblastoma. Am. J. Pathol. *157*, 1405–1412.

Clarke, A.R., Maandag, E.R., van Roon, M., van der Lugt, N.M.T., van der Valk, M., Hooper, M.L., Berns, A., and te Rielef, H. (1992). Requirement for a functional Rb-1 gene in murine development. Nature *359*, 328–330.

Dalgard, C.L., Van Quill, K.R., and O'Brien, J.M. (2008). Evaluation of the in vitro and in vivo antitumor activity of histone deacetylase inhibitors for the therapy of retinoblastoma. Clin. Cancer Res. *14*, 3113–3123.

Daniel, V.C., Marchionni, L., Hierman, J.S., Rhodes, J.T., Devereux, W.L., Rudin, C.M., Yung, R., Parmigani, G., Dorsch, M., Peacock, C.D., et al. (2009). A Primary Xenograft Model of Small Cell Lung Cancer Reveals Irreversible Changes in Gene Expression Imposed by Culture In-Vitro. Cancer Res. *69*, 3364.

Das, A. V., Bhattacharya, S., Zhao, X., Hegde, G., Mallya, K., Eudy, J.D., and Ahmad, I. (2008). The Canonical Wnt Pathway Regulates Retinal Stem Cells/Progenitors in Concert with Notch Signaling. Dev. Neurosci. *30*, 389–409.

Dyer, M.A. (2016). Lessons from Retinoblastoma: Implications for Cancer, Development, Evolution, and Regenerative Medicine. Trends Mol. Med. *22*, 863–876.

Dyer, M.A., Rodriguez-Galindo, C., and Wilson, M.W. (2005). Use of preclinical models to improve treatment of retinoblastoma. PLoS Med. *2*, 0971–0976.

Fiebig, H.H., Neumann, H.A., Henss, H., Koch, H., Kaiser, D., and Arnold, H. (1985). Development of three human small cell lung cancer models in nude mice. Recent Results Cancer Res. *97*, 77–86.

Fujita, M., Hayata, S., and Taguchi, T. (1980). Relationship of chemotherapy on human cancer xenografts in nude mice to clinical response in donor patient. J. Surg. Oncol. *15*, 211–219.

Gallie, B.L., Holmes, W., and Phillips, R.A. (1982). Reproducible growth in tissue culture of retinoblastoma tumor specimens. Cancer Res. *42*, 301–305.

Gao, D., Vela, I., Sboner, A., Iaquinta, P.J., Karthaus, W.R., Gopalan, A., Dowling, C., Wanjala, J.N., Undvall, E.A., Arora, V.K., et al. (2014). Organoid cultures derived from patients with advanced prostate cancer. Cell *159*, 176–187.

Gao, H., Korn, J.M., Ferretti, S., Monahan, J.E., Wang, Y., Singh, M., Zhang, C., Schnell, C., Yang, G., Zhang, Y., et al. (2015). High-throughput screening using patient-derived tumor xenografts to predict clinical trial drug response. Nat. Med. *21*, 1318–1325.

Giles, R.H., Van Es, J.H., and Clevers, H. (2003). Caught up in a Wnt storm: Wnt signaling in cancer. Biochim. Biophys. Acta *1653*, 1–24.

Gillet, J.-P., Calcagno, A.M., Varma, S., Marino, M., Green, L.J., Vora, M.I., Patel, C., Orina, J.N., Eliseeva, T.A., Singal, V., et al. (2011). Redefining the relevance of established cancer cell lines to the study of mechanisms of clinical anti-cancer drug resistance. Proc. Natl. Acad. Sci. U. S. A. *108*, 18708–18713.

Griegel, S., Hong, C., Frötschl, R., Hülser, D.F., Greger, V., Horsthemke, B., and Rajewsky, M.F. (1990). Newly established human retinoblastoma cell lines exhibit an 'immortalized' but not an invasive phenotype in vitro. Int. J. Cancer *46*, 125–132.

He, T.C., Sparks, A.B., Rago, C., Hermeking, H., Zawel, L., da Costa, L.T., Morin, P.J., Vogelstein, B., and Kinzler, K.W. (1998). Identification of c-MYC as a target of the APC pathway. Science *281*, 1509–1512.

Hidalgo, M., Bruckheimer, E., Rajeshkumar, N.V., Garrido-Laguna, I., Oliveira, E. De, Rubio-Viqueira, B., Strawn, S., Wick, M.J., Martell, J., and Sidransky, D. (2011). A Pilot Clinical Study of Treatment Guided by Personalized Tumorgrafts in Patients with Advanced Cancer. Mol. Cancer Ther. *10*, 1311.

Houghton, J.A., Houghton, P.J., and Green, A.A. (1982). Chemotherapy of childhood rhabdomyosarcomas growing as xenografts in immune-deprived mice. Cancer Res. *42*, 535–539.

Inomata, M., Kaneko, A., Saijo, N., and Tokura, S. (1994). Culture of retinoblastoma cells from clinical specimens: growth-promoting effect of 2-mercaptoethanol. J. Cancer Res. Clin. Oncol. *120*, 149–155.

Jacks, T., Fazeli, A., Schmitt, E.M., Bronson, R.T., Goodell, M.A., and Weinberg, R.A. (1992). Effects of an Rb mutation in the mouse. Nature *359*, 295–300.

Johnson, J.I., Decker, S., Zaharevitz, D., Rubinstein, L. V, Venditti, J.M., Schepartz, S., Kalyandrug, S., Christian, M., Arbuck, S., Hollingshead, M., et al. (2001). Relationships between drug activity in NCI preclinical in vitro and in vivo models and early clinical trials. Br. J. Cancer *84*, 1424–1431.

Kabiri, Z., Greicius, G., Zaribafzadeh, H., Hemmerich, A., Counter, C.M., and Virshup, D.M. (2018). Wnt signaling suppresses MAPK-driven proliferation of intestinal stem cells. J. Clin. Invest. *128*, 3806–3812.

Kaewkhaw, R., Kaya, K.D., Brooks, M., Homma, K., Zou, J., Chaitankar, V., Rao, M., and Swaroop, A. (2015). Transcriptome Dynamics of Developing Photoreceptors in Three-Dimensional Retina Cultures Recapitulates Temporal Sequence of Human Cone and Rod Differentiation Revealing Cell Surface Markers and Gene Networks. Stem Cells *33*, 3504–3518.

Klco, J.M., Spencer, D.H., Miller, C.A., Griffith, M., Lamprecht, T.L., O'Laughlin, M., Fronick, C., Magrini, V., Demeter, R.T., Fulton, R.S., et al. (2014). Functional heterogeneity of genetically defined subclones in acute myeloid leukemia. Cancer Cell *25*, 379.

Kohno, M., and Pouyssegur, J. (2006). Targeting the ERK signaling pathway in cancer therapy. Ann. Med. *38*, 200–211.

Kooi, I.E., Mol, B.M., Massink, M.P.G., De Jong, M.C., De Graaf, P., Van Der Valk, P., Meijers-Heijboer, H., Kaspers, G.J.L., Moll, A.C., Te Riele, H., et al. (2016). A Meta-Analysis of Retinoblastoma Copy Numbers Refines the List of Possible Driver Genes Involved in Tumor Progression.

Lad, E.M., Cheshier, S.H., and Kalani, M.Y.S. (2009). Wnt-Signaling in Retinal Development and Disease. Stem Cells Dev. *18*, 7–16.

Laplante, M., and Sabatini, D.M. (2012). mTOR Signaling in Growth Control and Disease. Cell *149*, 274–293.

Lee, W.H., Murphree, A.L., and Benedict, W.F. (1984). Expression and amplification of the N-myc gene in primary retinoblastoma. Nature *309*, 458–460.

Lees, E., Faha, B., Dulic, V., Reed, S.I., and Harlow, E. (1992). Cyclin E/cdk2 and cyclin A/cdk2 kinases associate with p107 and E2F in a temporally distinct manner. Genes Dev. *6*, 1874–1885.

Lemaitre, S., Poyer, F., Marco, S., Fréneaux, P., Doz, F., Aerts, I., Desjardins, L., Cassoux, N., and Thomas, C.D. (2017). Looking for the most suitable orthotopic retinoblastoma mouse model in order to characterize the tumoral development. Investig. Ophthalmol. Vis. Sci. *58*, 3055–3064.

Liu, X., Mazanek, P., Dam, V., Wang, Q., Zhao, H., Guo, R., Jagannathan, J., Cnaan, A., Maris, J.M., and Hogarty, M.D. (2008). Deregulated Wnt/β-catenin program in high-risk neuroblastomas without MYCN amplification. Oncogene *27*, 1478–1488.

MacPherson, D., Sage, J., Kim, T., Ho, D., Mclaughlin, M.E., and Jacks, T. (2004). Cell type-specific effects of Rb deletion

in the murine retina. Genes Dev. *18*, 1681–1694.

Madreperla, S.A., Whittum-Hudson, J.A., Prendergast, R.A., Chen, P.-L., and Lee, W.-H. (1991). Intraocular Tumor Suppression of Retinoblastoma Gene-reconstituted Retinoblastoma Cells1.

McFall, R.C., Sery, T.W., and Makadon, M. (1977). Characterization of a new continuous cell line derived from a human retinoblastoma. Cancer Res. *37*, 1003–1010.

Munier, F.L. (2014). Classification and management of seeds in retinoblastoma. Ophthalmic Genet. *35*, 193–207.

O'Brien, J.M., Marcus, D.M., Bernards, R., Carpenter, J.L., Windle, J.J., Mellon, P., and Albert, D.M. (1990). A transgenic mouse model for trilateral retinoblastoma. Arch. Ophthalmol. (Chicago, Ill. 1960) *108*, 1145–1151.

Paderova, J., Orlic-Milacic, M., Yoshimoto, M., Da, G., Santos, C., Gallie, B., and Squire, J.A. (2007). Novel 6p rearrangements and recurrent translocation breakpoints in retinoblastoma cell lines identified by spectral karyotyping and mBAND analyses. Cancer Genet. Cytogenet. *179*, 102–111.

Pascual-Pasto, G., Olaciregui, N.G., Vila-Ubach, M., Paco, S., Monterrubio, C., Rodriguez, E., Winter, U., Batalla-Vilacis, M., Catala, J., Salvador, H., et al. (2016). Preclinical platform of retinoblastoma xenografts recapitulating human disease and molecular markers of dissemination. Cancer Lett. *380*, 10–19.

Reid, T.W., Albert, D.M., Rabson, A.S., Russell, P., Craft, J., Chu, E.W., Tralka, T.S., and Wilcox, J.L. (1974). Characteristics of an established cell line of retinoblastoma. J. Natl. Cancer Inst. *53*, 347–360.

Robanus-Maandag, E., Dekker, M., van der Valk, M., Carrozza, M.L., Jeanny, J.C., Dannenberg, J.H., Berns, A., and te Riele, H. (1998). p107 is a suppressor of retinoblastoma development in pRb-deficient mice. Genes Dev. *12*, 1599–1609.

Rodgers, H.M., Belcastro, M., Sokolov, M., and Mathers, P.H. (2016). Embryonic markers of cone differentiation. Mol. Vis. *22*, 1455–1467.

Rodríguez-cruz, M., Prado, M., and Salcedo, M. (2005). Perspectivas en la genómica del retinoblastoma : Implicaciones del gen supresor de tumor RB1. Rev. Investig. Clínica *57*, 572–581.

Shields, C.L., Shields, J.A., Baez, K., Cater, J.R., and De Potter, P. (1994). Optic nerve invasion of retinoblastoma. Metastatic potential and clinical risk factors. Cancer *73*, 692–698.

Shorthouse, A.J., Peckham, M.J., Smyth, J.F., and Steel, G.G. (1980). The therapeutic response of bronchial carcinoma xenografts: a direct patient-xenograft comparison. Br. J. Cancer. Suppl. *4*, 142–145.

Singh, H.P., Wang, S., Stachelek, K., Lee, S., Reid, M.W., Thornton, M.E., Craft, C.M., Grubbs, B.H., and Cobrinik, D. (2018). Developmental stage-specific proliferation and retinoblastoma genesis in RB-deficient human but not mouse cone precursors. Proc. Natl. Acad. Sci. *115*, 9391–9400.

Siolas, D., and Hannon, G.J. (2013). Patient-derived tumor xenografts: transforming clinical samples into mouse models. Cancer Res. *73*, 5315–5319.

Smyth, G.K. (2005). limma: Linear Models for Microarray Data. In Bioinformatics and Computational Biology Solutions Using R and Bioconductor, (New York: Springer-Verlag), pp. 397–420.

Stewart, E., Federico, S., Karlstrom, A., Shelat, A., Sablauer, A., Pappo, A., and Dyer, M.A. (2016). The Childhood Solid Tumor Network: A new resource for the developmental biology and oncology research communities. Dev. Biol. *411*, 287–293.

Stewart, E., Federico, S.M., Chen, X., Shelat, A.A., Bradley, C., Gordon, B., Karlstrom, A., Twarog, N.R., Clay, M.R., Bahrami, A., et al. (2017). Orthotopic patient-derived xenografts of paediatric solid tumours. Nature *549*, 96–100.

Tentler, J.J., Tan, A.C., Weekes, C.D., Jimeno, A., Leong, S., Pitts, T.M., Arcaroli, J.J., Messersmith, W.A., and Eckhardt, S.G. (2012). Patient-derived tumour xenografts as models for oncology drug development. Nat. Rev. Clin. Oncol. *9*, 338.

Townsend, E.C., Murakami, M.A., Christodoulou, A., Christie, A.L., Köster, J., DeSouza, T.A., Morgan, E.A., Kallgren, S.P., Liu, H., Wu, S.-C., et al. (2016). The Public Repository of Xenografts (ProXe) enables discovery and randomized phase II-like trials in mice. Cancer Cell *29*, 574.

Trimarchi, J.M., Stadler, M.B., Roska, B., Billings, N., Sun, B.E.N., and Bartch, B. (2007). Molecular Heterogeneity of Developing Retinal Ganglion and Amacrine Cells Revealed through Single Cell Gene Expression Profiling. *1065*, 1047–1065.

Ts'O, M.O.M., Fine, B.S., and Zimmerman, L.E. (1970). The Nature of Retinoblastoma. Ii. Photoreceptor Differentiation: An Electron Microscopic Study. Am. J. Ophthalmol. *69*, 350–359.

Venditti, J.M., Wesley, R.A., and Plowman, J. (1984). Current NCI preclinical antitumor screening in vivo: results of tumor panel screening, 1976-1982, and future directions. Adv. Pharmacol. Chemother. *20*, 1–20.

Vidal, A., Muñoz, C., Guillén, M.-J., Moretó, J., Puertas, S., Martínez-Iniesta, M., Figueras, A., Padullés, L., García-Rodriguez, F.J., Berdiel-Acer, M., et al. (2012). Lurbinectedin (PM01183), a new DNA minor groove binder, inhibits growth of orthotopic primary graft of cisplatin-resistant epithelial ovarian cancer. Clin. Cancer Res. *18*, 5399–5411.

Wang, S., and Cepko, C.L. (2016). Photoreceptor fate determination in the vertebrate retina. Investig. Ophthalmol. Vis. Sci. *57*, ORSFe1-ORSFe6.

van de Wetering, M., Francies, H.E., Francis, J.M., Bounova, G., Iorio, F., Pronk, A., van Houdt, W., van Gorp, J., Taylor-Weiner, A., Kester, L., et al. (2015). Prospective derivation of a living organoid biobank of colorectal cancer patients. Cell *161*, 933–945.

Wortzel, I., and Seger, R. (2011). The ERK Cascade: Distinct Functions within Various Subcellular Organelles. Genes and Cancer *2*, 195–209.

Wu, F., Kaczynski, T.J., Sethuramanujam, S., Li, R., Jain, V., Slaughter, M., and Mu, X. (2015). Two transcription factors, Pou4f2 and Isl1, are sufficient to specify the retinal ganglion cell fate. Proc. Natl. Acad. Sci. *112*, E1559–E1568.

Xu, X.L., Fang, Y., Lee, T.C., Forrest, D., Gregory-Evans, C., Almeida, D., Liu, A., Jhanwar, S.C., Abramson, D.H., and Cobrinik, D. (2009). Retinoblastoma has properties of a cone precursor tumor and depends upon cone-specific MDM2 signaling. Cell *137*, 1018–1031.

Zarzosa, P., Navarro, N., Giralt, I., Molist, C., Almazan-Moga, A., Vidal, I., Soriano, A., Segura, M.F., Hladun, R., Villanueva, A., et al. (2017). Patient-derived xenografts for childhood solid tumors: a valuable tool to test new drugs and personalize treatments. Clin. Transl. Oncol. *19*, 44–50.

Zayed, A.A., Mandrekar, S.J., and Haluska, P. (2015). Molecular and clinical implementations of ovarian cancer mouse avatar models. Chinese Clin. Oncol. *4*, 30.

Zhang, J., Schweers, B., and Dyer, M.A. (2004). The first knockout mouse model of retinoblastoma. Cell Cycle *3*, 952–959.

Zhang, J., Benavente, C.A., McEvoy, J., Flores-Otero, J., Ding, L., Chen, X., Ulyanov, A., Wu, G., Wilson, M., Wang, J., et al. (2012). A novel retinoblastoma therapy from genomic and epigenetic analyses. Nature *481*, 329–334.

FINAL CONCLUSIONS AND PERSPECTIVES

During my doctoral research, I sought to perform a comprehensive characterization of one of the two molecular subtypes of retinoblastoma previously identified by my group: the retinoblastoma subtype 2. The different approaches and analyses performed, allowed us to build a portrait of these retinoblastomas and to highlight their main clinical characteristics, their genomic and mutational landscape, and their molecular background. We then used this same approach to characterize preclinical models of retinoblastoma, and we characterized the clinical and molecular profile of several patient-derived xenograft models obtained at Curie, and different cell lines commonly used in retinoblastoma research.

Doing a brief summary gathering the main results of my thesis, I would say that from a clinical point of view, retinoblastoma subtype 2 comes mostly from unilateral patients diagnosed after 18 months, with few cases presenting *RB1* germline mutations. These tumors seems to represent a more aggressive phenotype, since they harbor more somatic mutations per sample, display more genomic instability and are characterized by a more proliferative phenotype showing upregulation of *MYC* signaling pathway and cell cycle genes. Besides, *MYCN*-amplified tumors are classified in this molecular subtype. Retinoblastoma preclinical models shared many of these molecular characteristics, confirming our hypothesis that most PDXs models and cell lines would derived from a more aggressive retinoblastoma subtype. Indeed, most preclinical models were classified in the molecular subtype 2. PDXs and most of the cell lines express MYC and MYCN at the protein level, and show upregulation of MYC signaling-related pathways. We have explored MYC signaling as a new therapeutic target in retinoblastoma and found that the treatment with BET-bromodomain inhibitors (OTX015 and JQ1) strongly reduced viability of three retinoblastoma cell lines *in vitro*, accompanied by a MYC/MYCN downregulation at the mRNA and protein levels, in two of these cell models.

Throughout the four chapters of this thesis, I presented and discussed the main results obtained, which not only provided several important observations, but also opened the door to futures investigations that are discussed below.

OPEN QUESTIONS AND FUTURE DIRECTIONS

Do the preclinical models retain the intra-tumoral heterogeneity of subtype 2 tumors?

One distinctive characteristic of subtype 2 tumors that was not fully reproduced by the heterotopic PDXs models, was the intra-tumoral heterogeneity assessed on the retinal cone- (ARR3) and retinal ganglion cell- (EBF3, TFF1) associated protein pattern of expression. Analyzing orthotopic models would answer to the question whether the eye microenvironment play a role in the phenotypic

expression of the markers used. Single-cell analysis would be the method to analyze a possible heterogeneity existing in the cell lines.

Deregulated WNT-beta catenin and ERK signaling, do play important roles in retinoblastoma tumorigenesis? Could these signaling pathways represent new specific targets for retinoblastoma treatment?

We have identified two pivotal signaling pathways upregulated in each retinoblastoma subtype: WNT-beta catenin in subtype 2 and preclinical models, and ERK signaling in subtype 1 tumors. Undoubtedly, these pathways should be explored in depth in each retinoblastoma tumoral subtype to a better understanding of their significance in retinoblastoma tumorigenesis. These deregulated signaling pathways may also represents potential candidates for clinical therapeutic inhibition.

MYC signaling as a new therapeutic target in retinoblastoma

We provided preliminary results to explore this new therapeutic avenue of BET protein inhibition in retinoblastoma. Further functional experiments would be of interest to perform in order to analyze the gene expression profiling following exposure to BETi, and to explore the underlying mechanisms that affect cell viability and the alternative targets, besides *MYC* and *MYCN*, that BET proteins could have in the retinoblastoma context. *In vivo* experiments will be shortly performed with the PDXs models that were molecularly characterized and presented in this thesis. These PDXs models were subcutaneously derived (heterotopic models). Considering that the eye represents a special physiological compartment, it would be of interest also to explore the efficacy of BET inhibitors using orthotopic retinoblastoma models.

Does TFF1 truly play an oncogenic role in retinoblastoma?

Several results led us to suppose that TFF1 could have an oncogenic role in retinoblastoma, but we were not able to decipher a functional role of *TFF1* in subtype 2 retinoblastomas with the *in vitro* experiments performed. Future experiments regarding cell invasion, using stably transfected cells and orthotopic retinoblastoma models would be interesting to perform in order to evaluate *TFF1* action *in vivo* in a more natural microenvironment.

Do retinoblastoma subtypes display different RB1 mutation patterns?

Distribution of mutations alongside the *RB1* gene has so far been analyzed in terms of a single group of retinoblastomas. We showed that mutation distribution between our retinoblastoma subtypes was significantly different. We also showed that mutations occurring in exons 14 and 15 of the *RB1* gene were exclusively found in subtype 2 tumors, thus creating a “mutational gap” in subtype 1 tumors where virtually no mutations were detected. We have performed an analysis of an independent and larger cohort of patients carrying *RB1* germline mutations, and noted a significant enrichment of *RB1* mutations in exon 14 of non-enucleated patients, therefore possibly explaining

the absence of mutations in this exon in our cohort of enucleated patients: subtype 1 tumors with mutations in this exon would be less aggressive and/or more sensitive to treatment and would therefore not be enucleated and not considered in our analyses, which have been performed only in enucleated tumors. The analysis of a larger series would be required to test this hypothesis and to analyze the *RB1* mutation distribution along the RB1 protein.

université PARIS-SACLAY | ÉCOLE DOCTORALE Cancérologie, biologie, médecine, santé (CBMS)

Titre : Caractérisation approfondie du rétinoblastome humain de sous-type 2 et des modèles précliniques

Mots clés : rétinoblastome, sous-types moléculaires, *TFF1*, *MYC/MYCN*, OTX015/JQ1, modèles précliniques

Résumé : Le rétinoblastome, un cancer pédiatrique de la rétine en développement, est la tumeur intraoculaire la plus fréquente chez l'enfant et représente environ 4 % de tous les cancers infantiles. Notre groupe a précédemment caractérisé deux sous-types de rétinoblastomes. Les tumeurs de type « cone-like » ou sous-type 1 et les tumeurs « mixed-type » ou sous-type 2. Le but général de ma thèse était d'approfondir la caractérisation moléculaire des rétinoblastomes de sous-type 2. Nous avons caractérisé le paysage moléculaire et génomique du rétinoblastome dans une série de 102 tumeurs primaires, intégrant des échantillons de l'Institut Curie (France), l'Hôpital Garrahan (Argentine) et l'Hôpital Sant Joan de Déu (Espagne). L'analyse du paysage mutationnel a révélé que les tumeurs du sous-type 2 avaient plus de mutations somatiques par échantillon que les tumeurs du sous-type 1, notamment *BCOR* et *ARID1A,* les deux gènes mutés de manière récurrente. La distribution des mutations sur le gène *RB1* était significativement différente entre les deux sous-types. En plus des mutations somatiques, nous avons caractérisé deux événements récurrents de fusion chromosomique perturbant le gène *DACH1*. *TFF1*, non exprimée dans la rétine normale, est surexprimé dans le sous-type 2. L'analyse par immunohistochimie de TFF1 dans des tumeurs localement invasives a révélé la présence de cellules TFF1+ envahissant la région rétrolaminaire du nerf optique. Nous avons exploré un possible rôle oncogène de TFF1 dans le rétinoblastome lié à la survie, à la migration et à l'invasion cellulaire, qui n'a finalement pas été mis en évidence *in vitro*. Le sous-type moléculaire 2 regroupe les tumeurs *MYCN* amplifiées et les tumeurs avec une activation de la voie de signalisation MYC et des gènes cibles de *MYC*. L'utilisation de JQ1 et OTX015 (inhibiteurs des protéines BET) a fortement réduit la viabilité *in vitro* de lignées cellulaires de rétinoblastomes représentatives du sous-type 2, avec une régulation négative significative du gène et de la protéine MYC/MYCN. Nos résultats préliminaires suggèrent une nouvelle piste thérapeutique par l'inhibition des protéines BET dans le rétinoblastome. Pour caractériser les modèles précliniques largement utilisés dans la recherche sur le rétinoblastome nous avons utilisé la même approche que pour la classification des tumeurs primaires et avons constaté que la plupart des modèles cellulaires et PDX étudiés sont classés dans le sous-type 2 et partageaient des caractéristiques moléculaires, génomiques et protéiques des tumeurs primaires de ce sous-type moléculaire. Dans l'ensemble, j'ai effectué une caractérisation plus approfondie des rétinoblastomes de sous-type 2, qui semble représenter un phénotype plus agressif, et qui est le sous-type représenté dans les modèles précliniques analysés.

Title: In-depth characterization of human retinoblastoma subtype 2 and preclinical models

Keywords: retinoblastoma, molecular subtypes, *TFF1*, *MYC/MYCN*, OTX015/JQ1, preclinical models

Abstract: Retinoblastoma (RB) is a rare pediatric cancer of the developing retina that represents the most common intraocular tumor in children, and accounts for about 4% of all childhood cancers. Our group has previously characterized two RB subtypes. The cone-like or subtype 1 and the mixed-type or subtype 2 tumors. We characterized the molecular and genomic landscape of RB in a series of 102 primary tumors, integrating samples from the Curie Institute (France), the Garrahan Hospital (Argentina) and the Sant Joan de Déu Hospital (Spain). Analysis of the mutational landscape revealed that tumors from the subtype 2 had significantly more somatic mutations per sample than tumors from the subtype 1, including *BCOR* and *ARID1A,* two recurrently mutated genes. The distribution of mutations alongside the *RB1* gene was significantly different between the two subtypes. Besides somatic mutations, we characterized two recurrent chromosomal fusion events disrupting *DACH1*. Subtype 2 tumors overexpress *TFF1*, not expressed in the normal retina. Immunohistochemical analysis of TFF1 in locally invasive tumors revealed the presence of TFF1+ cells invading the retrolaminar region of the optic nerve. We explored a possible oncogenic role of TFF1 in RB related to cell survival, cell migration and cell invasion, which was not fully uncovered. Molecular subtype 2 regroups the *MYCN* amplified tumors and tumors with MYC signaling pathway activation and upregulation of hallmark MYC target genes. The use of JQ1 and OTX015 (BET inhibitors) strongly reduced the viability *in vitro* of retinoblastoma cell lines representatives of the subtype 2, together with a significant MYC/MYCN gene and protein downregulation, providing preliminary results to explore a new therapeutic avenue of BET protein inhibition in RB. In order to characterize preclinical models widely used in RB research, we used the same approach as for primary human tumor's classification, and found that most cellular and PDX models studied are classified in the molecular subtype 2 and shared many of the molecular, genomic and protein characteristics found in primary tumors of this molecular subtype. Taken together, I have performed a deeper characterization of subtype 2 retinoblastomas, which seems to represent a more aggressive phenotype, and is the represented subtype in the preclinical models analyzed.